Investigations of water splitting for hydrogen generation using layered chalcogenides, Weyl semimetals, and other materials as catalysts and for oxygen generation using oxide catalysts

A thesis submitted for the degree of

Doctor of Philosophy

In the faculty of Science

by

Uttam Gupta

Chemistry and Physics of Materials Unit
Jawaharlal Nehru Centre for Advanced Scientific Research
(*A Deemed University*)
Bangalore, India.

August 2018

Dedicated to my family

and teachers

DECLARATION

I hereby declare that the matter embodied in this thesis entitled "**Investigations of water splitting for hydrogen generation using layered chalcogenides, Weyl semimetals, and other materials as catalysts, and for oxygen generation using oxide catalysts**" is the result of investigations carried out by me under supervision of Prof. C. N. R. Rao, FRS at the Chemistry and Physics of Materials Unit, Jawaharlal Nehru Centre for Advanced Scientific Research, Bangalore, India and that it has not been submitted elsewhere for the award of any degree or diploma.
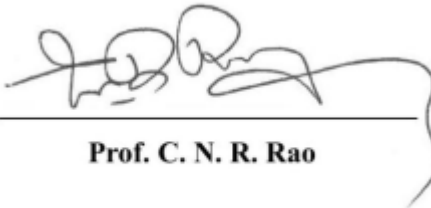
In keeping with the general practice of reporting scientific observations, due acknowledgment has been made whenever the work described is based on the findings of other investigators.

Uttam Gupta

CERTIFICATE

I hereby certify that the matter embodied in this thesis entitled "**Investigations of water splitting for hydrogen generation using layered chalcogenides, Weyl semimetals and other materials as catalysts, and for oxygen generation using oxide catalysts**" has been carried out by Mr. Uttam Gupta at the Chemistry and Physics of Materials Unit, Jawaharlal Nehru Centre for Advanced Scientific Research, Bangalore, India under my supervision and it has not been submitted elsewhere for the award of any degree or diploma.

Prof. C. N. R. Rao

(Research Supervisor)

Acknowledgments

I am extremely thankful to **Prof. C.N.R. Rao**, **FRS,** my research supervisor and take this opportunity to express my immense gratitude to him.

"Guru gobind dou khade,kaake lagoon pay (Guru and God both are here to whom should I first bow)
Balihari guru aapne gobind diyo batay (All glory be unto the guru the path to God who did bestow)"

He not only introduced me to the field of Material Science but also has helped me with his invaluable guidance and fascinating constant encouragement. He is a person of immense enthusiasm and wisdom. It is a vibrant and fulfilling experience to work under his guidance. He has taught me the various facts of science, the way of understanding the problem and how to maintain a level-headed approach when problems do not work.

I thank Prof. U. V. Waghmare, Prof. S. K. Pati, Dr. Ranjan Dutta, Dr. A. Govindaraj, Prof. C. Felser, Prof. R. Tenne, Prof. S. Parkin, Dr. D. J. Late, Dr. Mrinmoy De and Dr. B. Yan for their fruitful collaborations, support, and insightful suggestions.

I thank Dr. U. Maitra, Dr. B.S Naidu, Dr. K. Pramoda, Dr. D. S. Narang, Dr. A Singh, Dr. S. N. Shirodkar, Dr. A. Bandhyopadhyay, Dr. C. Shekhar, Dr. N. Kumar, Dr. C. R. Rajamathi, Dr. S. Kouser, Dr. M. K. Jana, Dr. I. Ahmad, Dr. K. Pal, Dr. B. E Prasad, Mr. M. Chettri and Mr. B. G. Rao for their fruitful collaborations. I have been greatly benefitted from their expertise and discussions and learned a lot in the process.

I extend my sincere thanks to Dr. A. Govindaraj who was cooperative whenever I approached him for help.

I would like to thank all my present and past lab mates, Dr. U. Maitra, Dr. N. Kumar, Dr. K. Moses, Dr. K. Vasu, Dr. P. Chithaiah, Dr. H.S.S.R. Matte, Dr. B. Das, Dr. B. Chitara, Dr. R. Saha, Dr. Gopal, Dr. R. Kumar, Dr. S. Dey, Dr. P.

Contents

PART 1. Photochemical H$_2$ generation from water splitting using transition metal dichalcogenides and other materials

Chapter 1. A general overview: Photochemical hydrogen evolution and transition metal dichalcogenides as a catalyst

Chapter 2. Dye-sensitized hydrogen generation by using 2H- and 1T-forms of group 6 transition metal dichalcogenides

Chapter 3. Photocatalytic water splitting based on covalently linked assemblies of MoS_2 with RGO and C_3N_4

Chapter 4. Visible-light-induced hydrogen evolution reaction by tungsten sulfoselenides

Chapter 5. Visible-light-induced generation of H_2 by nanocomposites of few-layer TiS_2 and TaS_2 with CdS nanoparticles

Chapter 6. Hydrogen evolution properties of layered gallium chalcogenides

PART 2. Photochemical hydrogen evolution reaction based on Weyl semimetals and topological insulators

PART 3. Electrochemical hydrogen evolution by MoS$_2$ Fullerenes

Effects of p-and n-type doping in inorganic fullerene (IF)-MoS$_2$ on the hydrogen evolution reaction

PART 4. Hydrazine as a hydrogen carrier in the photocatalytic generation of H$_2$

PART 5. Photochemical Water oxidation using Co and Mn-based oxides

Visible-light-induced oxidation of water by rare earth manganites, cobaltites and related oxides and remarkable effect of Pt nanoparticles

Preface

The thesis consists of five parts. **Part 1** deals with extensive study of photochemical hydrogen generation from water using transition metal dichalcogenides. Chapter 1 in **Part 1** gives an overview of photochemical hydrogen evolution and catalytic activity of transition metal dichalcogenides. In Chapter 2 reports dye sensitized hydrogen evolution by using 2H- and 1T- forms of group 6 transition metal dichalcogenides. The metallic 1T-form is found to be a superior catalyst than the 2H-form. Photocatalytic hydrogen evolution based of covalently linked assemblies of MoS_2 with RGO and C_3N_4 is discussed in Chapter 3. Charge-transfer between the C_3N_4 and MoS_2 or RGO promotes H_2 generation.

Synthesis, characterization and hydrogen evolution studies of tungsten sulfoselenides are described in Chapter 4. The sulfoselenides are superior catalysts than that of the sulfide of the selenides. Visible-light-induced hydrogen evolution reaction by nanocomposites of few-layer TiS_2 and TaS_2 with CdS nanoparticles is studied in Chapter 5. Hydrogen evolution employing layered gallium chalcogenides is described in Chapter 6.

Part 2 deals with photochemical hydrogen evolution reaction based on Weyl semimetals and topological insulators. These materials possess robust surface states which protect electron scattering thus providing guiding principle for the discovery of novel topological materials.

In **Part 3**, we describe the electrochemical hydrogen generation using doped MoS_2 fullerenes.

In **Part 4**, hydrazine has been used as the hydrogen carrier, photocatalytic generation of H_2 being catalysed by CdS quantum dots.

Part 5 deals with photochemical water oxidation using Co and Mn based oxides and also highlights the beneficial role of Pt on the reaction. $LaCoO_3$ and $LaMnO_3$ exhibit good water oxidation property which is further enhanced by Pt nanoparticles. We find that intermediate spin of Co^{3+} (e_g^1) is important for water oxidation.

Part 1

Photochemical H$_2$ generation from water splitting using transition metal dichalcogenides and other materials

A general overview: Photochemical hydrogen evolution and catalytic activity of transition metal dichalcogenides*

Summary

Generation of H_2 from water has emerged to be an important alternative for replacing fossil fuels. There are various challenges in hydrogen economy, and various methods offer solutions to overcome this challenge. Photocatalytic water splitting offers simple solution. However, photocatalytic water splitting suffers deeply from thermodynamic and kinetic restrictions which needs to be tackled. Various strategies have been developed to enhance the hydrogen evolution using solar energy to overcome the barriers in the process. 2D-Transition metal dichalcogenides offer unique solution to this problem. Understanding their role as hydrogen evolution catalysts can help us to devise better photocatalytic systems.

1. A general overview of photochemical hydrogen evolution

Energy and environmental issues have become the most significant technological challenges of today. The global energy demands have been stipulated to rise from the current level of 12 TW per day to 27 TW by 2050. The current sources of energy, primarily hydrocarbons, coal, and petroleum are non-renewable and will not be able to sustain the increasing demands of energy for it is getting consumed and also diminishing. It is expected that due to increasing consumption, fossil fuels will last for another 30-40 years. Also, burning of hydrocarbons emits CO_2, the primary greenhouse gas leading to environmental degradation and global warming. According to International energy agency, the goal of limiting global warming to 2°C is becoming more difficult to maintain with each passing year, and if no action is taken within 2020, all allowable CO_2 emissions would be locked. Therefore, alternative energy sources are urgently needed to limit our dependence on fossil fuels. Out of the major ways like hydroelectrical, wind power and harvesting sun energy, the solar energy is the most abundant and sustainable natural source of energy. The earth receives about 120,000 TW each day, way higher than all our energy needs. The conversion of solar energy to electricity for direct use or storage in batteries can be achieved by photovoltaic cells. Conversion of solar energy to fuels involving storage of solar energy in the form of energy of chemical bonds is another way to harvest energy, also known as artificial photosynthesis. The advantage of using artificial photosynthesis over

photovoltaic cells is that former gives the active fuel (like petrol, natural gas and etc.), which can be used for machines (car engines, heavy machinery, etc.) which need to withdraw a lot of power at once over a more extended period. Solar fuels can be in the form of H_2, produced from photoassisted water splitting or high-energy carbon compounds (CO, HCOOH, or CH_3OH) that are produced by light-driven reduction of CO_2. Hydrogen has the highest energy density per unit weight compared to contemporary fuels with an energy density of 142 MJ/kg compressed at 70 MPa while for methane gas it is 55.2 MJ/kg. Methane being the next to hydrogen in terms of energy efficiency. It is around 2.5 times as good as natural gas. Also, hydrogen is the cleanest source of energy as an only by-product of combustion of H_2 is water. This is why it has been advocated as the ultimate fuel for future. **Figure 1** compares the energy density of hydrogen and the contemporary fuels used today.
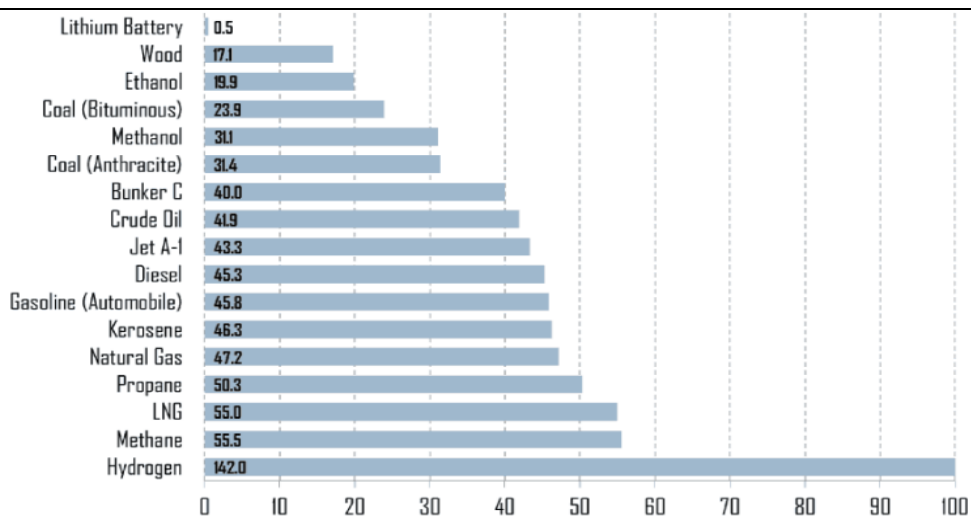
Figure 1. *Energy efficiency (MJ/kg) of various fuels in comparison with the hydrogen. (adapted from C. Ronneau (2004), Energie, pollution de l'air et developpement durable, Louvain-la-Neuve: Presses Universitaires de Louvain.)*

2. Challenges in hydrogen economy

Storage and production of hydrogen are essential elements of the hydrogen economy. Since hydrogen does not occur naturally on earth, it is produced chemically from processes such as steam-methane reforming and coal gasification. However, production of hydrogen has to be achieved from renewable sources which are possible with the processes highlighted in Figure 2 [1, 2]. As a forward-looking technology, catalytic water splitting has been a subject of extensive studies. Hydrogen has the highest energy density compared to fossil fuels and does not emit poisonous and polluting gases. As an excellent alternative to fossil fuels, hydrogen emits no polluting gases and is a constituent of water. Presently, hydrogen around the world is produced from the four primary sources, natural gas (48 %), oil (18%), coal (11 %) and water electrolysis (4 %) [3]. Power plants and natural gas are the most efficient ways to produce hydrogen. Consequently, hydrogen production methods rely on fossil fuels, harsh process conditions, and high costs. Steam methane reforming is an extensively used method to generate hydrogen from natural gas which is carried out at high temperatures (up to 900 ″C) and pressures (1.5–3 MPa) [4, 5]. Coal gasification through partial oxidation at high temperatures and pressures (up to 5 MPa) generates hydrogen [4]. Pyrolysis of biomass materials such as crops, plants and animal wastes via thermochemical routes generate hydrogen while gasification produces byproducts such as CO, CO_2, and methane [6]. Alternate methods to utilize renewable sources of energy for hydrogen production such as hydropower, sunlight and wind

power must, therefore, be explored. Solar energy has been considered as a promising since it is independent of location in comparison to hydropower and wind power.
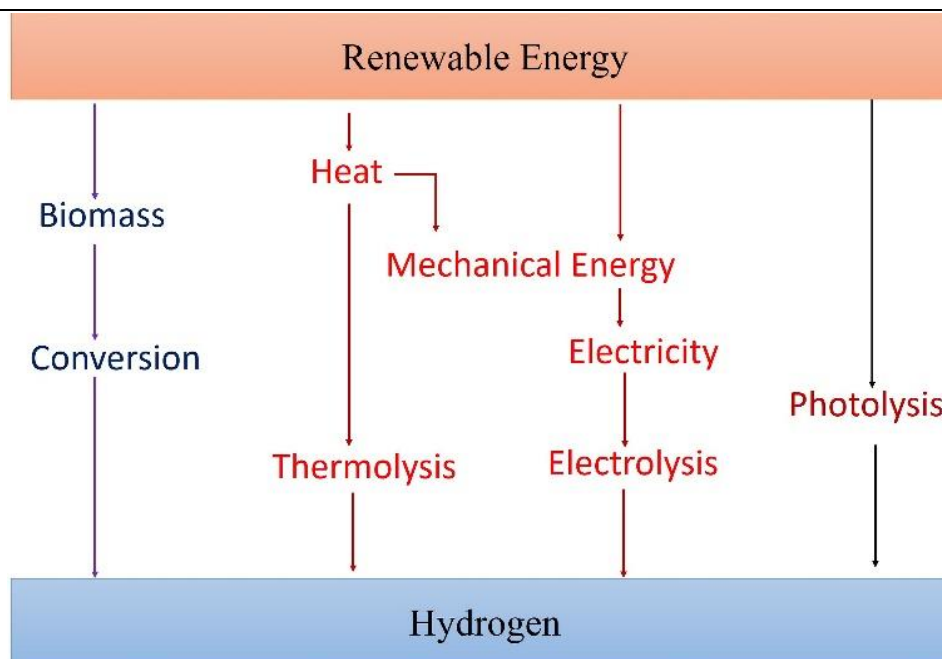
Figure 2. *Schematic of a sustainable strategy to generate H₂.*

The combination of abundant sunlight and water resources provides a reasonable scope for hydrogen generation by solar water splitting [7-9]. There are three major approaches to split water using sunlight [10]: (1) photobiological water splitting (2) photocatalytic water splitting and (3) thermochemical water splitting, the simplest being the thermochemical approach which, however, requires large solar concentrators making this method highly expensive and less preferred [11]. Biophotolysis is divided into water biophotolysis and organic biophotolysis depending on the microorganism, product and the reaction mechanisms [12]. Water biophotolysis is superior to organic biophotolysis regarding CO_2 emission [13], toxic effects of enzymes along with the yield of hydrogen and limitations of scaling up the process [14]. Photocatalytic water splitting possesses

several advantages over thermochemical and photobiological water splitting including low cost [1], higher efficiency and scalability of reactor size [15]. In order to realize the feasibility of solar to hydrogen energy 26 % as set by The US Department of Energy (DOE), aggressive research is needed [16].

The major technical challenge is to produce hydrogen from renewable sources, preferably water. In photocatalytic water splitting, the energy of photons is converted to the chemical energy of H_2 by breaking the bonds in water. This process is accompanied by large positive Gibbs free energy of 237 kJ mol^{-1}. This is an endothermic reaction, as in natural photosynthesis, this is an uphill reaction and is challenging to perform unlike photocatalytic degradation of organic compounds, which is a downhill reaction **(Figure 3)**. Water splitting involves two redox reactions involving four electrons:

Oxidation: $2H_2O \longrightarrow 4H^+ + O_2 + 4e^-$ (1.23V vs NHE) (1)

Reduction: $4H^+ + 4e^- \longrightarrow 2H_2$ (0V vs NHE) (2)
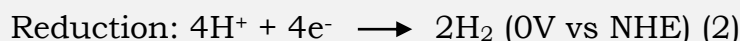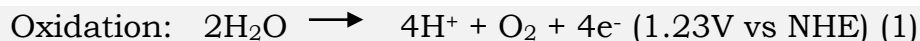
Water splitting can be achieved by electrochemical, photo-electrochemical and photochemical. The hydrogen evolution reaction can be carried out with energy from electricity, light-electricity, and light respectively. With the aid of suitable catalysts, one can lower the energy required to split water and enhance the yield of the hydrogen **(Figure 3)**. Photocatalytic water splitting is the simplest in design and hence, has been one of the most investigated fields of research over the past several years.
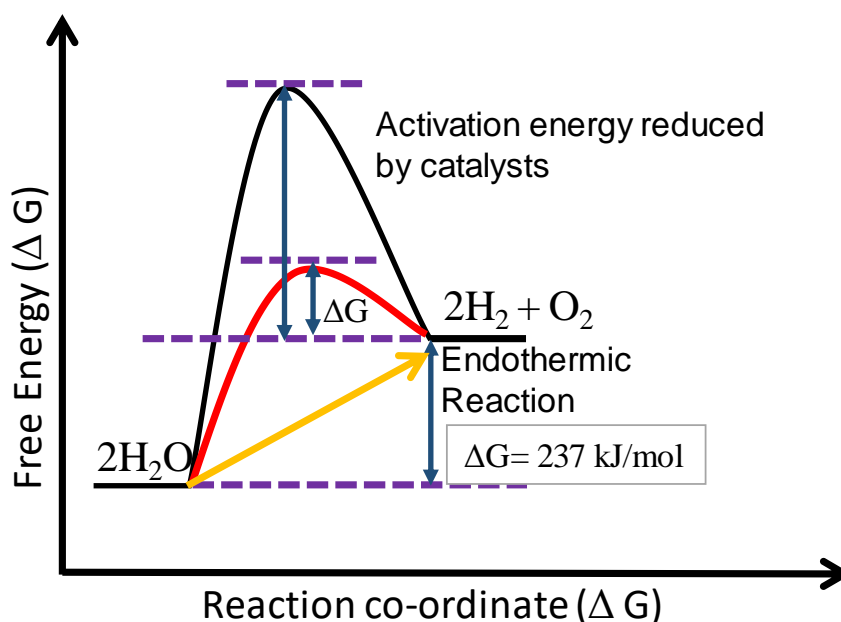
Figure 3. *Schematic describing the energy diagram for photocatalytic water splitting. The presence of catalyst lowers the activation energy and makes water splitting easier.*

Plants perform this conversion through natural photosynthesis where CO_2 and water get converted to oxygen and carbohydrates. Photosynthesis occurs in two stages. In the first stage, water is oxidized to O_2 generating a proton which gets bound to $NADP^+$ to give the energy carrier, NADPH. In the second stage, NADPH is used to reduce CO_2 to glucose. Glucose is the fuel generated during photosynthesis. Similarly, we have H_2 as the fuel source generated during the artificial photosynthesis (Artificial photosynthesis is discussed in details in part 4 of the thesis). The mechanism of photocatalytic hydrogen evolution is governed by thermodynamic as well as kinetic aspects. These criteria are needed to be understood for designing a suitable catalyst.

3. Thermodynamic and kinetic aspects of photocatalytic hydrogen evolution

3.1 Thermodynamic aspects

In principle, the ideal energy for overall water splitting a semiconductor must possess band gap of 1.23 eV **(Figure 4)**. The conduction band minimum (CBM) should be located at a more negative potential than the proton reduction potential (H^+/H_2), while the valence band maximum (VBM) should be positioned more positively than the oxygen reduction potential (O_2/H_2O). However, the band gap of about 1.7 eV is ideal for visible light active photocatalyst as well as the effective utilization of the solar energy. The additional energy is the onset potential required for the reaction to occur. In a much closer examination, the oxidizing power (denoted as Δ_2) that is defined as the difference between VBM band edge and the oxygen reduction potential. However, the reducing power (denoted as Δ_1), is defined as the difference between the proton reduction and the CBM edge potentials **(Figure 4)** [17].

The rate constant of a chemical reaction can be given by Arrhenius equation,

$$K = Ae^{RT/Ea} \qquad (3)$$

where A is the pre-exponential factor, R is the universal gas constant, and E_a is the reaction energy barrier. The reaction barrier in photocatalytic redox reactions of water is complicated. But, it can be understood by the difference between the reaction rate of reduction reaction and oxidation reaction. The energy barrier can be minimized by reducing the difference between Δ_1 and Δ_2, and improved efficiency of the reaction can be achieved. This also suggests that MoS_2 is a good

candidate for reduction but not oxidation. But our primary concern is the production of hydrogen from water.
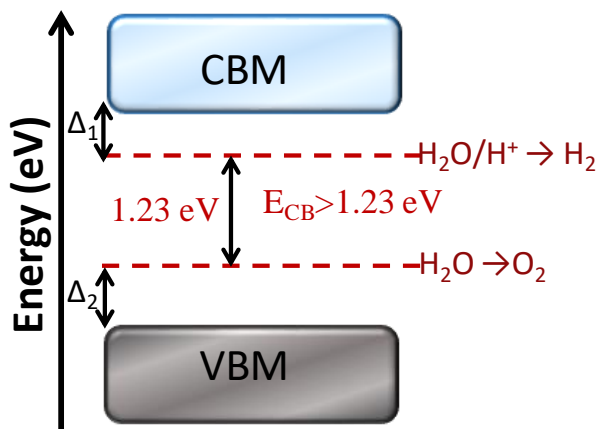
Figure 4. *The energy diagram of photocatalytic water splitting with a single semiconducting catalyst. Δ_1 and Δ_2 represent the reducing and oxidizing power of the catalyst respectively. The dotted lines represent the reduction and oxidation potential of water.*

The bigger the barrier or big difference between Δ_1 and Δ_2, would imbalance the reduction and oxidation reactions, which inhibits the progress of the overall redox reaction. If we can decrease the difference between Δ_1 and Δ_2, we can further improve its efficiency for water splitting [17]. In principle, an ideal catalyst must have a band gap of 1.23 eV, where CBM and VBM straddle along the HER and OER potential with the minimum thermodynamic drive. A proper tuning between the Δ_1 and Δ_2 can facilitate water splitting. Although the difference in the energy barrier is fixed, it can be controlled by substituting either OER or HER with a reaction which requires a low thermodynamic drive as well as having faster kinetics. The use of substrates which lowers the energy also facilitate the reaction. General strategies to achieve overall water splitting or photocatalytic hydrogen evolution is discussed in later part of the chapter.

3.2 Kinetic aspects

Photocatalysis for water splitting involves a series of complex photophysical and electrocatalytic processes [18]. The processes involved in photocatalytic reactions can be divided into the following six events, Photon absorption (1) followed by immediate exciton separation (2). Carrier diffusion (3) and carrier transport (4) to the surface of the catalyst. Catalytic efficiency (5) and Mass transfer (6) of reactants and products occurs on the surface. Events 3 and 4 can occur concurrently and coherently but are separated here for convenience. **Figure 5** shows this six-gear concept, which represents the photocatalytic water splitting process sequentially occurring at different time scales [18].
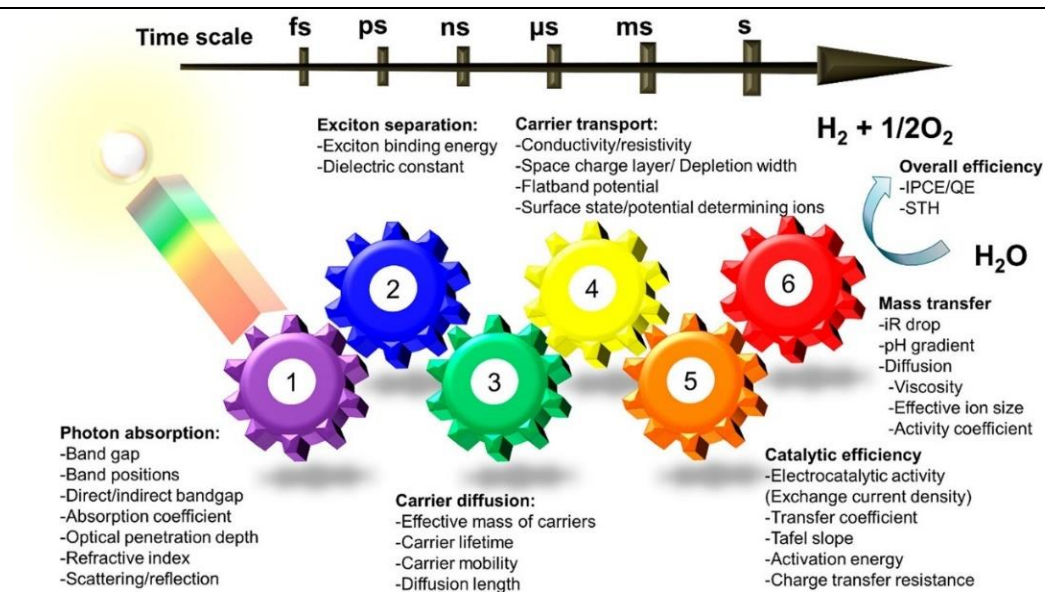
Figure 5. *The parameters and descriptors in photocatalysis. The Overall water splitting occurs only for all six gears depicted in the scheme should occur with high efficiency. The different time scales of the reactions are also shown Adapted with permission from reference 18.*

A non-equilibrium photophysical and photochemical processes are initiated by photon absorption. An exciton that is, excitation of an

electron in the valence band maxima (VBM) or the highest occupied molecular orbital (HOMO) to the conduction band minima (CBM) or the lowest unoccupied molecular orbital (LUMO) is generated. The probability to occupy the states is predominantly determined by the electronic structure of the semiconductor. The process is immediately followed by relaxation of the electron and the hole to the bottom of the CBM and the top of the VBM, respectively. Then exciton (electron−hole pair) are separated after overcoming the exciton binding energy determined by the electronic structure. The combination of carrier diffusion and transport effectively utilizes the introduced interfaces (i.e., potential differences) and successful charge transfer to the electrocatalysts decorated on the surface needs to occur [19].

A scheme based on a scale of the thermodynamic potential of electrons and holes, which visualizes the energy processes that occur during progressive photocatalytic processes. **Figure 6** shows an example which highlights the electronic process on a single semiconductor photocatalyst coupled with HER and OER electrocatalysts on the surface, portraying overall water splitting. The process is started with photon absorption, as represented in the middle of **Figure 6**. On light absorption, excitons (electron−hole pair) are generated in the valence band and conduction band, on the femtosecond time scale [19]. The excitons undergo rapid relaxation to the respective edges of their bands in femto- to picoseconds. The exciton is separated into free carriers, and the semiconductor-catalyst interface guides the electron and hole to the HER and OER co-catalysts, respectively, generally in nano- to microseconds [19].

Substantial losses of potentials are expected at the interface ("interfacial loss") and may originate from entropic contributions of electrons and potential interfacial barriers that are generated by poor alignment [20-22].
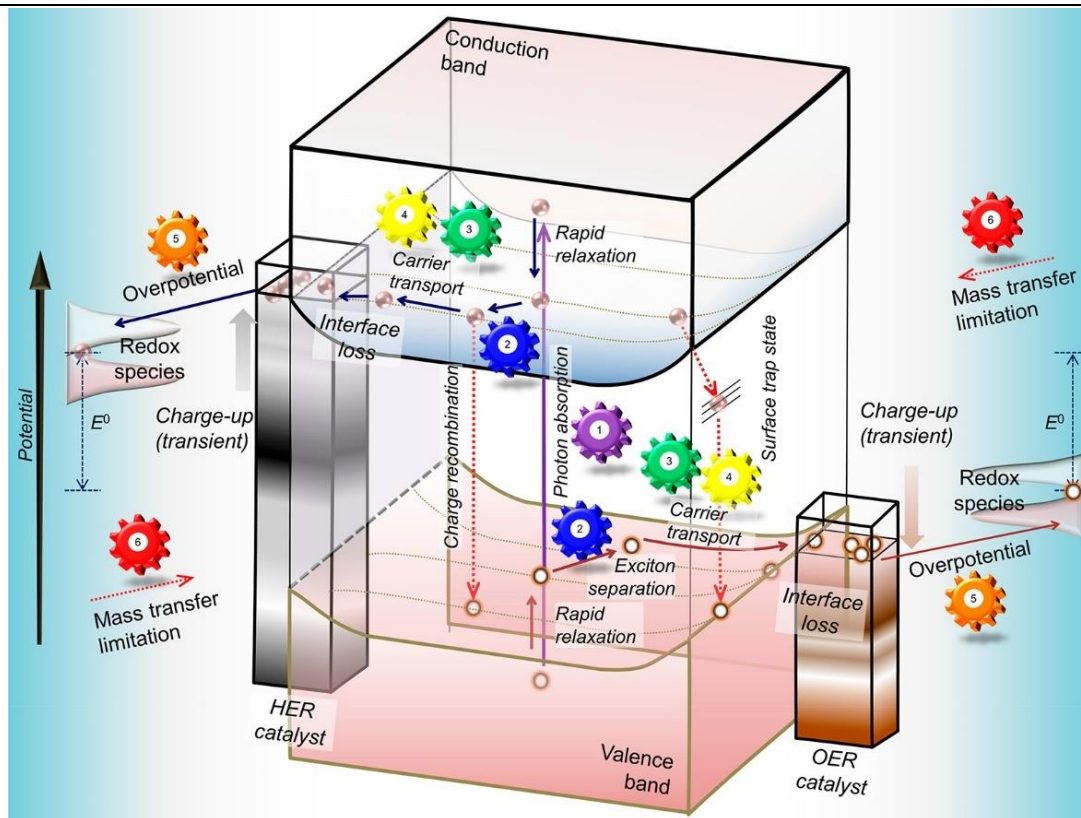
Figure 6. *Schematic of the photocatalytic water splitting process on a semiconductor surface attached with co-catalysts. The number indicates on the gear indicates the order of the photocatalytic process to be successful for overall water splitting. Adapted with permission from reference 18.*

Successful electron/hole transfer to the electrocatalyst shifts the potentials either negatively or positively at a transient time on the millisecond to second-time scales, and then maintain steady-state potentials that are allowed to drive steady-state electrochemical redox reactions to produce H_2 and O_2 [19]. The solution properties may influence the overall performance by limiting the mass transfer of the reactant ions,

for the kinetics of electrocatalysis are slow-moving compared to the preceding events. Thus, redox reactions occur on the time scale longer than microseconds since slow electrocatalytic redox reactions on the surface charge up the surface either negatively or positively [19].

The rate of charge reaction is intrinsic to the material, the density of excitons and charge recombination. The quantum efficiency for overall photocatalytic water splitting to low values is restricted by the competing recombination reaction. For photocatalytic reaction to proceed efficiently, an appropriate electron-hole scavenger (sacrificial agent) is required. The scavengers rapidly consume the respective photo-excited carriers and effectively prevent the charge recombination. In view to these thermodynamic and kinetic aspects of photocatalytic water splitting, different strategies have been designed to perform the reaction by minimizing the losses efficiently.

4. Strategies for photochemical hydrogen evolution

4.1 Semiconductor-based catalysts

In the water splitting process, the following reduction and oxidation reactions occur at the surface of the catalyst as shown in **Equations 1 and 2**. Overall water splitting refers to the splitting of water into hydrogen and oxygen in the ratio 2:1 by the use of appropriate photocatalysts. The mechanism of photocatalytic water splitting has been established [23, 24].

The simplest of all catalysts is the one where all three processes of photosynthesis are occurring in a single system. The semiconductor absorbs a photon with energy greater than its band gap and generates an

electron-hole pair, followed by the movement of the electrons and holes to the surface of the semiconductor which participates in surface chemical reactions with water or other sacrificial agents.
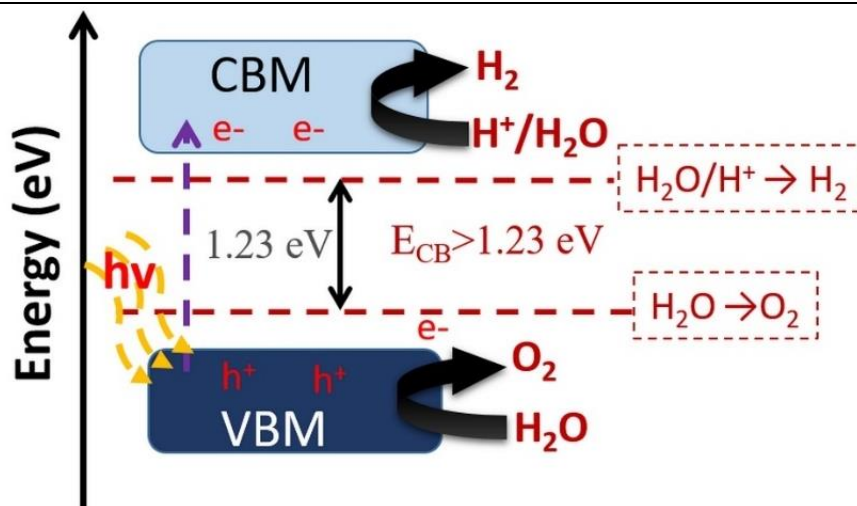
Figure 7. *Schematic of overall water splitting over a photocatalyst. Broken horizontal lines show water redox potential.*

Fujishima and Honda reported in 1972, photo-induced water splitting on TiO_2 electrodes. Since then, several photosystems have been developed to mimic photosynthesis and harvest solar energy to produce hydrogen and oxygen [25-28]. Photocatalytic water splitting over semiconductor materials has been considered as a promising approach for direct solar-to-hydrogen conversion [23, 29]. For a semiconductor to act as a catalyst for water splitting, it must satisfy the following energy level conditions. The bottom of the conduction band is required to be more negative than the reduction potential of H^+/H_2 (0 V vs. NHE), and the top of the valence band is required to be more positive than the water oxidation potential of O_2/H_2O (1.23 V) as shown in **Figure 7**, limiting the theoretical minimum band gap for water splitting to be 1.23 eV.
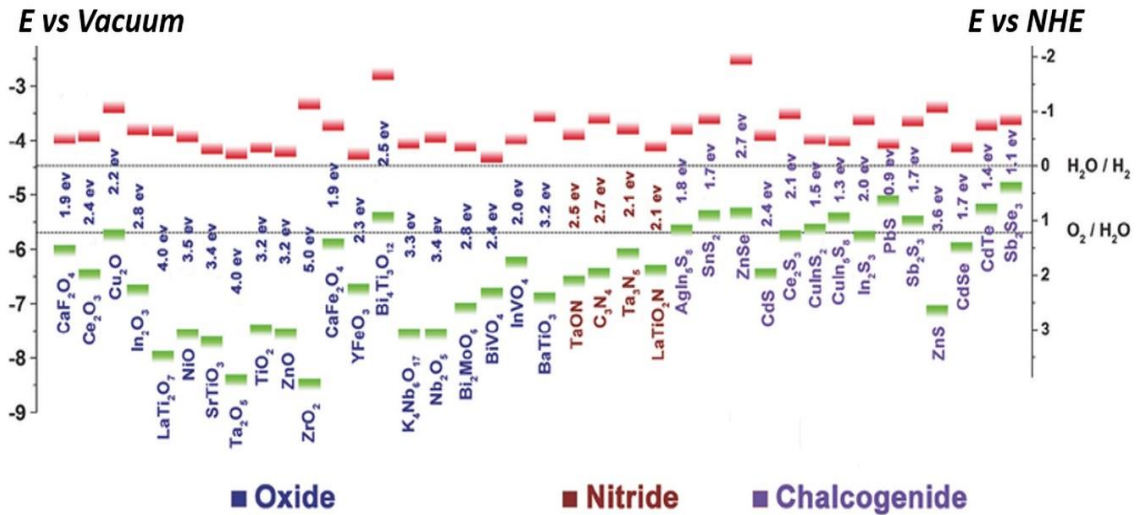
Figure 8. *Band gaps and band-edge positions for selected semiconductors with respect to the vacuum level and water reduction potential. The short thick green and red lines represent the valence band edges and the conduction-band edges respectively. The dashed lines represent the water redox reaction potentials. Reprinted with permission from 31. Copyright 2016. John Wiley and Sons*

Figure 8 gives an overview of the semiconductors and their band positions aligned with respect to the water redox potential derived [25, 28, 30, 31]. Semiconductors such as TiO_2, $SrTiO_3$, $BaTiO_3$, $FeTiO_3$, ZrO_2 and ZnO whose conduction band potential lie above the proton reduction potential can reduce water to produce H_2. On the other hand, semiconductors such as Fe_2O_3, SnO_2, WO_3, *etc.* can only oxidize water. Semiconductor oxides, photocatalysts are highly stable with respect to sulfides and nitrides and do not undergo oxidation or reduction during the processes of water splitting, they have an intrinsic limitation of having a highly positive valence band (O 2p). It is, therefore, difficult to find oxide semiconductors with a sufficiently negative conduction band to reduce H_2O to H_2, at the same time having a sufficiently small band gap to absorb visible light.

Metal sulfides and selenides (CdS or CdSe), on the other hand, are ideal for visible light photocatalytic H_2 production by virtue of the suitable conduction band position and a small band gap **(Figure 8)** [23].

Recombination of e^- and h^+ competes with the process of charge separation reducing the efficiency of photocatalysis. Defects and grain boundaries in the semiconducting particles act as a charge recombination centers. Charge recombination can be minimized by decreasing the size of the particle to a few nm [23]. The electrons and holes would then have a higher probability to traverse the surface and to be used to reduce and oxidize water respectively. Sometimes these can also be used up by a sacrificial electron or hole scavenger **(Figure 9 a and b)**.
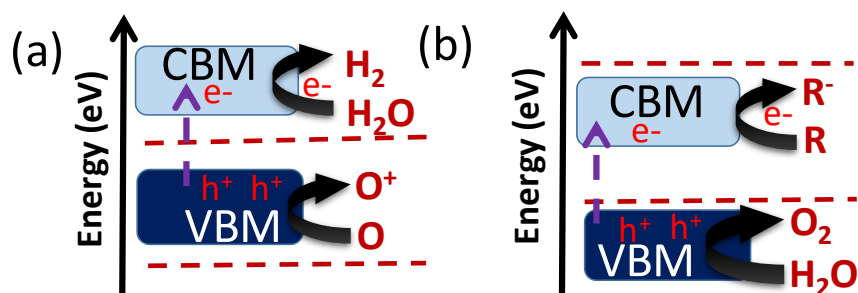
Figure 9. *Schematic which highlights the half-reaction (a) hydrogen evolution and (b) water oxidation. The sacrificial agent is used to enhance the targetted reaction (water oxidation or reduction). The $O \rightarrow O^+$ denotes representative oxidation reaction and $R \rightarrow R^-$ is representative reduction reaction. Broken horizontal lines show water redox potential.*

A hole-scavenger is a reducing agent such as an alcohol or a sulfide which gets oxidized by the photogenerated h^+ instead of water and thereby increases the system with electrons to be used for further reduction of water to generate H_2. The choice of such sacrificial agents is essential. For example, Na_2S/Na_2SO_3 is used as the electron donor to VBM of the

semiconductor to assist water reduction, while Ag^+ or Fe^{3+} is used as an electron acceptor to assist water oxidation [32, 33]. A sacrificial system thus eliminates back electron transfer and renders it feasible to examine only the oxidation or the reduction of water.

4.2 Dye-based catalysts

Semiconductors as photocatalysts impose a restriction in light harvesting due to its band gap. Semiconductors which possess a large band gap which can absorb light only in the UV region while neglecting the entire visible and near-infrared regions of the solar spectrum. Dye sensitization permits the use of semiconductors with energy levels matched with the redox potential of water, without compromising with the range of energies absorbed. In a typical dye-based system, light absorption occurs on the surface of the dye, and the electron transferred from the dye molecule to the CBM or the VBM of the semiconductor which then participates in hydrogen evolution **(Figure 10)**.
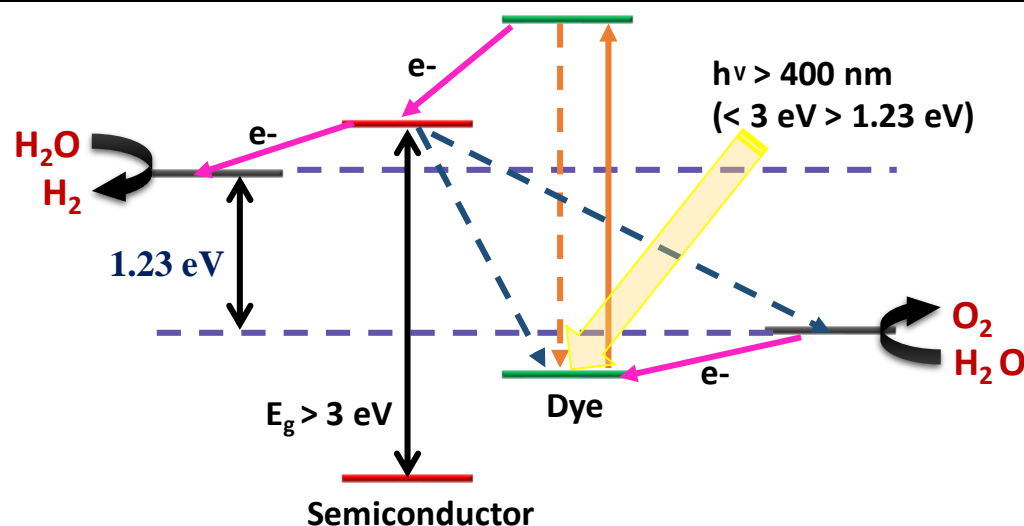
Figure 10. *Scheme of Kinetic for electronic processes in dye-sensitized water splitting. Adapted with permission from ref. 27. Copyright 2009 American Chemical Society.*

The process initiates when the dye molecule absorbs light and goes to the excited state. In the excited-state, dye molecule injects an electron into the conduction band of the semiconductor and subsequently transforms to the oxidized form. The oxidized dye is immediately reduced to the ground state by electron transfer from the photocatalyst for water oxidation [27]. The conduction band electrons reduce water to hydrogen on the hydrogen evolution site in the process of water splitting. The electron injecting species is highly active and therefore, if not used quickly to produce hydrogen, undergo back electron transfer to regenerate the sensitizer or bleaches out [27]. Sometimes, sacrificial electron donor or a redox shuttle such as the I^{3-}/I^- pair is used to regenerate the photosensitizer and sustain the reaction cycle [27].

Dye-sensitized photo-electrochemical cells having dye-sensitized photo electrodes also work on similar principles with the reduction of water occurring at the counter electrode and the sacrificial agent getting oxidized at the photosensitized electrode. Dye-sensitized TiO_2 electrodes bearing IrO_2 nanoparticles have been used for complete water splitting. On sensitization, the dye loses an e^- to TiO_2 which transfers to the counter (Pt) electrode generating H_2. The IrO_2 particles donate e^- to the oxidized dye to regenerate the photosensitizer [27].

4.3 Heterojunctions-based catalysts

Heterojunction interfaces between two semiconductors are employed to create a space-charge region to enhance separation of charge carriers across the catalyst and increase the photocatalytic activity of materials [26].

A promoter used to enhance the activity of the photocatalyst is termed as a co-catalyst. The difference between a photocatalyst and co-catalyst is that a catalyst is an independent entity where both absorptions of light and reaction occur while the co-catalyst cannot absorb light on its own and acts as a support to the catalyst to accelerate the reaction.
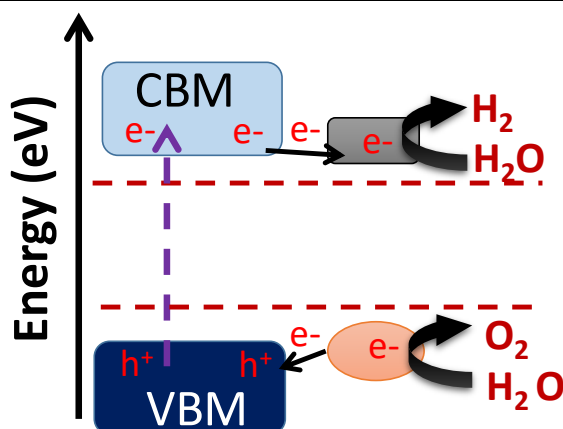
Figure 11. *Schematic of semiconductor-cocatalysts systems; a metal-semiconductor (Schottky barrier) gives good results. The $O → O^+$ denotes representative oxidation reaction and $R→ R^-$ is representative reduction reaction. Broken horizontal lines show water redox potential.*

A Schottky barrier by using a semiconductor-metal heterojunction for efficient charge separation across the interface **(Figure 11)**. The barrier acts as an efficient electron trap by preventing electron-hole recombination, causing enhanced photocatalytic performance. The barrier promotes charge transport and separation and improves photocatalytic activity [34, 35]. Appropriate co-catalysts serve as reaction sites to catalyze reactions along with assisting charge separation [23, 36, 37]. Noble metals were popular as co-catalysts and have been widely investigated to provide effective hydrogen evolution sites besides facilitating the separation of the carriers [36, 37]. Their use is however limited to the laboratory due to the

high cost and limited availability. Strategies have therefore been employed using earth-abundant cheaper materials such as graphene [38], 2D-transition metal dichalcogenides (TMDs) [29, 31, 39-41]. TMDs used include MoS_2 [42-47], WS_2 [42, 48, 49] as well as TaS_2 and TiS_2 [50].
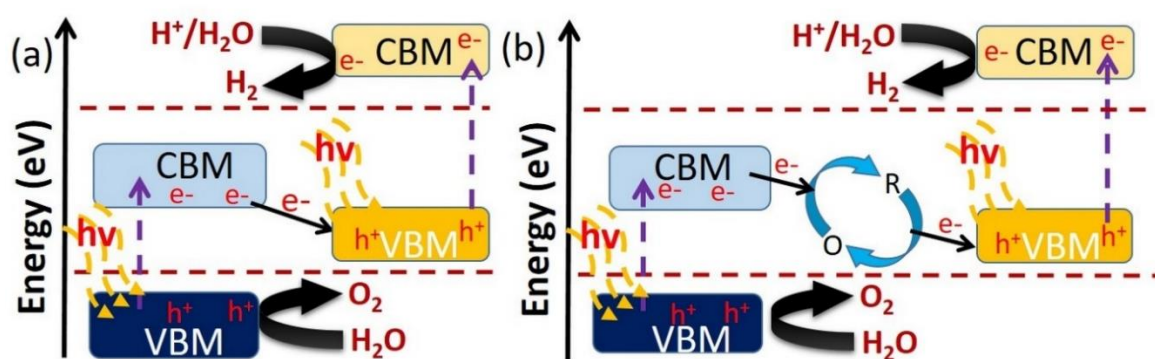
Figure 12. *Schematic of (a) heterojunction semiconductor and (b) Z-scheme for achieving overall water splitting. Broken horizontal lines show water redox potential.*

Two semiconductors with desirable band gaps are employed to create type II heterojunctions as a light-harvesting system where oxidation and reduction of water co-occur on the two different catalyst surfaces **(Figure 12 a)** [26]. The strategy becomes effective if the heterojunction is a p-n type interface [51]. Analogous to natural synthesis, the Z-scheme strategy is employed to achieve water splitting. The Z-scheme water splitting involves a two-step photoexcitation using two different semiconductors with a reversible donor/acceptor pair. The Z-scheme water splitting systems depend on finding a suitable semiconductor photocatalyst which efficiently works in the presence of a shuttle redox mediator, creating active sites to promote surface chemical reactions and suppressing the backward reactions **(Figure 12 b)** [51, 52].

5. Transition metal dichalcogenides as hydrogen evolution catalysts

Recently, 2D-materials have opened up a new aspect of research as not only their composition or structure but also dimension of the material will play a crucial role in their basic properties. A single layer of graphite also known as graphene shows remarkable properties which were absent in its 3D-form graphite [53-55]. Increasing interest in graphene has led to the exploration of other 2D-materials [56-69]. Among all the 2D materials transition metal dichalcogenides, having a structure similar to graphite, have been of particular interest for their different electronic properties, like from metallic to sizable band gaps. Also, these materials are readily earth-abundant. Graphene, by nature, is metallic in order to introduce band gap in graphene or some functionality we need to modify it with other molecules [70] or functional groups, which result in loss of some of its properties. However, in single-layered 2D transition metal dichalcogenides exhibit variety of properties and chemistry. This opens up a wide variety of applications in electronics, catalysis, energy storage and other applications. In bulk, they also exhibit a variety of properties like insulating HfS_2, semiconducting such as MoS_2, semi-metallic such as $TiSe_2$, to a true metallic system like NbS_2. Some transition metal dichalcogenides like exhibit low-temperature superconductivity, charge density waves and Mott metal to insulator transition [71-73]. Many transition metal dichalcogenides crystallize in a graphene-like layered structure which leads to anisotropy in their electrical, thermal, mechanical and sometimes chemical properties [74]. On exfoliating these materials into

mono to few-layers generally preserves their property and sometimes brings up new properties due to their confinement in particular dimension. [59-61].

5.1   Structure and electronic properties

Group 4–7 transition metal dichalcogenides are generally layered, whereas some of group 8–10 Transition metal dichalcogenides are commonly non-layered structures. Single-layered 2D transition metal dichalcogenides have the general formula of MX_2, where M is a transition metal of groups 4–10 and X is a chalcogenide. Metal atoms are hexagonally packed and sandwiched between two layers of chalcogen atoms. The intra-layer M–X bonds are covalent in nature, whereas the sandwich layers are weakly bonded by van der Waals force. Thus we can readily exfoliate the crystal along the layer surface. The single layers are stabilized by the development of a ripple structure similar to graphene. [75, 76]

There are two co-ordination type, trigonal prismatic (with point group as D_{3h}) or trigonal antiprismatic or octahedral (with point group as D_{3d}) which gives rise to three crystal phases **(Figure 13)** trigonal, hexagonal and rhombohedral. They are depicted as 1T, 2H, and 3R where letters stand for trigonal, hexagonal and rhombohedral, respectively, and the number represents the number of MX_2 units in the unit cell. Both 3R and 2H form has trigonal prismatic coordination, while 1T has octahedral coordination. In 2H crystal structure we have AbA type of packing, in the 1T phase, we have AbC type packing, and in the 3R phase, we have AbA CaC BcB type of packing [77], (the upper case shows chalcogen, and lower case shows

metal atoms.). This crystal structure can be differentiated by using different techniques like high-resolution transmission electron micrography in annular dark field mode [64, 78].
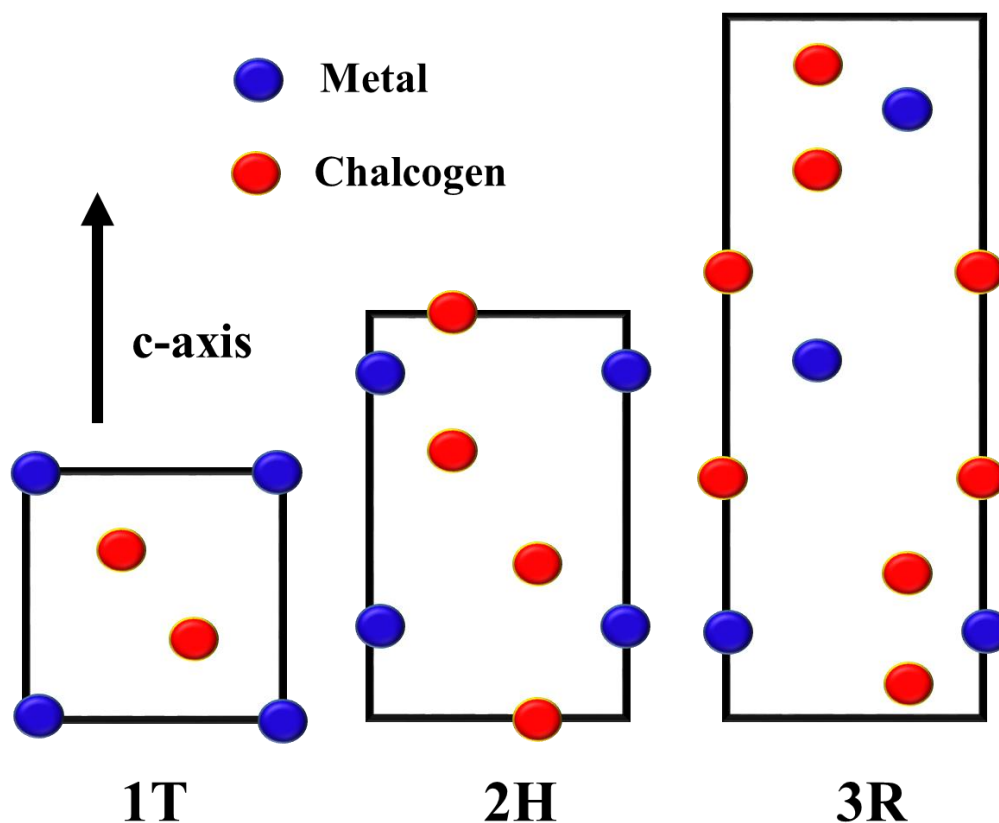
Figure 13. *Schematic of the stacking sequences and coordination in the 1T, 2H and 3R polytype of Metal (M is shown in blue) and chalcogen (X=shown in red). The structures are shown as projections onto the (110) plane.*

Metal atom provides four electrons to fill the bonding states so that the oxidation states of the metal (M) is +4 and chalcogen (X) atom is –2. The lone-pair electrons of the chalcogen atoms terminate the surfaces of the layers, and the absence of dangling bonds makes them stable against reactions in ambient conditions. The electronic structure of transition metal dichalcogenides depends upon the d-electron count of the metal atom.
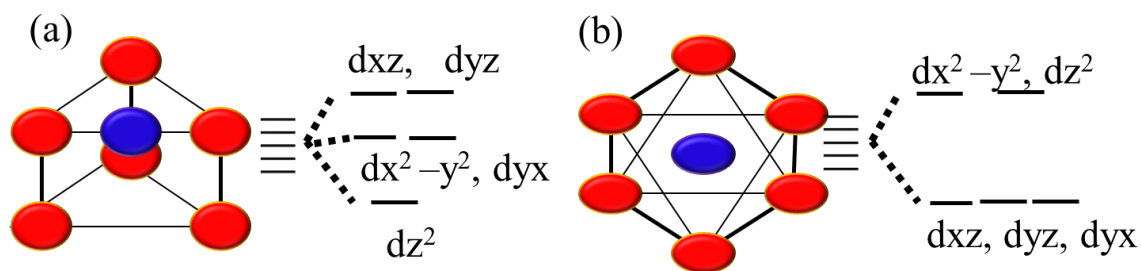
Figure 14. *Shows coordination and splitting of the d-orbital of the metal (shown in blue) ion coordinated by chalcogen (shown in red) in (a) trigonal prismatic field and (b) octahedral.*

The metal atom in transition metal dichalcogenides can be either trigonal prismatic or octahedral (trigonal-antiprismatic) typically distorted shown in **Figure 14**, depending on the combination of the metal and chalcogen elements, one of the two coordination modes are thermodynamically preferred. The splitting of these orbitals in their field is shown in **Figure 14**. In trigonal prismatic (D_{3h}) coordination the d-orbitals split into three sets of orbitals, d_z^2 (a_1), $d_{x^2-y^2}$, d_{yx} (e) and d_{zx}, d_{yz} (e') having a band gap nearly ~1eV between the a_1 to e set of orbitals. In octahedral (D_{3h}) environment, the d-orbitals split into two sets of degenerate orbitals d_z^2, $d_{x^2-y^2}$ (e_g) and d_{yx}, d_{zx}, d_{yz} (t_{2g}) (Shown in **Figure 14**).

For example, MoS_2 is naturally present in 2H-form, whereas TaS_2 is present as 1T-form in nature. In both the form, the non-bonding d-bands of the transition metal dichalcogenides are located in the gap between the bonding (σ) and non-bonding ($\sigma*$) bands of metal chalcogen bonds shown in **Figure 15** with respect to the Fermi level. Progressive increase in a number of d-electrons from group 4 to 10 gives different electronic property illustrated in **Figure 15**.
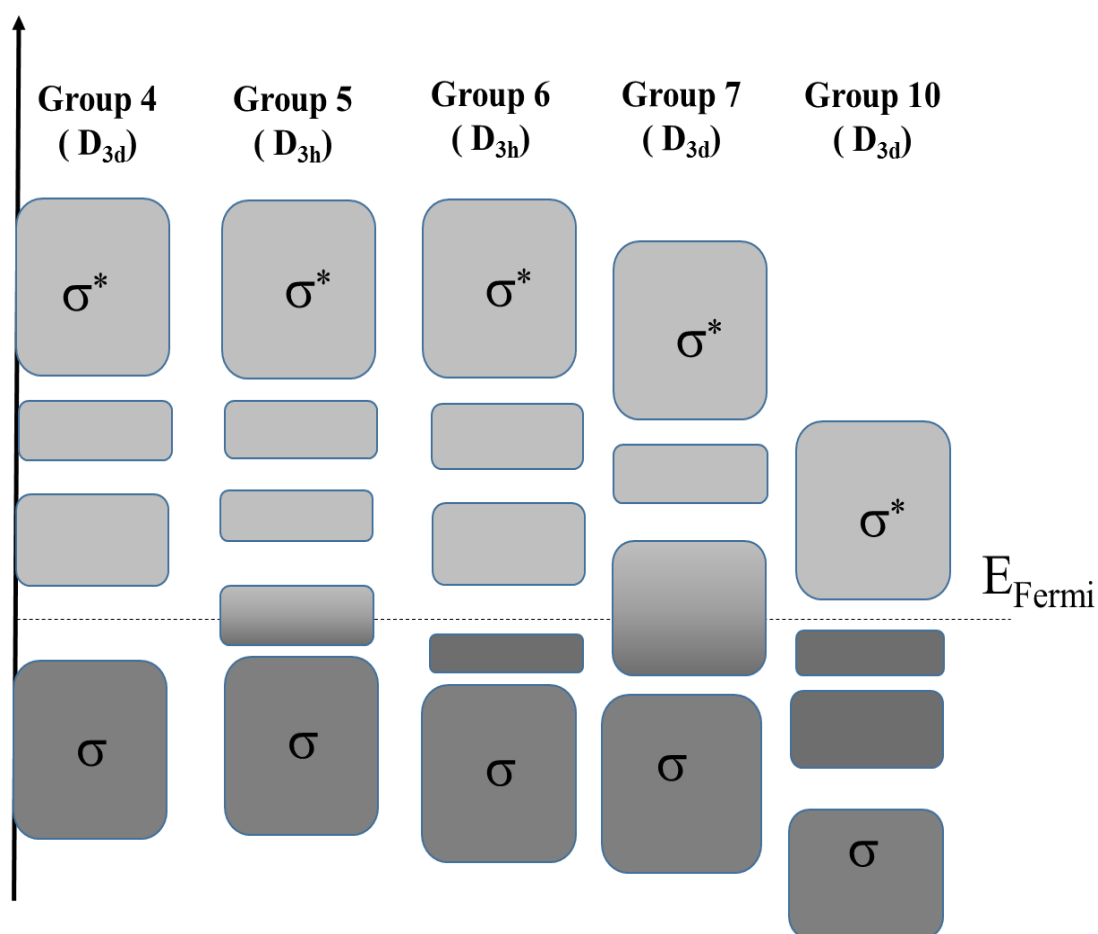
Figure 15. *Schematic representation showing filling of electrons in d orbitals that are located within the band gap of bonding (σ) and non-bonding (σ*) bands of transition metal dichalcogenides of Group 4-7, 10 of their naturally abundant state. The filled and unfilled orbitals are shaded as grey and light grey respectively.*

Transition metal dichalcogenides of Group 4 (d^0) can be present as semiconductors and their band gaps vary depending on the metal atom and chalcogen atom. Group 5 (d^1) is metallic in nature as the orbital is partially filled and Fermi level lies within the band. Group 6 (d^2) has a fully filled orbital, and the Fermi level is in the energy gap, so it is semiconducting in nature. Similarly, band gap varies with the nature of metal and chalcogen atom in group 6. Similar to group 5, group 7 (d^3) has a partially filled d orbital with Fermi level within the band, so it exhibiting

metallic properties. Similarly, for group 10 (d^{10}) we have fully filled d-orbital, and the Fermi level lies in the energy gap and hence, they are a semiconductor.

Interestingly one can change the electronic properties of the transition metal dichalcogenides by changing the crystal structure. For example, lithium intercalation in MoS_2 followed by exfoliation transforms it from 2H to 1T polymorph [77-81]. This implies that semiconducting 2H-MoS_2 will become metallic in 1T-MoS_2, in principle. The reverse takes places in case of TaS_2, 1T-phase to 2H-phase transition, on Li intercalation [82]. This destabilization of the original phase is because of the change in the *d*-electron count by transfer of an electron from the valence *s* orbital of the alkali metal to the *d* orbital of the transition metal and also due to the relative change in the free energy of the two-phases.

5.2 Guiding principle for designing TMDs catalysts

From empirical observation, we see that group 6 TMDs are highly active catalysts and hence well studied. Other compounds like TaS_2, TiS_2, V or Pt-based layered dichalcogenides have been studied but have not shown considerable high HER activity [83-85]. To use these materials as catalysts and to design new catalysts, it is necessary to understand the role of the metal, the chalcogen, metallicity, structure, and the surface of the TMDs. A theoretical investigation of the activity–stability relationships of TMDs has been carried out by Nørskov and coworkers to establish potential applications in HER [86].
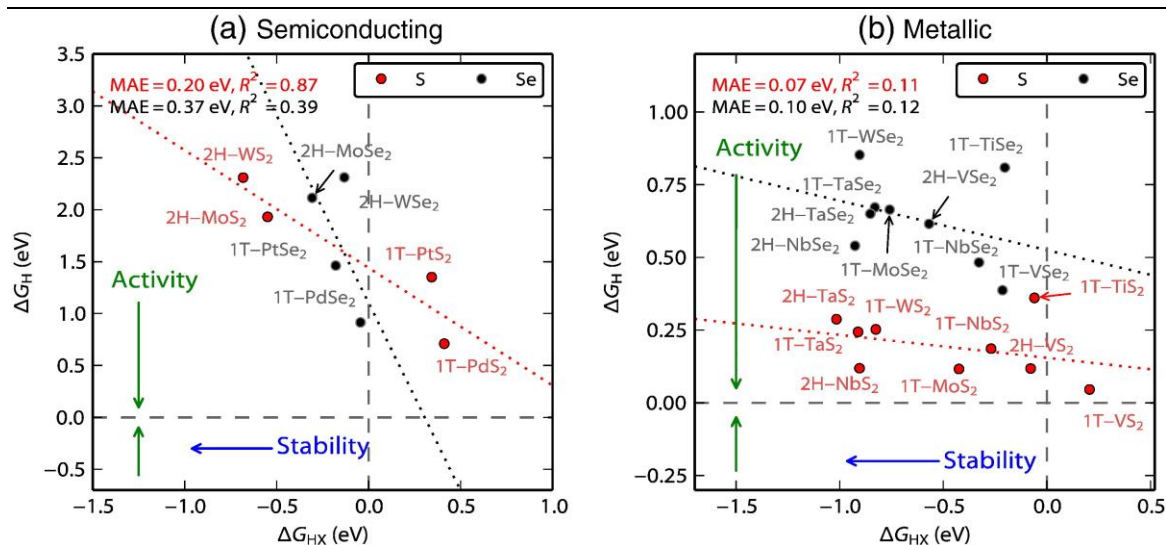
Figure 16. *The plot of hydrogen adsorption free energy, ΔG_H, against the HX adsorption free energy, ΔG_{HX} (X = S or Se) for (a) semiconducting single-layered TMD basal planes and (b) metallic single-layered TMD basal plane. The differential hydrogen adsorption free energy ΔG_H as a function of the HX adsorption free energy. Dotted lines are guides for the eye. Dashed lines are $\Delta G_H = 0$ eV and $\Delta G_{HX} = 0$ eV. Reproduced with permission from 86. Copyright 2015 Elsevier.*

Hydrogen adsorption free energy (ΔG_H) is used as a descriptor for HER activity, where an optimal catalyst would bind to H atom neither to weakly or strongly. Therefore, a catalyst with close to thermo-neutral results ($\Delta G_H = 0$) is the most active catalyst [87-89]. The strength of the hydrogen-chalcogen bond (HX) (ΔG_{HX}, X = S or Se) is inversely related to the H-bond onto the chalcogen X (ΔG_H). This implies that an unstable catalyst has positive ΔG_{HX} with weak H-X bonding while a stable catalyst is active if ΔG_H is negative with strong bonding. The inverse relationships indicate the crucial role of the transition metal in influencing the activity as the metal changes the strength of the chalcogen bond onto the basal plane. The binding strength of H with the chalcogen also changes with it.

Differences in the slopes of sulfides and selenides arise from the states present near the Fermi level for the metallic compounds **(Figure 16 a)** as compared to the semiconducting ones **(Figure 16 b)**. Therefore, a strong H-X bond leads to a weak H bond and vice versa. As all the ΔG_H values on the surface are ~0 eV, strategies for strengthening the H bond to improve catalytic activity make the catalyst less stable. In the case of semiconducting surfaces, both the sulfides and selenides have weak hydrogen binding energy (ΔG_H) from 0.5 eV to 2.5 eV **(Figure 16 a)** with a similar inverse relation between ΔG_H and ΔG_{HX}. As the ΔG_H approaches 0 eV with increasing ΔG_{HX}, the H bond energy can be tuned by the weakening of the HX bond. TMDs with ΔG_H ~0, have surfaces which are not active as hydrogen evolution catalysts. Metallic TMDs **(Figure 16 b)** possess hydrogen adsorption free energies close to 0.05 eV to 1.0 eV.

The inverse relationship between H-X and H binding has a smaller dependence of ΔG_H on ΔG_{HX} signifying weaker hydrogen binding of the selenides with a hydrogen atom. Hydrogen binding on Se is generally weaker compared to that on S. Metallic TM sulfides possess hydrogen adsorption free energies (ΔG_H) close to thermo-neutral values between 0.04 eV and 0.3 eV, indicating that they are catalytically active for HER. 1T-Analogues of 1T-MoS$_2$ and 1T-WS$_2$, are shown to be active for HER [90, 91]. For group 5 TMDS, both 2H and 1T-phases may be active HER. Metallic selenides show improved hydrogen binding with respect to the semiconducting selenides but are considerably weaker than the metallic TM sulfides (ΔG_H are ~0.3 eV).

The role of the transition metal is weaker in metallic TMDs compared to the semiconducting ones as observed from the smaller dependence of ΔG_H on ΔG_{HX}. Therefore, improvement in catalytic activity by strengthening the H bond makes the surface unstable as observed in metallic selenides where hydrogen binding is weak **(Figure 16 b)**.

The role of the structure is significant as it affects the semiconducting or metallic nature of the TMD. The inverse relationship does not strictly depend on the geometry. It is observed that edges are more active than the basal planes in all the cases, but the difference in the binding energies for metallic basal planes are similar to those of the edges. In selenides, hydrogen binding is weaker than sulfides, though the effect is less noticeable in semiconducting TMDs. In the case of the basal plane, the structure is important as it governs the nature of the TMD. Interestingly, basal planes of metallic catalysts all have hydrogen adsorption free energies near to ~0, which implies that they could be active as HER catalysts. Regardless of the metallicity, the edges are found to be a metallic basal plane with an inverse relationship that determines their activity and stability. The activity of basal planes in catalysts is compromised severely by their stabilities. The edges are active and stable while the basal planes are most active but tend to be unstable. Creation of a high concentration of edge sites instead of active basal planes can increase the activity of the catalyst. The electronic structure of TMDs plays a vital role in determining the activity of the catalyst. Some TMDs have their 2H-form active, while some have their 1T-form as the active form. Metallic TMDs have both edge

and basal plane and edge sites, but the basal plane is unstable. For photocatalytic HER we have to use a suitable sensitizer or a semiconductor (preferably large band gap semiconductors) with more positive potential compared to TMDs since most of the TMDs are inefficient in harvesting light on their own.

6. Contents of this part of the thesis

In the following chapters, we have explored the hydrogen evolution properties of the various materials, with theoretical predictions along with guidelines for new materials including non-trivial topological materials to boost photochemical HER. We explored the role of transition metal dichalcogenides especially group 6 (MX_2; M=Mo, W, and X=S, Se) transition metal dichalcogenides in photochemical HER. Transition metal dichalcogenides are of great interest because of their lamellar structure like graphene and versatility in electronic properties. We explored the bulk, as well as few-layers 2H-form of group 6 TMDs and discovered that they are potential catalysts for photochemical HER. We phase-engineered 2H-form to more metallic 1T-form. We discovered that indeed phase engineering drastically changes the properties of the catalyst. Further, we functionalized the 1T-form to stabilize it. However, we realized that functionalization captures the colloidal nature of the chemically exfoliated 1T-form but is in the 2H-form. The functionalized samples exhibit superior catalysis than 2H-form but poorer than 1T-form. These functionalized samples were further coupled with other 2D-materials by covalent-linking to improve their HER properties. We explored the role of

covalent-linking and effect of linkers. Further, we linked photo-active material with MoS_2 to overcome dye-restricted catalysis.

Other potential TMDs like group 4 (TiS_2) and group 5 (TaS_2) have been explored. Both TiS_2 and TaS_2 were inactive as a catalyst, but as co-catalyst, these materials enhance the photocatalytic activity of CdS. We further find that the metallic nature of the co-catalyst enhances the activity of the photocatalyst. It has become important to explore new materials for the process, which can be theoretically guided by first-principle calculations. Based on the theoretical calculations we explored HER properties of gallium chalcogenides and found them to be active for HER.

7. References

1.   N. S. Lewis and D. G. Nocera, Proc. Natl Acad Sci. USA, 2006, 103, 15729.

2.   J. A. Turner, Science, 1999, 285, 687.

3.   A. N. Laboratory, Configuration and Technology Implications of Potential Nuclear Hydrogen System Applications, 2005.

4.   G. L. Chiarello, M. H. Aguirre and E. Selli, J. Catal., 2010, 273, 182.

5.   K. Hou and R. Hughes, Chem. Eng. J., 2001, 82, 311.

6.   S. Czernik, R. Evans and R. French, Catal. Today, 2007, 129, 265.

7.   N.-L. Wu and M.-S. Lee, International Journal of Hydrogen Energy, 2004, 29, 1601-1605.

8.   J. Luo, J.-H. Im, M. T. Mayer, M. Schreier, M. K. Nazeeruddin, N.-G. Park, S. D. Tilley, H. J. Fan and M. Grätzel, Science, 2014, 345, 1593.

9.   Q. Xie, Y. Wang, B. Pan, H. Wang, W. Su and X. Wang, Catal. Commun., 2012, 27, 21.

10.   C.-H. Liao, C.-W. Huang and J. C. S. Wu, Catalysts, 2012, 2, 490.

11.   A. Steinfeld, Int. J. of Hydrogen Energy, 2002, 27, 611.

12.   I. Akkerman, M. Janssen, J. Rocha and R. H. Wijffels, Int. J. of Hydrogen Energy, 2002, 27, 1195.

13.   D. Das and T. N. Veziroglu, Int. J. of Hydrogen Energy, 2008, 33, 6046.

14.   Y. Guan, M. Deng, X. Yu and W. Zhang, Biochem. Eng. J., 2004, 19, 69.

15.   A. Kudo, Pure Appl. Chem., 2007, 79, 1917.

16.   D. o. Energy, Fuel Cell Technologies Office Multi-Year Research, Development, and Demonstration Plan, (http://energy.gov/eere/fuelcells/downloads/fuel-cell-technologies-office-multi-yearresearch-development-and-22.)

17.   J. Kang, S. Tongay, J. Zhou, J. Li and J. Wu, Appl. Phys. Lett., 2013, 102, 012111.

18. K. Takanabe, ACS Catalysis, 2017, 7, 8006.

19. N. J. Turro, V. Ramamurthy, and J. C. Scaiano, University Science Books, 2010, pp. pp 1– 38.

20. F. E. Osterloh, J. Phys. Chem. Lett., 2014, 5, 3354.

21. S. T. Omelchenko, Y. Tolstova, H. A. Atwater and N. S. Lewis, ACS Energy Lett., 2017, 2, 431.

22. A. Polman and H. A. Atwater, Nat. Mater., 2012, 11, 174.

23. A. Kudo and Y. Miseki, Chem. Soc. Rev., 2009, 38, 253.

24. Z. Zou, J. Ye, K. Sayama and H. Arakawa, Nature, 2001, 414, 625.

25. J. Li and N. Wu, Catal. Sci. Technol., 2015, 5, 1360.

26. H. Wang, L. Zhang, Z. Chen, J. Hu, S. Li, Z. Wang, J. Liu and X. Wang, Chem. Soc. Rev., 2014, 43, 5234.

27. W. J. Youngblood, S.-H. A. Lee, K. Maeda and T. E. Mallouk, Acc. Chem. Res., 2009, 42, 1966.

28. R. Marschall, Adv. Func. Mat., 2014, 24, 2421.

29. J. Ran, J. Zhang, J. Yu, M. Jaroniec and S. Z. Qiao, Chem. Soc. Rev., 2014, 43, 7787.

30. H. Zhou, Y. Qu, T. Zeid and X. Duan, Energy Environ. Sci., 2012, 5, 6732.

31. Q. Lu, Y. Yu, Q. Ma, B. Chen and H. Zhang, Adv. Mater., 2016, 28, 1917.

32. J. Schneider and D. W. Bahnemann, J. Phys. Chem. Lett., 2013, 4, 3479.

33. H. Liu, J. Yuan and W. Shangguan, Energy Fuels, 2006, 20, 2289.

34. W. Choi, N. Choudhary, G. H. Han, J. Park, D. Akinwande and Y. H. Lee, Mater. Today, 2017, 20, 116.

35. Y. Zhan, Z. Liu, S. Najmaei, P. M. Ajayan and J. Lou, Small, 2012, 8, 966.

36. K. Maeda and K. Domen, J. of Phys. Chem. Lett., 2010, 1, 2655.

37. J. Yang, D. Wang, H. Han and C. Li, Acc. Chem. Res., 2013, 46, 1900.

38. Q. Xiang and J. Yu, J. Phys. Chem. Lett., 2013, 4, 753.

39. I. Roger, M. A. Shipman and M. D. Symes, Nat. Rev. Chem., 2017, 1, 0003.

40. C. G. Morales-Guio, L.-A. Stern and X. Hu, Chem. Soc. Rev., 2014, 43, 6555.

41. D. Merki and X. Hu, Energy Environ. Sci., 2011, 4, 3878.

42. W. Ho, J. C. Yu, J. Lin, J. Yu and P. Li, Langmuir, 2004, 20, 5865.

43. F. A. Frame and F. E. Osterloh, J. Phys. Chem. C, 2010, 114, 10628.

44. Q. Xiang, J. Yu and M. Jaroniec, J. Am. Chem. Soc., 2012, 134, 6575.

45. S. Bai, L. Wang, X. Chen, J. Du and Y. Xiong, Nano Res., 2015, 8, 175.

46. Y. Hou, A. B. Laursen, J. Zhang, G. Zhang, Y. Zhu, X. Wang, S. Dahl and I. Chorkendorff, Angew. Chem. Int. Ed., 2013, 52, 3621.

47. L. Yang, D. Zhong, J. Zhang, Z. Yan, S. Ge, P. Du, J. Jiang, D. Sun, X. Wu, Z. Fan, S. A. Dayeh and B. Xiang, ACS Nano, 2014, 8, 6979.

48. X. Zong, J. Han, G. Ma, H. Yan, G. Wu and C. Li, J. of Phys. Chem. C, 2011, 115, 12202.

49. J. Chen, X.-J. Wu, L. Yin, B. Li, X. Hong, Z. Fan, B. Chen, C. Xue and H. Zhang, Angew. Chem., 2015, 127, 1226.

50. U. Gupta, B. G. Rao, U. Maitra, B. E. Prasad and C. N. R. Rao, Chem. Asian J., 2014, 9, 1311.

51. J. Low, C. Jiang, B. Cheng, S. Wageh, A. A. Al-Ghamdi and J. Yu, Small Methods, 2017, 1, 1700080.

52. K. Maeda, ACS Catal., 2013, 3, 1486.

53. K. S. Novoselov, A. K. Geim1, S. V. Morozov, D. Jiang, Y. Zhang, S. V. Dubonos, I. V. Grigorieva1, A. A. Firsov, Science, 2004, 306, 666.

54. A. H Castro Neto, F. Guinea, N.M.R Peres, K.S Novoselov, A.K Geim, Rev. Mod. Phys., 2009, 81, 109.

55. A.K Geim, Science, 2009, 324, 1530.

56. Q.H. Wang, K. Kalantar-Zadeh, A. Kis, J.N Coleman, M.S. Strano, Nat. Nanotech., 2012, 7, 699.

57. K. F. Mak, C.Lee, J. Hone, J. Shan, T.F Heinz, Phys. Rev. Lett., 2010, 105, 136805.

58. A. Splendiani et al., Nano Lett., 2010, 10, 1271.

59. Cao, T. et al. Nat. Commun., 2012, 3, 887.

60. H. Zeng, J. Dai, W. Yao, D. Xiao, X. Cui, Nat. Nanotech., 2012, 7, 490.

61. K.F Mak, K. He, J. Shan, T.F Heinz, Nat. Nanotech.,2012, 7, 494.

62. H. Li, G. Lu, Y. Wang, Z. Yin, C. Cong, Q. He, L. Wang, F. Ding, T. Yu and H. Zhang, Small, 2012, 8, 682.

63. G. Eda, H. Yamaguchi, D. Voiry, T. Fujita, M. W Chen, M. Chhowalla Nano Lett., 2011, 11, 5111.

64. G. Eda, T. Fujita, H. Yamaguchi, D. Voiry, M. W Chen, M. Chhowalla, ACS Nano 6, 2012, 7311.

65. Z. Yin, H. Li, H. Li, L. Jiang, Y. Shi, Y. Sun, G. Lu, Q. Zhang, X. Chen, H. Zhang, ACS Nano, 2012, 6, 74.

66. A. Castellanos-Gomez, M. Barkelid, A. M. Goossens, V. E. Calado, H. S. J. van der Zant and G. A. Steele, Nano Lett., 2012, 12, 3187.

67. J. Feng, L. Peng, C. Wu, X. Sun, S. Hu, C. Lin, J. Dai, J. Yang, Y. Xie, Adv. Mater., 2012, 24, 1969.

68. H.S.S.R Matte, A. Gomathi, A. K. Manna, D. J. Late, R. Datta, S. K. Pati, C.N.R. Rao, Angew. Chem. Int. Ed., 2010, 49, 4059.

69.   H. Li, Z. Yin, Q. He, H. Li, X. Huang, G. Lu, D. W. Fam, A. I. Tok, Q. Zhang, H. H. Zhang, Small, 2012, 8, 63.

70. K.P Loh, Q. L Bao, G. Eda, M. Chhowalla, Nat. Chem., 2010, 2, 1015.

71. B. Sipos, et al. Nat. Mater. 2008, 7, 960.

72. R.A Gordon, D. Yang, E.D Crozier, D.T Jiang, R.F Frindt, Phys. Rev. B, 2002, 65, 125407.

73. A. Kuc, N. Zibouche, T. Heine Phys. Rev. B, 2011, 83, 245213.

74. J. A. Wilson, F. J. Di Salvo, S. Mahajan, Adv. Phys., 1975, 24, 117.

75. J. C. Meyer, A. G. Geim, M. I Katnelson, K.S Novoselov, S. Roth, Nature, 2006 446, 60.

76. S. Bertolazzi, J. Brivio, A. Kis, ACS Nano, 2011, 5, 9703.

77. J. A Wilson, A. D Yoffe, Adv. Phys., 1969 18, 193.

78. U. Maitra, U. Gupta, M. De, R. Datta, A. Govindaraj, C. N. R. Rao, Angew. Chem. Int. Ed., 2013, 52, 13057.

79. R. Bissessur, M. G. Kanatzidis, J. L Schindler, C. R Kannewurf, J. Chem. Soc. Chem. Commun., 1993 1582.

80. R. F. Frindt, A. D Yoffe, Proc. R. Soc. Lond. A, 1963, 273, 69.

81. M.A Py, R. R Haering, Can. J. Phys., 1983, 61, 76.

82. P. Ganal, W. Olberding, T. Butz, Solid State Ionics, 1993, 59, 313.

83. Z. Zeng, C. Tan, X. Huang, S. Bao and H. Zhang, Energy Environ. Sci., 2014, 7, 797.

84. Y. Wang, Z. Sofer, J. Luxa and M. Pumera, Adv. Mater. Interfaces, 2016, 3, 1600433.

85. X. Chia, A. Adriano, P. Lazar, Z. Sofer, J. Luxa and M. Pumera, Adv. Func. Mater., 2016, 26, 4306.

86. C. Tsai, K. Chan, J. K. Nørskov and F. Abild-Pedersen, Surf. Sci., 2015, 640, 133.

87. R. Parsons, Trans. Faraday Soc., 1958, 54, 1053.

88. S. Trasatti, J. Electroanal. Chem., 1971, 33, 351.

89. J. K. Norskov, T. Bligaard, J. Rossmeisl and C. H. Christensen, Nat. Chem., 2009, 1, 37.

90.   D. Voiry, H. Yamaguchi, J. Li, R. Silva, D. C. B. Alves, T. Fujita, M. Chen, T. Asefa, V. B. Shenoy, G. Eda and M. Chhowalla, Nat. Mater., 2013, 12, 850.

91.   D. Voiry, M. Salehi, R. Silva, T. Fujita, M. Chen, T. Asefa, V. B. Shenoy, G. Eda and M. Chhowalla, Nano Letters, 2013, 13, 6222.

Dye-sensitized hydrogen evolution by using 2H- and 1T- forms of group 6 transition metal dichalcogenides*

Summary

The 2H polymorph of MoS_2 exhibits some catalytic for electrochemical as well as photochemical hydrogen evolution reaction. Band offset of Group 6 metal dichalcogenides have their conduction band minimum which lies above the water reduction position and would be an appropriate material for hydrogen evolution reaction (HER). Theoretical and experimental studies indicate that metallic edges of MoS_2 are catalytically active while the basal plane remains inert, so a metallic MoS_2 would greatly enhance its photocatalytic activity. On lithium intercalation and exfoliation of bulk Group 6 transition metal dichalcogenides yield the metallic 1T-form which can be employed for the visible-light induced generation of hydrogen. The 1T-form is found to be superior to the 2H-form in producing hydrogen from water which is supported by first principles calculations, which reveal that the 1T form has a lower work function than the 2H-form, making it easier to transfer an electron from 1T form for the production of H_2. It is found that 1T-$MoSe_2$ is superior not only to its 2H-form but also to both 1T- and 2H- MoS_2 as the conduction band minimum of $MoSe_2$ is ~0.37eV higher than that of MoS_2.
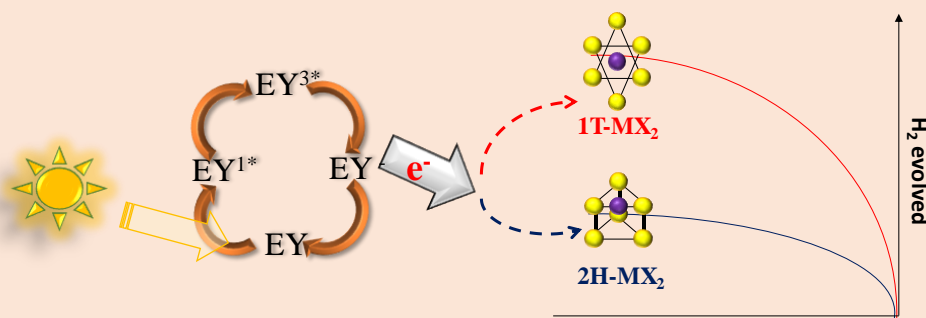
1. Introduction

O ver the past decade, replacing fossil fuels by renewable sources of energy has become a significant research goal not only because of the dwindling resources of fossil fuels but also due to harmful effects of CO_2 and other gases produced by combustion of the fuels. Hydrogen produced from water using solar energy is undoubtedly the ultimate source of clean, renewable energy. Traditionally, H_2 is generated from water using Pt electrodes, several catalysts have been used for the electrocatalytic, photocatalytic or photoelectrocatalytic production of hydrogen [1,2]. In natural systems, proton reduction is catalyzed by hydrogenase and nitrogenase, enzymes catalytic center of which is mainly composed of earth-abundant non-noble metal elements like Fe, Ni, Mo **(Figure 1)**.
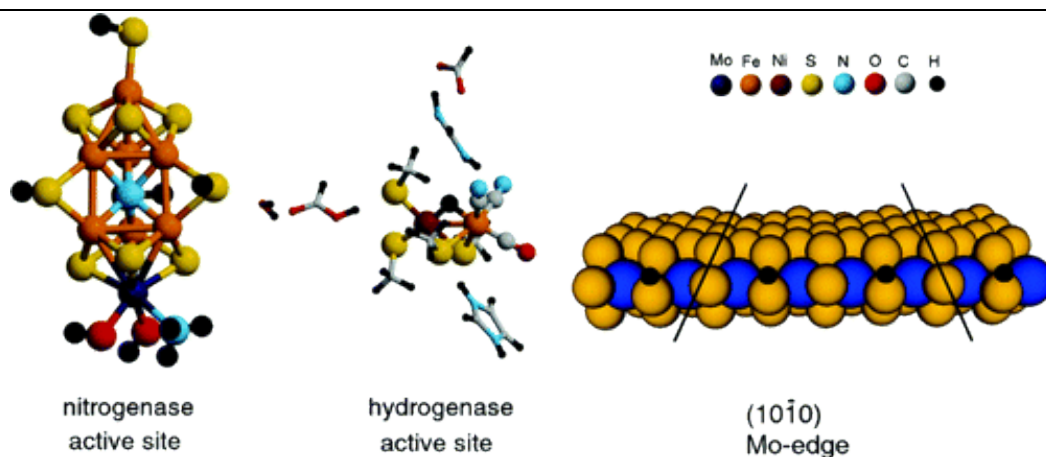
Figure 1. *(Left) Nitrogenase FeMo cofactor (FeMoCo) with three hydrogen atoms bound at the equatorial µ2S sulfur atoms. (Middle) Hydrogenase active site with one hydrogen atom bound. (Right) MoS₂ slab with sulfur monomers present at the Mo edge. The coverage is 50%, i.e., hydrogen is bound at every second sulfur atom. The lines mark the dimension of the unit cell in the x-direction. Adapted from reference. 3 Copyright Permission American Chemical Society.*

Recent DFT calculations also suggest that free energy of hydrogen evolution on MoS_2 is comparable to hydrogenase, nitrogenase as well as Pt. The free energy was calculated based on the consideration that a catalyst should bind atomic H with just the proper strength (not too strong and not too weak) such that both binding and release of hydrogen is equally feasible **(Figure 2)**. Based on this consideration the necessary condition for a catalyst to act as a good proton reduction catalyst is that the free energy of adsorbed H is close to that of the reactant and product, i.e., the $\Delta G^0 \approx 0$ [3]. It was also found that the edge structure of MoS_2 sheets has close resemblance with the catalytically active sites of nitrogenase and hydrogenase. MoS_2, which is an established catalyst for the hydrodesulfurization reaction [4] has proven to be a useful catalyst for electrochemical as well as photochemical hydrogen evolution reaction (HER) [5-8].
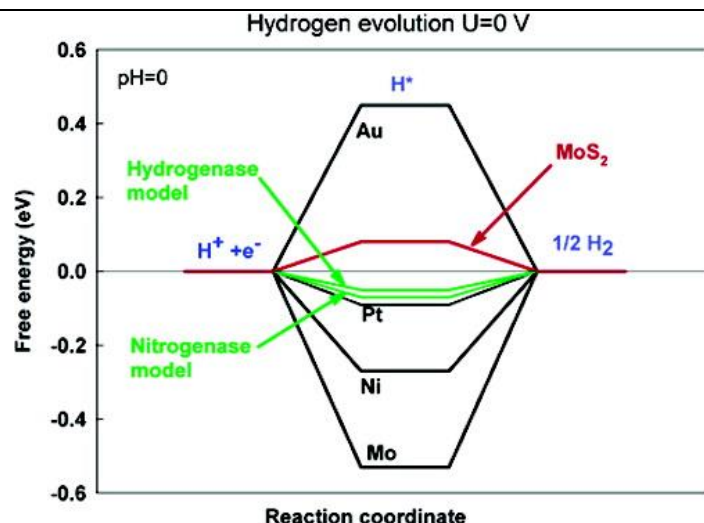
Figure 2. *The free energy of H atoms bound to different catalysts is then found by calculating the free energy with respect to molecular hydrogen including zero-point energies and entropy terms. Adapted with permission from reference 3. Adapted from reference. 3 Copyright Permission American Chemical Society.*

Theoretical and experimental studies indicate that edges of MoS_2 are catalytically active while the basal plane remains inert [3,9]. Nanoparticles of MoS_2 with single-layered truncated triangular morphology with exposed Mo edges, [9, 10] or those grown on highly ordered pyrolytic graphite [11] or graphitic carbon [12] are catalytically active. Electrochemical HER carried out with nanoparticles of MoS_2 supported on carbon [13], and fluorine-doped tin oxide electrode [14] show higher yields of H_2. Hydrogen evolution appears to be further enhanced by using graphene [15] or carbon nanotubes [4] to support nanocrystalline MoS_2, the favorable conductivity of the nanocarbon ensuring efficient electron transfer to the electrodes. The good photo-electrocatalytic activity of MoS_2 has been reported, with MoS_2 possessing the double gyroid structure with a large number of interconnected pores showing the highest efficiency [16]. While electrochemical HER by MoS_2 has been studied in detail, photocatalytic HER by MoS_2 has received less attention. Bulk MoS_2 being an indirect band gap (1.29 eV) semiconductor does not absorb the solar spectrum efficiently. If we somehow can put an electron on the conduction band of the MoS_2, we can expect MoS_2 to perform as photocatalytic HER. MoS_2 on sensitization with $[Ru(bpy)_3]^{2+}$ ions colloidal MoS_2 nanoparticles show photocatalytic HER activity with a turn over number (TON) of 93. The method utilizes a three-component system with ascorbic acid as the reductive quencher for the excited state $[Ru(bpy)_3]^{2+}$ which in turn transfers electrons to MoS_2 [17]. MoS_2 loaded on TiO_2 [18] and CdS [19] has been investigated for H_2 evolution where TiO_2 and CdS act as both light

absorbers and catalysts. A typical dye-sensitized HER with the catalyst is shown in **Scheme 1.**
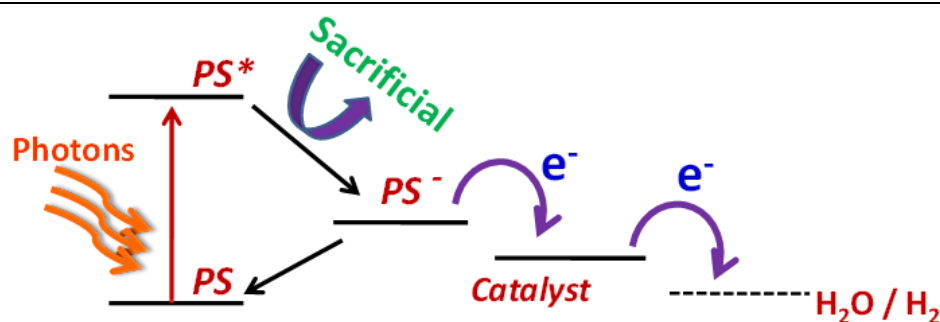
Scheme 1. *Schematic represents dye-sensitized photocatalytic hydrogen evolution from the water.*

Few-layer MoS_2 loaded on reduced graphene oxide (RGO) shows good HER activity compared to MoS_2 or its physical mixture with RGO, with EosinY as sensitizer [20]. Because graphene acts as a channel for transferring electrons to MoS_2 in graphene–MoS_2 composites, visible-light driven H_2 generation by few-layer 2H-MoS_2, Nitrogen incorporation in graphene is expected to improve the catalytic activity of the composite with 2H-MoS_2 layers since it enhances the electron donating ability of the graphene, composite with heavily nitrogenated RGO (%N ca. 15) which shows excellent HER activity of 10.8 mmol g^{-1} h^{-1} and a turn over frequency (TOF) of 2.9 h^{-1} under a 100W halogen lamp [21]. Nanoparticles of 2H-MoS_2, as well as composites of 2H-MoS_2 with graphene and other materials, have been employed as catalysts yielding 0.05-10 mmol g^{-1} h^{-1} of H_2 with a turn over frequency anywhere between of 0.2-6 h^{-1} [18-21].

2. Scope of the present investigations

Exfoliation of metal dichalcogenides and other 2D materials into single or few-layers often brings about drastic changes in the electronic structure

as compared to the bulk. Dichalcogenides of Mo and W mostly occur in the 2H form, *i.e.,* having a trigonal prismatic arrangement of hexagonal X-M-X (M = Mo/W; X=S, S) triple layer and are among the most studied of the layered metal chalcogenides owing to their interesting electronic properties. While 2H forms of these metal dichalcogenides are semiconducting, their 1T forms are metallic [22-24]. MoS_2 has been widely used as a catalyst for electrochemical, photoelectrochemical and photocatalytic H_2 generation from water [15-21] in consequence of having the conduction band minimum well above the H_2O reduction potential [25-26].
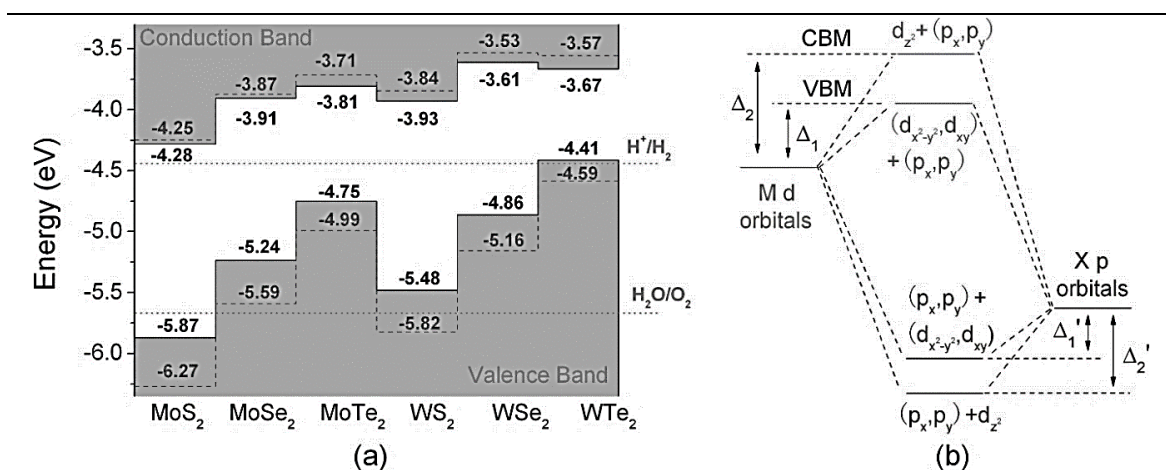
Figure 3. *(a) Calculated band alignment for MX$_2$ monolayers. Solid lines are obtained by PBE, and dashed lines are obtained by HSE06. The dotted lines indicate the water reduction (H$^+$/H$_2$) and oxidation (H$_2$O/O$_2$) potentials. The vacuum level is taken as zero reference. (b) Schematic of the origin of CBM and VBM in MX$_2$. Adapted from reference. 3 Copyright Permission American Chemical Society.*

From the band offset diagram of the Group 6 transition metal dichalcogenides **(Figure 3a),** we observe that the conduction band minimum (CBM) of all group 6 TMDs are more negative than the water reduction potential (H$^+$/H$_2$), while the valence band maximum (CBM) lies above water oxidation potential(O$_2$/H$_2$O) except for MoS_2 **(Figure 3a)** [26].

This implies than MoS_2 can both reduce and oxidize water but other TMDs in group 6 can only reduce water. Group 6 TMDs have a direct bandgap of about 1.7 eV which makes them ideal for visible light active photocatalyst as well as the effective utilization of the solar energy. In a much closer examination, the oxidizing power (denoted as Δ_2 that is defined as the difference between VBM band edge and the oxygen reduction potential **(Figure 3b)**. However, the reducing power (denoted as Δ_1), which is defined as the difference between the proton reduction and the CBM edge potentials.

The rate constant of a chemical reaction can be given by Arrhenius equation **(equation 1)**,

$$K = Ae^{RT/Ea} \quad (1)$$

where A is the pre-exponential factor, R is the universal gas constant, and E_a is the reaction energy barrier. The reaction barrier in photocatalytic redox reactions of water is complicated. But, it can be understood by the difference between the reaction rate of reduction reaction and oxidation reaction. The energy barrier can be minimized by reducing the difference between Δ_1 and Δ_2, and improved efficiency of the reaction can be achieved. Which also suggests that MoS_2 is a good candidate for reduction but not oxidation. But our primary concern is the production of hydrogen from water. The bigger barrier or (big difference between Δ_1 and Δ_2), would imbalances the reduction and oxidation reactions, which inhibits the progress of the overall redox reaction. If we can decrease the difference between Δ_1 and Δ_2, we can further improve its efficiency for water splitting. The difference between Δ_1 and Δ_2, can loosely be termed as the band gap of

the material, and if we can reduce the band gap of the material we can increase the activity of MoS_2 one of the ways would be using Se, as band gap of $MoSe_2$ is less than that of MoS_2 and other would by using 1T-MoS_2. In literature, 1T-MoS_2 is a better catalyst is a better catalyst than its 2H form electrochemically [27-28]. As in case of 1T-MoS_2, the 1T form of $MoSe_2$ too is metallic and could be expected to be a better catalyst than its 2H analog for visible-light-induced water reduction for oxidative power is completely diminishes and only reducing power is responsible for HER.

However, the imbalance between the reduction reaction and oxidation reaction would prevent the process of redox reactions. It can only be continued when excessive oxidization species are reduced. If we can find an oxidizing material which oxidizes at a lower potential, then water this process can be enhanced very effectively. We have studied the photocatalytic activity of 2H- and 1T- phase of group 6 TMDs. We have used dye as an electron-injecting group and bypassing the oxidation on the catalyst surface to enhance the Hydrogen evolution reaction (HER).

3. Experimental section

3.1 Synthesis

3.1.1 Synthesis of 1T-MX$_2$ samples: The bulk samples of MX_2 (M= Mo, W; X= S, Se) were procured from Alfa Aesar. 300 mg of MX_2 was taken in a 20 ml vial with a cap and to it 10 ml of 1.6M n-butyl lithium in Hexane was added and was stirred for certain period of time (in case of MoS_2 we stirred for 3 days, WS_2 for one week and Mo(W)Se_2 for 3 weeks). The sample was washed with hexane 3 times and centrifuged at 8000 rpm for 5 minutes each. The centrifuged product was then exfoliated in water by

sonication. The dispersion was dialyzed for 12 hours to remove excess of LiOH from the solution. [29-31]

3.1.2 Synthesis of few-layer MoX$_2$ (X=S, Se):

Few-layer 2H-MoS$_2$ was synthesized using thiourea, where molybdic acid and thiourea in mass ratio 1:24 was heated at 500°C under N$_2$ flow for 5 hours. 2H-MoSe$_2$ were synthesized under similar conditions with selenourea for a selenium source for comparison [32].

3.1.3 Synthesis of functionalized MX$_2$ (M= Mo, W; X=S, Se):

The exfoliated 1T-form was functionalized using bromoacetic acid. The exfoliated sample was dialyzed, and to it, the excess amount of bromoacetic acid was added. The precipitate was washed by centrifuged and dried in vacuum at 60 ^{o}C.

3.2 Characterization

HRTEM was performed in the FEI TITAN cubed double aberration corrected 80–300 kV microscope. Negative Cs imaging was used (Cs ≈ 35–40 mm, Df≈ +8 nm) to image atoms with white contrast and direct interpretation. Raman spectra were recorded with a Horiba-Jobin Yvon LabRAM HR Raman spectrometer using Ar laser (λ = 514.5nm) with D1 filter. Inductively coupled plasma optical emission spectroscopy (ICP–OES) was used to determine the concentration of MoSe$_2$ and MoS$_2$ in the water dispersion of 1T-MoX$_2$ using a Perkin-Elmer Optima 7000 DV instrument.

3.3 Hydrogen evolution measurements

Photocatalytic measurements of the sample were carried out as follows. The required amount of dispersion of the catalyst was taken and dispersed

in water (40 mL) and triethanolamine (15%v/v; 8 mL). The vessel was thoroughly purged with N_2. 1ml of 0.015 mM solution Eosin Y in Ethanol was then added as the sensitizer. The vessel was irradiated under 100W halogen lamp with constant stirring of the mixture. 2 mL of evolved gases were manually collected from the headspace of the vessel at a regular time interval and analyzed in PerkinElmer Clarus ARNEL 580 gas chromatograph.

Turn over frequency (TOF) was calculated as follows,

$$TOF\ (h^{-1}) = \frac{Activity\ of\ the\ catalyst}{Moles\ of\ the\ catalyst\ used}\ (2)$$

4. Results and discussion

4.1 Synthesis and characterization

The bulk samples of group 6 transition metal dichalcogenides (TMDs) of MoS_2, $MoSe_2$, WS_2, and WSe_2 were commercially purchased and characterized using X-ray diffraction and Raman. The group 6 TMDs naturally crystallizes in 2H-form in a hexagonal lattice with space group P63/mmc. They form a honeycomb lattice-like graphene in the 2D-plane **(Figure 4a)**. The individual layers consist of X-M-X (M= Mo, W; X=S, Se) units which are covalently bonded while the adjacent layer has van der Waals' interaction **(Figure 4b)**. Therefore, it is easy to exfoliate these materials or intercalate various ions mechanically. The X-ray diffraction patterns for the bulk samples are shown in **Figure 4c**.
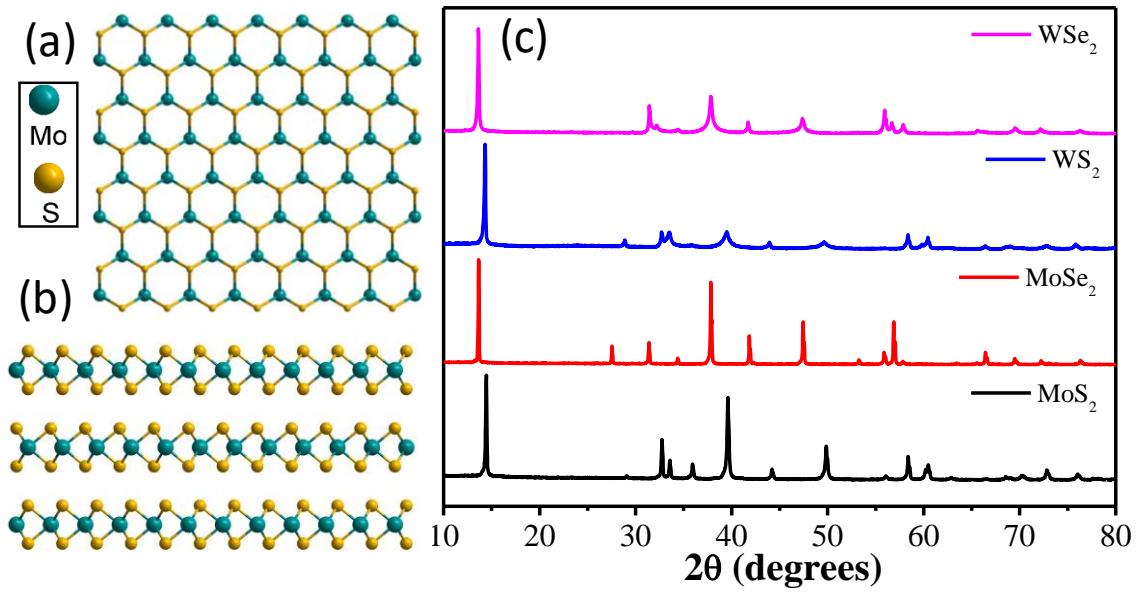
Figure 4. *Atomic arrangement of MX$_2$ as viewed from (a) c-direction and (b) side view. (c) X-ray diffraction of MoS$_2$, MoSe$_2$, WS$_2$, and WSe$_2$. The compound naturally exists in 2H-form with space group P63/mmc.*

The point group of 2H-MX$_2$ is D$_{3h}$, and the Raman allowed modes are E$_{1g}$, E$^1_{2g}$, E$^2_{2g}$ and A$_{1g}$ are shown in **Figure 5a**. The Raman spectra for these samples were recorded using a green laser (514 nm). For MoS$_2$ the Raman bands due to out-of-plane (A$_{1g}$) mode appear at 405 cm^{-1} while in-plane mode (E$^1_{2g}$) appear at 378 cm^{-1} respectively. In MoSe$_2$ the prominent peaks are out of plane A$_{1g}$ at 255 cm^{-1} and in-plane (E$_{1g}$) at 171 cm^{-1} respectively. There are a slight variation of Raman band of the sulfides and selenide even though the symmetry allowed peaks are same. This was observed even in tungsten sulfide and selenide. The Raman bands in 2 due to out-of-plane (A$_{1g}$) mode appears at 423 cm^{-1} while in-plane mode (E$^1_{2g}$) appear at 359 cm^{-1} respectively. For WSe$_2$ the prominent bands are out of plane A$_{1g}$ at 252 cm^{-1} and in-plane (E$_{1g}$) at 176 cm^{-1} respectively **(Figure 5b)**. The prominent Raman bands of 2H-MX$_2$ are listed in **Table 1**.
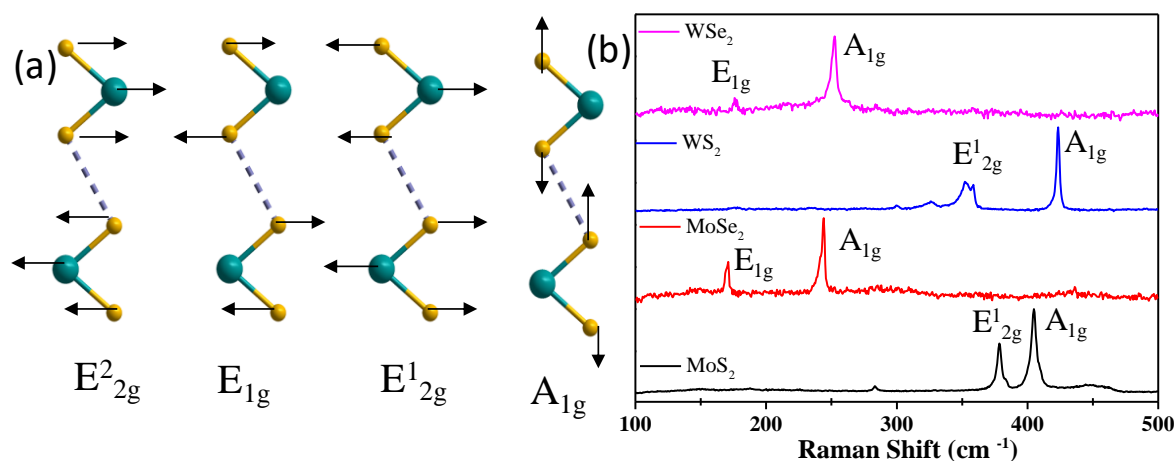
Figure 5. *(a) Raman allowed modes of 2H-MX$_2$ crystals. Raman of MoS$_2$, MoSe$_2$, WS$_2$ and WSe$_2$ spectra.*

Table 1. List of Raman modes and bands of in 2H-MX$_2$ (M= Mo, W; X= S, Se)

Raman Modes	MoS$_2$ (cm^{-1})	MoSe$_2$ (cm^{-1})	WS$_2$ (cm^{-1})	WSe$_2$ (cm^{-1})
E$_{1g}$	---	171	---	176
E$^1_{2g}$	378	---	352	---
A$_{1g}$	405	244	423	252

Bulk MX$_2$ in the 2H form was intercalated with lithium using n-butyl lithium and exfoliation carried out by reacting the intercalated product with water [29-31]. The energy liberated during the formation LiOH is highly exothermic and provides the driving for the formation of layers of the 1T-form **(Figure 6a)**. The exfoliation of sulfides and selenides of molybdenum is comparatively easy as compared to tungsten dichalcogenides. WS$_2$ was difficult to exfoliate, and yield of 1T-phase was less as compared to MoS$_2$. The difficulty in the intercalation of WS$_2$ is attributed to either due to an oxide formation on WS$_2$ powder that has been exposed to air or water

vapor, sealing the edges against intercalation which on ultrasonic treatment, inducing stress and distorts the interlayer bonds and breaks the seal. The other possibility is in the course of the ultrasonic treatment slippage between basal planes is induced, and during such slippage, the hexane or the Li can more easily penetrate [33] WSe_2 was unstable during exfoliation. Therefore, we have characterized 1T-phase of MoS_2, $MoSe_2$, and WS_2.
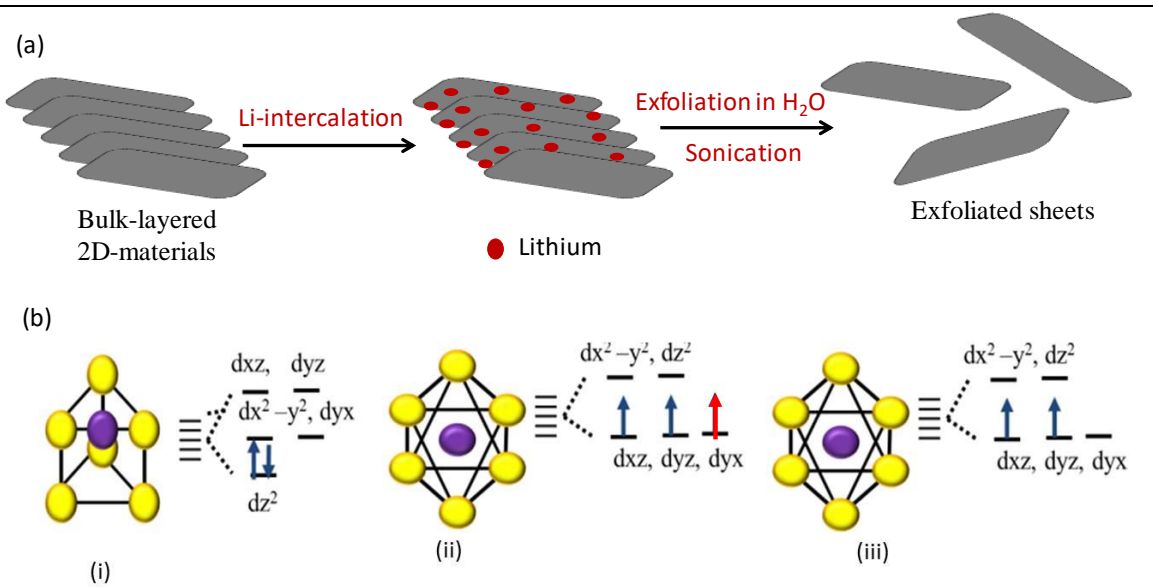
Figure 6. *(a) Schematic of lithium intercalation and exfoliation in water for MX_2 sheets. (b) The electronic configuration of (i) 2H-form, (ii) in Li-intercalated state and (iii) exfoliated 1T-sheets. The change in the electronic is the driving force for this transformation.*

The electronic structure of 1T-MoX_2 is different from that of 2H-MoX_2. The electronic structure proposed by Tenne *et al.* [23] in the case of MoS_2 would apply to other chalcogenides. The valence band of 2H-MX_2 is composed of X np states and the conduction band (CB) composed of M nd states that lie above the Fermi level. According to crystal-field theory, hexagonal (D_{3h}) symmetry in 2H-MX_2 would induce splitting of the M nd orbitals into three sets of orbitals of closely spaced energies: $d_{z^2}(a_1)$ and

two pair of doubly degenerate orbitals composed of d_{yx}, $d_{x^2-y^2}$ (e) and d_{xz}, d_{yz} (e') as shown in **Figure 6b (i).** The M nd_{z^2} level is occupied and spin-paired forming the valence band minimum (VBM), while the other four orbitals form the empty conduction band minimum (CBM). The symmetry of 1T-MX$_2$ is D_{3d}, with Mo in octahedral coordination. The crystal-field splitting of M nd under the octahedral O_h field generates three triply degenerate orbitals d_{yx}, d_{zx}, d_{zy} (t_{2g}) containing two unpaired electrons and two empty doubly degenerate orbital $d_{x^2-y^2}$, d_{z^2} orbitals The incompletely filled d_{yx}, d_{zx}, d_{zy} (e_g) orbital. It has now partially filled (M nd^3) d orbital with Fermi level within the band, so it exhibits metallic properties **(Figure 6b (ii))**. Based on the electronic configuration of 1T and 2H phases of MX$_2$ it is clear that when an extra electron is added to 2H-MX$_2$, it resides in the degenerate d_{yx}, $d_{x^2-y^2}$ states and destabilizes the lattice, while in case of 1T-MX$_2$ the extra electron induces half-filled configuration of d_{yx}, d_{zx}, d_{zy} and increases the stability of the 1T-phase **(Figure 6b (iii))**.

Since 1T- and 2H- form have different atomic configuration and symmetries, they can be distinguished using high-resolution TEM (HRTEM) or Raman. We characterize 1T-samples with Raman and HRTEM. The electron diffraction pattern of 2H-MoS$_2$ shows the usual hexagonal spot pattern **(Figure 7a)**, but 1T-MoS$_2$ shows an extra the electron diffraction pattern and the HRTEM images of 2H and 1T MoS$_2$ are given in Figure hexagonal spot at 30º angular spacing in between the hexagonal spots of the 2H structure **(Figure 7b)**. **Figure 7c** shows the schematic representation of 2H- and 1T-MoS$_2$ structures. 2H-MoS$_2$ has a trigonal prismatic arrangement of Mo and S atoms, with the S atoms in the lower

layer lying directly below those of the upper layer. In 1T-MoS$_2$, on the other hand, the S atoms in the upper and lower planes are offset from each other by 30° such that the Mo atoms lie in the octahedral holes of the S layers. The extra spot in electron diffraction arises from this rotation of one of the S atomic layers with respect to another. **Figure 7d** and **7e** show the HRTEM images for a single layer of 2H-MoS$_2$ and 1T-MoS$_2$.
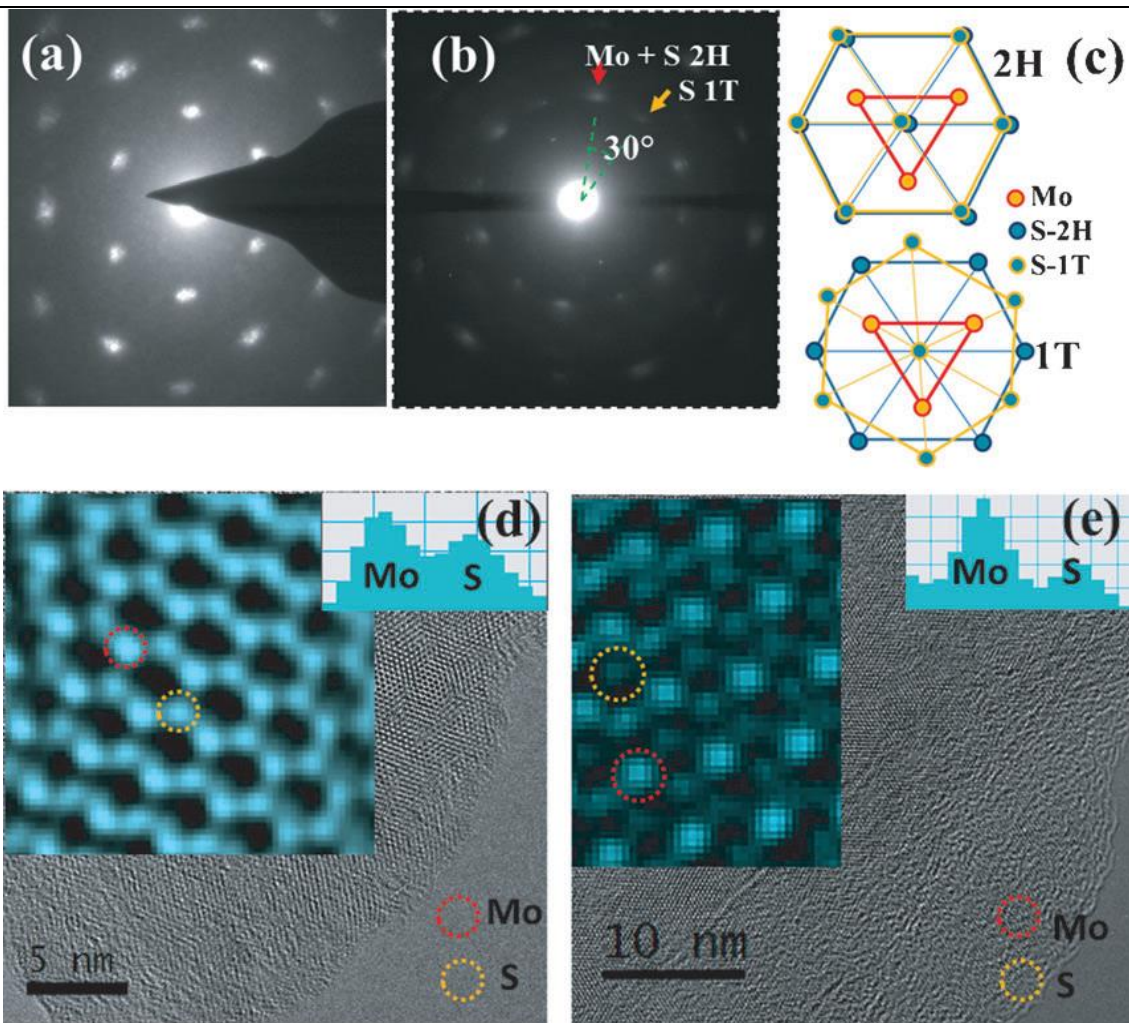
Figure 7. *Electron diffraction patterns from single-layer MoS$_2$ with a) the 2H and b) 1T structures. c) Schematic structural model corresponding to the 2H and 1T structures. HRTEM images of the d) 2H and e) 1T structures. The insets in (d) and (e) show magnified images of Mo and S atomic arrangements in 2H and 1T structures, as well as intensity line, scans through Mo and S atoms.*

In case of 2H-MoS$_2$, three S atoms surround one Mo atom whereas for the 1T structure six S atoms can be seen surrounding one Mo atom. Intensity line scans through Mo, and S atoms show a higher intensity difference for the 1T structure (one S atom in projection) compared to the 2H structure (2S atoms together in projection). This difference, in contrast, is related to the corresponding phase shift (related to the net atomic number) under negative Cs (third-order spherical aberration coefficient) imaging conditions. [34]
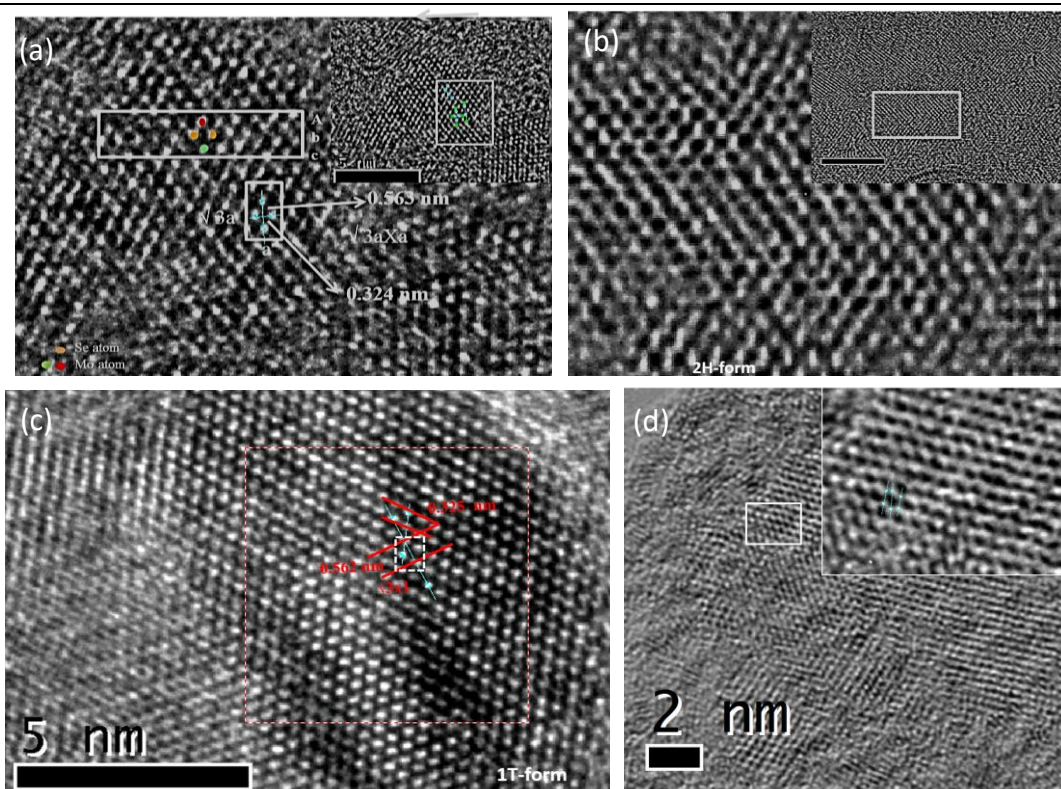
Figure 8. *HRTEM of (a) 1T-MoSe$_2$, (b) 2H-MoSe$_2$, (c) 1T-WS$_2$ and (d) 2H-WS$_2$*

HRTEM of 1T-MoSe$_2$ (**Figure 8a**) form has the √3a × an arrangement which is related to its electronic structure. [30,35] The shifting of the atoms from their equilibrium positions, probably arises because of the Jahn-Teller instability, resulting in chain clustering of the metal atoms with the formation of a superlattice [36]. The Mo atoms in the 2H form of MoSe$_2$ have

trigonal prismatic coordination as is evident from the high-resolution TEM image in **Figure 8b**. The packing of atoms in 2H $MoSe_2$ is AbA type while in the 1T form it is AbC type. Similarly, in 1T-WS_2 we observe √3a × an arrangement arising due to clustering of the W atoms **(Figure 8c)**. The 2H-form has hexagonal honeycomb lattice structure **(Figure 8d)**. We clearly see the difference in TEM of 1T and 2H-form in their atomic arrangement.
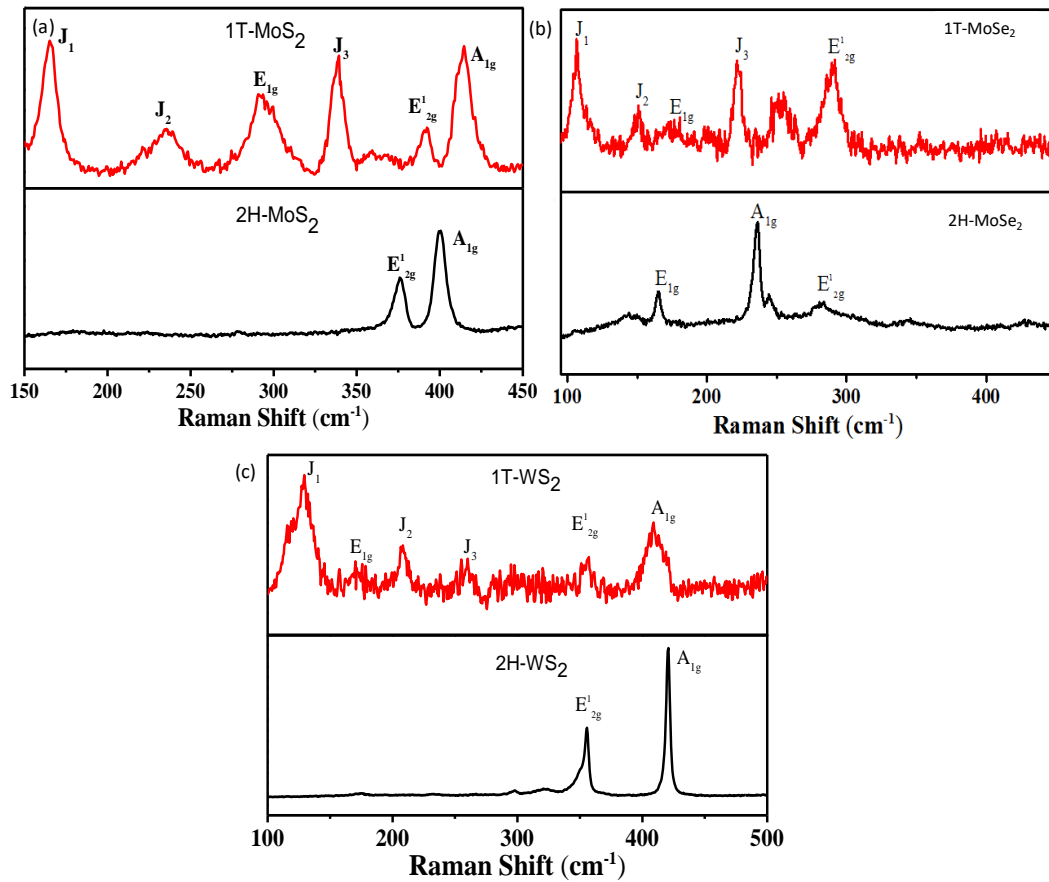
Figure 9. *Comparison of Raman spectra of 1T and 2H-form of (a) MoS₂, (b) MoSe₂, and (c) WS₂.*

Due to the difference in their symmetry, we expect characteristic peaks in Raman. The point group of the trigonal prismatic 2H-MX_2 and MX_2 is D_{3h} while the 1T polytype belongs to the D_{3d} point group [35]. The 1T phase exhibits a Raman spectrum which is distinctly different from that of the 2H-phase in **Figure 9.**

The Raman spectrum of 2H-MoSe$_2$ shows E_{1g}, A_{1g} and E^1_{2g} bands at 165, 236 and 284 cm^{-1}, while the 1T phase exhibits J_1, J_2 and J_3 bands at 106, 151 and 221 cm^{-1} respectively, not present in 2H-MoSe$_2$. The E^1_{2g} band, corresponding to the in-plane vibration of MoSe$_2$ sheets is observed at 289 cm^{-1} in the 1T form and at 284 cm^{-1} in the 2H form. Interestingly, the A^1_g band corresponding to the out-of-plane vibration of MoSe$_2$ does not appear in the spectrum of the 1T form. **(Figure 9b)**. The signature peaks of 1T-phase J_1, J_2, and J_3 for 1T-WS$_2$ appears at 129, 209 and 260 cm^{-1}. The peaks corresponding to A_{1g} and E^1_{2g} peaks appear at 409 and 356 cm^{-1} respectively. In 2H-phase we do not observe J_1, J_2, and J_3 peaks but A_{1g} and E^1_{2g} peaks at 423 and 359 cm^{-1} respectively. **(Figure 9c)**. In **Table 2**, a comparative table of the Raman frequencies of the 1T and 2H polytypes of MoS$_2$, MoS$_2$, and WS$_2$.

Table 2. Raman band positions of 1T- and 2H- forms of MoS$_2$, MoSe$_2$ and WS$_2$.

Raman Modes	1T-MoS$_2$ (cm^{-1})	2H-MoS$_2$ (cm^{-1})	1T-MoSe$_2$ (cm^{-1})	2H-MoSe$_2$ (cm^{-1})	1T-WS$_2$ (cm^{-1})	2H-WS$_2$ (cm^{-1})
J_1	165	---	106	---	129	---
J_2	237	---	151	---	209	---
J_3	339	---	221	---	260	----
A_{1g}	414	405	---	244	409	423
E_{1g}	292	283	---	171	---	300
E^1_{2g}	391	378	289	---	356	359

4.2 Hydrogen evolution studies

The hydrogen evolution activity of MoX_2 was studied using Eosin Y as the sensitizer and triethanolamine as the sacrificial electron donor. The reaction of dye-sensitized H_2 evolution over MX_2 involves photosensitization of Eosin Y followed by formation of Eosin Y anion (EY$^-$). EY$^-$ being highly reactive donates this electron to MX_2, which then catalyzes the reduction of a proton to H_2 as shown in **Figure 10**.
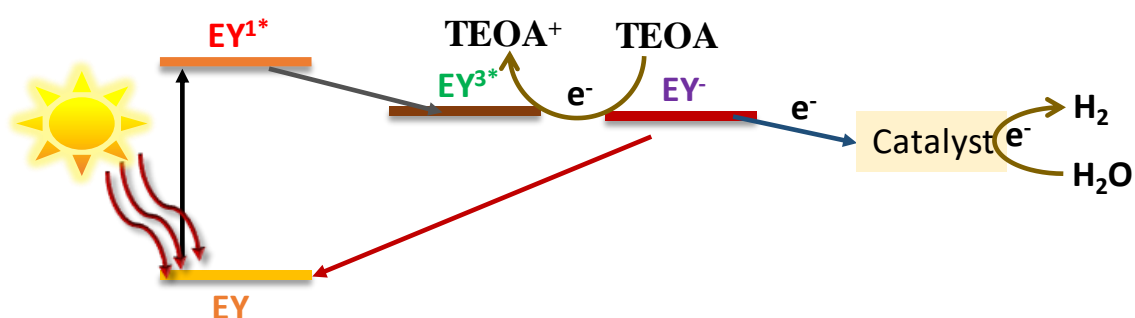
Figure 10. *The simplified electronic state diagram of Eosin Y and plausible mechanism of the H_2 reaction. The model represents a singlet ground-state as EY, excited singlet state EY^{1*}, and low lying triplet state EY^{3*}. The highly reducing negatively charged state (EY-) forms in the presence of triethanolamine (TEOA). The electron from the reducing species is transferred to the catalyst for hydrogen evolution reaction.*

The hydrogen evolution of 2H-MoS_2, $MoSe_2$, WS_2 and WSe_2 are 0.16, 1.0 and 0.6 and 1.8 mmol g^{-1} h^{-1} with TOF of 0.03, 0.25, 0.15 and 0.6 h^{-1} respectively **(Figure 11)**. Selenides have better activity than sulfides. This is due to the difference in hydrogen binding energy (HBE) of the atoms in the crystal with the hydrogen. In sulfides, HBE of sulfur is higher as compared to the metal atoms. This also explains why Mo-sites are active sites in MoS_2 for HER. In selenides, the HBE for both metal and selenium atoms are similar thus both can serve as HER site. **Figure. 11** shows the

time course of hydrogen evolution by 2H MoS_2 and $MoSe_2$. The 2H form of MoS_2 has an activity of 0.05 mmol g^{-1} h^{-1} with TOF of 0.02 h^{-1} while $MoSe_2$ has an activity of 0.08 mmol g^{-1} h^{-1} with a TOF of 0.008 h^{-1} shows better activity than that of 2H-MoS_2.
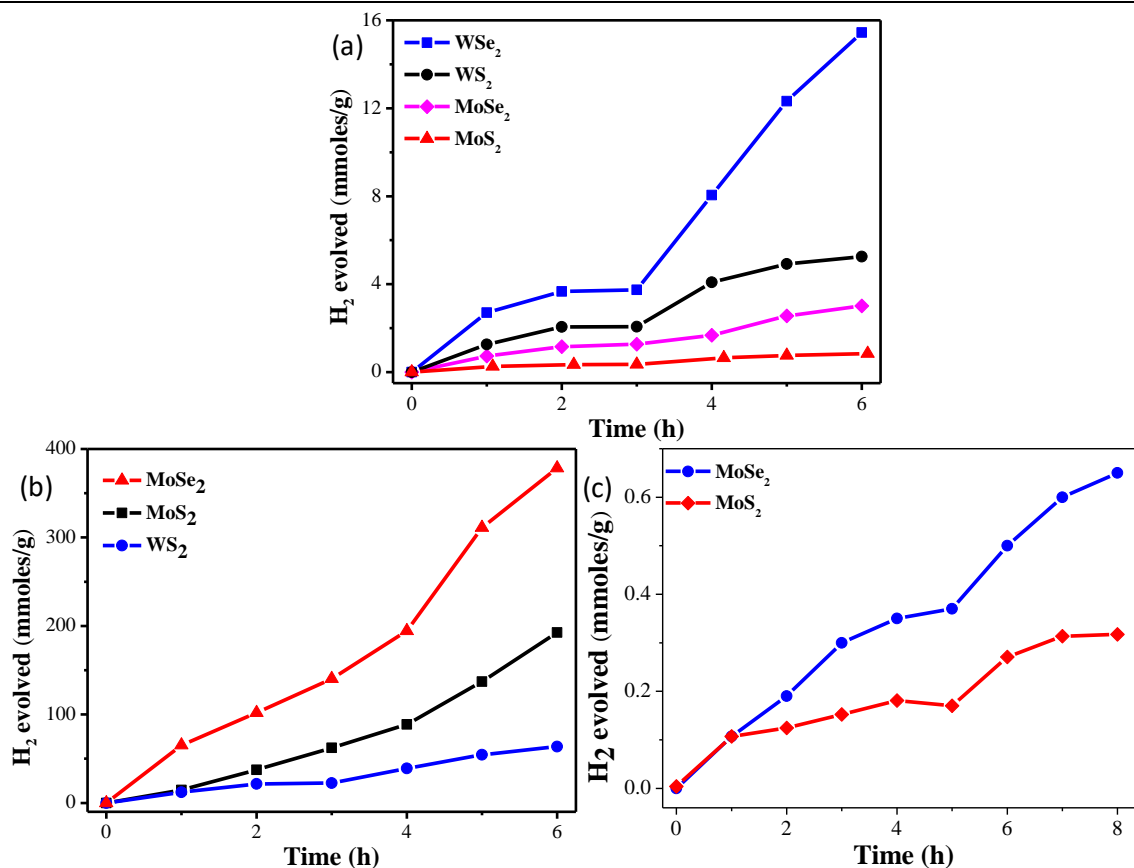
Figure 11. *Comparison of the time course of H_2 evolution of (a) 2H-MX_2, (b) 1T-MX_2 and (c) few-layer 2H- MoS_2 and $MoSe_2$.*

In case of 2H MoX_2, only metallic edge sites are active and not the basal plane [3, 9]. When 2H-phase we have when an electron is transferred from EY^- to 2H-MoX_2, the extra e^- added goes to conduction band $d_{x^2-y^2}$, and from there it is transferred to water which then catalyzes the reduction of a proton to H_2. Since 1T-MoX_2 is metallic in nature; it enhances the charge separation and also increases the mobility on its surface. EY^- donates this electron to $4d_{yx}$ which then catalyzes the reduction of a proton to H_2. The

photocatalytic generated hydrogen was collected and regular time intervals and calculated.

Photocatalytic activities of 1T-MoS$_2$ were studied by taking 2 ml of the dispersion of the sample in 50 ml 15% TEOA/water. The concentration of MoS$_2$ in the dispersion was determined from ICP-OES analysis. The concentration varied between 0.5 mg/ml to 2 mg/ml. We show the time course of H$_2$ evolution of single-layer 1T-MoS$_2$ in **Figure 12(a)**. This catalyst evolved almost 30 mmol g^{-1} h^{-1} of H$_2$, 600 times higher than few-layer 2H-MoS$_2$. Even under 100W irradiation, the TOF of the catalyst is estimated to be 6.2 h^{-1}, higher than any MoS$_2$ based system reported so far. The highest TOF reported thus far is 6 h^{-1}(under 300W Xe lamp) for [Ru(bpy)$_3$]$^{2+}$ sensitized colloidal MoS$_2$ nanoparticles. 1T-MoS$_2$ evolves around 250 mmol of H$_2$ corresponding to about 5.6 L of H$_2$ per g of MoS$_2$ for 10 h.

The activity of the 1T-MoS$_2$ samples prepared by us varies from sample to sample depending on the amount of 1T phase present in the sample. Coexistence of metallic 1T-phase and semiconducting 2H-phases within chemically homogeneous nanosheets is known to occur in single-layer MoS$_2$ prepared by Li-intercalation and exfoliation. **Figure 12(a)** shows the time course of H$_2$ evolution by the sample showing the least yield among 10 experiments on different samples carried out by us, while **Figure 12 (b)** shows that for the sample with the highest yield. The sample showing the highest yield evolved ~55 mmol g^{-1} h^{-1} with a TOF of ~ 11 h^{-1}. **Figure 12 (b)** shows the time course of H$_2$ evolution by 1T-MoS$_2$ over a period of 30 h, with the sample being purged after every 6 h. The catalytic activity slowly degrades over the period from 55 mmol g^{-1} h^{-1} to 30 mmol g^{-1} h^{-1}. This could

probably be because of the slow degradation of the 1T phase under the effect of heat from the light source. However, no significant quenching of the dye was observed even after 30 h of reaction indicating and photogenerated species EY⁻ does transfer its electrons to 1T-MoS₂ efficiently.
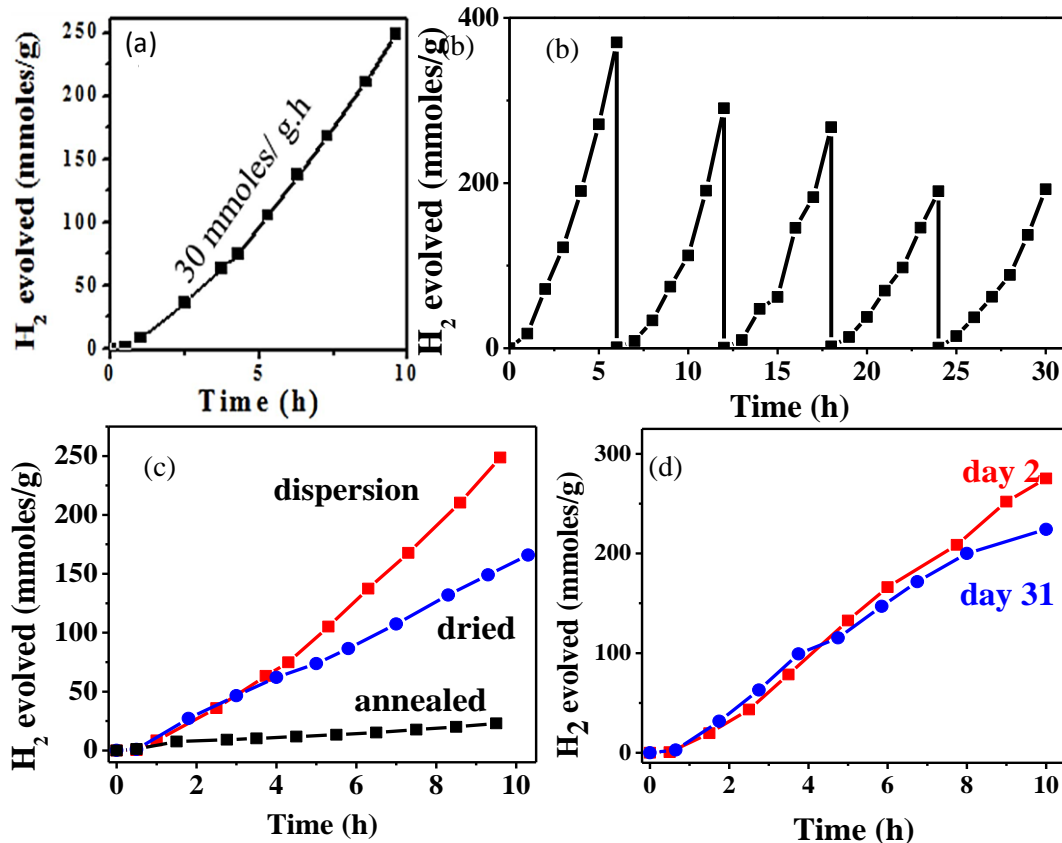
Figure 12. *Time course of H₂ evolution by 1T-MoS₂ - (a) sample showing the lowest yield of H₂, (b) sample showing the highest yield of H₂ shown over a period of 30 hrs with purging after every 6 hrs, (c) as prepared dispersion, dried by lyophilization and annealed at 300°C for 1 hr and (d) as prepared dispersion, dispersion stored for 30 days.*

To confirm that the high catalytic activity of MoS₂ prepared by Li-intercalation and exfoliation arises from 1T phase and is not a result of better dispersion and other such extrinsic factors we carried out control experiments with 2H-MoS₂ obtained directly from the 1T-MoS₂. 1T-MoS₂ is reported to get converted to the 2H analog on annealing under an inert

atmosphere. [36] We dried the dispersion by lyophilization to obtain the fluffy mass of 1T MoS_2. Since lyophilization is carried out at low temperatures 1T-phase of MoS_2 is retained after lyophilization. The lyophilized sample was annealed at 300°C for 1h to obtain the 2H analog. We observe a drastic reduction in the catalytic activity of the annealed sample with the rate of H_2 evolved being only 2.5 mmol g^{-1} h^{-1} a value closer to that found with 2H-MoS_2 **(Figure 12 (c))**. The 1T phase, of MoS_2 being the metastable polytype of MoS_2, is known to readily undergo a transition to more stable 2H-polytype with time [37]. We, therefore, carried out photocatalytic H_2 evolution studies on fresh and 1-month-old samples. The rate of H_2 evolution reduced only slightly over this period from 30 mmol g^{-1} h^{-1} to 26 mmol g^{-1} h^{-1} **(Figure 12 (d))**.

Based on these findings we have explored HER properties of $MoSe_2$, 2H, and 1T form because of the fact that CBM of $MoSe_2$ is higher than that of MoS_2. The yields of hydrogen are in the range of the 60-75 mmol g^{-1} h^{-1}. The turn over frequencies (TOF) is in the range 15-19 h^{-1} **(Figure 13)**. The catalytic activity of the 1T form of $MoSe_2$ is nearly 750-900 times higher than that of the few-layer 2H form (the activity of 0.08 mmol g^{-1} h^{-1}) **(Figure 11)**. It is noteworthy that the yield of H_2 and TOF with 1T-$MoSe_2$ is superior even to those found with 1T MoS_2. The exfoliated sample on restacking decreases the activity to 13.0 mmol g^{-1} h^{-1} because of lesser available surface area for catalysis as well transformation from 1T to 2H phase. On annealing to 300°C in N_2 atmosphere 1T-$MoSe_2$ transforms entirely to 2H-form thereby reducing the activity of H_2 evolution drastically to 0.55 mmol g^{-1} h^{-1} **(Figure 13b)**. The cycling studies of 1T-$MoSe_2$ show stable HER over

the period of 30 hours **(Figure 13 c)**. The photochemical HER activity and TOF of group 6 TMDs are listed in **table 3**.
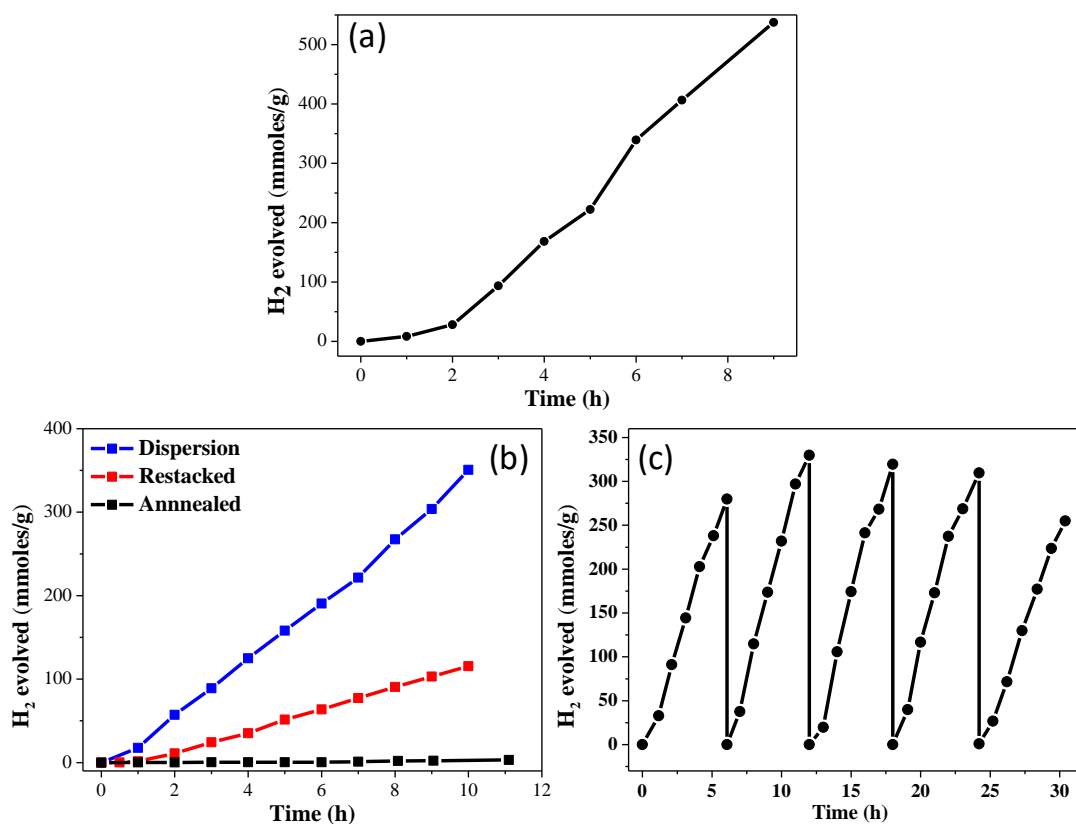
Figure 13. *Time course of H$_2$ evolution by (b) 1T-MoSe$_2$ (b) as prepared dispersion, dried by lyophilization and annealed at 300°C for 1 hr and (b) cycling studies over a period of 30 hours with purging after every 6 h (c)*

Table 3. Comparison of photocatalytic hydrogen evolution of 1T- and 2H-phases of group 6 TMDs

Compounds	Light Source	Activity (mmol g^{-1} h^{-1})	TOF (h^{-1})
2H-MoS$_2$	100 W Halogen lamp	0.16	0.03
2H-MoSe$_2$	100 W Halogen lamp	1.0	0.25
2H-WS$_2$	100 W Halogen lamp	0.6	0.15
2H-WSe$_2$	100 W Halogen lamp	1.8	0.6
1T MoS$_2$	100 W Halogen lamp	30	6
1T-MoSe$_2$	100 W Halogen lamp	75	19.0
1T-WS$_2$	100 W Halogen lamp	11	2.7

4.3 Theoretical results

(First-principles study were carried out by Dr. Anjali Singh, Dr. Sharmila Shirodkar and Prof. U.V. Waghmare of the Theoretical Science Unit, JNCASR)

In order to understand the higher activity of $1T\text{-}MoSe_2$ in comparison to $2H\text{-}MoSe_2$ and the 1T- and 2H- forms of MoS_2, we have carried out first-principles calculations based on density functional theory as implemented in Quantum ESPRESSO package [39], in which the ionic and core-valence electron interactions are modeled with ultrasoft pseudopotentials [40]. The exchange-correlation energy of electrons is treated within a Generalized Gradient Approximation (GGA) functional as parametrized by Perdew, Burke and Ernzerhof (1996) [41]. We use an energy cutoff of 35Ry to truncate the plane wave basis used in representing the Kohn-Sham wave functions, and an energy cutoff of 280 Ry to represent the charge density. Structures are relaxed until the Hellman-Feynman forces on each atom are less than 0.02 eV/Å. We have used a periodic supercell geometry to simulate a 2D sheet, including vacuum of 15 Å to separate the adjacent periodic images of the sheet. For self-consistent Kohn-Sham (SCF) calculations, configurations of $\sqrt{3}\text{x}\sqrt{3}$ and $\sqrt{3}\text{x}1$ supercells, the BZ integrations are sampled over uniform meshes of 7x7x1 and 12x7x1 k-points respectively. Since KS-DFT typically underestimates electronic band gaps (a known limitation), we employ hybrid functional based on Hartree-Fock-Exchange (HSE) [42] with screened Coulomb potential to estimate the band gaps more accurately. The calculations were based on first-principles DFT using Projector Augmented Wave (PAW) method [43, 44] as implemented in the VASP (Vienna Ab-initio Simulations Package) [45]. We have studied

two super-structures of 1T-MoX$_2$ (where X = S and Se),√3x√3 and √3x1 **(Figure 14)** [46]. Amongst the two superstructures, √3x1 is metallic and shows dimerization of Mo atoms, and √3x√3 is semiconducting with trimerized Mo atoms. From phonon dispersion, we find that both MoS$_2$ and MoSe$_2$ are stable in the √3x√3 and √3x1 superstructures. However, MoS$_2$ is energetically more stable in the √3x√3 compared to √3x1 by 27 meV/f.u., while the √3x1 super-structure of MoSe$_2$ is energetically more stable than the √3x√3 super-structure by 33 meV/f.u. Experimentally, MoSe$_2$ is found to be in the √3x1 super-structure, in agreement with our first-principles results. Hence-forth, we shall consider the √3x√3 superstructure for MoS$_2$ and √3x1 superstructure for MoSe$_2$.

(a)   (b)
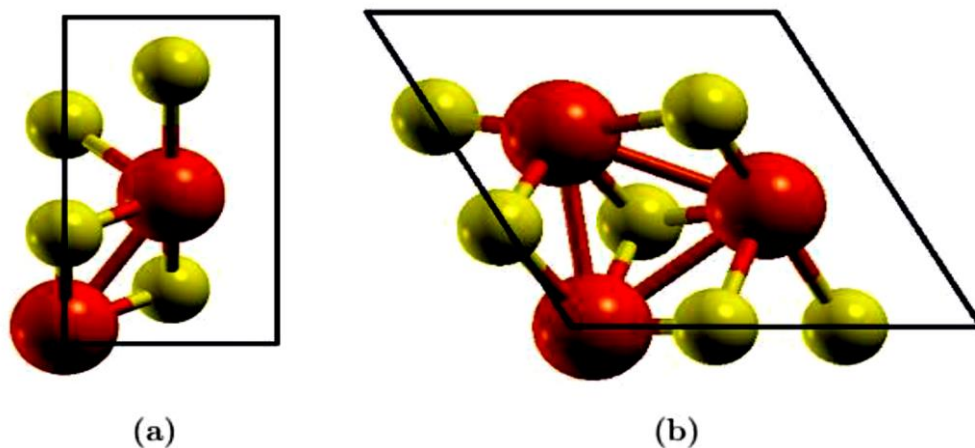
Figure 14. *√3x1 and √3x√3 superstructures of 1T-MoX$_2$ (where X= S and Se). (a) The √3x1 superstructure of 1T-MoX$_2$ showing dimerization of Mo atoms. (b) The √3x√3 superstructure of 1T-MoX$_2$ showing trimerization of Mo atoms. Mo atoms are shown in orange color, and X atoms are in yellow*

To determine the efficiency of MoX$_2$ in reducing a proton to hydrogen as observed in experiments, we have estimated their electron affinities (EA) and work function (φ). For 1 metallic states, the relevant property here is the work function. The EA is estimated as the difference between the

vacuum potential (E_{vac}) and the lowest energy conduction band (ECB). Since DFT is a ground state theory, estimation of the band gap and hence the ECB is not accurate. Hence, we replace the ECB with EVB + Eg, where EVB is the energy of the highest energy valence band and Eg is the band gap. Since Eg is grossly underestimated in DFT calculations, we use the HSE corrections (using VASP) to determine Eg accurately. For the monolayered MoS_2, the experimental value of bandgap (1.8 eV [47]) is available.

Comparison of the experimental bandgap with calculated bandgap for 2H-MoS2 reveals that Kohn Sham bandgap is underestimated by 7.2% and the HSE bandgap is overestimated by 17.7% **(Table 4)**, in agreement with Ahuja *et al.* [47] It is thus clear that the HSE method overestimates the experimental bandgap, whereas the KS-DFT calculation (GGA) yields a better estimate. Since band gap of $MoSe_2$ is lower than MoS_2, it would be a better catalyst as energy barrier is less (From Arrhenius equation).

Table 4. The calculated and experimental values of bandgaps for 2H and 1T ($\sqrt{3}x\sqrt{3}$ superstructure) structures of MoX_2. HSE and KS-DFT bandgaps are calculated using VASP.

Compounds	Bandgap (eV)		
	KS-DFT (VASP)	HSE (VASP)	Exp.
2H–MoS_2	1.67	2.12	1.834
2H–$MoSe_2$	1.45	1.88	1.35
1T–MoS_2 ($\sqrt{3}$ X$\sqrt{3}$)	0.76	1.28	
1T–$MoSe_2$($\sqrt{3}$ X$\sqrt{3}$)	0.64	1.16	

We use estimates of E_g obtained from KS-DFT calculations in this work. The work function is calculated as $\varphi = E_{vac} - E_F$, where E_F is the Fermi

energy. We find that (a) the 2H and 1T-polytypes of MoS_2 have a greater φ than that of the respective structure of $MoSe_2$ (refer to Table 4). This implies that it is easier to extract an electron from $MoSe_2$ compared to that of MoS_2 in both 1T and 2H polytypes, (b) The 1T polytype has a lower φ than that of 2H, which means that its easier for the 1T to donate electron compared to the 2H-structure. This explains why the 1T-polytype of $MoSe_2$ produces hydrogen more efficiently than the 2H-polytype as observed in experiments. The electron affinities of both 1T- and 2H- polytypes indicate that MoS_2 has a stronger electron affinity (indicating a higher tendency to attract electrons) than that of $MoSe_2$ **(Table 5)**, and the work function is also larger for MoS_2. Thus, though MoS_2 more readily attracts/accepts electrons, it does not donate it that easily. Hence, $MoSe_2$ is efficient in hydrogen evolution as compared to that of MoS_2 as observed in experiments here.

Table 5. The calculated values of electron affinity (EA) and work function (WF) for 1T (for both √3x√3 and √3x1 superstructures) and 2H structures of MoX₂ (MoS₂ and MoSe₂)

Superstructure	1T-form √3x√3		1T-form √3x1		2H-form	
Compound	MoS_2	$MoSe_2$	MoS_2	$MoSe_2$	MoS_2	$MoSe_2$
EA (eV)	4.95	4.42	-	-	4.22	3.78
WF (eV)	5.68	5.20	5.63	5.00	5.86	5.35

4.4 Photochemical hydrogen generation from colloidal 2H-MX₂ (M= Mo, W and X= S, Se).

From the previous sections, we see that the excellent activity of 1T-phase is due to active basal planes, increased metallicity, and colloidal state. However, 1T-state is unstable and therefore it is difficult to harness the

HER property. However, we can maintain the colloidal state of these samples if we suitably functionalize 1T-samples. 1T-samples were functionalized using bromoacetic acid and characterized by Raman and infrared spectroscopy. In a typical synthesis, bulk MoS_2 is exfoliated via Li-intercalation and exfoliation in water. In the dispersion excess of bromoacetic was added, the precipitate was then washed and dried. The functionalized samples become colloid in triethanolamine solution. The triethanolamine is the sacrificial agent for eosin Y sensitized H_2 evolution. Triethanolamine act as both sacrificial as well as a stabilizing agent for these colloids. The colloids exhibit Tyndall effect as seen in **figure 15.**

Water   1T-MoS$_2$ Colloid-MoS$_2$

Colloid-MoSe$_2$ Colloid-WS$_2$
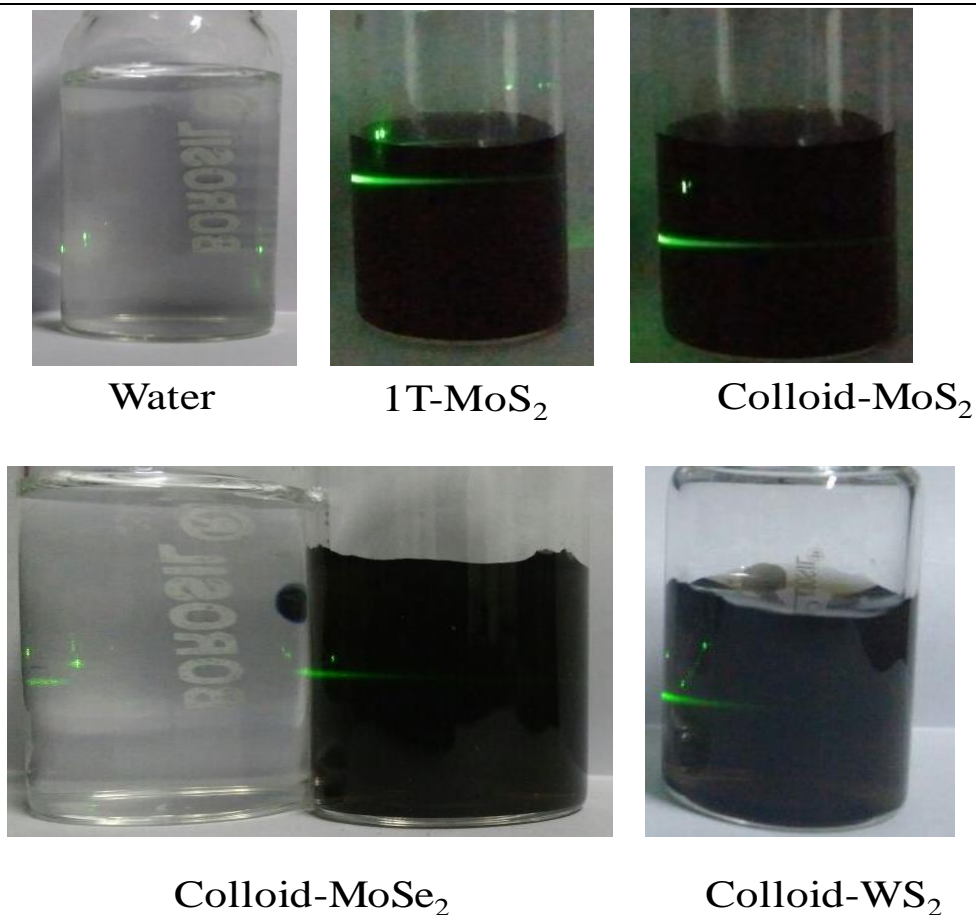
Figure 15. *Optical image of a colloidal solution of functionalized MoS$_2$. MoSe$_2$ and WS$_2$. The colloidal solution exhibit Tyndall effect. The colloidal nature of functionalized MoS$_2$ is compared with 1T-phase.*

The IR spectra of functionalized samples of MoS_2, $MoSe_2$, and WS_2 were recorded and is shown in **figure 16**. The IR-bands at 3200 and 1702 cm^{-1} corresponds to -OH and -C=O bonds stretching modes respectively. The C-S stretching band at 700 cm^{-1} which arises from covalent functionalization of MX_2 **(Figure 16a)**. The Raman of functionalized MoS2 suggests that they are 2H-phase **(Figure 16 b-d)**.
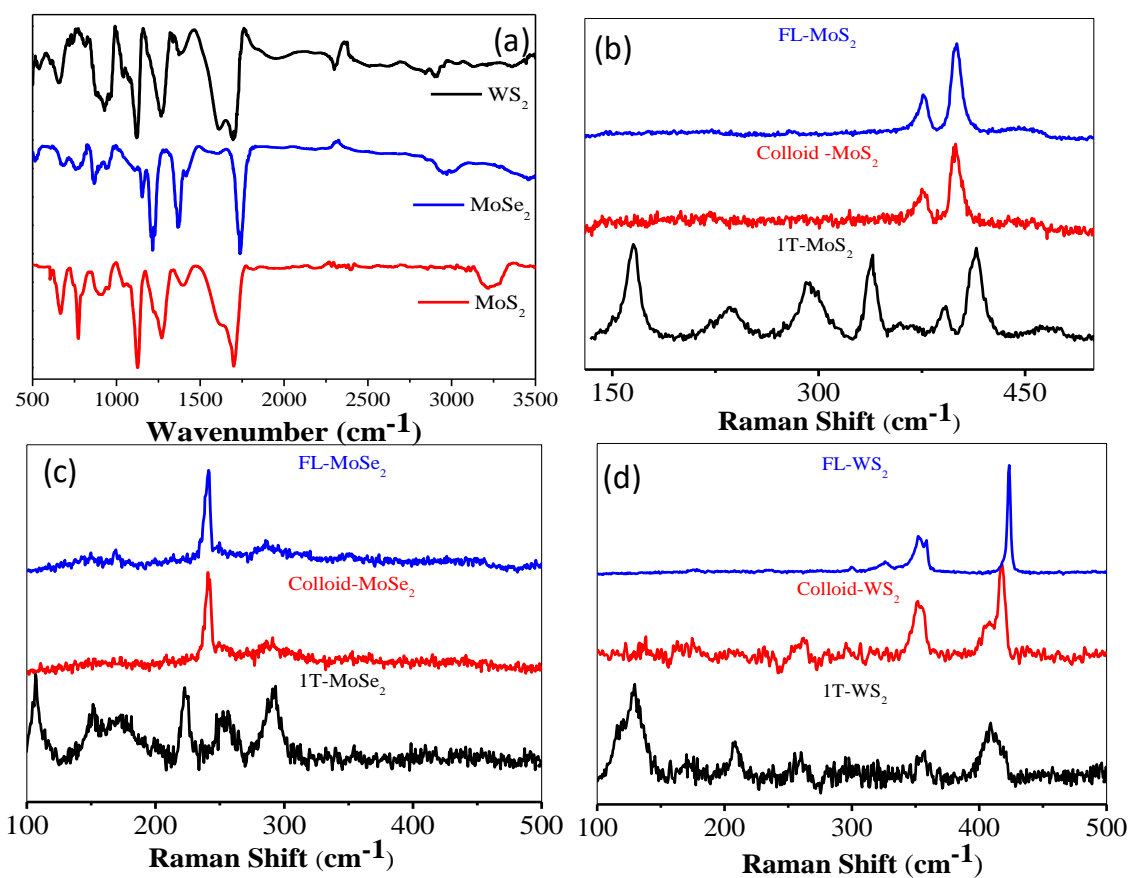
Figure 16. (a) *Infrared spectra of covalently functionalized MoS_2. $MoSe_2$ and WS_2. Comparison of Raman of 1T-, colloids and few-layer (FL) (b) MoS_2, (c) $MoSe_2$ and (d) WS_2.*

The approximate amount of functionalization was inferred from thermogravimetric analysis (TGA). In **Figure 17** the curves show a loss in three stages. Initial loss is due from 100-175 $^{\circ}$ C is used for desorption of water from the surface. The later stage is due to 180-400 is due to

decarboxylation of the functionalized group followed by complete removal of carbon at higher temperatures. The total functionalization from the weight loss is around c.a ~15 %.
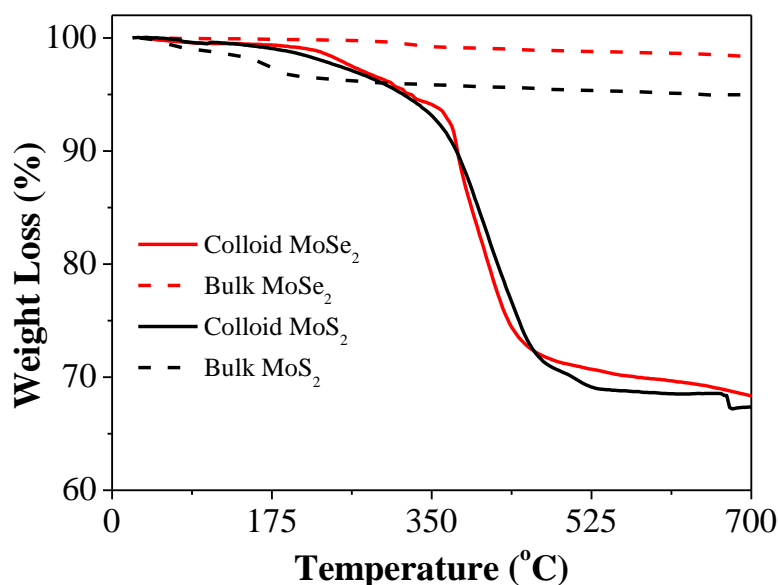
Figure 17. *Comparison of the thermogravimetric curve of functionalized MoS₂ and MoSe₂ with their bulk samples.*

The photocatalytic hydrogen evolution for colloidal phase- of group 6 TMDs were studied and compared to respective its 1T-phase and few-layer samples. We observe HER for functionalized colloidal MoS_2 is 18.0 mmol g⁻¹ h⁻¹, while that of 1T-phase and few-layer 2H-MoS_2 was 21.0 and 2.3 mmol h⁻¹ g⁻¹ respectively **(Figure 18a)**. The activity of the colloidal phase was similar to 1T-phase. $MoSe_2$ colloid, has activity of 29.5 mmol g⁻¹ h⁻¹ while that 1T- and few-layer $MoSe_2$ exhibited activity of 79.0 and 6.6 mmol g⁻¹ h⁻¹ **(Figure 18 b)**. In case of WS_2, the activity of the colloid, 1T- few-layers were 3.2, 10.8 and 0.83 mmol g⁻¹ h⁻¹ respectively **(Figure 18 c)**. It is to be noted that not only it difficult to exfoliate WS_2 but also difficult to functionalize it and therefore colloids of WS_2 was inferior to molybdenum chalcogenides for HER activity.
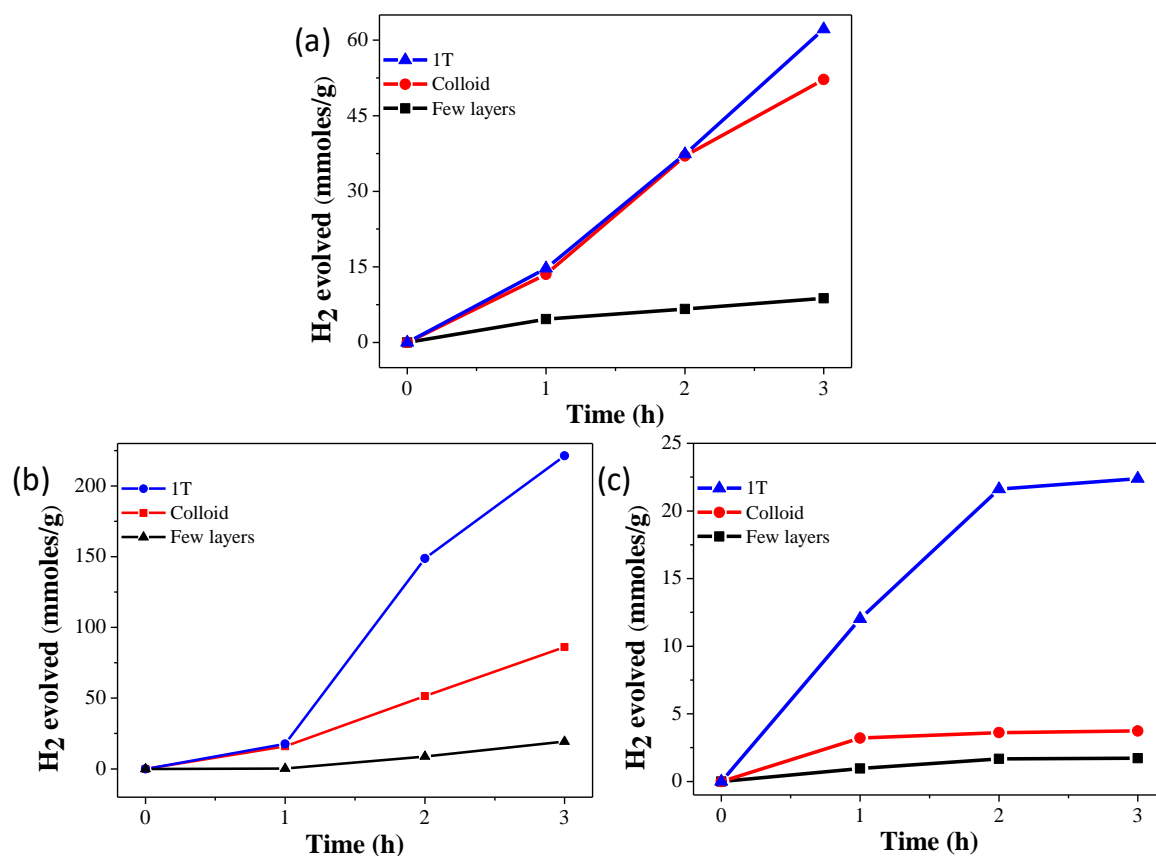
Figure 18. *Comparison of the time course of hydrogen evolution of colloid, 1T and few-layer (a) MoS₂, (b) MoSe₂ and (c) WS₂.*

The colloids of group 6 TMDs have exhibited very high activity owing to enhancement in the surface area of the colloids when dispersed in triethanolamine solution. The high activity of colloid state is due physical state of the catalyst. The superior HER performance 1T-phase compared to colloid phase is highlights the importance of 1T-phase as a superior catalyst.

Colloidal $MoSe_2$ has superior activity as compared among all group 6 TMDs **(Figure 19 a)**. The cyclic studies studied with $MoSe_2$ colloids to check the long-term stability of these colloids as a long-term catalyst. We observe stable HER evolution of for 4 cycles over a period of 12 hours **(Figure 19 b)**. Unlike in 1T-phase where the activity decreases over time due to the

conversion of 1T to 2H-phase, the activity of these colloids are stable. In **table 6**, we compare the activity of colloid, 1T- and 2H- phase.
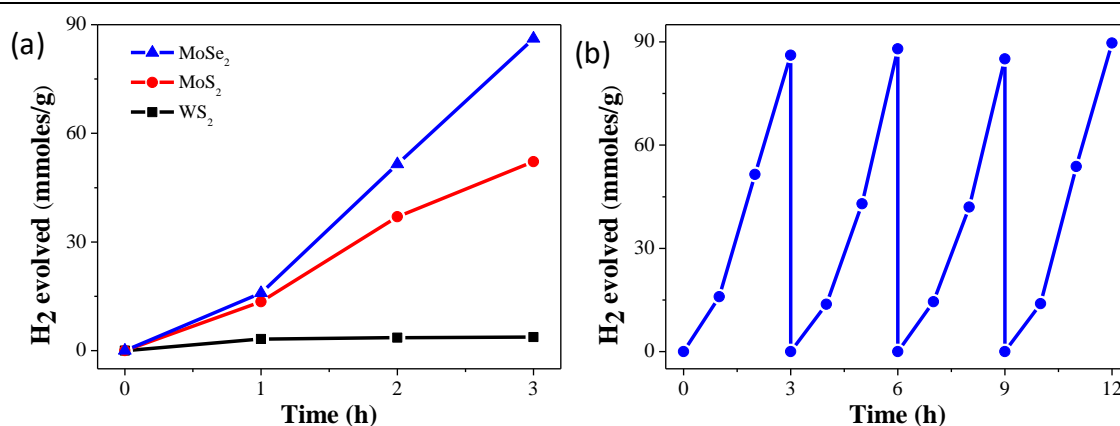
Figure 19. *(a) Comparison of the HER activity of colloids of MoS$_2$, MoSe$_2$, and WS$_2$ over the time course. (b) Cyclic studies of MoSe$_2$ colloid over a period. We stable HER activity.*

Table 6. Comparison of photochemical HER activity of colloid, 1T- and 2H- phase of group 6 TMDs

Compound	Sample	Activity (mmol g^{-1} h^{-1})
MoS$_2$	Few-layers	2.3
	1T	21.0
	Colloid	18.0
MoSe$_2$	Few-layers	6.6
	1T	79.0
	Colloid	29.5
WS$_2$	Few-layers	0.83
	1T	10.8
	Colloid	3.2

5. Conclusions

The band gap of MoSe$_2$ is lower than that of MoS$_2$ and exhibits better HER activity than MoS$_2$. Furthermore, metallic-1T is much more catalytic than 2H form. Among all the catalysts we have studied in this chapter, metallic 1T-MoSe$_2$ prepared by Li intercalation followed by exfoliation of bulk 2H-MoSe$_2$, shows excellent H$_2$ evolution activity in comparison to few-layered semiconducting 2H-MoSe$_2$. Interestingly, 1T-MoSe$_2$ shows better H$_2$ evolution activity than 1T-MoS$_2$ as well. Our first-principles analysis reveals that MoSe$_2$ has a lower work function as compared to MoS$_2$ and that the 1T-structure exhibits lower work function than the 2H-structure for both MoX$_2$ (X=S, Se). This results in the easy transfer of an electron from the MoSe$_2$ for the reduction to hydrogen, and hence MoSe$_2$ is more efficient for hydrogen evolution reaction compared to MoS$_2$. Colloidal form of 2H-MX$_2$ exhibits superior activity as compared to the few-layer structures.

6. References

1. J. Barber, Chem. Soc. Rev. 2009, 38, 185.

2. A. Kudo, Y. Miseki, Chem. Soc. Rev. 2009, 38, 253.

3. B. Hinnemann, P. G. Moses, J. Bonde, K. P. Jørgensen, J. H. Nielsen, S. Horch, I. Chorkendorff and J. K. Nørskov. J. Am. Chem. Soc. 2005, 127, 5308.

4. R. R. Chianelli, M. H. Siadati, M. P. De La Rosa, G. Berhault, J. P. Wilcoxon, R. Bearden, B. L. Abrams, Catal. Rev. 2006, 48, 1.

5. A. B. Laursen, S. Kegnaes, S. Dahl and I. Chorkendorff. Energy Environ. Sc. 2012, 5, 5577.

6. H. Tributsch and J. C. Bennett. J. Electroanal. Chem. Interfac. Electrochem 1977, 81, 97.

7. H. Tributsch, J. C. Bennett, J. Electroanal. Chem. 1977, 81, 97.

8. K. Sakamaki, K. Hinokuma, A. Fujishima, J. Vac. Sci. Technol. B 1991, 9, 944.

9. T. F. Jaramillo, K. P. Jørgensen, J. Bonde, J. H. Nielsen, S. Horch, I. Chorkendorff, Science 2007, 317, 100.

10. S. Helveg, J. V. Lauritsen, E. Lægsgaard, I. Stensgaard, J. K. Nørskov, B. S. Clausen, H. Topsøe, F. Besenbacher, Phys. Rev.Lett. 2000, 84, 951.

11. J. Kibsgaard, J. V. Lauritsen, E. Lægsgaard, B. S. Clausen, H.Topsøe, F. Besenbacher, J. Am. Chem. Soc. 2006, 128, 13950.

12. M. Brorson, A. Carlsson, H. Topsøe, Catal. Today 2007, 123, 31.

13. J. Bonde, P. G. Moses, T. F. Jaramillo, J. K. Nørskov, I. Chorkendorff, Faraday Discuss. 2009, 140, 219.

14. D. Merki, S. Fierro, H. Vrubel, X. Hu, Chem. Sci. 2011, 2, 1262.

15. Y. Li, H.Wang, L. Xie, Y. Liang, G. Hong, H. Dai, J. Am. Chem. Soc. 2011, 133, 7296.

16. Z. Chen, J. Kibsgaard, T. F. Jaramillo, Proc. SPIE 2010, 7770, DOI:10.1117/12.860659.

17. Wang, L. Sun, C. Li, Chem. Commun. 2009, 4536.

18. Q. Xiang, J. Yu,M. Jaroniec, J. Am. Chem. Soc. 2012, 134, 6575.

19. X. Zong, H. Yan, G. Wu, G. Ma, F. Wen, L. Wang, C. Li, J. Am. Chem. Soc. 2008, 130, 7176.

20. S. Min, G. Lu, J. Phys. Chem. C 2012, 116, 25415.

21. U. Maitra, U. Gupta, M. De, R. Datta, A. Govindaraj, and C. N. R. Rao, Angew. Chem. Int. Ed., 2013, 52, 13057.

22. F. Wypych, Th. Weber, R. Prins, Chem. Mater., 1998, 10, 723.

23. A. N.Enyashin, L. Yadgarov, L. Houben, I. Popov, M. Weidenbach, R. Tenne, M. Bar-Sadan, G. Seifert, J. Phys. Chem. C., 2011, 115, 24586.

24. C. Rovirat, M. Whangbo, Inorg. Chem., 1993, 32, 4094.

25. H. Jiang, J. Phys. Chem. C. 2012, 116, 7664.

26. J. Kang, S. Tongay, J. Zhou, J. Li, J. Wu, Appl. Phys. Lett.,2013, 102, 012111

27. A. M. Lukowski, A. S. Daniel, F. Meng, A. Forticaux, L. Li, S. Jin, J. Am. Chem. Soc., 2013, 135, 10274.

28. D. Voiry, H. Yamaguchi, J. Li, R. Silva, D. C. B. Alves, T. Fujita, M. Chen, T. Asefa, V. B. Shenoy, G. Eda, M. Chhowalla, Nat. Mat., 2013, 12, 850.

29. S. J. Sandoval, D. Yang, R. F. Frindt, and J. C. Irwin, Phys. Rev B., 1991, 44, 3955.

30. J. Heising, M. G. Kanatzidis, J. Am. Chem. Soc.,1999, 121, 11720–117323.

31. R. A. Gordon, D. Yang, E. D. Crozier, D. T. Jiang, R. F. Frindt, Phys. Rev. B, 2002, 65, 125407.

32. H. S. S. Ramakrishna Matte, A. Gomathi, A. K. Manna, D. J. Late, R. Datta, S. K. Pati, C. N. R. Rao, Angew. Chem., 2010, 122, 4153.

33. B. K. Miremadi and S. R. Morrison, J. Appl. Phys., 1988, 63, 4970.

34. C. L. Jia, M. Lentzen, K. Urban, Science 2003, 299, 870.

35. J. A Wilson, F.J Di Salvo, S. Mahajan Adv. Phys., 1975, 24, 117.

36. A. H. C. Neto, Phys. Rev. Lett., 2010, 86, 4382.

37. G. Eda, H. Yamaguchi, D. Voiry, T. Fujita, M. Chen and M. Chhowalla. Nano Lett. 2011, 11, 5111.

38. U. Gupta, B. G. Rao, U. Maitra, B. E. Prasad, and C. N. R. Rao, Chem. Asian J. ,2014, DOI: 10.1002/asia.201301537.

39. P. Giannozzi et al., J. Phys.: Cond. Matt. 21, 2009,395502.

40. D. Vanderbilt, Phys. Rev. B, 41, 1990, 7892.

41. J. P. Perdew, K. Burke, and M. Ernzerhof, Phys. Rev. Lett., 1996, 77, 3865.

42. J. Heyd, G. E. Scuseria, and M. Ernzerhof, J. Chem. Phys, 2003, 118, 8207.

43. P. E. Blöchl, Phys. Rev. B, 1994, 1994, 50, 17953.

44. G. Kresse and D. Joubert, Phys. Rev. B, 1999, 59, 1758.

45. G. Kresse and J. Furthmüller, Phys. Rev. B, 1996, 54, 11169.

46. J. Heising and M. G. Kanatzidis, J. Am. Chem. Soc., 1991 121, 11720.

47. K. F. Mak, C. Lee, J. Hone, J. Shan, and T. F. Heinz Phys. Rev. Lett., 2010, 105, 136805.

48. Y. Li, Y. L. Li, C. M. Araujo, W. Luo and R. Ahuja., Catal. Sci. Technol., 2013 3, 2214.

Photocatalytic hydrogen evolution based on covalently linked assemblies of MoS₂ with RGO and C₃N₄*

Summary

Edge sites are active for HER by MoS_2. We have exfoliated bulk $2H$-MoS_2 to obtain single layers and linked the latter by Sonogashira coupling. The activity of the cross-linked MoS_2 was ~20 times (1.75 mmol g^{-1} h^{-1}) higher than few-layer MoS_2 (0.07 mmol g^{-1} h^{-1}). The enhancement was in the order of the increasing surface area of the composite. The locking of MoS_2 sheets may provide more exposed edges but still, lack of efficient electron transport. Directed linking of C_3N_4 with MoS_2 by ethylcarbodiimide (EDC) coupling with uniform layer by layer assembly of C_3N_4 as verified from TEM and elemental mapping. The activity of the composite catalyst was 12.8 mmol g^{-1} h^{-1}, which was 246 times higher than C_3N_4 alone. The activity of covalently linked composites was compared with the physical mixture and solid state composite which had an activity of 0.18 and 1.16 mmole mmol g^{-1} h^{-1} respectively. The enhanced activity by the following method is noteworthy and is attributed to efficient charge transfer across the network via space and bonds due to efficient directed overlapping of the layers and short conducting bonds respectively. DFT calculations give an insight of the charge transfer between the layers across the network.
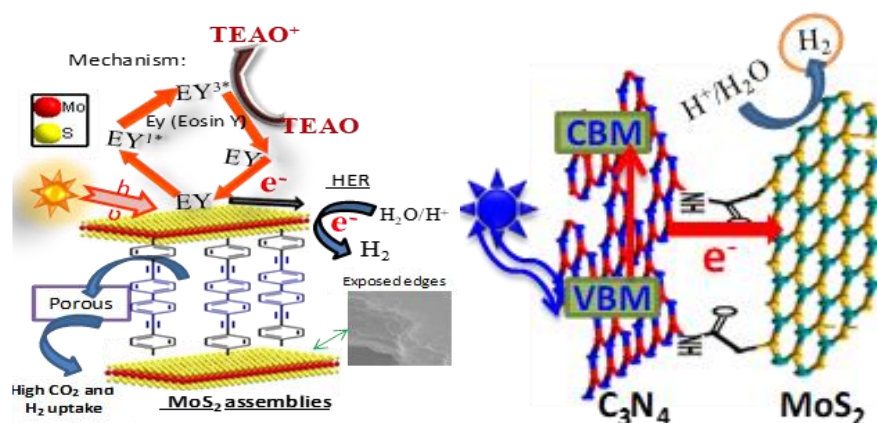
1. Introduction

Functionalization of two-dimensional (2D) materials such as graphene and boron nitride (BN) has received considerable attention and has been used for solubilization and other purposes [1, 2]. Many of the transition-metal chalcogenides (TMDCs) such as MoS_2 and $MoSe_2$ require chemical modifications to make them suitable for a wide variety of applications. Unlike graphene and BN, efforts in the functionalization of 2D sheets of TMDCs materials have been limited owing to the inert nature of their basal-plane [3-7]. Among the chalcogenide family, MoS_2 is distinctive with its unique electronic and optical properties, field-effect transistor characteristics and gas sensing properties [8, 9]. MoS_2 has been found to be a promising catalyst for visible-light-induced photocatalytic and photoelectrocatalytic hydrogen generation from water, replacing traditionally used catalysts [10, 11]. Theoretical and experimental studies indicated that the edges sites of MoS_2 are catalytically active while the basal plane remains inert [5]. Chemical modifications of TMDCs surface is necessary to improve their versatility, for example, enhancing solubility in common organic solvents keeps thin-layer characteristics intact by way of avoiding restacking of layers due to van der Waals interactions.

Various surface modification strategies have been reported to enhance the processability as well as the chemical reactivity of MoS_2. For example, covalent functionalization of 2D MoS_2 can be achieved at sulfur defect sites through thiol-terminated ligands [12, 13]. A single-step reaction to exfoliate and functionalize MoS_2 by an organosulfur reaction has been

carried out [14]. Thiol groups as in thiophenol chemically grafted to MoS_2 alter the electronic properties significantly [15]. Covalently cross-linked MoS_2–polymer composites have been explored, while surface modification of MoS_2 achieved with metal acetates [16, 17]. Nylon-6 polymers covalently linked to MoS_2 show enhancement in thermal and mechanical properties [18].

A more successful effort in forming covalent bonds between organic functional groups and the sulfur atoms of MoS_2 has been reported by Chhowalla et al. [3]. They carried out covalent functionalization of MoS_2 starting with the metallic 1T phase, obtained through lithium intercalation followed by exfoliation. The 1T-phase has octahedral coordination of the Mo atoms unlike the stable semiconducting 2H-phase, which has the trigonal-prismatic coordination of the Mo atoms. The functionalization reaction is carried out by electron transfer between the metallic 1T phase and an organoiodine reactant to form covalent C–S bonds, leading to marked changes in the optoelectronic and other properties of the MoS_2. A similar reaction involving water-soluble electrophilic diazonium salts with 1T-MoS_2 has been reported, which showed that defects are not required to achieve covalent functionalization [4]. Pratap et al. [6] recently reported the reaction of 1T- and 2H-MoS_2 nanosheets with *para*-substituted iodobenzenes and showed that the electron-withdrawing molecules favor covalent functionalization. First-principles calculations have shown that the benzene derivatives bind much more strongly to the 1T form than to the 2H form [6]. The work function is considerably tunable with the

functionalization of MoS$_2$ and increases the potential for applications in photocatalysis as well as electronic and optoelectronic devices.

Apart from functionalization, constructing 3D hierarchical architectures based on 2D MoS$_2$ nanosheets of is another effective approach to solve the problem of re-stacking of layers because of their high surface energy and interlayer van der Waals (vdW) attractions [8]. These architectures are highly desirable for practical applications (for example, high-energy anode materials, catalysis, and hydrogen generation by water splitting). Intercalation of guest molecules such as lithium, sodium, and naphthalenide between the van der Waals gap of MoS$_2$ layers also enhance inter-layer spacing [5]. Jeffery *et al.* [6] synthesized assemblies of MoS$_2$ and RGO arranged in a layer-by-layer fashion (van der Waals heterostructures) by a simple exfoliation-co-stacking method which exhibits improved catalytic activity [7].

We synthesized covalently cross-linked MoS$_2$ assemblies and of MoS$_2$-RGO assemblies by Sonogashira coupling forms rigid organic linkers pillar with individual 2D layers. Pillaring of MoS$_2$ and RGO nanosheets with organic linkers generates slit-shaped pores with the more exposed edge sites (catalytically more active), thereby results in enhanced photochemical HER activity compared to individual MoS$_2$ and RGO. From the study, we observed that due to long linkers and absence of integrated photoactive material the light harvesting process is significantly compromised. Integrating integrated a layered photoactive through directional linking with MoS$_2$ and graphene and studied their HER properties. Since, there is a significant thrust in investigating cost-

effective, stable catalysts for hydrogen evolution reaction (HER), preferably those which are metal-free [8].

Among metal-free catalysts, graphitic carbon nitride (C_3N_4) especially attractive because of the suitable band gap (E_g=2.7 eV) and stability in harsh chemical environments. [19, 20] However, pure g-C_3N_4 has low photochemical activity due to the rapid recombination of the photogenerated electron-hole pair. It has been suggested that coupling of C_3N_4 with a suitable co-catalyst like MoS_2 could improve the catalytic activity owing to effective charge separation [21, 22]. Such composites would also be used as catalysts for photoelectrochemical HER [23, 24]. Due to the poor electronic conductivity of MoS_2 and C_3N_4, their layers have been grown on reduced graphene oxide (RGO) to enhance the HER activity [25, 26]. The composite of MoS_2 with nitrogenated RGO (NRGO) is a reasonably good catalyst for dye-sensitized photochemical hydrogen evolution [27]. Synthesis of nanohybrids of C_3N_4 with MoS_2 or RGO has been achieved by solid-state chemistry route or hydrothermal methods, [25, 21] but such systems would consist of randomly distributed constituents with hetero domains. Assemblies of RGO with C_3N_4 or MoS_2 in a layer-by-layer fashion (van der Waals heterostructures) exhibit improved catalytic activity because of better interconnectivity [28, 29]. It has been recently reported that assemblies of covalently cross-linked nanosheets of MoS_2 with MoS_2 or RGO sheets display superior HER activity compared to the individual components [30]. In this scenario, we considered it most worthwhile to synthesize covalently bonded assemblies of C_3N_4 with MoS_2 and NRGO by through appropriate coupling reaction and examine the effect of such

bonding on the photochemical hydrogen generation. The present study presents the remarkable results obtained by us on the catalytic activity of covalently cross-linked C$_3$N$_4$-NRGO and C$_3$N$_4$-MoS$_2$ composites in photochemical HER. Interestingly, we find significant improvement in photochemical HER catalytic activity of the covalently cross-linked composites, especially in the case of C$_3$N$_4$-MoS$_2$, compared to that of the physical mixture of the two. Encouraged by these results, we have extended the study to examine the use of these chemically bonded composites in electrochemical HER. Furthermore, we have performed detailed density functional theoretical studies to get insights into the physical processes involved.

2. Scope of the present investigations

Generation of hydrogen by photochemical, electrochemical and other means is a vital area of research today, and a variety of materials has been explored as catalysts for this purpose. MoS$_2$ has the S–Mo–S sandwich structure in which the hexagonal molybdenum plane is sandwiched between layers of sulfur atoms with the van der Waals interactions between the layers. In most of the practical application such as catalysis, sensing, and lithium-ion battery, the main process in MoS$_2$ occurs either on the surface or on the exposed edge sites which are closely related to the huge specific surface area of 2D layers. However, freshly prepared MoS$_2$ layers tend to restack during practical applications even while drying process which causes a reduction in the number of active sites as well as other unusual properties of ultrathin 2D layers.

Constructing hierarchical 3D architectures based on 2D layers would be an efficient approach to solve this problem [8]. Graphene sheets pillared by rigid organic linkers have shown high surface area and good gas storage properties [31].

Covalent pillaring of MoS_2 sheets through rigid organic linkers could generate high surface areas and porous 3D assemblies. While Pd(0) catalyzed C–C coupling has been explored widely[18] to the best of our knowledge there are no reports of its application in chalcogenide chemistry. We have employed the Sonogashira coupling strategy to prepare assemblies of covalently cross-linked MoS_2 sheets by rigid organic linkers. We have also employed this reaction to prepare assemblies of covalently linked sheets of MoS_2 with reduced graphene oxide. Graphene composites of MoS_2 and other layered materials obtained through different synthetic strategies seem to show enhancement in their observed photochemical and electrochemical properties. [32-34]. In this study, we have examined the surface area and gas adsorption properties of MoS_2 and MoS_2–RGO assemblies and studied their photochemical catalytic activity for hydrogen generation. Linking layered-materials with shorter ligands and a photoactive material would try to solve the problem with shorter ligands and integrated photoactive material.

C_3N_4, MoS_2 and nitrogenated RGO (NRGO) are some of the important catalytic materials investigated for the HER reaction, but the observed catalytic activities are somewhat marginal. Composite of C_3N_4 with MoS_2 or NRGO showed enhanced H_2 evolution activity compared to individual

components due to the effective charge separation. Most of the C_3N_4-MoS_2 and C_3N_4-NRGO composites reported in the literature prepared from either hydrothermal or solid-state reactions. These routes often need high temperature, and one cannot have precise control over the composition of individual components in the final composites. Secondly, while preparing these composites at high temperatures, there are chances of partial conversion of MoS_2 to MoO_3 due to oxygen impurity which decreases the catalytic activity.

In this study, we have prepared covalently cross-linked composites of C_3N_4-MoS_2 and C_3N_4-NRGO by the relatively simple carbodiimide method at room temperature, and composition of individual components in final composites can be controlled since we start from a known amount of functionalized C_3N_4 and MoS_2 or NRGO. Moreover, MoS_2 grown on C_3N_4 by the hydrothermal method is few-layer. Cross-linking strategy allowed us to cross-link individual MoS_2 layer with C_3N_4 and vice versa where we can expect a maximum interaction between heterolayers which reflected in their superior HER activity as compared to a physical mixture of two. Additionally, covalent cross-linking of heterolayers generates pores, contributing to the enhanced HER activity which is absent in nanocomposites prepared from other reported methods. The catalytically active edge sites of MoS_2 are more exposed on covalent pillaring with C_3N_4 which can also contribute to the enhanced HER activity. In case of C_3N_4 or NRGO, we have utilized the residual functional for cross-linking thereby preventing alterations in their electronic structure.

3. Experimental section

3.1 Synthesis

3.1.1 Functionalization of MoS$_2$ and RGO by iodobenzene

The Li-intercalation of bulk MoS$_2$ prepared exfoliated MoS$_2$ with n-butyllithium followed by an exfoliation using water as reported elsewhere in the literature [3]. Graphene oxide was prepared by modified Hummer's method [35], and the reduction was carried out with hydrazine hydrate to obtain reduced graphene oxide (RGO). Iodobenzene functionalization of MoS$_2$ was carried out through an in-situ diazotization reaction. Initially, the diazonium salt was prepared by dissolving 4-iodoaniline (9 mmol) in water through the slow addition of concentrated hydrochloric acid (HCl). The resultant solution cooled to an ice-cold temperature, NaNO$_2$ (15 mmol) and 8 ml 20% HCl (6.4 M) was added and allowed to stir until the color changes to yellow confirming the diazonium salt formation. Exfoliated MoS$_2$ (100 ml, 1 mg ml^{-1}) in water was added drop-wise to the diazonium salt solution at ice-cold temperature for 2 h followed by stirring at room temperature for 4 h. The product was vacuum filtered and washed with copious amounts of water and acetone. Iodobenzene functionalized RGO (100 mg) prepared by dispersing RGO in 100 ml of 1 wt% dodecylbenzenesulfonate surfactant through probe sonication was added to the diazonium salt of 4-iodoaniline. The above procedure was repeated with RGO.

3.1.2 Synthesis of assemblies of MoS$_2$ and RGO

MoS$_2$ assemblies were prepared by dispersing MoS$_2$-IBz (20 mg) in N, N-dimethylformamide (DMF) (4 ml) and triethylamine (TEA) (4 ml) through

bath sonication in a Schlenk flask. To the resultant dispersion, Pd (PPh$_3$)$_4$ (5 mg) and CuI (3 mg) were added under stirring, and the temperature was increased to 80 °C. 4,4′-Diethynylbiphenyl (50 mg) dissolved in 1 ml DMF in a separate vial was added drop-wise to the reaction mixture in an inert atmosphere, and the temperature was increased to 140 °C and was allowed to stir for 12 h. The final product obtained was collected by vacuum filtration and washed several times with hexane and DMF. Further purification was carried out in a Soxhlet extractor with methanol and dried at 60 °C in a vacuum oven. To prepare MoS$_2$–RGO (2 : 1) assemblies, MoS$_2$-IBz (14 mg) and RGO-IBz (7 mg) were mixed and dispersed in a solution of DMF (4 ml) and TEA (4 ml). The procedure mentioned above was repeated for the preparation of MoS$_2$–RGO assemblies. The MoS$_2$/RGO (2:1) physical mixture was prepared in the absence of the 4,4′-diethynylbiphenyl linker by dispersing MoS$_2$-IBz (14 mg) and RGO-IBz (7 mg) in DMF through sonication. The resultant mixture was heated at 140 °C, and the final product was collected through vacuum filtration.

3.1.3   Synthesis of g-C$_3$N$_4$: Thiourea (2g) powder was heated in an alumina crucible at 550 °C for 4 h [36].

3.1.4   Functionalization of 1T-MoS$_2$

Bulk MoS$_2$ (300 mg) powder was stirred in a solution of n-butyllithium (n-BuLi, 3ml, 1.6 M hexane), and refluxed at 70 °C under nitrogen atmosphere over a period of 48 h [3]. The black Li-intercalated (Li$_x$MoS$_2$) sample was collected by filtration under nitrogen and washed extensively with hexane (3*100 ml). The obtained Li$_x$MoS$_2$ sample was

ultrasonicated in water (1mg/ml) for 1 h, and the resultant solution centrifuged at high speed (8000 rpm) to remove LiOH and any non-exfoliated material. From inductively coupled plasma (ICP) analysis we have obtained the final concentration of exfoliated MoS_2 in water, and it is ~ 0.7 mg/ml.

To synthesize carboxylate functionalized MoS_2, ten-fold excess of 2-Bromoacetic acid was added to the exfoliated $1T$-MoS_2 (1mg/ml) solution and allowed to stir for 5 days at room temperature. The precipitated product was filtered and washed with 2-propanol, water, and ethanol, and dried at 60 °C under vacuum [20]. NRGO sample was prepared by grinding graphene oxide (GO) with urea to obtain homogeneous mixture then pelletized, and heated in a microwave reactor (900 W) for 60 s [38].

3.1.5 Synthesis of covalently cross-linked assemblies of C_3N_4 with NRGO and MoS_2

C_3N_4 (50 mg) and NRGO (50 mg) were mixed in Schlenck flask, sealed using a septum and 5 ml dry DMF added under N_2 atmosphere to obtain a uniform dispersion of the mixture after bath sonication. To the above dispersion N-(3-dimethylaminopropyl)-N'-ethyl carbodiimide hydrochloride (EDC.HCl, 20 mg) and 1-hydroxybenzotriazole (HOBt, 20 mg) were added along with N,N-diisopropylethylamine (DIPEA, 300 μl) and stirred at room temperature for 48 h. An inert atmosphere was maintained during the reaction. The solid product obtained was collected by filtration (0.45 μm, PTFE membrane), washed with copious amounts of DMF and water to remove byproducts and dried at 60 °C under vacuum. For the synthesis of C_3N_4-MoS_2 composites, C_3N_4 (50 mg) and MoS_2-CH_2COOH (50 mg) were

dispersed in dry DMF and the above-mentioned procedure repeated. For the preparation of a physical mixture of C$_3$N$_4$ and NRGO (MoS$_2$), C$_3$N$_4$ (50 mg) and NRGO (MoS$_2$) (50 mg) were dispersed in aqueous solution by bath sonication and then filtered to get a solid product. For comparison, C$_3$N$_4$-MoS$_2$ composite was prepared by the solid state route by heating few-layer MoS$_2$ with thiourea in the N$_2$ atmosphere at 550 °C for 4 hr.

3.2 Characterization

Infrared (IR) spectra of C$_3$N$_4$ -NRGO and C$_3$N$_4$ -MoS$_2$ composites were recorded using Bruker ATR-FTIR spectrometer. Morphological analysis has been performed using Nova Nano SEM 600, FEI Company while TEM imaging has been carried out with FEI TITAN3TM with an accelerating voltage of 80 kV. Electron energy loss spectra were recorded in Titan FEI, TEM with an accelerating voltage of 300 kV. Raman spectra were recorded using a HORIBA LabRam HR800 at several different spots. The N$_2$ isotherms of covalently cross-linked composites obtained from QUANTACHROME QUADRASORBSI analyzer instrument

3.3 Hydrogen evolution measurements

3.3.1 Assemblies of MoS$_2$ and RGO: MoS$_2$ and MoS$_2$-RGO assemblies were dispersed in a solution of water and triethanolamine (TEAO) (15% v/v) by sonication, to this 14 μmol of Eosin Y dye were added.

3.3.2 Assemblies of C$_3$N$_4$ with NRGO and MoS$_2$: The catalyst (3 mg) was dispersed in water (40 mL) by sonication in a glass vessel. To this, a solution of triethanolamine (20 % v/v; 10 mL) was added as the sacrificial agent and the mixture thoroughly purged with N$_2$. The vessel was

illuminated under Xenon lamp (400 W) with constant stirring of the mixture. 2 mL of evolved gas was collected from the headspace of the glass vessel and analyzed using thermal conductivity detector equipped gas chromatograph (Perkin Elmer ARNL 580C). Turnover frequency (TOF) for catalyst was calculated per mole of C_3N_4, considering the fact that light absorption happens in C_3N_4 only. TOF values are estimated by using the following equation.

$$TOF\ (h^{-1}) = \frac{Activity\ of\ the\ catalyst}{moles\ of\ the\ active\ catalyst} \quad (1)$$

3.4 Computational details

The geometry of the composites was optimized using density functional theory (DFT) as implemented in the Gaussian 09 program package [39]. We have used the CAM-B3LYP functional which is the long-range corrected version of B3LYP [40] and employs the Coulomb-attenuating method. This is important for the composite systems which show charge-transfer interactions [41]. We have used the 6-31g basis set for C, N, O, H and S atoms and LANL2DZ for Mo atoms. For the C_3N_4-MoS_2 composites, we kept the MoS_2 layer fixed and optimized the edge atom, linker bonds, and C_3N_4 layers.

4. Results and discussion

(Thanks are due to Dr. K. Pramoda in the synthesis and characterization work)

4.1 Covalently cross-linked assemblies of MoS$_2$ and RGO

4.1.1 Synthesis and characterization

The Sonogashira coupling strategy employed by us to pillar iodobenzene functionalized MoS$_2$ with a 4,4′-diethynylbiphenyl linker is shown in Scheme 1. The scheme shows the various steps involved in synthesizing covalently pillared MoS$_2$ and MoS$_2$–RGO assemblies. Initial exfoliation of bulk MoS$_2$ is achieved with n-butyllithium (n-BuLi) leading to the formation of mono- or bi-layers. Exfoliated MoS$_2$ is treated with the diazonium salt of 4-iodoaniline prepared in situ at 0°C to obtain iodobenzene functionalized MoS$_2$ (MoS$_2$-IBz). Subsequent steps involve obtaining the MoS$_2$-IBz dispersion in dry N,N-dimethylformamide (DMF) and cross-linking it with the 4,4′-diethynylbiphenyl (DEBP) linker in the presence of Pd(0) and Cu(+1) salts. The synthetic steps involved in generating the MoS$_2$–RGO assemblies are similar to those of MoS$_2$ assemblies, except for the initial reduction of graphene oxide (GO) in hydrazine hydrate to obtain reduced graphene oxide (RGO). Prior to the coupling reaction, iodobenzene functionalized MoS$_2$ and RGO are mixed and dispersed in dry DMF through sonication (for details see the Experimental section). MoS$_2$ mentioned in this manuscript refers to exfoliated MoS$_2$, whereas the MoS$_2$–RGO assembly refers to the 2 : 1 (wt%) ratio of MoS$_2$ and RGO.
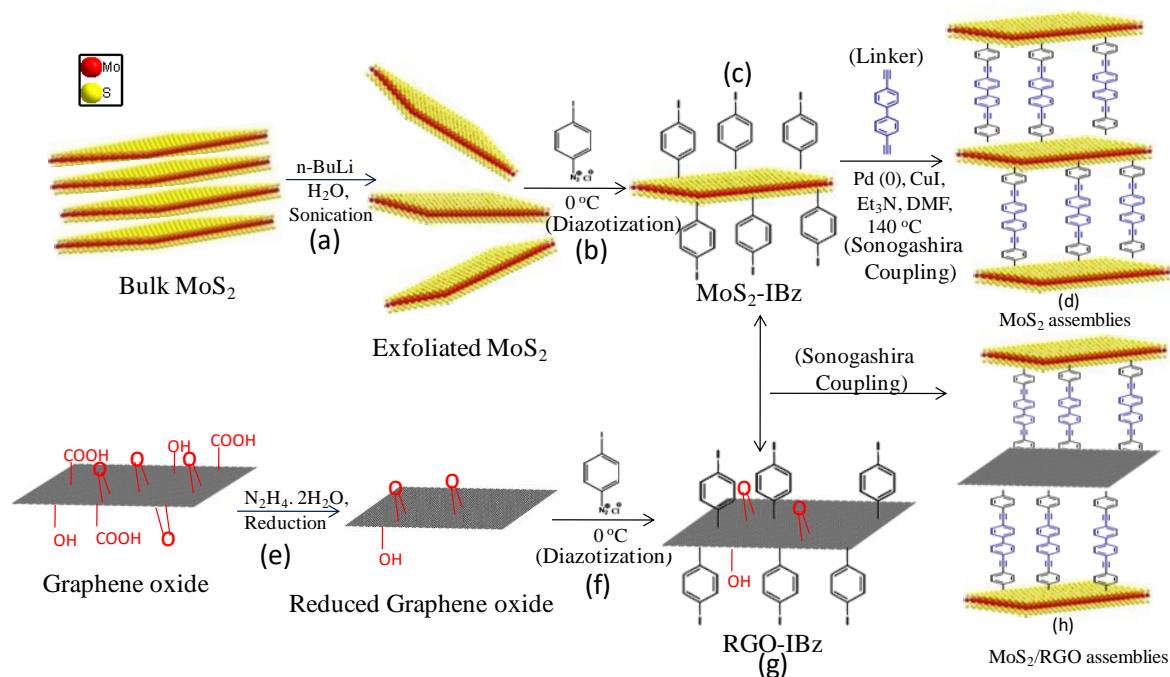
Scheme 1. *Schematic representation of the synthesis of MoS$_2$ and MoS$_2$–RGO assemblies through Sonogashira coupling; (a) exfoliation of bulk MoS$_2$ with n-butyllithium, (e) reduction of graphene oxide with hydrazine hydrate, (b and f) diazotization of MoS$_2$ and reduced graphene oxide (RGO) with 4-iodobenzenediazonium chloride salt, (c and g) iodobenzene functionalized MoS$_2$ and RGO and (d and h) MoS$_2$ and MoS$_2$–RGO assemblies.*

Figure 1 shows the Raman spectra of exfoliated MoS$_2$ and RGO. Exfoliated MoS$_2$ exhibits characteristic 1T-polytype J$_1$, J$_2$, J$_3$ Raman bands at 156, 236 and 330 cm^{-1} along with E$^1_{2g}$ and A$_{1g}$ modes from the 2H-phase at 384 and 405 cm^{-1}, respectively [23]. Iodobenzene functionalized MoS$_2$ (MoS$_2$-IBz, **Figure 1)** shows an enhancement in the E$^1_{2g}$ and A$_{1g}$ band intensities with respect to exfoliated MoS$_2$ due to the partial 1T → 2H transition after functionalization. Raman spectra of RGO show the D and G bands at 1340 and 1590 cm^{-1}, respectively [24]. After functionalization, the relative intensity of the D band increases due to the formation of sp^3 centers. The MoS$_2$ assemblies show only the E$^1_{2g}$ and A$_{1g}$ bands of 2H-

MoS$_2$ and a band at 1590 cm^{-1} due to the C=C stretching bond of the linker [25]. In the MoS$_2$–RGO assemblies, we observed Raman modes of 2H-MoS$_2$ along with D and G bands of RGO. Enhancement in G-band intensity with respect to RGO is attributed to C=C stretching of the linker.
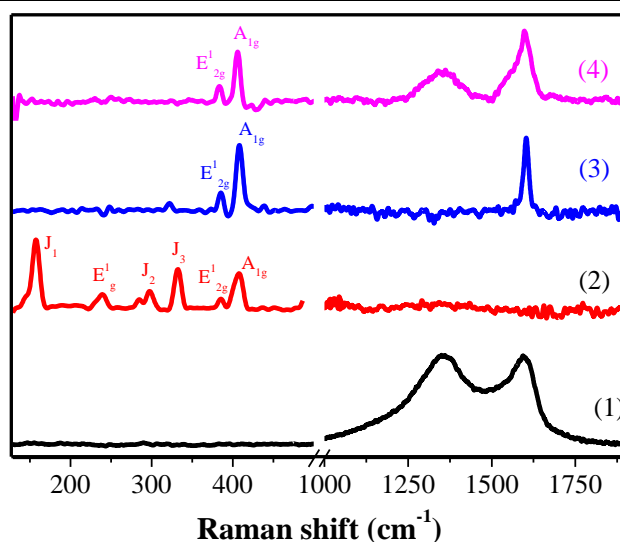
Figure 1. *Raman spectra of (a) RGO (green), Exfoliated MoS₂ (black); (b) iodobenzene functionalized RGO (green), iodobenzene functionalized MoS₂ (black), (3) MoS₂ assemblies (blue) and MoS₂–RGO (red) assemblies.*

Iodobenzene functionalization of MoS$_2$ and RGO results in anchoring of the functional groups on both sides of the 2D sheets. **Figures 2a, b** show the iodine (3d) core level spectrum of MoS$_2$-IBz and RGO-IBz, showing iodine signals at 620.5 and 632.0 eV due to I (3d$_{5/2}$) and I (3d$_{3/2}$), respectively [26, 27]. Sonogashira coupling involves the oxidative addition of Pd(0) to the C–I bond of iodobenzene to give a Pd(+2) intermediate, followed by the transmetallation of the Pd complex with copper acetylide by eliminating iodine and forming the C–C bond through reductive elimination by regenerating Pd(0).[28]
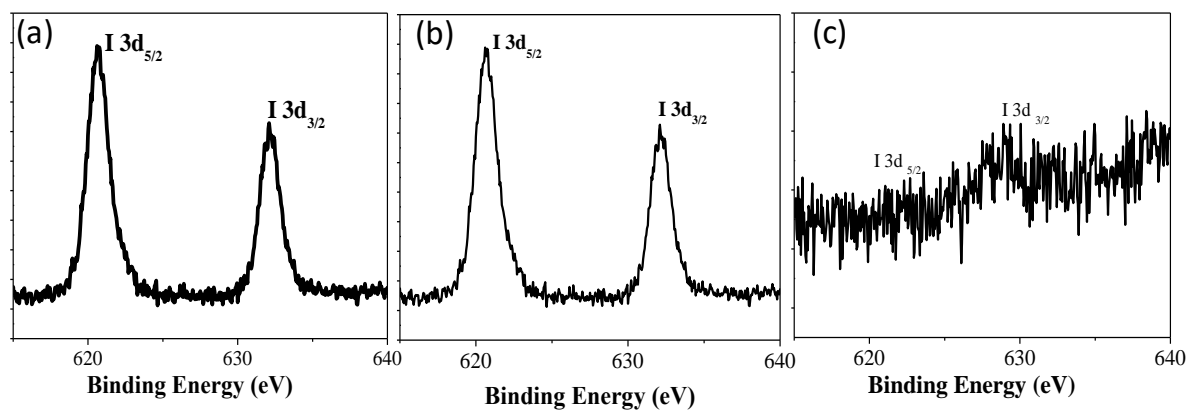
Figure 2. *(a) Iodine (3d) X-ray photoelectron spectrum of iodobenzene functionalized MoS₂, iodobenzene functionalized RGO and MoS₂ assemblies.*

The extent of cross-linking between MoS_2 sheets can be interpreted by comparing the intensity of the I (3d) signal in the initial MoS_2-IBz and the final assemblies. In **Figure 2c** we show the I (3d) core level spectra of MoS_2 assemblies to point out the absence of any significant signal from I, while MoS_2-IBz displays a strong I (3D) signal as shown in **Figure 2a.** The disappearance of the I (3d) signal confirms the efficient cross-linking of MoS_2-IBz sheets through C–C bonds leading to the elimination of iodine. The MoS_2–RGO assemblies also exhibit negligible I (3d) signals indicating the formation of C–C bonds between MoS_2 and RGO sheets.

Figure 3 shows the ATR-FTIR spectra of assemblies of MoS_2 and MoS_2–RGO. MoS_2 assemblies exhibit the C=C stretching bands of benzene at 1600, 1498 and 1390 cm^{-1} along with Mo–S stretching band at 470 cm^{-1}. The bands at 2250 and 3060 cm^{-1} of the assemblies are attributed to C≡C and C–H stretching bands of the DEBP linker which confirm the presence of DEBP between MoS_2 sheets [29, 30]. In the MoS_2–RGO assemblies, in addition to the bands mentioned above, we see an additional

band in the range of 1040–1320 cm⁻¹ due to residual OH and epoxy groups of RGO. The C–S stretching band at 695 cm⁻¹ in the IR spectra of assemblies as well as MoS₂-IBz confirms the covalent attachment of iodobenzene to MoS₂ [31].
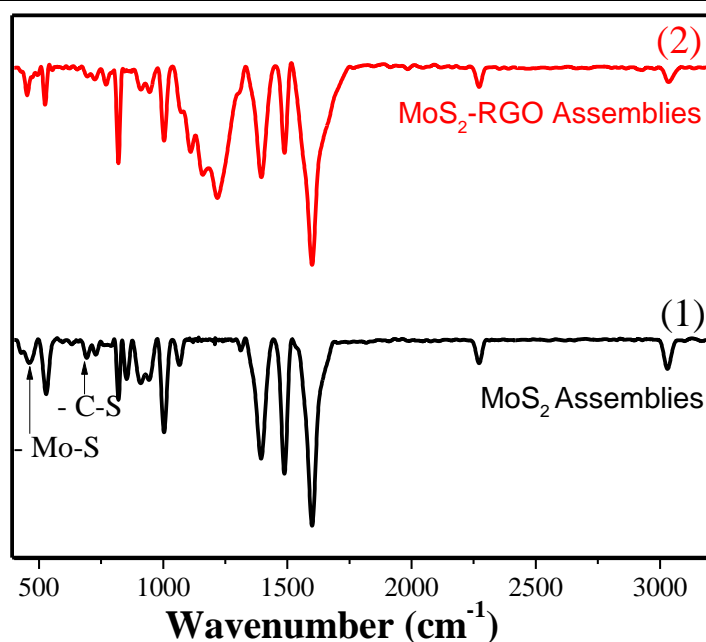
Figure 3. *(a) ATR-FTIR spectra of MoS₂ assemblies (black) and MoS₂–RGO (red) assemblies.*

In **Figure 4a** we have shown the PXRD patterns of MoS₂ and MoS₂–RGO assemblies. A broad reflection at 2θ of ~3.5° is observed corresponding to a separation of ~2 nm between the sheets in the assemblies. This value closely matches the length of the DEBP linker between the sheets. The PXRD pattern of MoS₂-IBz and RGO-IBz shows (002) peaks at 2θ of 14.3° and 26°, respectively, which are absent in the assemblies **(Figure 4b)**. Thus the PXRD patterns along with the IR and XPS spectra of the assemblies confirm the covalent pillaring of MoS₂ and RGO sheets through the linker.
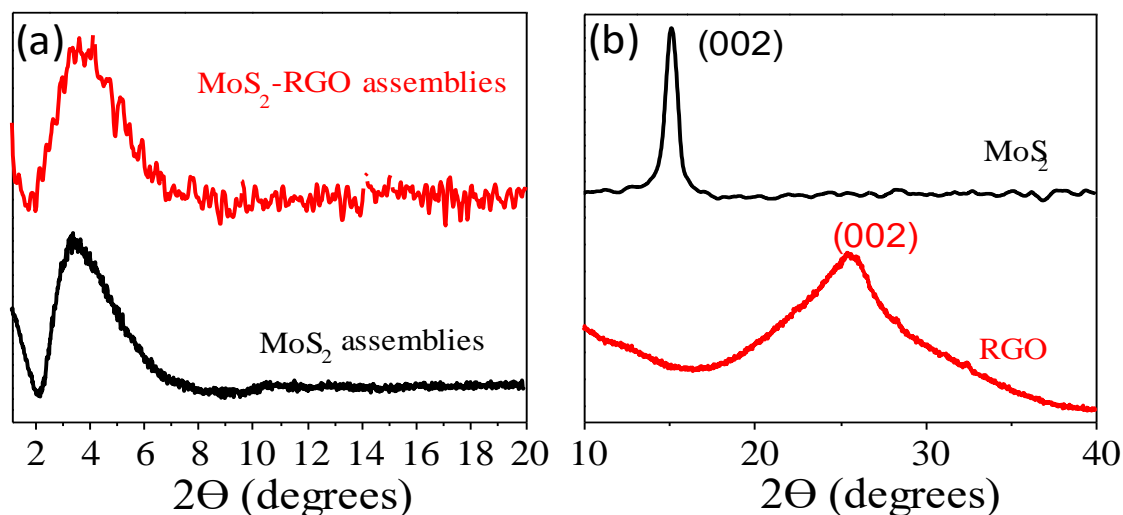
Figure 4. *X-Ray diffraction patterns of (a) MoS₂ assemblies (black) and MoS₂–RGO (red) assemblies; (b) MoS₂ (black) and RGO (red).*

Figure 5a shows the transmission electron microscopy (TEM) images of exfoliated MoS_2 containing bi-layers with lateral dimensions of 200–300 nm. Field emission scanning electron microscopy (FESEM) images of MoS_2 assemblies show that 2–5 µm sized monoliths are formed on pillaring unlike those of exfoliated MoS_2 **(Figure 5b)**. **Figure 5c** presents a TEM image of MoS_2 assemblies, revealing stacking of several MoS_2 sheets due to pillaring. **Figure 5d** shows the HRTEM image of MoS_2 assemblies containing cross-linked MoS_2 bi-layers (white circle) with an interlayer spacing of ~0.7 nm. The TEM **(Figure 5e)** image of MoS_2–RGO assemblies shows the cross-linked MoS_2 and RGO sheets (confirmed by the EDAX pattern, inset in **Figure 5e)**. **Figure 5d** shows the HRTEM image of MoS_2 assemblies containing cross-linked MoS_2 bi-layers (white circle) with an interlayer spacing of ~0.7 nm. The TEM **(Figure 5e)** image of MoS_2–RGO assemblies shows the cross-linked MoS_2 and RGO sheets (confirmed by the EDAX pattern, inset in **Figure 5e)**. FESEM and TEM images confirm

the formation of 3D assemblies due to cross-linking. In contrast, the HRTEM image of the MoS$_2$/RGO physical mixture shows thick regions of non-uniformly distributed MoS$_2$ sheets over transparent graphene **(Figure 5f).**
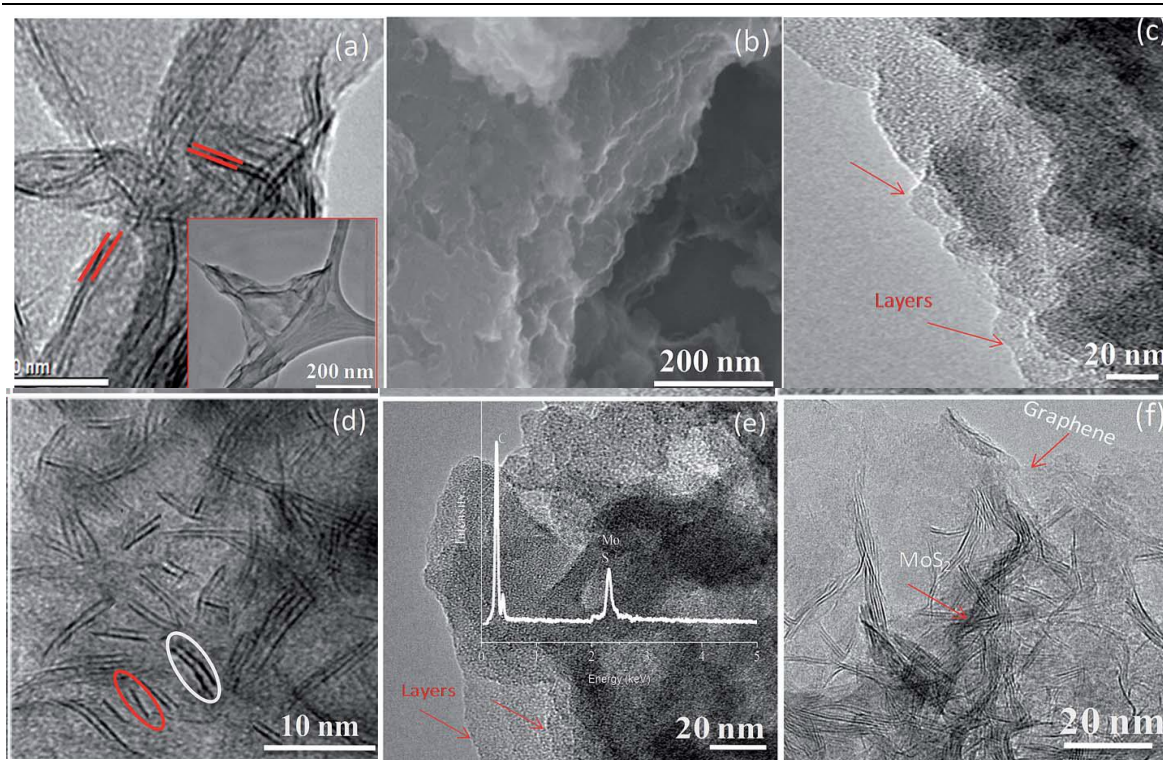
Figure 5. *(a) HRTEM image of exfoliated MoS$_2$ (parallel lines indicate bi-layers) (inset: TEM), (b) FESEM image of MoS$_2$ assemblies, (c and d) TEM and HRTEM images of MoS$_2$ assemblies (red and white circles show mono- and bi-layers of MoS$_2$), (e) TEM image of MoS$_2$–RGO assemblies (inset: EDAX pattern), and (f) HRTEM image of the MoS$_2$/RGO physical mixture.*

We have studied surface area and gas adsorption characteristics of the MoS$_2$ and MoS$_2$–RGO assemblies. **Figure 6a** shows N$_2$ sorption profiles of MoS$_2$ assemblies, MoS$_2$–RGO assemblies, MoS$_2$ and RGO at 77 K. The N$_2$ isotherms of assemblies show type-I and type-II characteristics in low and high-pressure regions, respectively, following the IUPAC classification

[32]. The type-1 feature is attributed to the adsorption in micropores, whereas type-II is due to macropores on three-dimensional assemblies. The steep increase in the low-pressure region up to $P/P_o \sim 0.1$ is attributed to adsorption in micropores.
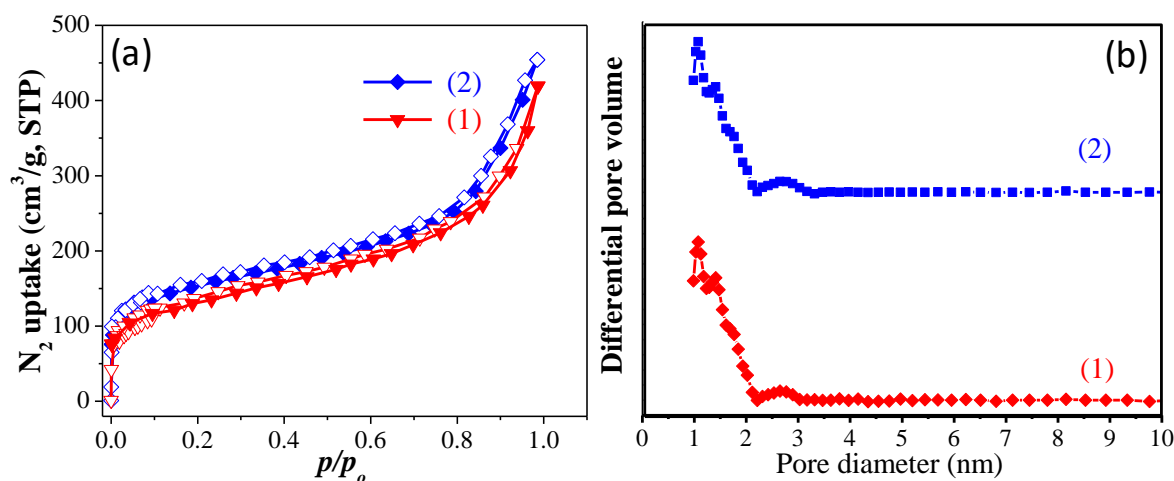
Figure 6. *(a) Nitrogen sorption profile of MoS₂ (black), RGO (green), MoS₂ assemblies (blue) and MoS₂–RGO assemblies (red) at 77 K; (b) Pore size distribution curve; (c) CO₂ sorption profile of MoS₂ assemblies (blue) and MoS₂–RGO assemblies (red) at 298 K; (b) Hydrogen sorption profile at 77 K of MoS₂ assemblies (red) and MoS₂-RGO assemblies (blue).*

The Brunauer–Emmet–Teller (BET) surface areas of MoS₂ and MoS₂–RGO assemblies are 498 and 512 $m^2\ g^{-1}$, respectively. RGO displays type-II characteristics and a BET surface area of 80 $m^2\ g^{-1}$, whereas few-layer MoS₂ is non-porous with a low surface area of 30 $m^2\ g^{-1}$. **Figure 6b** shows pore size distribution obtained from the nitrogen isotherms fitted using non-local density functional theory (NLDFT); we see pores majorly in the 1.2–2 nm range and some in the 2–3 nm range. The pore size distribution of assemblies depends on the length and density of the linker pillaring the sheets. The pore volumes of MoS₂ and MoS₂–RGO assemblies are 0.60 and

0.64 cm^3 g^{-1}, respectively, whereas RGO has a low pore volume of 0.15 cm^3 g^{-1}. The enhanced pore volume and surface area of the assemblies are attributed to the pillaring of the RGO and MoS$_2$ sheets; pores generated thereby. It is interesting that the MoS$_2$ assembly exhibits a high surface area comparable to that of the MoS$_2$–RGO assembly as evident from BET analysis.

4.1.2 Hydrogen evolution studies

MoS$_2$ is a known promising catalyst for the hydrogen evolution reaction [41, 42]. The high surface area and uniform 3D porous (~1–2 nm) network of assemblies are motivational factors for us to examine the hydrogen evolution activity. The hydrogen evolution experiments are carried out in the presence of Eosin Y (EY) dye under visible light illumination. The mechanism of photochemical hydrogen evolution of MoS$_2$ in EY dye is described elsewhere in the literature [23].
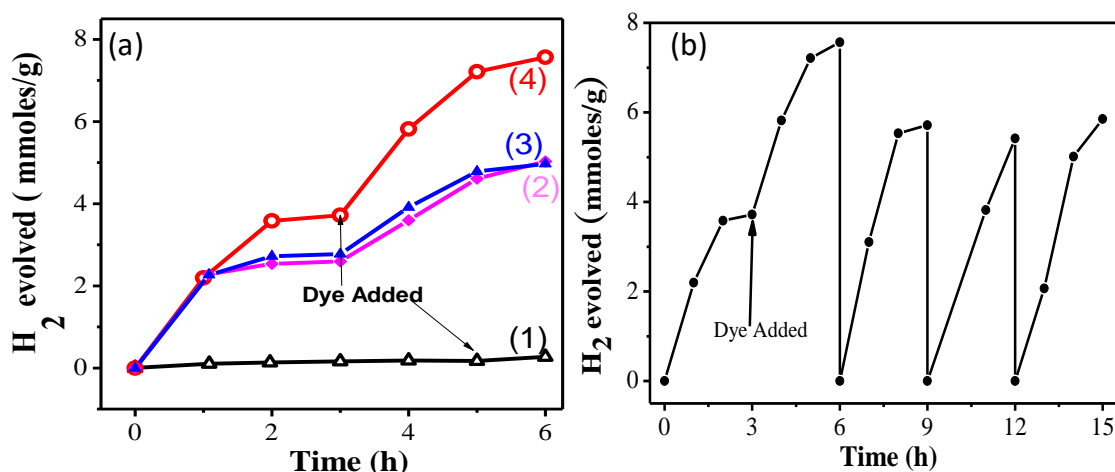
Figure 7. *(a) H$_2$ evolved per gram of catalyst by using few-layer MoS$_2$ (black), MoS$_2$–RGO (1 : 1) (green), MoS$_2$–RGO (2 : 1) (magenta), MoS$_2$–RGO (3 : 1) (blue) and MoS$_2$ assemblies (red) (arrows indicate the addition point of eosin dye); (b) Cycling studies of MoS$_2$ assemblies.*

In **Figure 7a** we show the yield of H_2 evolved by using assemblies of MoS_2 and MoS_2–RGO as well as by using few-layer MoS_2. The cross-linked MoS_2 assembly shows the activity of 1.75 mmol g^{-1} h^{-1} with a turnover frequency (TOF) of 0.84 h^{-1}, whereas few-layer $2H$-MoS_2 exhibits an activity of 0.07 mmol g^{-1} h^{-1} with a TOF of 0.01 h^{-1}. The enhanced catalytic activity of MoS_2 assemblies is attributed to the increased surface area as well as more exposed edges on pillaring. The catalytic activities of MoS_2–RGO (3 : 1) and (2 : 1) assemblies are comparable with 3 : 1 assembly has an activity of 1.38 mmol g^{-1} h^{-1} (TOF = 0.98 h^{-1}) and the 2 : 1 assembly shows an activity of 1.30 mmol g^{-1} h^{-1} (TOF = 0.94 h^{-1}). The MoS_2–RGO (1 : 1) assembly shows a lower activity of 0.35 mmol g^{-1} h^{-1} (TOF = 0.40 h^{-1}) among the MoS_2–RGO assemblies. Cycling studies on MoS_2 assemblies carried out over a period of 15 h (4 cycles) with a 14 μmol dye show that the activity increases in the second cycle and then becomes stable in subsequent cycles **(Figure 7b)**. The above results suggest that MoS_2 is the active component for hydrogen evolution in these assemblies and the activity decreases with the increase in graphene content. MoS_2 assemblies show superior hydrogen evolution activity as compared to few-layer MoS_2 possibly due to the more exposed catalytically active edge sites of MoS_2 on pillaring by organic linkers. Though covalent-cross linking gives an edge over few-layer compounds, the challenge to design a well-defined size, interface, and controllable thickness and morphology of TMDs, which are critical for creating a higher number active edge sites for hydrogen evolution and realizing efficient hole-electron separation and migration in photocatalytic reactions. Directed linking of C_3N_4 with MoS_2 by

ethylcarbodiimide (EDC) coupling between the layers tackles the problem of integrating a photoactive material along with shorter ligands for better communication between the layers. In the next part, the strategy is discussed in details. **Table 1** presents the hydrogen evolution activity of assemblies that are compared with the literature reports on MoS_2 based catalysis.

Table 1: Comparison of photocatalytic activity of catalyst with other systems.

Photocatalyst	Activity (mmol g^{-1} h^{-1})	TOF (h^{-1})	References
FL-MoS$_2$	0.07	0.01	Present Work
MoS$_2$ assemblies	1.75	0.84	Present Work
MoS$_2$/RGO (3:1) assemblies	1.38	0.98	Present Work
MoS$_2$/RGO (2:1) assemblies	1.30	0.94	Present Work
MoS$_2$/RGO Composite	3	0.68	Ref (10).
MoS$_2$/EG Composite	0.54	0.21	Ref (10).

4.2 Covalently cross-linked assemblies of C_3N_4 with MoS_2 and nitrogenated RGO

4.2.1 Synthesis and Characterization

In **scheme 2**, we present the synthetic strategy to obtain amide-bond cross-linked C_3N_4-NRGO and C_3N_4-MoS_2 composites.
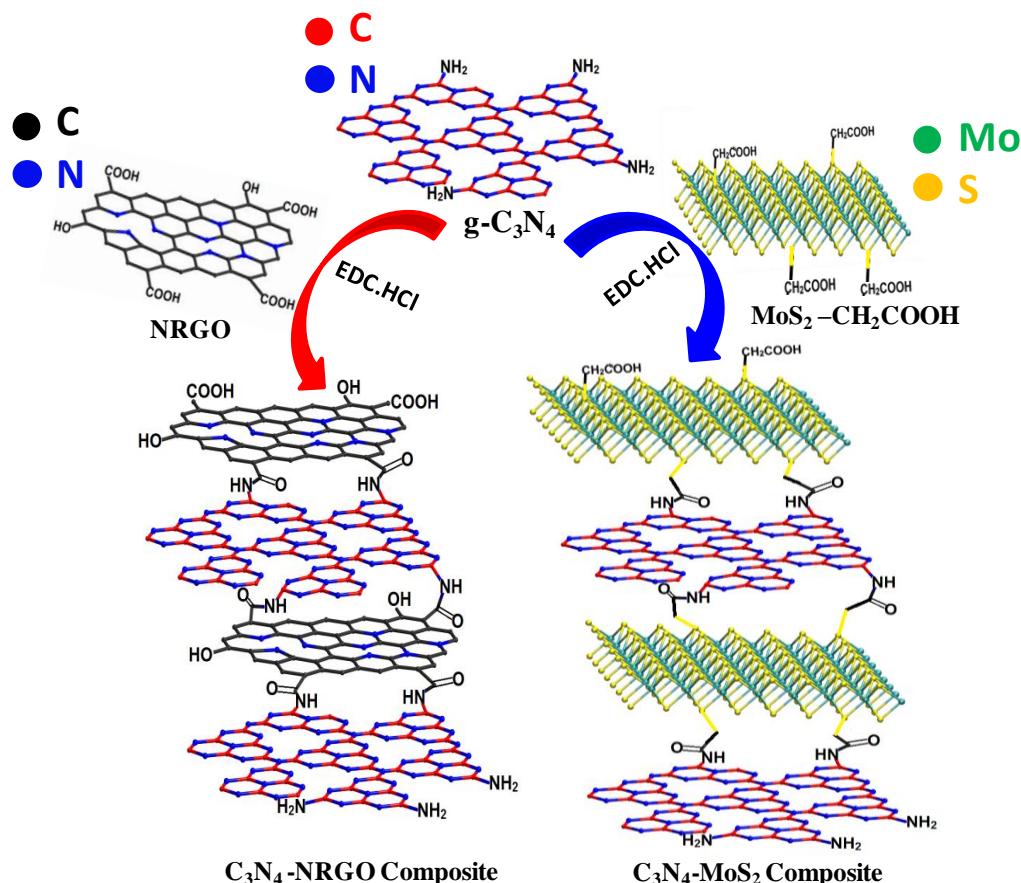
Scheme 2. *A synthetic strategy for covalently bonded C_3N_4-NRGO and C_3N_4–MoS_2 composites*

C_3N_4-NRGO composite was obtained by reacting nitrogen-doped reduced graphene oxide (NRGO), prepared from the microwave irradiation of a mixture of graphene oxide (GO) and urea, [21] with amine-functionalized C_3N_4 in the presence of 1-ethyl-3-(3-dimethylaminopropyl) carbodiimide (EDC). Carboxylate functionalized MoS_2 (MoS_2-CH_2COOH), obtained by the reaction of metallic 1T-MoS_2 with bromoacetic acid, [20] was

reacted with amine-functionalized C$_3$N$_4$ in the presence of EDC to obtain the C$_3$N$_4$-MoS$_2$ assembly (1T-MoS$_2$ sheets were obtained by Li intercalation in bulk MoS$_2$ followed by exfoliation in water). These coupling reactions with EDC result in amide bonds between the C$_3$N$_4$ and NRGO or MoS$_2$. EDC coupling has an advantage over SOCl$_2$-based activation in that no HCl is liberated, and the urea byproduct is soluble in water. We have used the terms C$_3$N$_4$-NRGO and C$_3$N$_4$-MoS$_2$ in the manuscript to refer to the composites generated by the covalent cross-linking strategy.
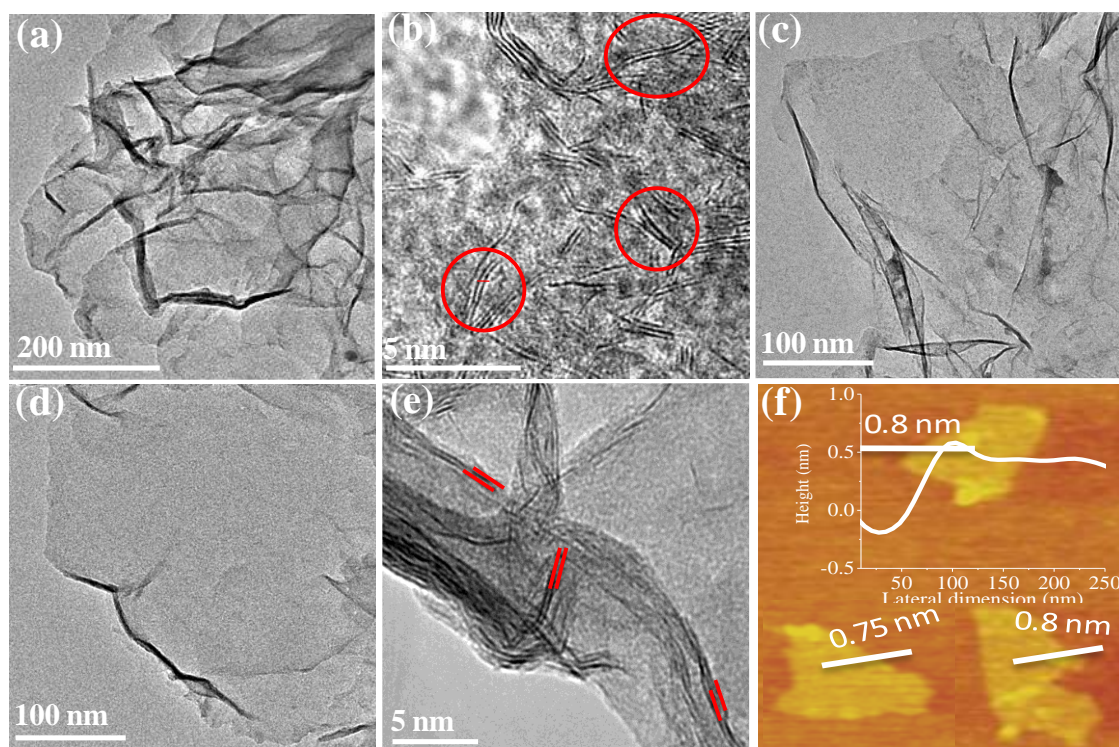
Figure 8. (a, b) TEM and HRTEM images (circles indicate layers with inter-layer spacing of ~0.4 nm) of C$_3$N$_4$, (c) TEM image of NRGO, (d, e) TEM and HRTEM images (parallel lines indicate layers with inter-layer spacing ~0.62 nm) of MoS$_2$ (f) AFM images of MoS$_2$-CH$_2$COOH.

We have established the identities of the composites by a variety of methods. **Figures 8 a, c and d** present the transmission electron microscope (TEM) images of C$_3$N$_4$, NRGO and MoS$_2$ used as the starting

materials, showing a wrinkled morphology due to the thin-layers. Atomic force microscopy (AFM) images of MoS_2-CH_2COOH indicate it contains monolayers of MoS_2 (~ 80 %) with a layer thickness of ~ 0.8 nm **(Figure 8f)**.
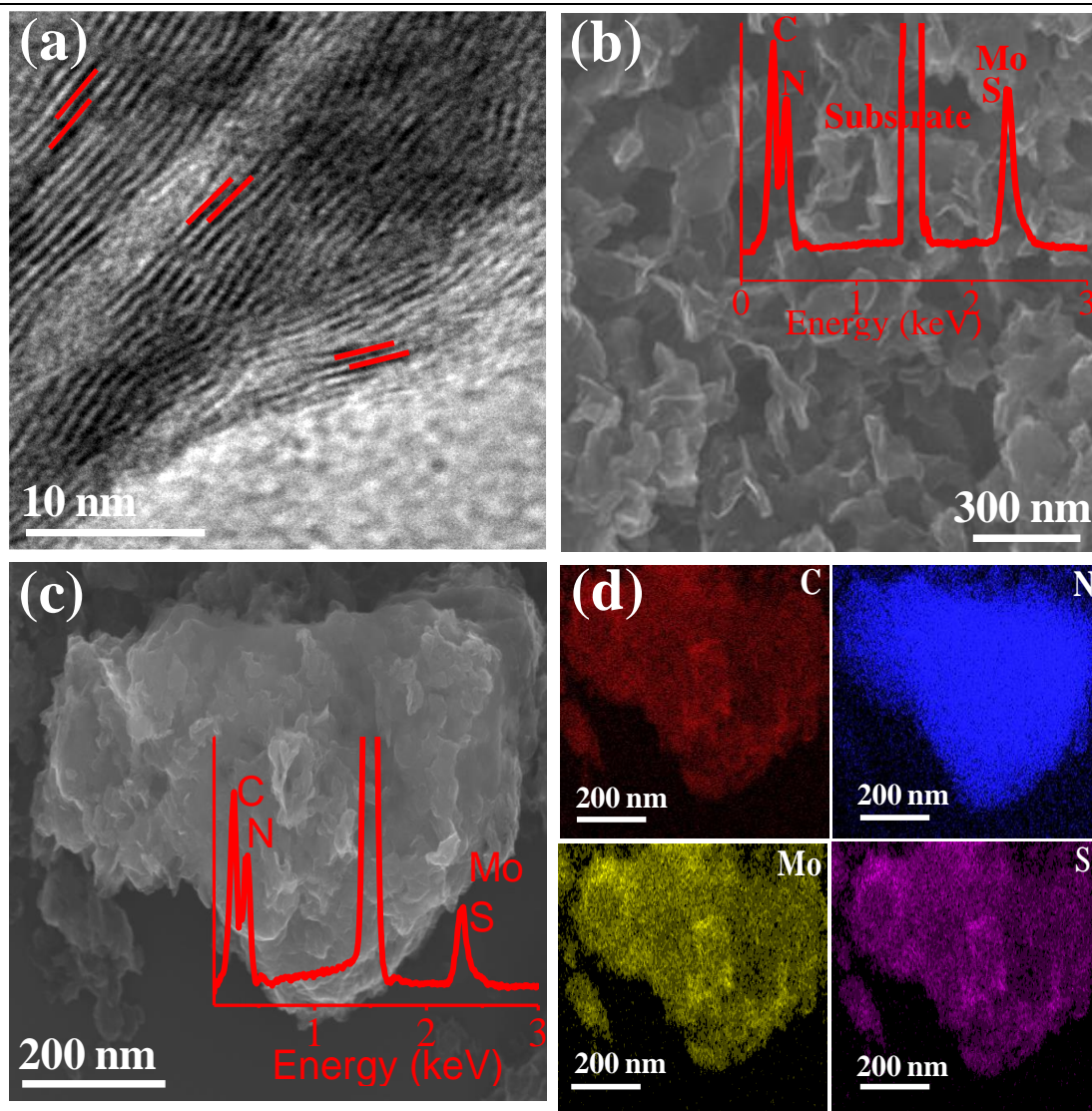
Figure 9. *(a) HRTEM image of C_3N_4–MoS_2 composite, (b) FESEM image of physical mixture of C_3N_4 and MoS_2, (c) FESEM image (Inset; Energy dispersive spectrum) and d) elemental mapping (C (red), N (blue), Mo (yellow), S (magenta)) images of the C_3N_4-MoS_2 composite.*

Figure 9 a shows the HRTEM image of the C_3N_4-MoS_2 composite with the edge region of the basal plane parallel to the direction of the

electron beam. The inter-layer spacing (~0.75 nm, indicated by red lines) is higher compared to that in C_3N_4 (0.40 nm, **Figure 8b**) or in MoS_2 (0.62 nm, **Figure 8 e)**. We do not observe any region corresponding to either C_3N_4 or MoS_2 alone, apparently suggesting the occurrence of cross-linking between monolayers of MoS_2-CH_2COOH and C_3N_4 by forming the amide bond. The observed inter-layer spacing (~0.75, HRTEM) in the C_3N_4-MoS_2 composite is in agreement with the theoretically calculated bond distance (Mo-**S-CH₂-CO-NH-C₃**N_4) between cross-linked C_3N_4 and MoS_2 layers. In **Figures 9 c** we show the FESEM image of C_3N_4-MoS_2 composites, illustrating the formation of 3D assemblies due to layer-by-layer stacking.

A physical mixture of C_3N_4 with MoS_2 or NRGO contains randomly oriented layers and does not display any stacking order due to lack of directing bonds **(Figure 9 b)**. During cross-linking, the amine functional groups on either side of the C_3N_4 layer form amide bonds with the carboxyl-functionalized MoS_2 or NRGO giving rise to a layer-by-layer assembly takes place on both sides of the 2D sheets. Elemental mapping images of patterned cross-linked layers of MoS_2 with C_3N_4 using the energy dispersive X-ray spectroscopy (EDS) exhibits a uniform distribution of C, N, Mo, and S confirming the homogeneous nature of the nanocomposite **(Figure 9 d)**. Sonication of a mixture of C_3N_4 and MoS_2-CH_2COOH or NRGO in DMF medium carried out prior to the coupling reaction favors exfoliation as well as the homogeneous mixing of layers.

Electron energy-loss spectrum (EELS) obtained at different locations of the C_3N_4-MoS_2 nanocomposite show characteristic peaks of C (K edge), N (K edge), Mo (M-edge) and S (L-edge), confirming the uniform nature of

cross-linked assemblies **(Figure10a)** [4]. The infrared (IR) spectrum of C_3N_4 has bands at 1240, 1414, 1564 and 1634 cm^{-1} due to C=N and C–N stretching modes **(Figure 10 b)** and a band at 812 cm^{-1} due to the breathing mode of the s-triazine ring. The broad band in the 3000-3400 cm^{-1} region is due to the presence of amine groups [25]. NRGO exhibits -C=O and –OH stretching modes at 1715 and 3110 cm^{-1}, assigned to the residual carboxyl groups in the basal plane, whereas MoS_2–CH_2COOH shows bands at 1702 and 3200 cm^{-1} corresponding to -C=O and –OH stretching modes along with a C-S stretching band at 700 cm^{-1} arising from covalent functionalization of MoS_2. The IR spectrum of the C_3N_4-NRGO composite **(Figure 10 b)** exhibits a C=O stretching band at 1660 cm^{-1} due to the amide bond between the C_3N_4 and NRGO layers along with other characteristic vibration frequencies. C_3N_4-MoS_2 nanocomposites show the carbonyl stretching band at 1660 cm^{-1}, confirming cross-linking of carboxylated MoS_2 nanosheets with amine functionalized C_3N_4 by amide bonds. Raman spectra of the C_3N_4-NRGO and C_3N_4-MoS_2 composites along with those of individual components are shown in **Figure 10 c**. MoS_2-CH_2COOH shows only bands due to the 2H-polytype, similar to the behavior observed after reactions of 1T-MoS_2 with metal precursors and diazonium salts.[18, 26] Compared to MoS_2-CH_2COOH, the A_{1g} mode of the C_3N_4-MoS_2 composite is red-shifted, whereas the physical mixture does not exhibit any significant shift, this indicates that covalent cross-linking leads to better interconnectivity between the individual components which results in efficient charge-transfer from C_3N_4 to MoS_2 **(Figure 10 c)**.[27] Raman spectra of both NRGO and C_3N_4-MoS_2 composite show D and G-

bands at 1346 and 1588 cm^{-1}, respectively with an enhancement in the FWHM of the bands in the latter case. Cross-linking causes intercalation of C$_3$N$_4$ between the NRGO layers and vice versa thereby increases the FWHM. Thus, IR and Raman spectra of the nanocomposites confirm cross-linking of C$_3$N$_4$ and NRGO or MoS$_2$ sheets by layer-by-layer assembly through amide bonds.
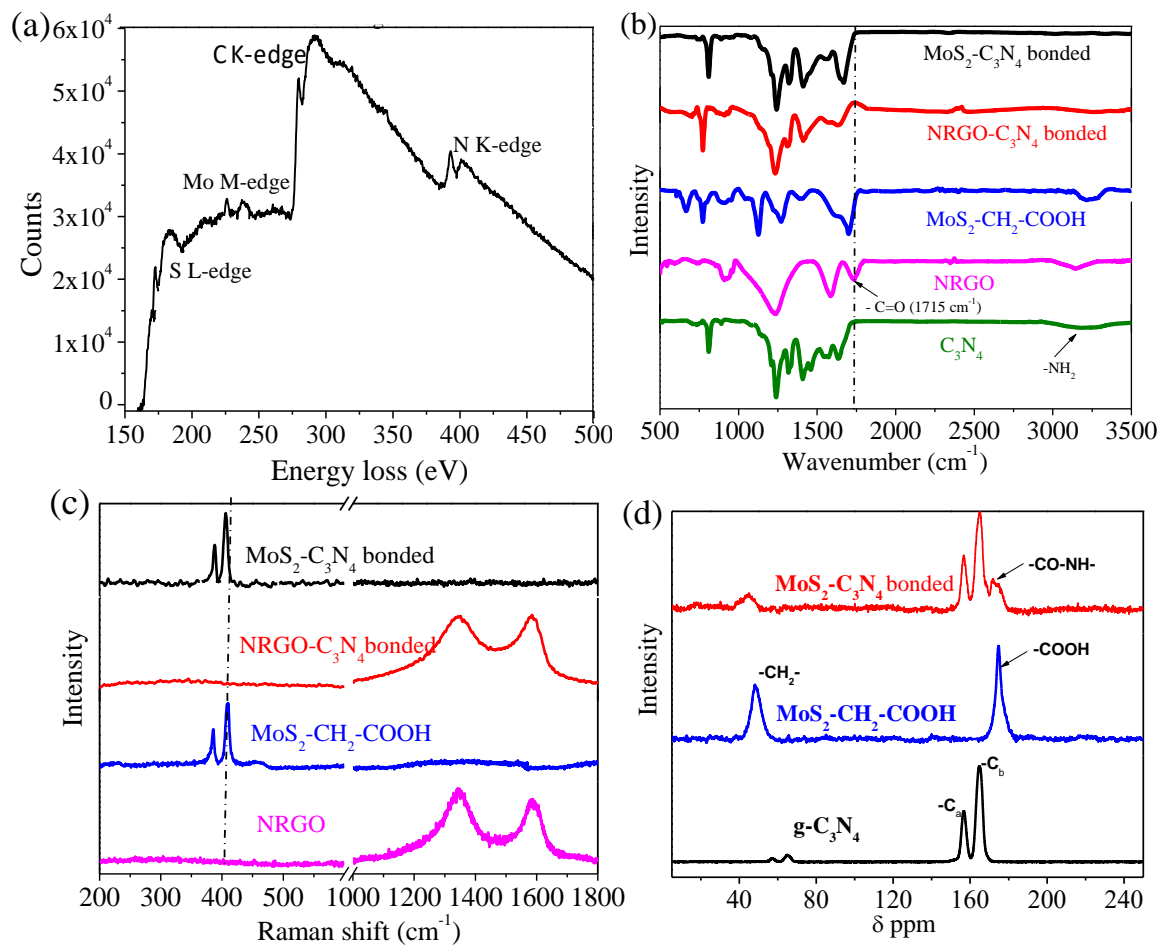
Figure 10. *(a) EELS spectrum of C$_3$N$_4$-MoS$_2$ nanocomposites, showing S (Ledge), Mo (M-edge), C (K-edge) and N (K-edge); b) Infrared spectra of C$_3$N$_4$, NRGO, acid functionalized MoS$_2$, C$_3$N$_4$-NRGO, and C$_3$N$_4$–MoS$_2$ composites; c) Raman spectra of NRGO, acid functionalized MoS$_2$, C$_3$N$_4$-NRGO, and C$_3$N$_4$ - MoS$_2$ composites; (d) Solid-state ^{13}C CP-MAS NMR spectra of C$_3$N$_4$, acid functionalized MoS$_2$, C$_3$N$_4$-MoS$_2$ composite.*

The nitrogen content in the NRGO sample is 8.2 wt% as obtained from the elemental analysis as well as XPS measurements. To further confirm the formation of the amide bond in the composites we have performed solid-state ^{13}C CP-MAS NMR spectroscopy **(Figure 10 d)**. Two distinct signals dominate the spectrum of C_3N_4 at 165 and 154 ppm due to the sp^2 carbon atoms [28]. MoS_2-CH_2COOH shows characteristic ^{13}C signals at 46.5 and 171 ppm corresponding to aliphatic carbons (CH_2) and carbonyl groups, respectively. Compared to MoS_2-CH_2COOH, the signals in the C_3N_4-MoS_2 composite are slightly downshifted to $\delta=169$ ppm, indicating the cross-linking of C_3N_4 and MoS_2 nanosheets by forming an amide bond.
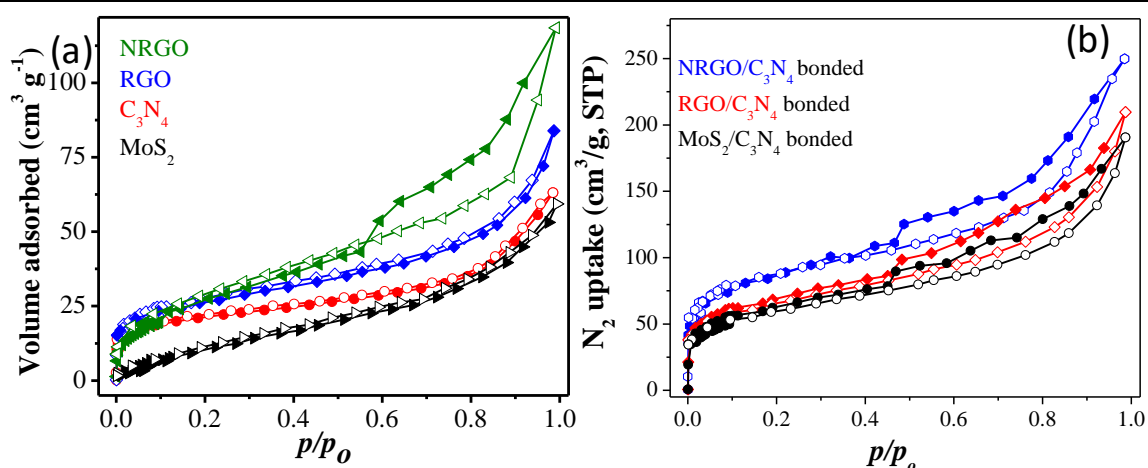
Figure 11. *N$_2$ sorption profiles of (a) NRGO, RGO, C$_3$N$_4$, MoS$_2$ and (b) C$_3$N$_4$-NRGO and C$_3$N$_4$–MoS$_2$ nanocomposites.*

Surface area and porosities of C_3N_4, NRGO, MoS_2, C_3N_4-NRGO and C_3N_4-MoS_2 composites were obtained by N_2 adsorption-desorption measurements at 77 K **(Figure 11)**. Brunauer-Emmet-Teller (BET) surface area of C_3N_4 and few-layer MoS_2 show much lower surface areas of 65 and 40 m^2/g respectively, NRGO has a surface area of 130 m^2/g with a type-IV

mesoporous sorption profile **(Figure 11 a).** C_3N_4-NRGO and C_3N_4-MoS$_2$ composites are 186 and 151 m²/g while a physical mixture of C_3N_4 and NRGO or MoS$_2$ show low surface areas of 98 and 69 m²/g, respectively **(Figure 11 b)**. The cross-linked composites show microporous type-1 adsorption behavior at low pressures along with a type H4 hysteresis loop associated with narrow slit-like pores **(Figure 11b)**. The enhanced surface area is attributed to the generated pores due to stacking and cross-linking between the C_3N_4 and NRGO (or) MoS$_2$ layers which is evident in the N$_2$ isotherms.

4.2.2 Hydrogen evolution studies

Cross-linked C_3N_4-NRGO and C_3N_4-MoS$_2$ composites were examined for the photochemical hydrogen evolution in an aqueous solution of triethanolamine (TEOA, 20% v/v) as sacrificial agent under UV-Vis light illumination. C_3N_4 alone has an activity of 52 μmoles h^{-1}g^{-1} with a TOF 0.005 h^{-1} while the chemically bonded C_3N_4-NRGO composite exhibits an enhanced activity of 308 μmoles h^{-1}g^{-1} with a TOF of 0.06 h^{-1} **(Figure 12 a)**. The physical mixture of C_3N_4 and NRGO shows the activity of only 32 μmoles h^{-1}g^{-1} with a TOF 0.006 h^{-1} **(Figure 12a)**. The covalently linked C_3N_4-MoS$_2$ composite shows an extraordinarily high activity of 12778 μmoles h^{-1}g^{-1} with a TOF of 2.35 h^{-1}. The physical mixture of C_3N_4 and MoS$_2$, and their composite obtained by the solid-state route exhibit low photochemical activity of 187 and 1157 μmoles h^{-1}g^{-1} with a TOF 0.04 and 0.22 h^{-1}, respectively **(Figure 12b)**. The composites show stable HER over the period of time **(Figure 12 c)** suggesting use as a long-term catalyst.
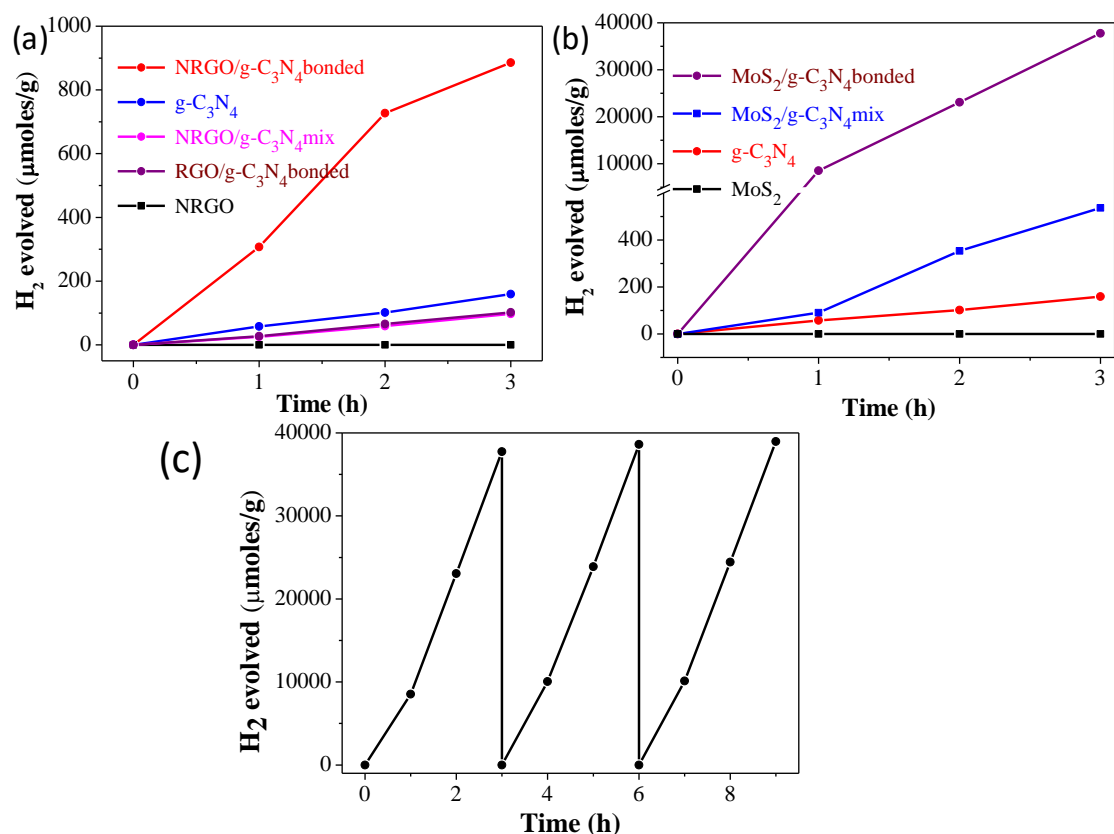
Figure 12. *Comparison of the H_2 evolution activity of a) C_3N_4, NRGO, a physical mixture of C_3N_4 and NRGO and the covalently bonded C_3N_4-NRGO nanocomposite; b) C_3N_4, MoS_2, a physical mixture of C_3N_4 and MoS_2, C_3N_4-MoS_2 composite (SS, obtained by solid state route) and the covalently bonded C_3N_4-MoS_2 nanocomposite. (c) Cycling study of H_2 evolution on C_3N_4-MoS_2 composite.*

We have carried out control experiments on individual C_3N_4, MoS_2 and NRGO in the presence of TEOA, C_3N_4 (52 µmoles $h^{-1}g^{-1}$) are photoactive for HER, while NRGO and MoS_2 are inactive **(Figure 13a)**. We have also examined the H_2 evolution activity only in the presence of the photosensitizer (Eosin Y dye) to indicate active HER sites on NRGO or MoS_2 and found that NRGO is inactive whereas, MoS_2 shows H_2 evolution due to the appropriate band positions **(Figure 13b)**.
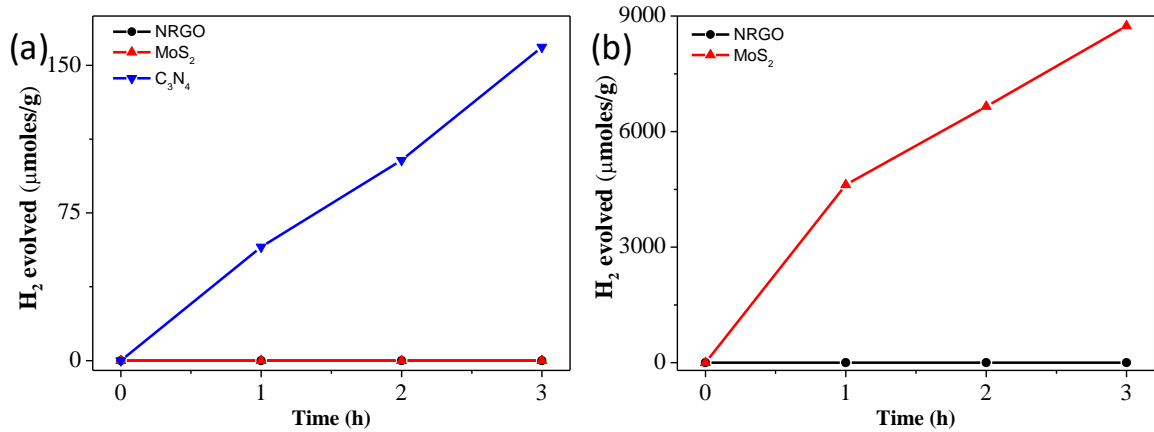
Figure 13. *(a) Hydrogen evolution of C$_3$N$_4$, MoS$_2$, and NRGO in light and triethanolamine; (b) Eosin Y dye assisted hydrogen evolution in NRGO and MoS$_2$ under the light in the presence of triethanolamine.*

Photoluminescence studies were carried out on C$_3$N$_4$-NRGO and C$_3$N$_4$-MoS$_2$ composites to understand the photoexcited electron transfer mechanism between the cross-linked layers **(Figure 14)**.
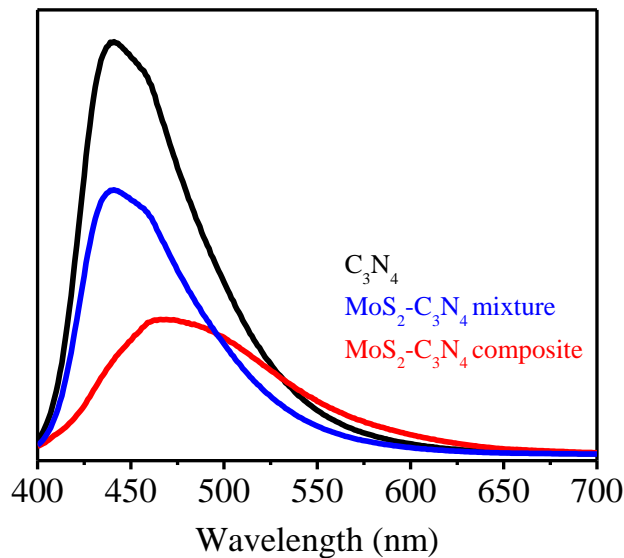
Figure 14. *Photoluminescence spectra of C$_3$N$_4$, C$_3$N$_4$-NRGO composite, and C$_3$N$_4$-MoS$_2$ composite.*

These studies confirm that the PL signal of C$_3$N$_4$ at 440 nm is drastically quenched in the cross-linked composites due to charge-transfer (CT) from C$_3$N$_4$ to MoS$_2$ or NRGO. Electron transfer from C$_3$N$_4$ to MoS$_2$ (NRGO) is thermodynamically favorable since the conduction band

minimum (CBM) of C_3N_4 is higher in energy than that of MoS_2 (NRGO). [11, 13]

4.2.3 Theoretical analysis

(The first-principles studies were carried out by Dr. A. Bandyopadhyay and Prof. S. K. Pati of the New Chemistry Unit, JNCASR)

Using density functional theory (DFT), we have calculated the energy of the orbitals of cross-linked C_3N_4-NRGO and C_3N_4-MoS_2 composites and the corresponding wavefunction plots obtained by considering maximum contribution from the individual components to these orbitals **(Figures 15a and b).**
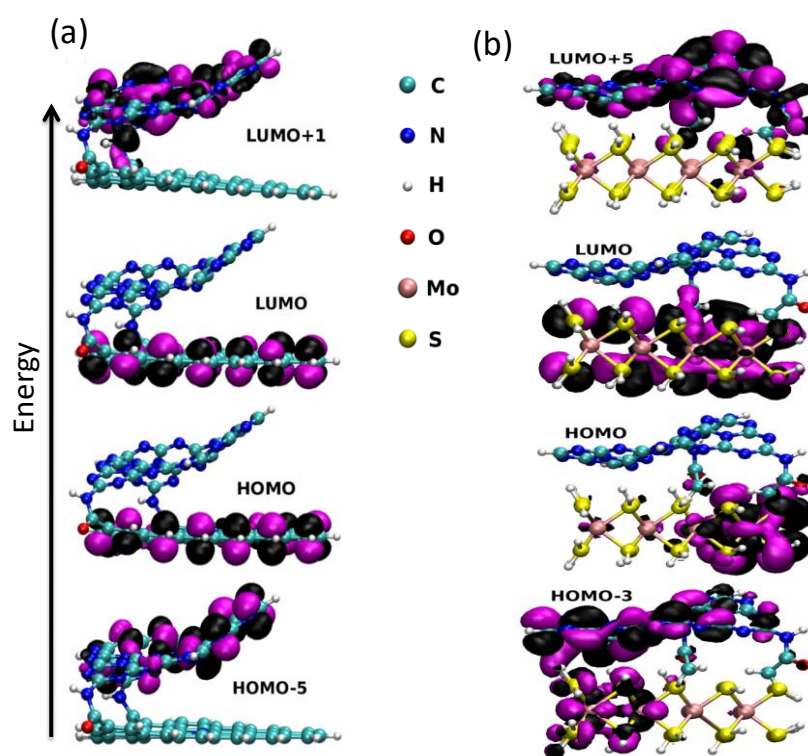
Figure 15*. Wavefunction plots of (a) C₃N₄-NRGO nanocomposite and (b) C₃N₄-MoS₂ nanocomposites, where the upper layer is C₃N₄ for both the cases (Inter-layer spacing in C₃N₄-NRGO and C₃N₄-MoS₂ composites are 0.30 and 0.73 nm, respectively which are comparable with the experimentally observed values).*

The wave function plots of the C_3N_4-NRGO composite shows that there is a possibility of CT from the highest occupied molecular orbital (HOMO), mainly contributed by NRGO to the lowest unoccupied molecular orbital (LUMO+1) with a significant contribution from C_3N_4 **(Figure 15a).** On the other hand, the C_3N_4-MoS₂ composite shows that there is a possibility of CT from the HOMO-3 (on C_3N_4) to LUMO (on MoS₂) **(Figure 15b)**. The magnitude of CT in C_3N_4-NRGO and C_3N_4-MoS₂ composites are 0.31 and 0.29 e⁻.
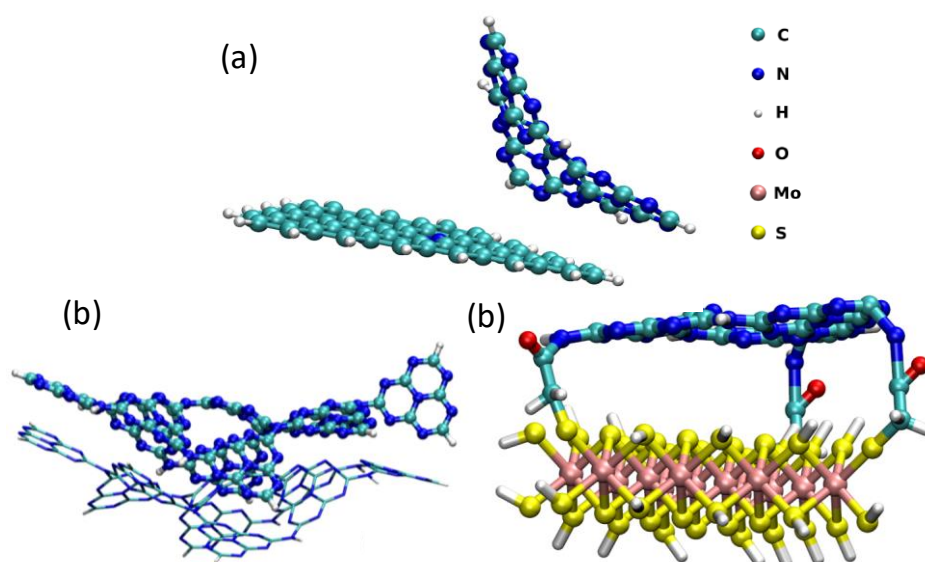
Figure 16. *(a) Physical mixture of C_3N_4 and NRGO (upper layer is C_3N_4), where two flakes are optimized for random slipped stack pattern; (b) Bi-layer C_3N_4 (nanosheets show buckling nature due to N atom lone pair repulsions) and (c) C_3N_4-MoS₂ composites (upper layer is C_3N_4) showing planar nature of C_3N_4 due to extensive cross-linking.*

Without considering the cross-linked bonds, they show a decrease in CT to 0.23 and 0.18 e⁻, respectively. This implies that CT in the composites co-occurs through space and bonds between the cross-linked

layers. The different orientation of physical mixture or NRGO MoS_2, C_3N_4 sheets as wells as covalently linked C_3N_4 MoS_2 is shown in **Figure 16**. The orientation of the sheets is controlled and directed by these bonds. Furthermore, the magnitude of CT in randomly oriented slipped stack pattern of C_3N_4, and NRGO is similar to those observed experimentally in the case of physical mixtures, decreasing to 0.07 e- **(Figure 16 a)**. It is therefore suggested that cross-linked systems have better CT efficiency.

DFT calculations also suggest that cross-linking induces planarity, which leads to efficient CT in composites due to better orbital overlapping. The wave function plots of composites also elucidate the photo-induced CT in cross-linked composites, since C_3N_4 LUMO is higher in energy and can transfer an electron to LUMO of NRGO or MoS_2 on photoexcitation. The water molecules were adsorbed at different sites, and their relative binding energy was calculated **(Figure 17)**. The relative binding energy of water molecule for MoS_2 edge site, surface and on C_3N_4 is 0.0, 0.04 and 0.27 eV respectively.
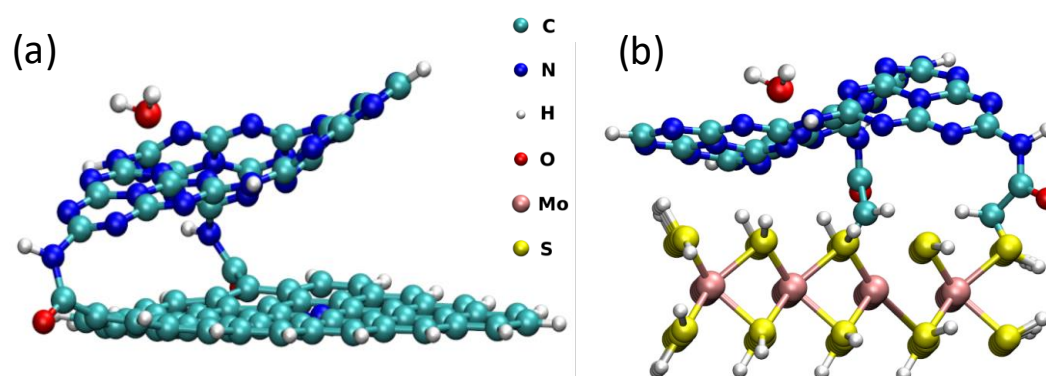
Figure 17. *Water molecule adsorption on the C_3N_4 layer (upper layer) in (a) C_3N_4-NRGO and (b) C_3N_4-MoS_2 composites.*

4.2.4 Discussion

Schematic energy band diagrams for composites are derived on the basis of control experiments, PL studies as well as theoretical calculations which highlights electronic events during photoexcitation **(Scheme 3).** On photoexcitation, an electron from valence band maxima (VBM, orange arrow) of C_3N_4 is excited to conduction band minima (CBM) and then transfers to CBM of NRGO or MoS_2 (red arrows). Since CBM of NRGO is below the water reduction potential, electrons transferred from C_3N_4 to NRGO will not participate in HER unlike in MoS_2. H_2 evolution occurs in the presence of TEOA which reduces the photogenerated holes by donating electrons to the VBM of C_3N_4 and favors the forward reaction.
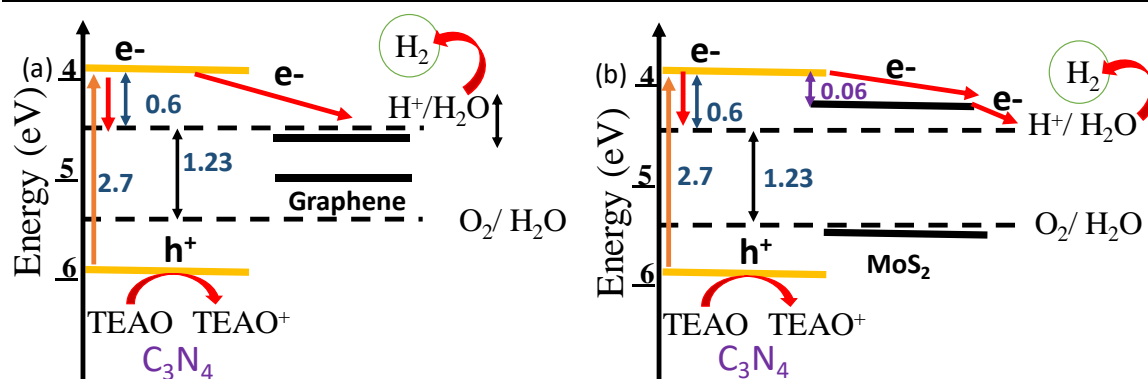
Scheme 3. *Schematic energy band diagram highlighting different electronic process during HER in (a) C_3N_4-NRGO and (b) C_3N_4–MoS_2 composites (orange arrow indicates photoexcitation of electron from VBM to CBM of C_3N_4 and red arrows indicates different electronic events in the composites during HER).*

The increase in photochemical catalytic activity with respect to C_3N_4 is more pronounced in the C_3N_4–MoS_2 composite compared to C_3N_4-NRGO. Cross-linked C_3N_4–MoS_2 exhibits enhancement of ~246 times as compared to C_3N_4 whereas, C_3N_4-NRGO shows only ~6 times. The lower activity of

C_3N_4-NRGO composite over C_3N_4–MoS_2 can be attributed to the different electronic processes occurring on the catalytic surface during HER. In **Scheme 3a** we show a schematic of the energy band diagram of C_3N_4-NRGO which indicates that photoexcited electrons (orange arrow) of C_3N_4 can either transferred to CBM of NRGO or undergo water reduction on the C_3N_4 surface (red arrows). As the CBM energy gradient between C_3N_4 and NRGO is more compared to the water reduction potential, chances of electrons moving from the CBM of C_3N_4 to NRGO is less favored. DFT calculated relative binding energies of a water molecule with the C_3N_4 and NRGO are 0.0 and 0.86 eV respectively suggesting that C_3N_4 is preferred for HER in the C_3N_4-NRGO composite. Furthermore, H_2 evolution occurs on the C_3N_4 surface alone since the CBM of NRGO is below water reduction potential. This indicates that in the C_3N_4-NRGO composite enhanced activity arises mostly because of the increased planarity of the layers and the enhanced surface area due to cross-linking while some electrons can still shuttle across the network through NRGO. The physical mixture of C_3N_4 and NRGO does not show any increased activity as compared to C_3N_4 which supports this rationale. **Scheme 3b** shows a schematic of the energy band diagram of the C_3N_4–MoS_2 composite, where the photoexcited electrons of C_3N_4 either reduce water or transfer to the CBM of MoS_2 (red arrows) for H_2 evolution. As the thermodynamic gradient between the CBM of C_3N_4 and of MoS_2 (0.06 eV) is less compared the HER potential (0.6 eV), there is a high probability of electron transfer from C_3N_4 to MoS_2 which also participate in water reduction (red arrows). The relative binding energy of water molecule (as calculated from DFT) for MoS_2 edge site, surface and

on C$_3$N$_4$ suggests that MoS$_2$ is preferred for HER, particularly the edge sites. The physical mixture and solid-state composite of C$_3$N$_4$ and MoS$_2$ also show increased activity compared to C$_3$N$_4$, supporting this reasoning. Apart from the achieved planarity and enhanced surface area, additional factors like favored CT due to cross-linking and active MoS$_2$ sites gives better H$_2$ evolution activity in C$_3$N$_4$–MoS$_2$ composite as compared to C$_3$N$_4$–NRGO.

In the case of a physical mixture of C$_3$N$_4$ and MoS$_2$, enhancement in photochemical HER activity with respect to C$_3$N$_4$ is ~4 times, whereas the C$_3$N$_4$–MoS$_2$ composite obtained by the solid-state route shows an increase by ~23 times **(Figure 12b)**. This result clearly suggests that C$_3$N$_4$ grown on MoS$_2$ layers provides greater interaction between the two, thereby exhibiting higher HER activity compared to the physical mixture where layers are randomly oriented **(Figure 12b)**. On the other hand, cross-linked C$_3$N$_4$-MoS$_2$ shows an enhancement of ~246 times with respect to C$_3$N$_4$ which is ~11 and 68 times higher than the sample obtained by solid state route and the physical mixture respectively. The superior performance of the cross-linked assemblies is attributed to the enhanced interfacial area as well as planarity between the layers due to directional layer-by-layer cross-linking which increases the magnitude of CT between C$_3$N$_4$ and MoS$_2$ as it co-occurs through both space and bonds between the individual layers. Secondly, the 3D network formed due to cross-linking causes additional increment in the magnitude of CT due to effective electronic coupling between the heterolayers in the cross-linking direction,

contributing to the improved HER performance. This reasoning is supported by both PL and theoretical studies. Lack of directional bonds in the physical mixture as well as in the composite obtained from the solid-state route reduces the magnitude of CT between layers, homogeneity in the order of heterolayers, planarity as well as the formation of the extended 3D network which limits their HER performance. Furthermore, efficient electron channeling across 3D network through space as well as by bonds between cross-linked layers makes better charge separation and thereby enhancing the activity. We also note that in physical mixtures, the layers are stacked by weak van der Waals interaction which can get disrupted during sonication, as sample dispersion is a prerequisite for photochemical studies.

We have compared the activity of covalently cross-linked C_3N_4-MoS_2 composite with other similar systems in the literature and found it to be higher than any C_3N_4 or MoS_2 based system **(Table 2)**.

Table 2: Comparison of hydrogen evolution data of covalently bonded NRGO-C₃N₄ and MoS₂-C₃N₄ composites compared with few of the literature reports.

Catalyst	Activity (μmole h^{-1} g^{-1})	TOF [a] (h^{-1})	Reaction Conditions
C_3N_4	52	0.005	
C_3N_4-MoS_2 (Composite)	12778	2.35	TEOA: H_2O (1:4) (400 W Xe lamp; λ>265-800 nm)
C_3N_4-MoS_2 (Composite SS)	1157	0.22	
C_3N_4-NRGO (Composite)	308	0.06	
C_3N_4/Pt (1 wt%)[55]	122	0.011	Methanol: H_2O (1:3) (300 W Xe lamp; λ>400 nm)
C_3N_4/Pt-Co[56]	60	0.006	Pure H_2O (300 W Xe lamp; λ>300 nm)
C_3N_4-Co^{III}(dmgH)$_2$pyCl[57]	250	0.023	TEOA: H_2O (1:6) (300 W Xe lamp; λ>350-740 nm)
C_3N_4-Carbon Quantum Dots[58]	105	0.010	Pure H_2O (300 W Xe lamp; λ>420 nm)
C_3N_4-MoS_2 Quantum dots/Pt[59]	394	0.036	TEOA: H_2O (1:9) (300 W Xe lamp; λ>420 nm)
Layered C_3N_4-MoS_2 nanojunctions[20]	968	0.091	Lactic acid: H_2O (1:9) (300 W Xe lamp; λ>420 nm)
C_3N_4-MoS_2[21]	252	0.024	TEOA : H_2O (1:9) (300 W Xe lamp; λ>400 nm)

[a]TOF is calculated for photoactive component C_3N_4 since MoS_2, NRGO, Pt, Carbon Quantum Dots and Cobaltoxime are co-catalysts.

5.   Conclusions

In conclusion, we have been able to generate robust MoS_2 and MoS_2-RGO frameworks with organic linkers using the Sonogashira coupling strategy. The pillared frameworks generated by us are somewhat comparable to the 3D pillared layer MOFs reported by Kitagawa *et al.* [60] where 2D metal carboxylates are pillared by organic linkers. The entirely new metal chalcogenide-based porous solids based on pillared MoS_2 frameworks reported here imply the possibility of designing related materials with advantageous attributes. MoS_2 assemblies show superior hydrogen evolution activity as compared to few-layer MoS_2 possibly due to the more exposed catalytically active edge sites of MoS_2 on pillaring by organic linkers.

We have been able to covalently cross-link nanosheets of C_3N_4 with sheets of MoS_2 as well as of NRGO by the carbodiimide method. The cross-linked composites show better catalytic activity relative to the physical mixtures or C_3N_4 alone. The present study clearly demonstrates the beneficial effects of covalent bonding in the case of C_3N_4-MoS_2 and C_3N_4-NRGO composites, particularly in the case of the former. Photochemical HER activity of the C_3N_4-MoS_2 nanocomposite is noteworthy with ~246 times increased activity compared to C_3N_4. Furthermore, cross-linked C_3N_4-MoS_2 shows an enhancement of ~11 and 68 times higher photochemical HER activity than that obtained by the solid-state method and the physical mixture respectively. We conclude from theoretical and experimental studies that enhanced HER activity in cross-linked

composites arises from the increased planarity, enhanced charge-transfer and higher surface area. DFT calculations show that the magnitude of charge-transfer is maximum in the case of cross-linked composite since it occurs between the cross-linked layers simultaneously through space as well as bonds. Electrochemical HER activity of the nanocomposites is also superior, showing that covalent cross-linking to be useful for HER and related catalytic reactions. This strategy may also be of value in a variety of other applications as well.

6. References

1.   J. M. Englert, C. Dotzer, G. Yang, M. Schmid, C. Papp, J. M. Gottfried, H.-P. Steinrück, E. Spiecker, F. Hauke, A. Hirsch, Nat. Chem., 2011, 3, 279.

2.   T. Sainsbury, A. Satti, P. May, A. O'Neill, V. Nicolosi, Y. K. Gun′ko, J. N. Coleman, Chem. Eur. J., 2012, 18, 10808.

3. D. Voiry, A. Goswami, R. Kappera, E. SilvaCecilia de Carvalho Castro, D. Kaplan, T. Fujita, M. Chen, T. Asefa, M. Chhowalla, Nat. Chem., 2014, 7, 45.

4.   K. C. Knirsch, N. C. Berner, H. C. Nerl, C. S. Cucinotta, Z. Gholamvand, N. McEvoy, Z. Wang, I. Abramovic, P. Vecera, M. Halik, S. Sanvito, G. S. Duesberg, V. Nicolosi, F. Hauke, A. Hirsch, J. N. Coleman, C. Backes, ACS Nano, 2015, 9, 6018.

5.   J. Zheng, H. Zhang, S. Dong, Y. Liu, C. Nai, H. Shin, H. Jeong, B. Liu, K. Loh, Nat. Commun., 2014, 5, 2995.

6.   P.Vishnoi, A.Sampath, U. V. Waghmare,C. N. R. Rao, Chem.Eur. J., 2017, 23, 886.

7.   A. Jeffery, S. R. Rao, M. Rajamathi, Carbon, 2017, 112, 8.

8.   P. P. Wang, H. Y. Sun, Y. J. Ji, W. H. Li, X. Wang, Adv. Mater., 2014, 26, 964.

9.   X. Chia, A. Y. S. Eng, A. Ambrosi, S. M. Tan, M. Pumera, Chem. Rev., 2015, 115, 11941.

10.   U. Maitra, U. Gupta, M. De, R. Datta, A. Govindaraj, C. N. R. Rao, Angew. Chem. Int. Ed., 2013, 52, 13057.

11.   A. B. Laursen, S. Kegnaes, S. Dahl, I. Chorkendorff, Energy Environ. Sci., 2012, 5, 5577.

12.   S. Presloski, M. Pumera, Mater. Today., 2015, 19, 140

13.   S. S. Chou, M. De, J. Kim, S. Byun, C. Dykstra, J. Yu, J. Huang, V. P. Dravid, J. Am. Chem. Soc., 2013, 135, 4584.

14.   R. H. Gonçalves, R. Fiel, M. R. S. Soares, W. H. Schreiner, C. M. P. Silva, E. R. Leite, Chem. Eur. J., 2015, 21, 15583.

15.	E. P. Nguyen, B. J. Carey, J. Z. Ou, J. van Embden, E. D. Gaspera, A. F. Chrimes, M. J. S. Spencer, S. Zhuiykov, K. K. Zadeh, T. Daeneke, Adv. Mater., 2015, 27, 6225.

16.	Y. Liu, Z. Tan, X. Xie, Z. Wang, X. Ye, Chem. Asian J, 2013, 8, 817.

17.	C. Backes, N. C. Berner, X. Chen, P. Lafargue, P. LaPlace, M. Freeley, G. S. Duesberg, J. N. Coleman, A. R. McDonald, Angew. Chem. Int. Ed., 2015, 54, 2638.

18.	X. Wang, E. N. Kalali, D-Y. Wang, J. Mater. Chem. A, 2015, 3, 24112.

19.	X. Zou, Y. Zhang, Chem. Soc. Rev., 2015, 44, 5148.

20.	Y. Hou, A. B. Laursen, J. Zhang, G. Zhang, Y. Zhu, X. Wang, S. Dahl, I. Chorkendorff, Angew. Chem. Int. Ed., 2013, 52, 3621.

21.	H. Zhao, Y. Dong, P. Jiang, H. Miao, G. Wang, J. Zhang, J. Mater. Chem. A, 2015, 3, 7375.

22.	L. Ye, D. Wang, S. Chen, ACS Appl. Mater. Interfaces, 2016, 8, 5280.

23.	Y. Hou, Z. Wen, S. Cui, X. Guo, J. Chen, Adv. Mater., 2013, 25, 6291.

24.	Y. Zheng, Y. Jiao, Y. Zhu, L. H. Li, Y. Han, Y. Chen, A. Du, M. Jaroniec, S. Z. Qiao, Nat. Commun., 2014,5, 3783

25.	D. Chen, W. Chen, L. Ma, G. Ji, K. Chang, J. Y. Lee, Mater. Today, 2014, 17, 184.

26.	U. Maitra, U. Gupta, M. De, R, Datta, A. Govindaraj, C. N. R. Rao, Angew. Chem., Int. Ed., 2013, 52, 13057.

27.	J. Duan, S. Chen, M. Jaroniec, S. Z. Qiao, ACS Nano, 2015, 9, 931.

28.	D. Pierucci, H. Henck, J. Avila, A. Balan, C. H. Naylor, G. Patriarche, Y. J. Dappe, M. G. Silly, F. Sirotti, A. T. C. Johnson, M. C. Asensio, A. Ouerghi, Nano Lett., 2016, 16, 4054.

29.	K. Pramoda, U. Gupta, I. Ahmad, R. Kumar, C. N. R. Rao, J. Mater. Chem. A, 2016, 4, 8989.

30.	R. Kumar, V. M. Suresh, T. K. Maji, C. N. R. Rao, Chem. Commun., 2014, 50, 2015.

31.	Y. Liu, Y. Zhao, L. Jiao, J. Chen, J. Mater. Chem. A, 2014, 2, 13109.

32.	S. Min, G. Lu, J. Phys. Chem. C, 2012, 116, 25415.

33.   Y. Liu, H. Kang, L. Jiao, C. Chen, K. Cao, Y. Wang, H. Yuan, Nanoscale, 2015, 7, 1325.

34.   W. S. Hummers, R. E. Offeman, J. Am. Chem. Soc., 1958, 80, 1339

35.   Z. Zhao, Y. Sun, Q. Luo, F. Dong, H. Li, W.-K. Ho, Sci. Rep., 2015, 5, 14643.

36.   D. Voiry, A. Goswami, R. Kappera, E. Castro, D. Kaplan, T. Fujita, M. Chen, T. Asefa, M. Chhowalla, Nat. Chem., 2015, 7, 45.

37.   K. Gopalakrishnan, A. Govindaraj, C. N. R. Rao, J. Mater. Chem. A, 2013, 1, 7563.

38.   Gaussian 09, Revision D.01, M. J. Frisch, G. W. Trucks, H. B. Schlegel G. E. Scuseria, M. Robb, J. R. Cheeseman, G. Scalmani, V. Barone, B. Mennucci, G. A. Petersson, H. Nakatsuji, M. Caricato, X. Li, H. P. Hratchian, A. F. Izmaylov, J. Bloino, G. Zheng, J. L. Sonnenberg, M. Hada, M. Ehara, K. Toyota, R. Fukuda, J. Hasegawa, M. Ishida, T. Nakajima, Y. Honda, O. Kitao, H. Nakai, T. Vreven, J. A. Montgomery, Jr., J. E. Peralta, F. Ogliaro, M. Bearpark, J. J. Heyd, E. Brothers, K. N. Kudin, V. N. Staroverov, R. Kobayashi, J. Normand, K. Raghavachari, A. Rendell, J. C. Burant, S. S. Iyengar, J. Tomasi, M. Cossi, N. Rega, J. M. Millam, M. Klene, J. E. Knox, J. B. Cross, V. Bakken, C. Adamo, J. Jaramillo, R. Gomperts, R. E. Stratmann, O. Yazyev, A. J. Austin, R. Cammi, C. Pomelli, J. W. Ochterski, R. L. Martin, K. Morokuma, V. G. Zakrzewski, G. A. Voth, P. Salvador, J. J. Dannenberg, S. Dapprich, A. D. Daniels, Ö. Farkas, J. B. Foresman, J. V. Ortiz, J. Cioslowski, D. J. Fox, Gaussian, Inc., Wallingford CT, 2009.

39.   T. Yanai, D. P. Tew, N. C. Handy, Chem. Phys. Lett. 2004, 393, 51.

40.   A. D. Becke, J. Chem. Phys., 1993, 98, 5648.

41.   U. Gupta, B. S. Naidu, U. Maitra, A. Singh, S. N. Shirodkar, U. V. Waghmare and C. N. R. Rao, APL Mater., 2014, 2, 092802.

42.   S. Stankovich, D. A. Dikin, R. D. Piner, K. A. Kohlhaas, A. Kleinhammes, Y. Jia, Y. Wu, S. T. Nguyen, R. S. Ruoff, Carbon, 2007, 45, 1558.

43.   K. Yoo, S.-W. Joo, J. Colloid Interface sci., 2007, 311, 491.

44.   D. Sloan, Y. M. Sun, H. Ihm, J. M. White, J. Phys. Chem. B, 1998, 102, 6825.

45.   H. Cabibil, H. Ihm, J. M. White, Surf. Sci., 2000, 447, 91.

46.   R. Chinchilla, C. Najera, Chem. Soc. Rev., 2011, 40, 5084

47.   T. Weber, J. C. Muijsers, J. H. M. C. van Wolput, C. P. J. Verhagen, J. W. Niemantsverdriet, J. Phy. Chem., 1996, 100, 14144.

48.   D. W. Mayo, F. A. Miller, R. W. Hannah, in Course Notes on the Interpretation of Infrared and Raman Spectra, Wiley, 2003 DOI:10.1002/0471690082.

49.   G. Socrates, Infrared, and Raman Characteristic Group Frequencies: Tables and Charts, Wiley, 2001.

50.   K. S. W. Sing, D. H. Everett, R. A. W. Haul, L. Moscou, R. A. Pierotti, J. Rouquerol, T. Siemieniewska, Pure Appl. Chem., 1984, 57, 603.

51.   H. Xu, J. Yan, X. She, L. Xu, J. Xia, Y. Xu, Y. Song, L. Huang, H. Li, Nanoscale, 2014, 6, 1406.

52.   K. Pramoda, M. Kaur, U. Gupta, C. N. R. Rao, Dalton Trans., 2016, 35, 13810.

53.   W. Fu, H. He, Z. Zhang, C. Wu, X. Wang, H. Wang, Q. Zeng, L. Sun, X. Wang, J. Zhou, Q. Fu, P. Yu, Z. Zhen, C. Jin, B. Yakobson, Z. Liu, Nano Energy, 2016, 27, 44.

54.   Y. Chen, B. Lin, W. Yu, Y. Yang, S. M. Bashir, H. Wang, K. Takanabe, H. Idriss, J.-M. Basset. Chem. Eur. J., 2015, 21, 10290.

55.   L. Ge, C. Han, X. Xiao, L. Guo, Y. Li, Mater. Res. Bull., 2013, 48, 3919.

56.   G. Zhang, Z. Lan, L. Lin, S. Lin and X. Wang, Chem. Sci., 2016, 7, 3062.

57.   S. W. Cao, X. F. Liu, Y. P. Yuan, Z. Y. Zhang, J. Fang, S. C. J. Loo, J. Barber, T. C. Sum, C. Xue, Phys. Chem. Chem. Phys., 2013, 15, 18363.

58.   J. Liu, Y. Liu, N. Liu, Y. Han, X. Zhang, H. Huang, Y. Lifshitz, S.-T Lee, J. Zhong, Z. Kang, Science, 2015, 347, 970.

59.   J. X. Jin, X. Fan, J. Tian, R. Cheng, M. Li, L. Zhang, RSC Adv., 2016, 6, 52611.

60.   R. Kitaura, K. Fujimoto, S. Noro, M. Kondo, S. Kitagawa, Angew. Chem., 2002, 114, 141.

Visible-light-induced hydrogen evolution reaction by tungsten sulfoselenides[*]

Summary

WS_2 is a promising catalyst for the hydrogen evolution reaction (HER). The effect of substitution in Se substitution in MoS_2 is known to enhance the electrochemical properties, however, in photochemical HER it is not known. We have explored photocatalytic properties of ternary sulfoselenides of tungsten (WS_xSe_{2-x}) by the dye-sensitized hydrogen evolution. $WS_{2-x}Se_{2x}$ solid solutions are found to exhibit high activity reaching 2339 µmole h^{-1} g^{-1} for WSSe which is three times higher than that of WS_2 alone (866 µmole h^{-1} g^{-1}). The turnover frequency (TOF) is also high (0.7 h^{-1}). Such synergistic effect of selenium substitution in WS_2 is noteworthy.
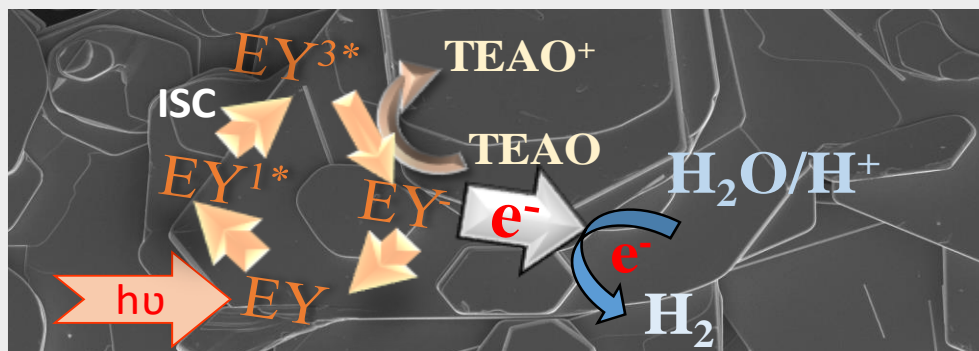
1. Introduction

Transition metal dichalcogenides (TMDs) have emerged as an important class of materials with unique properties [1-4]. They are layered sandwiched X-M-X units (M= metal and X= chalcogenides) with strong in-plane bonding and with weak out-of-plane van der Waals interaction between layers. Among the layered TMDs MoS_2 and $MoSe_2$ have attracted the significant attention in the last few years due to their properties related to transistors [5,6], catalysis [8-10] and gas sensors [10]. They are also useful as a hydrogen evolution catalyst. Theoretical and experimental studies indicate that the (0001) planes are catalytically inert while, (10-10) planes are catalytically active due to the low Gibbs free energy for hydrogen evolution [11,12]. Various strategies have been employed to improve the HER either by creating many active edge sites [13,14-17] or by chemical modification with Fe, Co, Ni and Re. [17,18]. The phase-engineered metastable 1T-phase exhibit improved catalytic activity for HER. Ternary composites of TMDs $MoS_{2(1-x)}Se_{2x}$ [19, 20] and MoS_xCl_y [21] are reported to show improved performance compared to binary compounds in electrochemical hydrogen evolution reaction.

We have synthesized ternary WS_xSe_{2-x} (x= 0.0, 0.50, 1.0, 1.5, 2.0) and examined their photocatalytic HER activity. Interestingly we found, synergistic effect wherein the ternary sulfoselenide are superior catalysts compared to the binary compounds.

2. Scope of the present investigations

The activity of 2D-TMDs is mainly due to edge sites or vacant sites present on the surface. Therefore, the creation of new sites is primary strategy to increase the activity of TMDs. One of the strategies is to make active basal planes. 1T-form although have an active basal plane but are not stable. It was observed that selenium substitution in MoS_2 induces a slight distortion in the structure due to the larger radius of selenium as compared to S which could facilitate bond breaking of the molecules adsorbed on the basal plane. The basal plane with unsaturated bonds provides the favorable hydrogen binding energy from the tensile regions on the surface with active sites mainly located in the basal plane. From our previous studies in **Chapter 2** with bulk group 6 TMDs, we observed tungsten based chalcogenides have higher photochemical HER activity. We, therefore, chose WS_2 over MoS_2 for our studies.

3. Experimental Section

3.1 Synthesis of tungsten sulfoselenides

Tungsten sulfoselenides, WS_xSe_{2-x} (x=0, 0.5, 1, 1.5, 2.0), were synthesized by the solid-state reaction of a stoichiometric mixture of tungsten (W) (99.99+% Sigma Aldrich) with sulfur (S) (99.99% Sigma Aldrich) and selenium (Se) (99.99% Sigma Aldrich) purity. The mixture was loaded in a high-quality quartz tube (12 mm OD, 10 mm ID, 22 cm length) and sealed under vacuum at 10^{-6} Torr. The sealed tube was introduced into a furnace and slowly heated to 850 °C over 15 hrs. The quartz tube was kept at the same temperature for 48 h and cooled slowly to room temperature.

3.2 Characterization

The products were also characterized by X-ray diffraction using Bruker D8 Advance X-ray diffractometer (Cu K_α; $\lambda=1.54$ Å). Raman spectra were recorded with 514 nm Argon laser using Jobin-Yvon Labram HR spectrometer. The SEM images were taken using NOVA nano FESEM. The BET surface area measurement was calculated by N_2 adsorption in Quantachrome Autosorb instrument at 77 K.

3.3 Hydrogen evolution measurements

$WS_{2.0-x}Se_x$ samples (x= 0.0, 0.50, 1.0, 1.5, 2.0) were dispersed in a solution of triethanolamine (15% v/v) in water. To this dispersion, 0.014 mM of Eosin Y dye was added and the system purged with N_2. Hydrogen evolution studies were carried out with a 100W halogen lamp under constant stirring. The evolved gas analyzed over a period in Perkin Elmer 580 C Clarus GC-TCD.

Turnover frequency (TOF) was calculated using the equation,

$$TOF\ (h^{-1}) = \frac{Activity\ of\ the\ catalyst}{Moles\ of\ the\ catalyst\ used} \qquad (1)$$

4. Results and Discussion

4.1 Synthesis and characterization

Tungsten sulfoselenides, WS_xSe_{2-x} (x=0, 0.5, 1, 1.5, 2.0), were synthesized by the solid-state reaction of a stoichiometric mixture of Tungsten (W) with sulfur (S) and selenium (Se). The compounds were bulk samples which were characterized using X-ray diffraction and Raman. The effect of substitution was clearly observed in these compounds from these techniques. The composition of these compounds was determined using energy dispersive X-ray spectroscopy. The X-ray diffraction patterns for these samples are given in **Figure 1a** confirms the hexagonal 2H-structure for all the $WS_{2-x}Se_x$ compositions, with a prominent peak due to the (002) reflection.
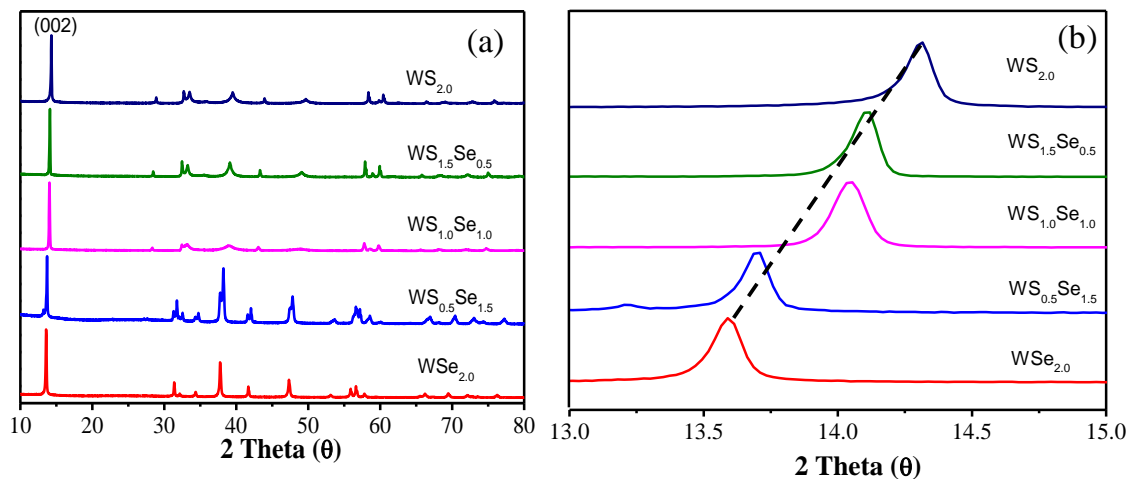

Figure 1. *(a) The X-ray diffraction (XRD) and (b) The shift in the (002) peak in XRD of bulk WS_xSe_{2-x} (x=0, 0.5, 1.0, 1.5, 2.0).*

There is a shift in the reflection to lower angles with increasing in substitution of sulfur by selenium **(Figure 1b)**. Typical SEM images shown in Figures **2a and b** show the flake-like morphology of the

samples. The lateral size of the flakes is ~10 μm while the thickness is < 1μm. The composition of the samples was ascertained by energy dispersive spectra (EDS).
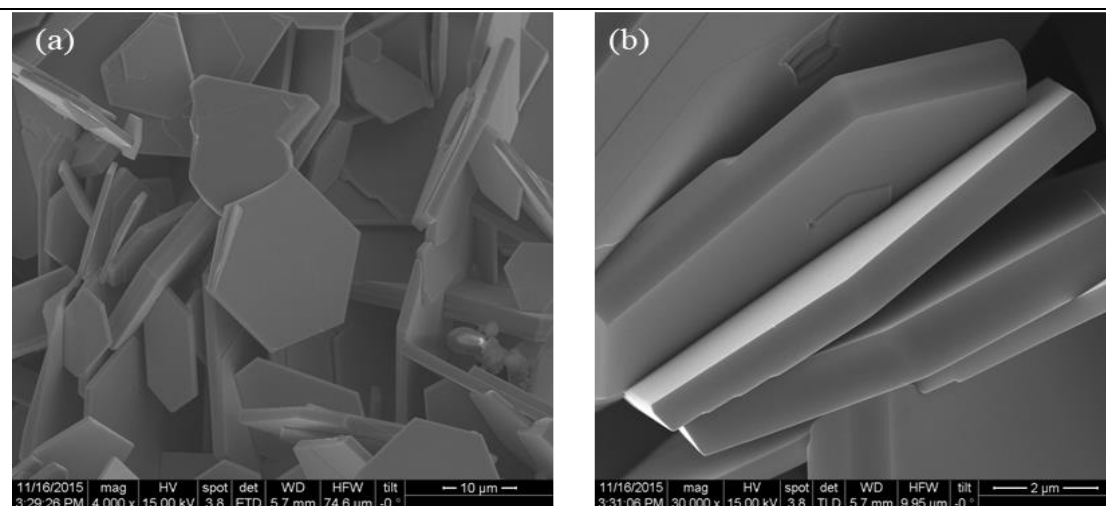
Figure 2 (a) and (b). *The typical scanning electron microscope image of the horizontal and cross-sectional view of the particles of the compound. The size and thickness of the particles is on an average of ~10 μm and ~1 μm respectively.*

Raman spectra recorded using a 514 nm unpolarised Ar laser with backscattered geometry **(Figure 3a)** show two prominent first-order modes E_{2g} and A_{1g} modes at 358 cm^{-1} 423 cm^{-1} respectively. The other first-order mode due to the longitudinal acoustic mode appears as a small hump at 177 cm^{-1}. WSe$_2$ shows a prominent band at 253 cm^{-1} due to the out of plane second order mode of the longitudinal 2LA mode at 251 cm^{-1} which overlaps with the E^1_{2g} mode [22-24]. With the increase in Se content WS$_x$Se$_{2-x}$, a redshift is observed in the A_{1g} band, but the E_{2g} band shows no significant change **(Figure 3b)**. Disorder in the crystallites induces some broadening of the Raman peaks [25, 26].
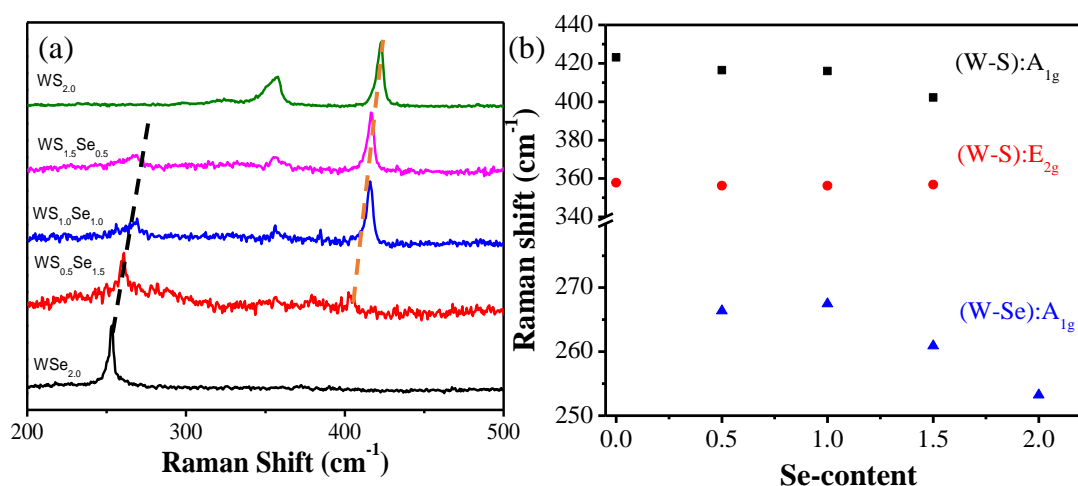
Figure 3. *(a) Raman spectra and (b) Shift in the W-Se A_{1g}, W-S E_{2g} and W-S A_{1g} bands in Raman of bulk WS_xSe_{2-x} (x=0, 0.5, 1.0, 1.5, 2.0).*

4.2 Hydrogen evolution studies

Dye-sensitized photochemical solution performed using triethanolamine (TEAO) as a sacrificial agent with Eosin Y as a photosensitizer.
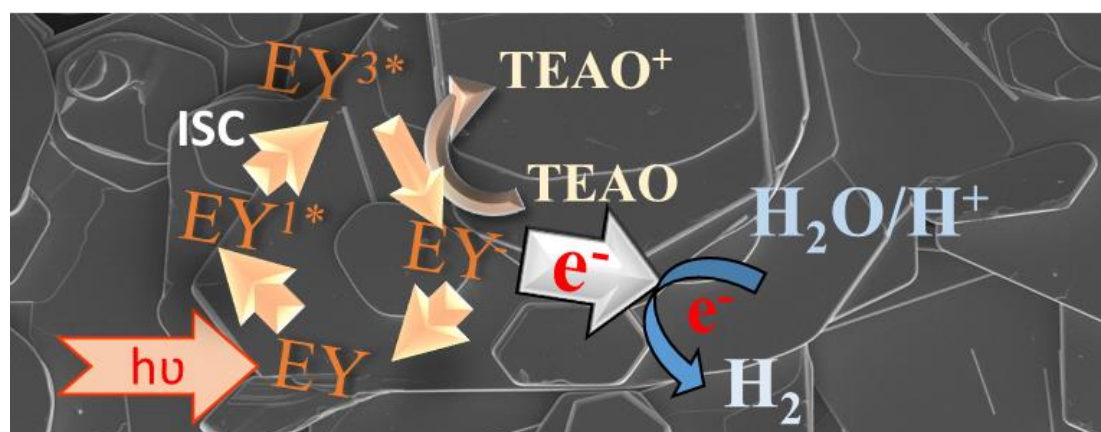
Figure 4. *The plausible mechanism of dye-assisted photocatalytic hydrogen evolution on WS_xSe_{2-x}.*

Eosin Y on the absorption of photon undergoes a transition from a singlet to a lowest lying triplet state (EY^{3*}) through intersystem crossing. EY^{3*} takes up an electron from (TEAO) and gets converted to EY^-. EY^- is

highly reactive and transfers the electron to the hydrogen evolution site
[8, 9]. The plausible mechanism of dye-sensitized photocatalytic HER
taking place over the surface of WS_xSe_{2-x} is shown in **Figure 4.** Time
course of hydrogen evolution for this catalyst was done over a period of
6 hours with dye added after three hours **(Figure 5 a)**. The activities in
the first three hours of WS_2 and WSe_2 were 691 and 1732 µmoles $g^{-1} h^{-1}$
of hydrogen with turnover frequency (TOF) of 0.17 and 0.59 h^{-1}
respectively. The activities of the solid solutions of $WS_{0.5}Se_{1.5}$, $WS_{1.0}Se_{1.0}$,
and $WS_{0.5}Se_{1.5}$ compounds were 880, 1567, and 1202 µmoles $g^{-1} h^{-1}$ with
TOF of 0.24, 0.36, and 0.38 h^{-1} respectively **(Figure 5b and c)**.
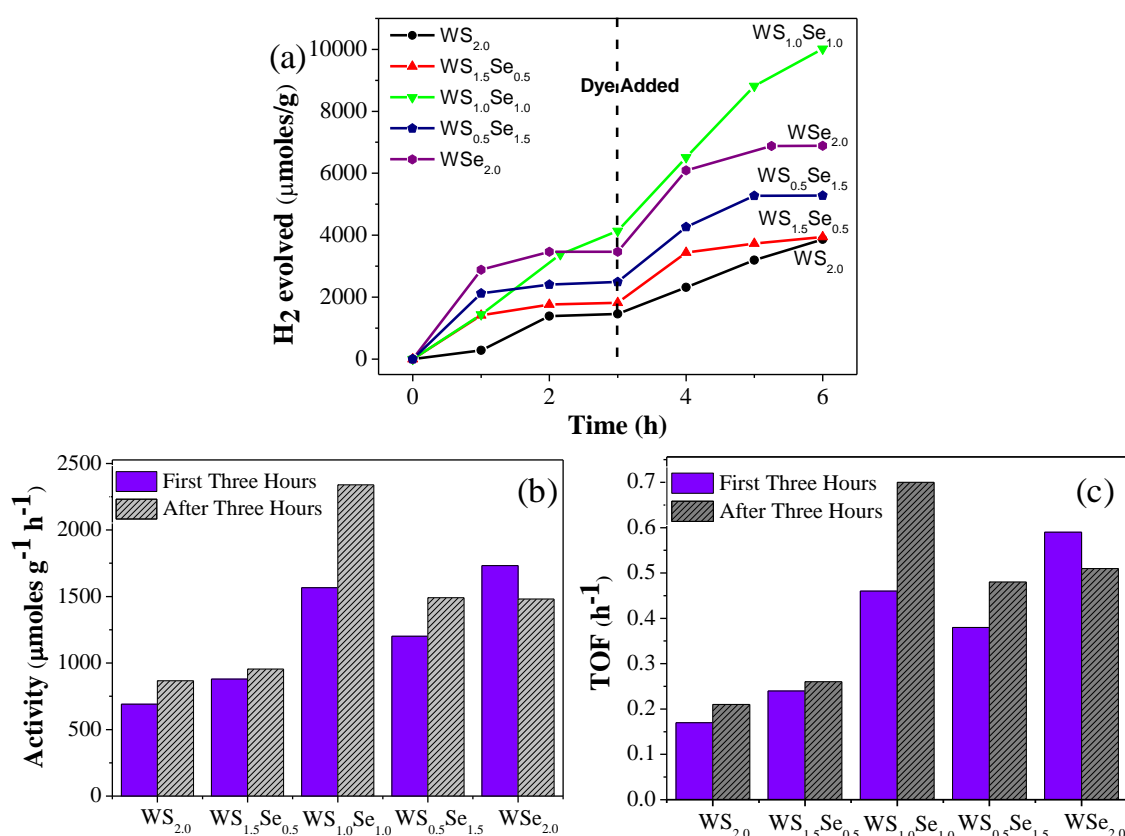
Figure 5. *Comparative study of hydrogen evolution WS_xSe_{2-x} (x=0, 0.5, 1.0, 1.5, 2) (a) over a period of time. The bar graphs compare (b) the activity and (c) turnover frequency (TOF).*

The activity of the catalyst increases on further addition of the dye with activities of WS_2, $WS_{1.5}Se_{0.5}$, $WS_{1.0}Se_{1.0}$, $WSe_{1.5}S_{0.5}$ and WSe_2 are 866, 955, 2339, 1491 and 1480 µmoles g^{-1} h^{-1} with TOF of 0.21, 0.26, 0.70, 0.47 and 0.51 respectively **(Figure 5b and c)**. The activity of bulk WSe_2 (1732 µmoles g^{-1} h^{-1} is slightly higher than the $WS_{1.0}Se_{1.0}$ (1567 µmoles h^{-1} g^{-1}) in the first three hours but decreases after three hours. The activity of WSSe is 2339 µmoles g^{-1} h^{-1} while 1480 µmoles g^{-1} h^{-1} for WSe_2 **(Figure 5b)**. However, we observe a decrease in the activity of WSe_2 on further addition of dye after 3 hours suggests that it will not be optimal choice as a long-term catalyst. **Figure 5 b and c** show the comparative activities and turnover frequency (TOF) of these compounds where we can clearly see the enhanced hydrogen evolution (2-3 times higher than WS_2) of the solid solution with maxima at $WS_{1.0}Se_{1.0}$ which indicate synergistic effect.
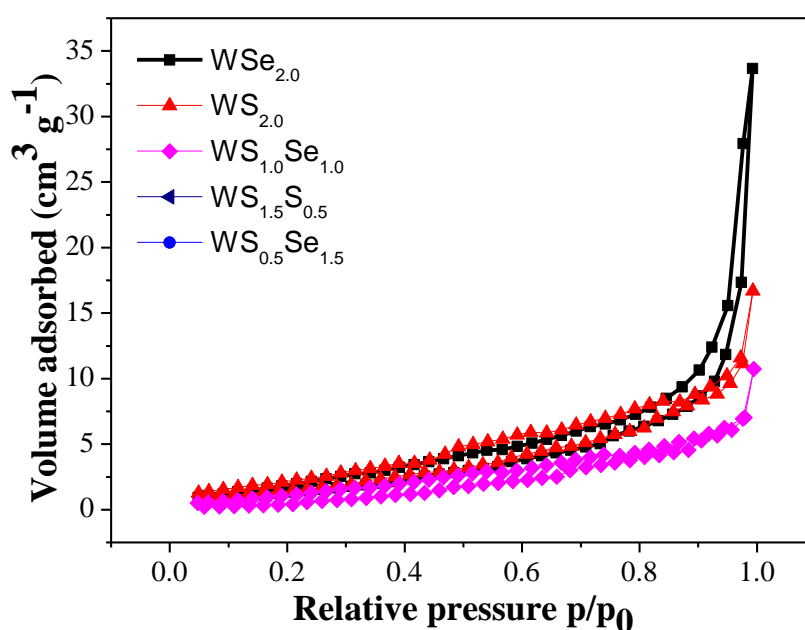
Figure 6. *The BET N_2 Adsorption isotherm of the WS_2, WSe_2 and $WS_{1.0}Se_{1.0}$.*

To rule out the possibility of the increased activity related to the surface area, we adsorbed N_2 gas adsorption on the surface of the catalysts and determined their surface area. BET Surface areas of $WS_{2-x}Se_x$ composition are in the 4-6 m²/g range with type III isotherm **(Figure 6).** Catalytic activities of these compounds would, therefore, be independent of the surface area. Comparative study of activities of solid ternary solutions with binary compounds is shown in **table 1.** Clearly, we observe ternary compounds are better than binary compounds.

Table 1: Comparison of hydrogen evolution of bulk WS_xSe_{2-x}

Compound	Activity (μmol g^{-1} h^{-1})	TOF (h^{-1})
$WS_{2.0}$	866	0.21
$WS_{1.5}Se_{0.5}$	955	0.26
$WS_{1.0}Se_{1.0}$	2339	0.70
$WS_{0.5}Se_{1.5}$	1491	0.47
$WSe_{2.0}$	1480	0.51

The activity and TOF values are after three hours and further addition of dye.

The introduction of selenium into WS_2 induces a slight distortion in the structure because of the larger radius of selenium as compared to S. This could facilitate bond breaking of the molecules adsorbed on the basal plane. The basal plane with unsaturated bonds provides the favorable hydrogen binding energy from the tensile regions on the surface with active sites mainly located in the basal plane. [27, 28].

Previous studies of alloys of Se, S, and W suggest that distortions can make the surface active and thus provide more sites for hydrogen samples compared to the binary compounds [29-31].

Hydrogen evolution was stable for 5 cycles (over a period of 15 hours) as shown in **Figure 7 a**. There was no change in the sample before and after the HER **(Figures 7 b and c)**. $WS_{1.0}Se_{1.0}$ may be used as a long-term catalyst for HER evolution
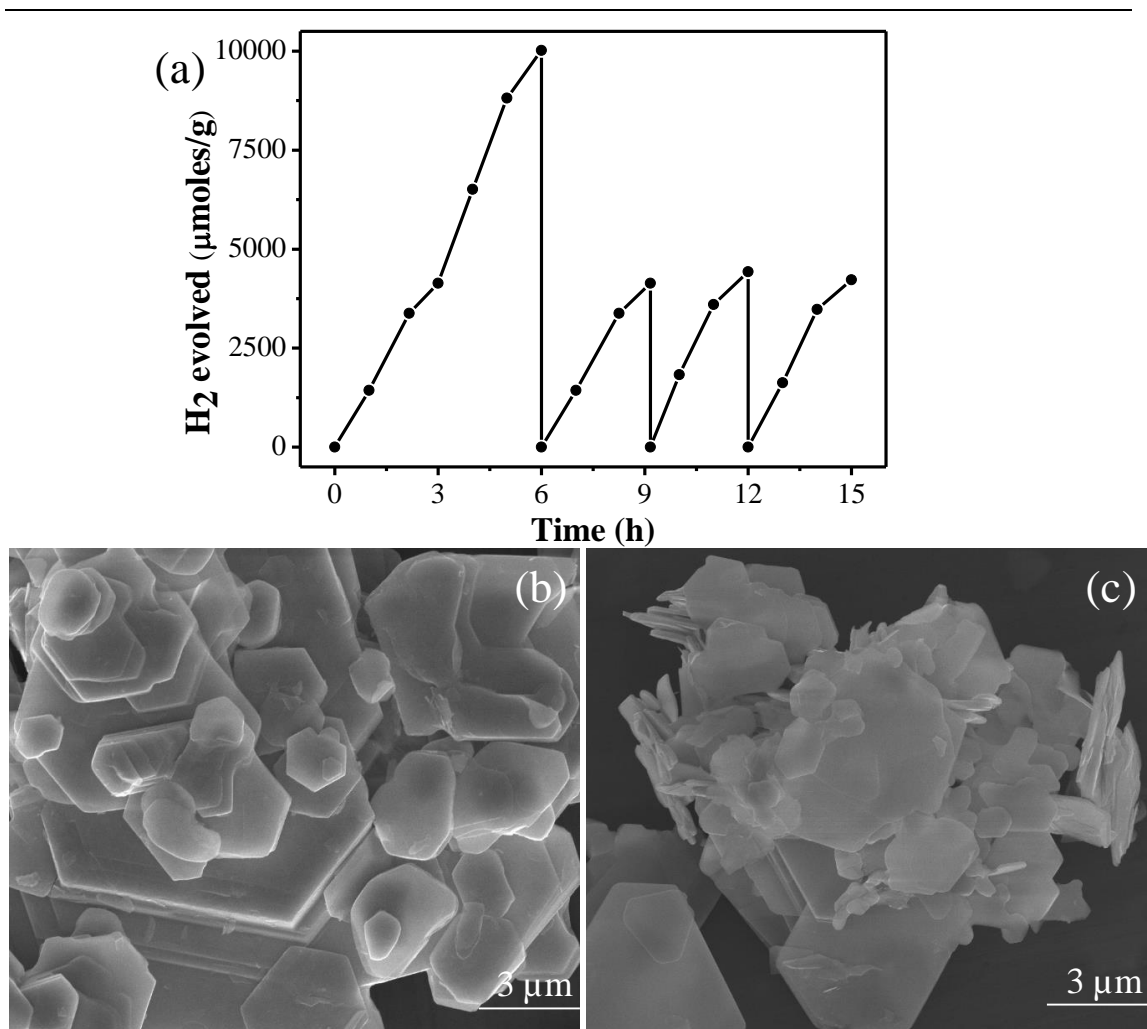
Figure 7. *The cyclic study of photocatalytic HER on $WS_{1.0}Se_{1.0}$ dye was added after every three hours. The SEM images (a) before and (b) after photocatalytic HER. The morphology is unchanged after the cycling studies.*

5. Conclusions

In summary, we have synthesized layered binary solid solutions of WS_2 and WSe_2 by a sealed tube reaction and characterized them appropriately. Visible-light dye-induced photocatalytic study indicates higher hydrogen evolution studied in $WS_{2-x}Se_{2x}$ compared to the parent binary counterparts showing maximum yield at the WSSe. The result suggests a synergistic effect of substitution of Se in the HER activity of the solid solutions.

6. References

1. M. Chhowalla, H. S. Shin and G. Eda, L. Li, K. P. Loh, H. Zhang, Nat. Chem., 2013, 5, 63.

2. C. N. R. Rao, U. Maitra and U.V. Waghmare, Chem. Phys. Lett., 2014, 609, 172.

3. C. N. R. Rao, H.S.S. R. Matte and U. Maitra, Angew. Chem. Int. Ed., 2013, 52, 13162.

4. C. N. R. Rao and U. Maitra, Annu. Rev. Mater. Res., 2015, 45, 29.

5. B. Radisavljevic, A. Radenovic, J. Brivio, V. Giacometti and A. Kis, Nat. Nanotechnol., 2011, 6, 147.

6. D. J. Late, B. Liu, H. S. S. R. Matte, V. P. Dravid and C. N. R. Rao, ACS Nano, 2012, 6, 5635.

7. J. Chen, X.-J. Wu, L. Yin, B. Li, X. Hong, Z. Fan, B. Chen, C. Xue and H. Zhang, Angew. Chem., Int. Ed., 2015, 127, 1226.

8. U. Maitra, U. Gupta, M. De, R. Datta, A. Govindaraj, C. N. R. Rao, Angew. Chem. Int. Ed., 2013, 52, 13057.

9. U. Gupta, B. S. Naidu, U. Maitra, A. Singh, S. N. Shirodkar, U. V. Waghmare, C. N. R. Rao, APL Mater., 2014, 2, 092802.

10. D. J. Late, Y.K. Huang, B. Liu, J. Acharya, S. N. Shirodkar, J. Luo, A. Yan, D. Charles, U. V. Waghmare, V. P. Dravid, C. N. R. Rao, ACS Nano, 2013, 7, 4879.

11. J. V. Lauritsen, J. Kibsgaard, S. Helveg, H. Topsoe, B. S. Clausen, E. Laegsgaard, F. Besenbacher,Nat. Nanotechnol., 2007, 2, 53 ;

12. T. F. Jaramillo, K. P. Jørgensen, J. Bonde, J. H. Nielsen, S. Horch, I. Chorkendorff, Science, 2007, 317, 100.

13. A.Y.S. Eng, A. Ambrosi, Z.Sofer, P. Simek, M. Pumera, ACS Nano, 2014, 8, 12185.

14. J. Xie, J. Zhang, S. Li, F. Grote, X. Zhang, H. Zhang, R. Wang, Y. Lei, B. Pan, Y. Xie, J. Am. Chem. Soc., 2013, 135, 17881.

15. N. Liu, P. Kim, J. H. Kim, J. H. Ye, S. Kim, C. J. Lee, ACS Nano, 2014, 8, 6902.

16. M. S. Faber, S. Jin, Energy Environ. Sci., 2014, 7, 3519.

17.   M. Chettri, U. Gupta, L. Yadgarov, R. Rosentveig, R. Tenne, C.N.R Rao, Dalton Trans., 2015, 44, 16399.

18.   D. Merki, H. Vrubel, L. Rovelli, S. Fierro, X. Hu, Chem. Sci., 2012, 3, 2515.

19.   V. Kiran, D. Mukherjee, R. N. Jenjeti, S. Sampath, Nanoscale, 2014, 6, 12856.

20.   C. Xu, S. Peng, C. Tan, H. Ang, H. Tan, H. Zhang, Q. Yan, J. Mater. Chem. A, 2014, 2, 5597.

21.   X. Zhang, F. Meng, S. Mao, Q. Ding, M. J. Shearer, M. S. Faber, J. Chen, R. J. Hamers, S. Jin, Energy Environ. Sci., 2015, 8, 862.

22.   C. Cong, J. Shang, X. Wu, B. Cao, N. Peimyoo, C. Qiu, L. Sun, T. Yu, Adv. Opt. Mater., 2014, 2, 131.

23.   A. Berkdemir, H. R. Gutierrez, A. R. Botello-Mendez, Nestor PereaLopez, A. L. Elias, C-I Chia, B. Wang, V. H. Crespi, F. Lopez-Urias, J-C Charlier, H. Terrones, M. Terrones, Sci. Rep., 2013, 3, 1755.

24.   A. L. Elias, N. Perea-Lopez, A. Castro-Beltran, A. Berkdemir, R. Lv, S. Feng, A. D. Long, T. Hayashi, Y. A. Kim, M. Endo, H. R. Gutierrez, N. R. Pradhan, L. Balicas, T. E. Mallouk, F. Lopez-Urias, H. Terrones, M. Terrones, ACS Nano, 2013, 7, 5235.

25.   K. Nakamura, M. Fujitsuka, M. Kitajima, Phys. Rev. B, 1990, 41, 12260.

26.   G. Gouadec , P. Colomban ,Prog. Cryst. Growth Charact. Mater., 2007, 53, 1.

27.   D. Voiry , M. Salehi , R. Silva , T. Fujita , M. Chen , T. Asefa , V. B. Shenoy , G. Eda , M. Chhowalla ,Nano Lett., 2013, 13, 222.

28.   G. A. Somorjai, Topics Catal., 2002, 18, 158.

29.   F. Wang, J. Li, F. Wang, T. K. A. Shifa, Z. Cheng, Z. Wang, K. Xu, X. Zhan, Q. Wang, Y. Huang, C. Jiang, J. He, Adv. Funct. Mater., 2015, 25, 6077.

30.   K. Xu, F. Wang, Z. Wang, X. Zhan, Q. Wang, Z. Cheng, M. Safdar, J. He, ACS Nano, 2014, 8, 8468.

31.   Q. Fu, L. Yang, W. Wang, A. Han, J. Huang, P. Du, Z. Fan, J. Zhang and B. Xiang, Adv. Mater., 2015, 27, 4732.

Visible-light-induced hydrogen evolution reaction by nanocomposites of few-layer TiS₂ and TaS₂ with CdS nanoparticles*

Summary

Graphene analogues of TaS_2 and TiS_2 (3-4 layers) have been characterized and their photochemical hydrogen evolution properties examined. Theoretical calculations reveal that both naturally abundant forms of TaS_2 and TiS_2 are not good catalysts on their own but can assist photocatalysis due to conducting properties. Nanocomposites of CdS nanoparticles with few-layer TiS_2 and TaS_2 have been investigated for visible-light-induced H_2 evolution reaction (HER). Benzyl alcohol was used as the sacrificial electron donor, which gets oxidized to benzaldehyde during the reaction. Few-layer TiS_2 is a semiconductor with a band gap of 0.7 eV and its nanocomposites with CdS shows an activity of 1.0 mmol g^{-1} h^{-1}. The nanocomposite of few-layer TaS_2, on the other hand, gives rise to higher activity of 2.320 mmol g^{-1} h^{-1}. The higher activity is attributed to the metallic nature of the few-layer TaS_2. The amount of hydrogen evolved after 20 hours in the case of CdS/TiS_2 and CdS/TaS_2 was 14.8 mmol and 28.1 mmol respectively after 16 hours with turn over frequencies of 0.24 h^{-1} and 0.57 h^{-1} respectively.
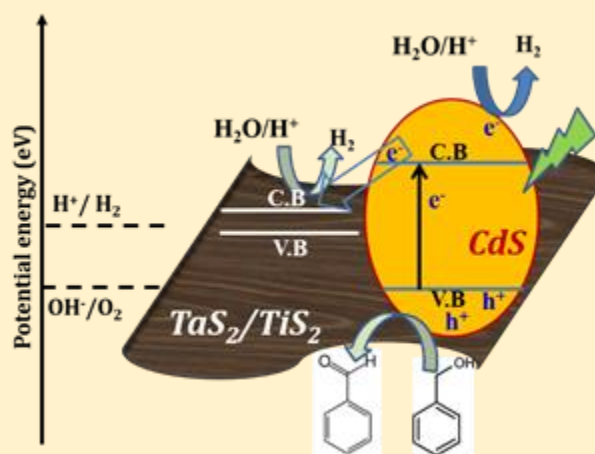
1. Introduction

Artificial photosynthesis has emerged as a potential means of splitting water for the generation of H_2. Of the various strategies employed for this purpose, dye sensitization and use of semiconducting nanostructures or their heterostructures are some of the most explored ones. TiO_2 was the first used photocatalyst for H_2 generation from water [1]. Since then various photocatalysts, especially oxides, have been used for the generation of H_2 from water, either photocatalytically or photoelectrochemically [2-3]. Though oxide photocatalysts are highly stable with respect to sulfides and nitrides and do not undergo oxidation or reduction during the processes of water splitting, they have an intrinsic limitation due to a highly positive valence band (O 2p). It is, therefore, difficult to find oxide semiconductors with a sufficiently negative conduction band (with respect to water reduction potential) to reduce H_2O to H_2, at the same time having a sufficiently small band gap to absorb visible light [4-5]. Metal sulfides and selenides, on the other hand, generally possess a low energy positive valence band and are visible-light-active. Sulfides and selenides of Cd possess a sufficiently negative conduction band to reduce protons to H_2 and can be used for the photocatalytic hydrogen evolution reaction (HER) [6-11].

CdS is a n-type semiconductor with a band gap of 2.4 eV and is suitable for HER due to the fact that it shows high activity in almost the entire visible range (up to 600 nm) [12] and has a negative flat band potential [13]. CdS alone is, however, less active in photocatalytic H_2 production due

to high charge recombination and degradation of the catalyst during the reaction [14]. In the presence of co-catalysts such as Pt and Pd, it shows good photocatalytic activity [15-16] and the challenge that we face today is to develop cost-effective catalysts and co-catalysts comprising non-noble metals. Numerous efforts have been made to replace noble metals with low-cost co-catalysts. Cost-effective substitutes for the co-catalysts would require materials which are metallic or highly conducting like graphene [17-23] to allow easy transfer of electrons to water thus enhancing water splitting.

Transition metal dichalcogenides (TMDs) exhibit a range of electronic properties, from semiconducting TiS$_2$ to metallic TaS$_2$ and can offer the possibility of replacing noble metals as co-catalysts. In this chapter, we report the role of co-catalysts with metallic (TaS$_2$) and semiconducting (TiS$_2$) TMDs with the aid of photocatalytically active CdS. We have synthesized composites of CdS with TMDs and studied the HER activity in the presence of sacrificial agents. We observe that metallic TaS$_2$ exhibits higher HER with CdS as compared to semiconducting TiS$_2$.

2. Scope of the present investigations

Most of the transition metal dichalcogenides are indirect or low bandgap semiconductors and therefore cannot be used as the stand-alone material. They need to be assisted either by a dye or a semiconductor. Composites with CdS gives us opportunities to explore HER activities of these compounds. These metallic dichalcogenides have high in-plane conductivities and can be used for separation of photogenerated charge

carriers. TiS_2 being a semiconducting layer structure, while TaS_2 is metallic helps to understand the role of the co-catalyst in charge separation of photogenerated charge carriers and its effect on the HER.

3. Experimental section

3.1 Synthesis

3.1.1 Exfoliation of TiS₂ and TaS₂: TiS_2 was prepared by using sealed tube method. In a typical experiment, Ti metal powder was ground with sulfur powder, and the homogeneous powder was filled in a quartz tube and heated in a box furnace at 800 °C for 72 hours. TaS_2 sample used for all the experiments was procured commercially (Alfa Aesar 99.8% metal basis).

Bulk TiS_2 and TaS_2 were exfoliated by solvent induced exfoliation in N-Methyl-2-pyrrolidone (NMP). To 1g of metal disulfide (TaS_2 and TiS_2), 50 ml of NMP was added and was sonicated for 10 hours. The supernatant was then removed periodically. The supernatant has few-layers samples. The suspension was centrifuged and the solid product collected.

3.1.2 Synthesis of nanocomposites of few-layer TiS₂ and TaS₂ with CdS:

CdS nanoparticles were prepared by adding 0.1mM (10 mL) of sodium sulfide into 0.1mM (10 mL) of cadmium acetate under stirring; the precipitate formed was centrifuged and dried at 60 °C. 10 mg of TiS_2 or TaS_2 was dispersed in water (10mL) by sonication for one hour. 0.1 mM of $Cd(CH_3COO)_2$ (CdS/Ti(Ta)S_2 = 1.4:1.0) was added to the above dispersion, and the mixture was stirred for eight hours, followed by addition of 0.1 mM

of Na$_2$S in 10 ml water. Yellow CdS particles were obtained as the final product was centrifuged and dried in air at 60 ℃ for 12 hours. To prepare nanocomposite with different mass ratios of the CdS/TaS$_2$ (0.7:1.0, 1.4:1.0 and 2.1:1.0 of CdS/TaS$_2$) required amounts of Cd(CH$_3$COO)$_2$ were added to 10 mg of TaS$_2$ in 10 mL of water.

3.2 Characterization

All the samples were characterized by using powder X-ray diffractometer (Bruker D8 Advance, Cu Kα source, λ = 1.541 Å). Transmission electron microscope (TEM) images were obtained by using a JEOL TEM 3010 instrument fitted with a Gatan CCD camera operating at an accelerating voltage of 300 kV. Atomic force microscopic (AFM) measurements were performed using an Innova atomic force microscope. Electronic absorption spectra were recorded on a Perkin–Elmer Lambda 650 UV/Vis Spectrometer. Raman spectra of samples were recorded by using a 632 nm He-Ne laser on a Jobin Yvon LabRam HR spectrometer. Surface area measurement of few-layer samples was done by using Quantachrome Autosorb instrument at 77K.

3.1.1 Conductivity measurements: Conductivity measurements were done using 6 μm gap gold electrodes on SiO$_2$/Si substrates. The device characteristics were measured using a Keithley 4200 semiconductor characterization system.

3.3 Hydrogen evolution measurements

Photocatalytic activities of the CdS/TaS$_2$ (TiS$_2$) nanocomposites were evaluated by the generation of hydrogen in the presence of benzyl alcohol

in acetic acid as sacrificial agents under visible light irradiation. In a typical photocatalytic study, 2.5 mg of the photocatalyst was dispersed in a 50ml of water. 2ml of benzyl alcohol was dissolved in 5ml of acetic acid. It was then added to the dispersion, of catalyst and water, in a cylindrical quartz cell with flat surfaces being exposed to light. The solution was purged with N_2 for 30 min prior to activity tests to remove all dissolved gases and to maintain an inert atmosphere. The solution was exposed to light using 450 W Xe arc lamp (working at 400 W) (New Port, 6280) fitted with water filter and 399 nm cut-off filter. The H_2 evolved was quantified using gas chromatography (Perkin Elmer, Clarus 580 GC) equipped with TCD detector by manually injecting 1 ml of evolved gases from the headspace of the quartz vessel after every 1 h. A similar experiment was performed using 0.1M Na_2S and 0.1M Na_2SO_3 as a sacrificial reagent.

Turn over frequency (TOF) and turn over number (TON) was calculated as follows:

$$TOF\ (h^{-1})\ = (Activity\ of\ the\ catalyst)/(Moles\ of\ the\ catalyst\ used)\ (1)$$

4. Results and discussion

4.1 Synthesis and characterization

The phase purity of the as-synthesized and exfoliated TiS_2 samples was confirmed by x-ray diffraction (XRD). The bulk samples were exfoliated via solvent induced method in N-Methyl-2-pyrrolidone (NMP). The exfoliated samples where characterized and compared with their bulk. In the XRD pattern of exfoliated TiS_2, the intensity of the reflection

corresponding to stacking direction (001) was considerably lower, and line-widths were larger **(Figure 1a)**. A similar change was observed for TaS$_2$ when we exfoliated it from bulk to few-layers **(Figure 1b)**. The peaks in stacking direction are reduced in relative intensity.
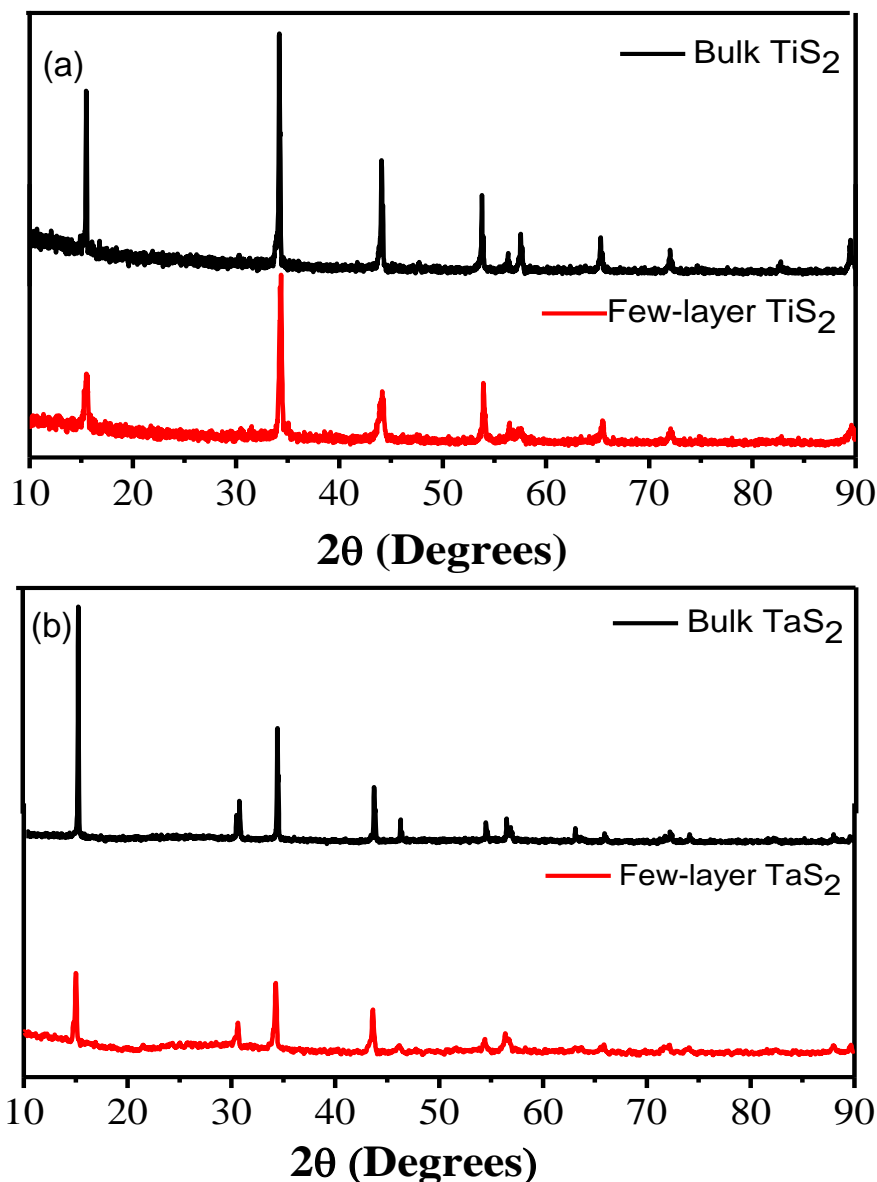
Figure 1. *Comparison of X-Ray diffraction between bulk and exfoliated few-layers (a) TiS$_2$ and (b) TaS$_2$.*

The A$_{1g}$ band in Raman spectrum (~330 cm^{-1}) of few-layer TiS$_2$ **(Figure 2a)** shows a redshift of 4 cm^{-1} of the A$_{1g}$ mode compared to the bulk sample. We observe that in few-layers TaS$_2$ there is a slight shift as compared to

bulk. As the number of layers decreases, the restoring forces decrease causing a softening and broadening of the in-plane A_{1g} mode [24].
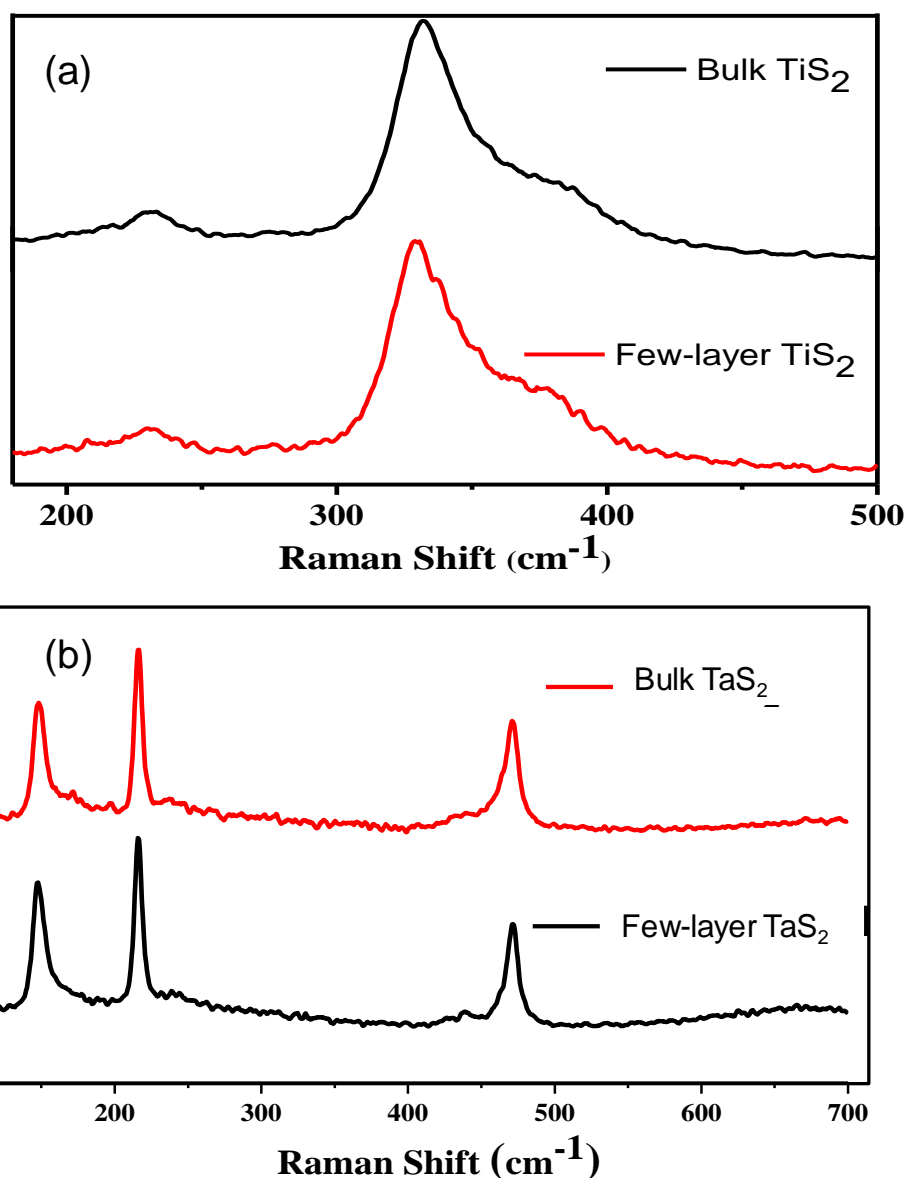
Figure 2. *Comparison of Raman spectra between bulk and exfoliated few-layers (a) TiS_2 and (b) TaS_2. We observe a slight shift in their few-layer samples compared to bulk samples due to softening of bands.*

The few layer samples were further characterized by using AFM and TEM. In **Figure 3a**, we show a TEM image of the few-layer TiS_2 obtained after exfoliation of the Li intercalated material. **Figure 3b** shows the

AFM image and the corresponding height profile of few-layer TiS$_2$. The height profile gives a layer thickness of 3.0 nm corresponding to 4 layers, with a lateral dimension of 1.5 μm. A TEM image of exfoliated TaS$_2$ is shown in **Figure 3c** and the AFM image in **Figure 3d**. The AFM height profile of the few-layer TaS2 has a layer thickness of 2.6 nm corresponding to 3 layers, with a lateral dimension of 2.5 μm.

Figure 3. *(a) TEM and (b) AFM images of few-layer TiS$_2$ (c) TEM and (d) AFM images of few-layer TaS$_2$ both prepared by liquid phase induced exfoliation.*

Figure 4 gives surface areas of 48 m^2/g and 21 m^2/g respectively for few-layer TiS$_2$ and TaS$_2$. TaS$_2$ shows type II adsorption isotherm this

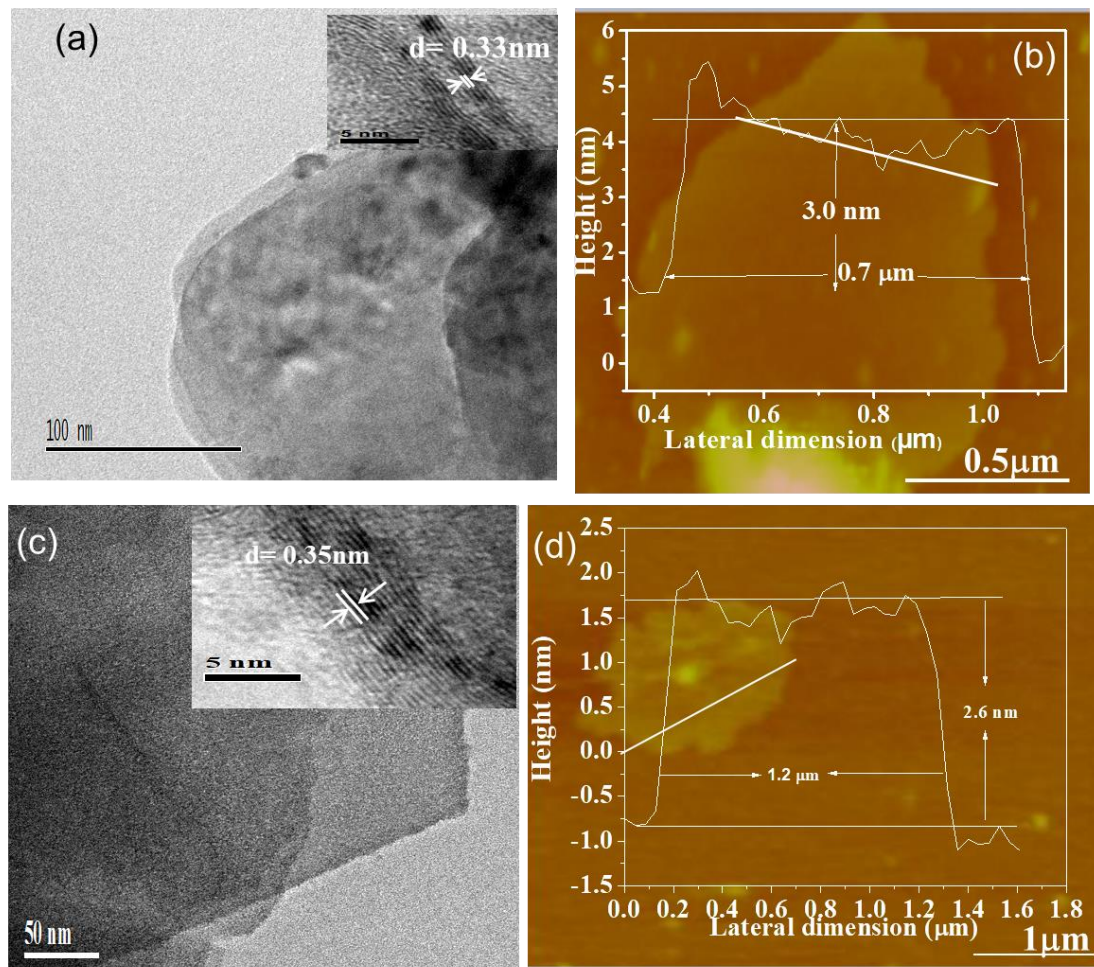signifying unrestricted monolayer-multilayer adsorption. Beyond p/p_0 of 0.025 (the beginning of the almost linear middle section of the isotherm), we see evidence of completion of monolayer coverage and initiation of multilayer adsorption. TiS_2, on the other hand, shows type IV adsorption isotherm, with a hysteresis loop near 0.45 relative pressure, associated with capillary condensation taking place in the mesopores, and the limiting uptake over a range of high p/p_o. The initial part of the isotherm shows Type II behavior [25].
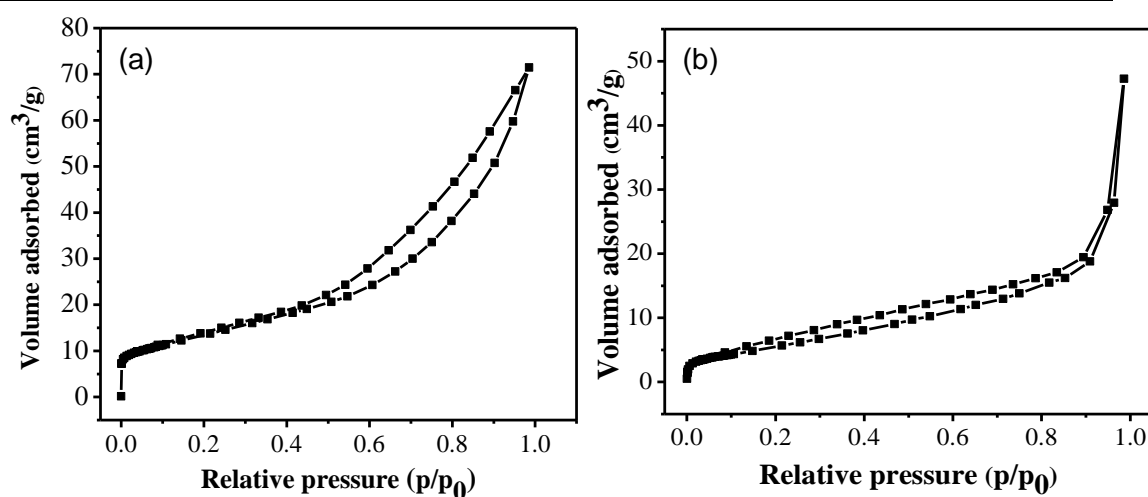
Figure 4. *N_2 adsorption isotherm of few-layer **(a)** TiS_2 and **(b)** TaS_2 recorded at 77K.*

Conductivity measurements of bulk and few-layer samples of TiS_2 and TaS_2 were carried out on 6 μm gap gold electrodes on SiO_2/Si substrates **(Figures 5 a and b)**. **Figure 6** shows the I vs. V plots of few-layer TiS_2 in comparison with that of TaS_2. While the current vs. voltage plot changes from linear to non-ohmic behavior on the reduction of the bulk to few-layers in the case of TiS_2 [26], few-layer TaS_2 remains Ohmic even in the few-layer samples [27-28].
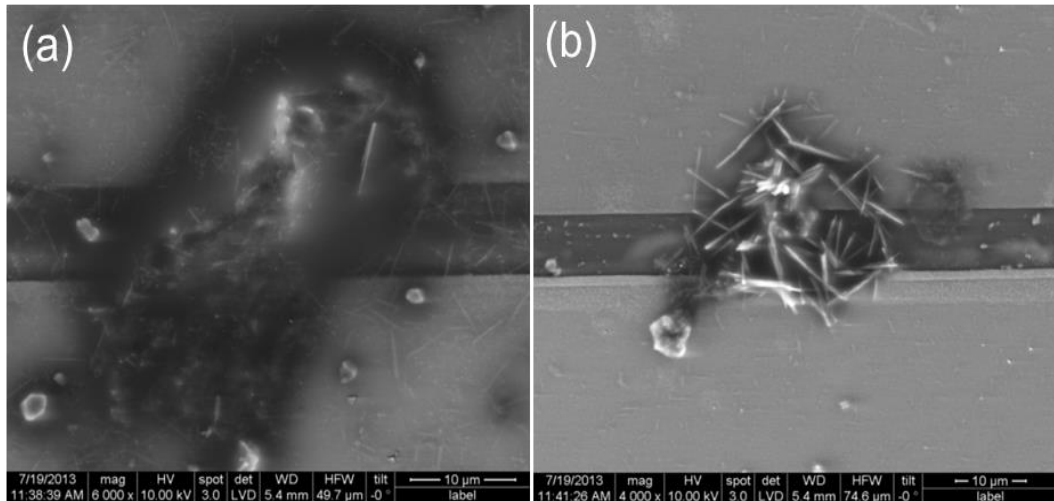
Figure 5. *FESEM images of (a) few-layer TiS$_2$ and (b) few-layer TaS$_2$ at gap electrode at gap electrode.*
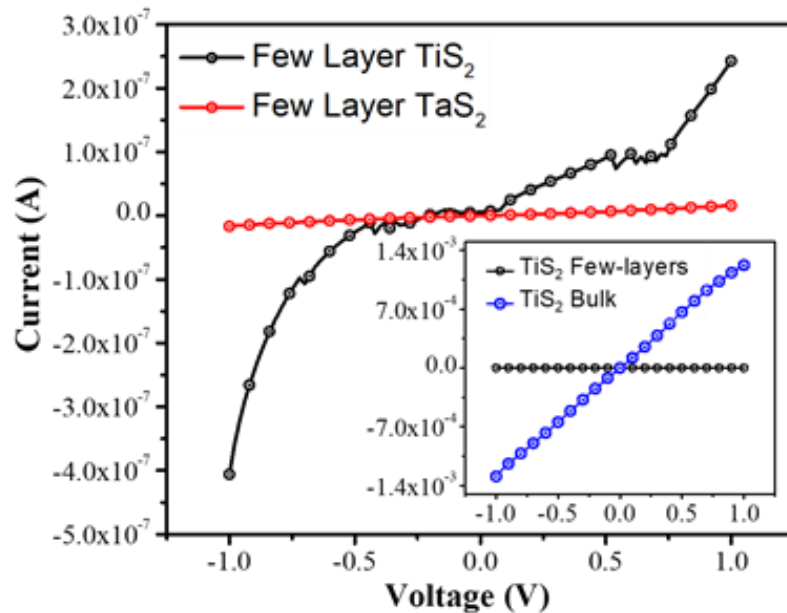
Figure 6. *Current versus voltage plots of few-layer TiS$_2$ and TaS$_2$. The inset shows current versus voltage plots for bulk and few-layer TiS$_2$*

Theoretical calculations do suggest bulk TiS$_2$ is to be semi-metallic while the few-layer material is semiconducting. The surface layer has an electronic structure similar to that of a semiconductor with a small energy gap of 0.7 eV. The semiconducting nature decreases (metallicity increases) as the number of layers increases from few-layers to that of bulk [26].
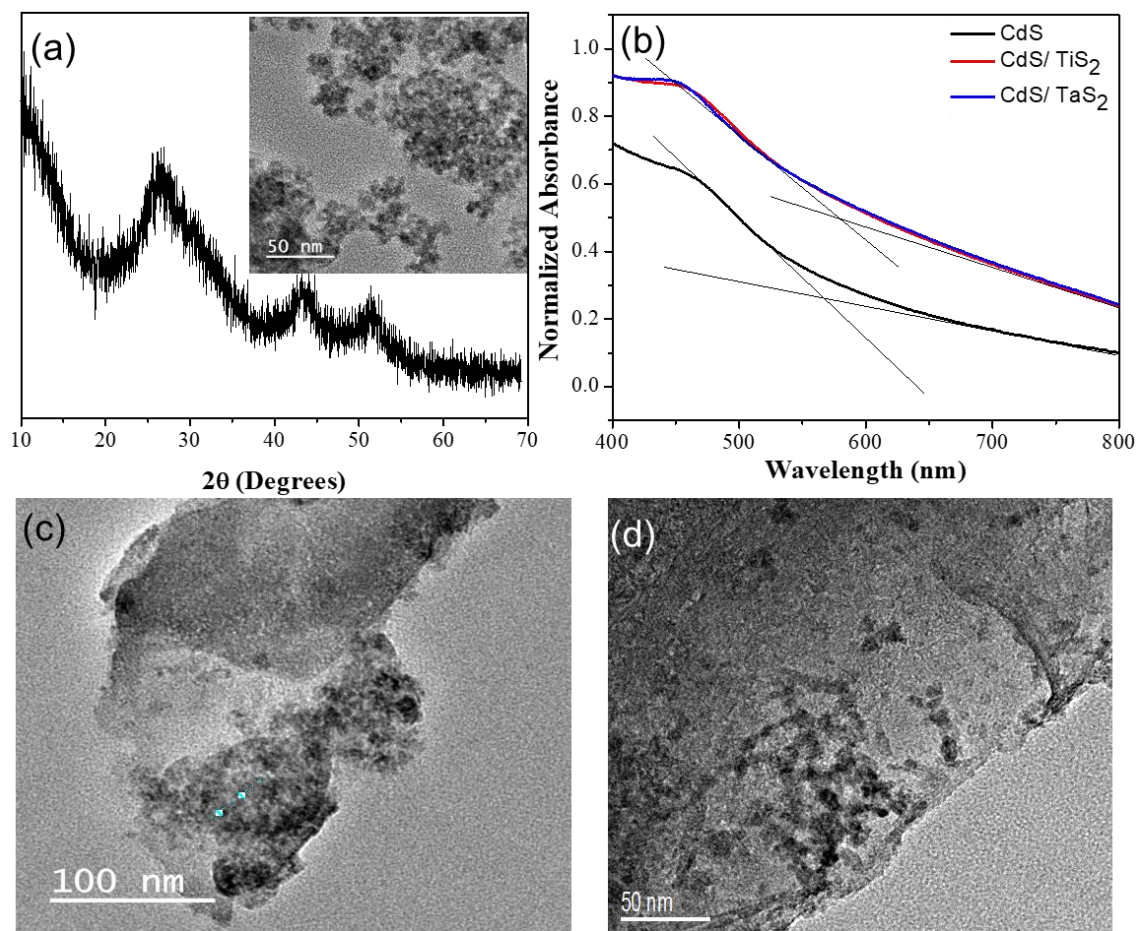
Figure 7. *(a) XRD pattern of CdS nanoparticles. Inset in (a) shows a TEM image of CdS nanoparticles. (b) Diffused reflectance absorbance spectra of these composites. (c) TEM image of the nanocomposite of CdS with TiS$_2$ (CdS: TiS$_2$=1.4:1.0) and TaS$_2$ (CdS: TaS$_2$=1.4:1.0).*

Figure. 7a gives the XRD pattern of as-prepared CdS. Broad reflections in the x-ray pattern confirm the presence of small particles. The TEM image of the CdS nanoparticles, shown in the inset of **Figure 7a** reveals the presence of 5-12 nm nanoparticles. The diffused reflectance spectra of these composites show that there is negligible red-shift in the absorbance in the composites. TEM images of the composites of CdS/TiS$_2$ and CdS/ TaS$_2$ in **Figure 7 c and d** show the dispersion of CdS nanoparticles on the two-dimensional sheets.

4.2 Hydrogen evolution studies

We have carried out H$_2$ evolution studies using few-layer TaS$_2$ and TiS$_2$ as co-catalysts for CdS, by using the nanocomposites of TaS$_2$ and TiS$_2$ with CdS nanoparticles. The role of benzyl alcohol as a sacrificial agent in enhancing photocatalytic H$_2$ evolution has been described by Rao et al. [29] Benzyl alcohol gets converted to benzaldehyde, while acting as hole scavenger and thereby minimizing electron-hole recombination. CdS nanoparticles alone show an activity of 0.34 mmol g^{-1} h^{-1} with TOF of 0.05 h^{-1} **(Figure 8a)**.

Figure 8. *H$_2$ evolution activity of (a) CdS nanoparticles, (b) CdS/TiS$_2$ (1.4:1.0) nanocomposite and (c) CdS/TaS$_2$ (1.4:1.0) nanocomposite. (d) Comparison of HER activities of individual samples with the composites.*

The amount of H_2 evolved after 8 hours for 2.5mg catalyst was 7.2 µmol. CdS do not show any activity in acetic acid, but the acid inhibits photocorrosion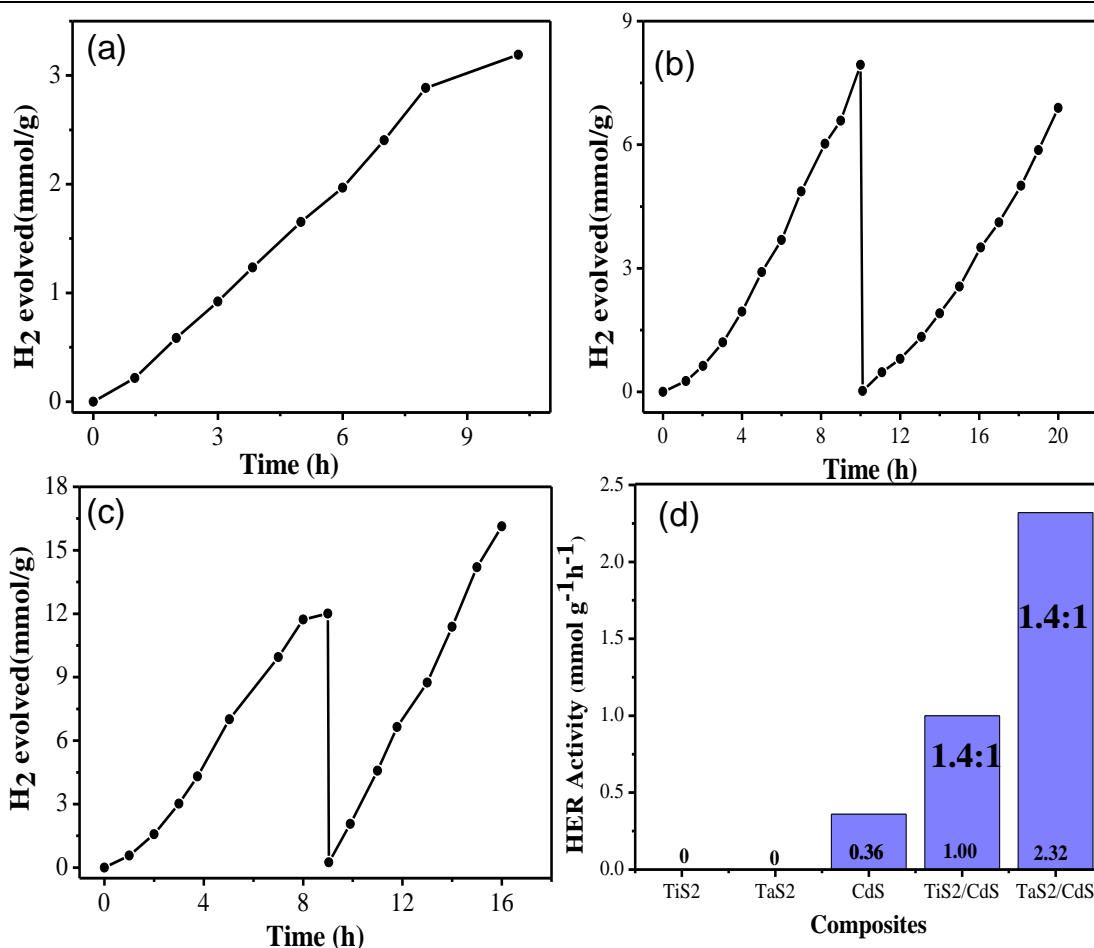 of CdS [30]. We studied HER activity at dilute concentrations (2.5 mg/ 50 ml of water) to enhance the total absorption of light by the catalyst. Being a low bandgap semiconductor, TiS_2 alone does not show any HER. However, on coupling with CdS, it increases the activity of CdS from 0.34 to 1000 µmol g^{-1} h^{-1} as shown in **Figure 8b**. The TOF increases from 0.05 h^{-1} to 0.24 h^{-1}, a five-fold increase for CdS/TiS_2. The total amount of H_2 evolved after 20 hours by 2.5 mg of the composite is 37.2 µmol. Clearly, few-layer TiS_2 aids electron transport from CdS to water. The electron transfer probability becomes considerably higher by the use of metallic TaS_2 in place of semiconducting TiS_2. The hydrogen evolution activity of the CdS/TaS_2 nanocomposite is shown in **Figure 8c** While TaS_2 alone does not show any activity by itself, CdS/TaS_2 has as an activity of 1.73 mmol g^{-1} h^{-1}, with a TOF of 0.43 h^{-1}. Note that the activity has increased almost 8 fold after 8 hours. Interestingly, the activity of the composite increases with further cycling to 2.320 mmol g^{-1} h^{-1} with a nearly 11-fold increase in the activity as compared to CdS a TOF as 0.57 h^{-1}. This could possibly arise due to further oxidation of benzaldehyde. The total amount of H_2 evolved after 16 hours for 2.5mg was 70.5 µmol. The comparison of HER activities and with composites and parent compound is shown in **Figure 8d**. Since the conduction band minimum (CBM) of CdS is above the conduction band of TiS_2, the interface between the two allows electron transfer from the CBM of CdS to that of TiS_2, thereby allowing electron-

hole separation. Furthermore, the CB level of TiS$_2$ is slightly more negative than the water reduction potential and aids H$_2$ evolution **(Figure 9)**. TaS$_2$ favors electron-hole separation by taking away the electron generated on the surface of CdS nanoparticles just as nanoparticles of Pt, Pd, Rh and such metals. From the electronic structure of TaS$_2$, we see that the, e$_g$ orbitals in the 5d conduction band lie close to the Fermi level [27], making it suitable for the hydrogen evolution reaction. Conductivity measurements reveal the metallic nature of few-layer TaS$_2$ while few-layer TiS$_2$ is semiconducting, showing thereby why TaS$_2$ acts as a better co-catalyst for CdS than few-layer TiS$_2$. The determining factor is the ease of transfer of photogenerated electrons from CdS to the co-catalyst.
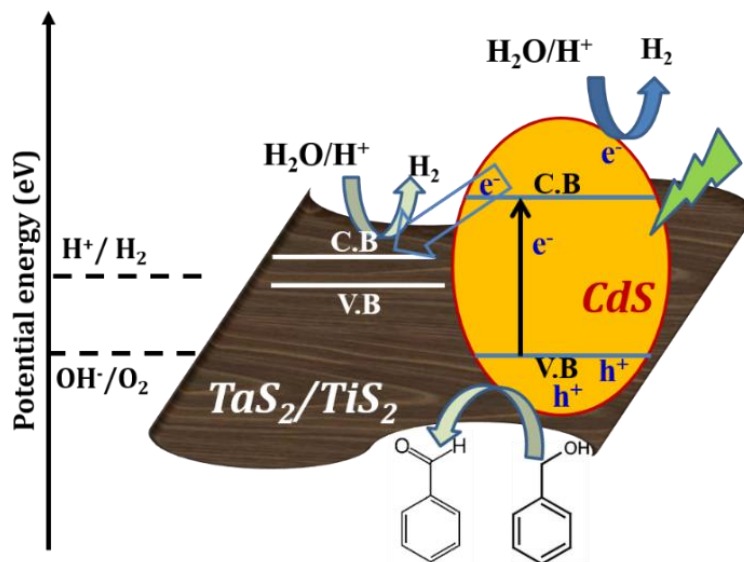

Figure 9. *Plausible mechanism visible light induced H$_2$ evolution on CdS/Ti(Ta)S$_2$ composites.*

We have studied the effect of changing the ratio of CdS to TaS$_2$ in the nanocomposite **(Figure 10)**. While TaS$_2$ alone does not show any activity, H$_2$ evolution increases with increasing ratio of CdS reaching a maximum

around a CdS: TaS$_2$ of 1.4:1.0 with the activity of 1.73 mmol h^{-1} g^{-1} with TOF 0.43 h^{-1}. For CdS: TaS$_2$ of 0.7:1.0 has an activity of 0.03 mmol h^{-1} g^{-1} with TOF is only 0.18 h^{-1} but is twice that of CdS: TaS$_2$ = 2.1:1.0 which exhibited the activity of 0.38 mmol h^{-1} g^{-1} and TOF of 0.08 h^{-1}. The activity is low for more TaS$_2$ composite due to the shielding effect of black TaS$_2$ samples which inhibits light absorption; it reaches a synergistic value at ratio 1.4:1.0 and decreases when CdS amount increases due to lack of interaction between the two components. This observation demonstrates the role of TaS$_2$ in enhancing the activity of CdS.
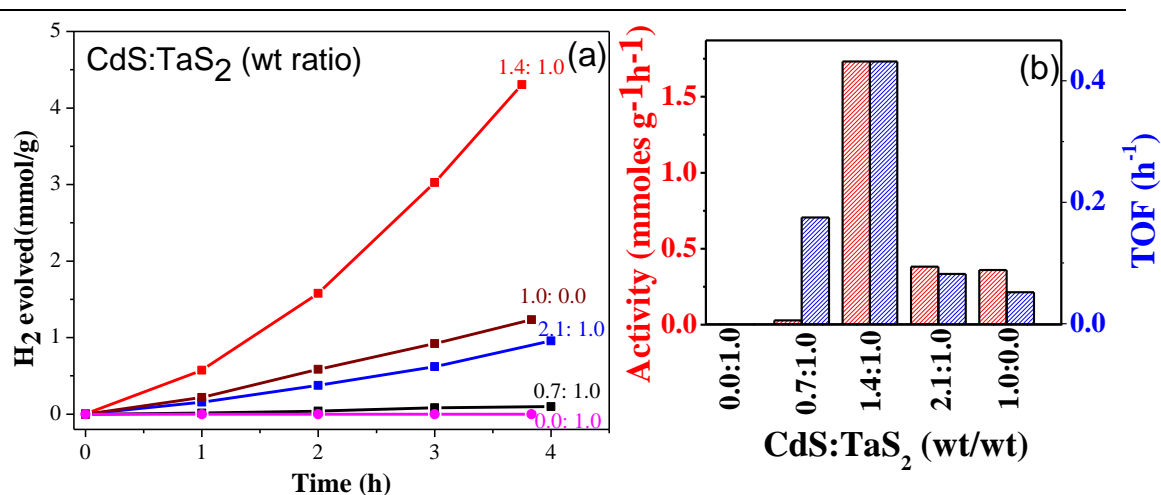
Figure 10. *Time course of H$_2$ evolution activity of TaS$_2$, CdS and their composites with different weight ratios (0.7: 1.0, 1.4:10 and 2.1:1.0). The histogram compares the activity of H$_2$ evolution and TOF values for CdS/TaS$_2$ composites with different weight ratios.*

In Table 1, we compare the results reported in the literature on CdS-based catalysts with the results of the present study. The activity of CdS/Pt in UV light is generally higher than with visible light as in the present study, and the visible light activity of CdS/Pt composite is generally small in most cases [31-34]. We see the present results on CdS/TaS$_2$, and CdS/TiS$_2$

compare favorably in HER activity with other materials reported in the literature including CdS/NiS and CdS/N-graphene [35].

Table 1. The comparative result of photocatalytic HER of CdS/cocatalyst systems of the composite

Composite	Sacrificial Agent & (wt of catalyst used/ water)	Activity (mmole g^{-1} h^{-1})	TOF (h^{-1})
CdS[a]	2ml Benzyl alcohol,(2.5 mg/50ml)	0.34	0.05
CdS/TiS_2[a]	2ml Benzyl alcohol, (2.5 mg/50ml)	1.0	0.24
CdS/TaS_2[a]	2ml Benzyl alcohol, (2.5 mg/50ml)	2.3	0.57
CdS/Pt[17,b]	0.35M Na_2SO_3 and 0.25M Na_2S (50mg/80ml)	0.72	0.12
CdS/Pt [19,b]	0.1 M Na_2S and 0.1 M Na_2SO_3 (100mg/100ml)	0.40	0.06
CdS/N-Graphene [18,b]	0.1M Na_2S and 0.1M Na_2SO_3 (200mg/300ml)	1.05	0.16
CdS/NiS[17,b]	0.35M Na_2SO_3 and 0.25M Na_2S (50mg/80ml)	1.1	0.17
CdS/MoS_2[20,b]	10% (v/v) Lactic acid(100mg/200ml)	5.4	0.78

[a]400W Xe Lamp (λ >399nm) [b] 300W Xe Lamp (λ >420nm)

5. Conclusions

The present study reveals that few-layer TiS_2 having a band gap of 0.7 eV and few-layer TaS_2 which is metallic can both be employed as co-catalysts for CdS for HER, favoring H_2 evolution in the visible range. That TaS_2 is superior to TiS_2 in performance is related to metallic its nature.

The present results lend further support to the earlier work on H_2 evolution from metallic 1T-MoS_2 [36].

6. References

1. A. Fujishima and K. Honda, Nature, 1972, 238, 37.

2. R. Abe, J. of Photochem. Photobiol. C: Photochem. Rev., 2010, 11, 179.

3. A. Kudo and Y. Miseki, Chem. Soc. Rev., 2009,38, 253.

4. J. G. Yu, L. F. Qi, M. Jaroniec, J. Phys. Chem. C, 2010,114, 13118.

5. X. Chen, S. S. Mao, Chem. Rev., 2007, 107, 2891.

6. A. L. Linsebigler, G. Lu, J. T. Yates, Chem. Rev., 1995, 95, 735.

7. J. G. Yu, J. Zhang, S. W. Liu, J. Phys. Chem. C, 2010, 114, 13642.

8. J. G. Yu, J. Zhang, Dalton Trans., 2010, 39, 5860.

9. J. Zhang, J. G. Yu, M. Jaroniec, J. R. Gong, Nano Lett., 2012, 12, 4584.

10. J. G. Yu, B. Yang, B. Cheng, Nanoscale, 2012, 4, 2670.

11. Q. J. Xiang, J. G. Yu, M. Jaroniec, J. Am. Chem. Soc., 2012, 134, 6575.

12. S. Shen, L. Guo, X. Chen, F. Ren, S. S. Mao, Int. J. Hydrogen Energ., 2010, 35, 7110.

13. M. Matsumura, S. Furukawa, Y. Saho H. Tsubomura, J. Phys. Chem., 1985, 89, 1327.

14. D. J. Fermı́n, E.A. Ponomarev, L.M. Peter, J. Electroanal. Chem., 1999, 473, 192.

15. X. Zong, H. Yan, G. Wu, G. Ma, F. Wen, L. Wang, C. Li, J. Am. Chem. Soc., 2008, 130, 7176.

16. H. Yan, J. Yang, G. Ma, G. Wu, X. Zong, Z. Lei, J. Shi, C. Li, J. Catal, 2009, 266, 165.

17. Q. Li, B. Guo, J. Yu, J. Ran, B. Zhang, H. Yan and J. R. Gong, J. Am. Chem. Soc., 2011, 133, 10878.

18. Q. Xiang, J. Yu, M. Jaroniec, Chem. Soc. Rev., 2012, 41, 782.

19. Q. Xiang, J. Yu, J. Phys. Chem. Lett., 2013, 4, 753.

20. G. Xie, K. Zhang, H. Fang, B. Guo, R. Wang, H. Yan, L. Fang, J. R. Gong, Chem. Asian J., 2013, 8, 2395.

21. G. Xie, K. Zhang, B. Guo , Q. Liu , L. Fang , J. R. Gong, Adv. Mater. 2013, 25, 3820.

22. K. Zhang, L. Guo, Catal. Sci. Technol., 2013, 3, 1672.

23. Q. Xiang, J. Yu, M. Jaroniec, J. Phys. Chem. C, 2011, 115, 7355.

24. Yi Ding, Yanli Wang, Jun Ni, Lin Shi, Siqi Shi, Weihua Tang, Physica B, 2011, 406, 2254.

25. K. S. W. Sing, D.H. Everett, R. Haul, L. Moscou, R.A. Peirotti, J. Rouquerol, T.Siemieniewska, Pure Appl. Chem., 1982, 54, 2201.

26. C. M. Fang, R. A. de Groot, and C. Haas, Phys. Rev. B, 1977 ,56, 445.

27. R. A. Pollak, D. E. Eastman, F. J. Himpsel, P. Heimann, Phys. Rev. B, 1981, 24, 7435.

28. Q. Yan-Bin, L. Yan-Ling, Z. Guo-Hua, Chin. Phys., 2007, 16, 3809.

29. S. R. Lingampalli, U. K. Gautam, C. N. R. Rao, Energy Environ. Sci., 2013, 2013, 6, 3589.

30. J. Jin, J. Yu, G. Liu, P. K. Wong, J. Mater. Chem. A, 2013, 10927.

31. Q. Yan-Bin, L. Yan-Ling, Z. Guo-Hua, Chin. Phys., 2007, 16, 3809.

32. J. Zhang, S. Z. Qiao, L. Qi, J. Yu, Phys.Chem. Chem. Phys., 2013, 15, 12088.

33. L. Jia, D. Wang, Y. Huang, A. Xu, H. Yu, J. Phys. Chem. C, 2011, 115, 11466.

34. Y. Wang,Y. Wang, R. Xu, J. Phys. Chem. C, 2013, 117, 783.

35. X. Zong, G. Wu, H. Yan, G. Ma, J. Shi, F. Wen, L. Wang, C. Li, J. Phys. Chem. C, 2010, 114, 1963.

36. U. Maitra, U. Gupta, M. De, R. Datta, A. Govindaraj, and C. N. R. Rao, Angew. Chem. Int. Ed., 2013, 52, 13057.

Hydrogen evolution employing of layered gallium chalcogenides*

Summary

First-principles studies of the layer-dependent electronic structure and properties of gallium monochalcogenides, GaX where X = S, Se/ or Te, using GGA, LDA and HSE-06 functionals have shown that these materials can be used for water splitting. Layered GaTe is found to be a good catalyst in dye-sensitized hydrogen evolution reaction.
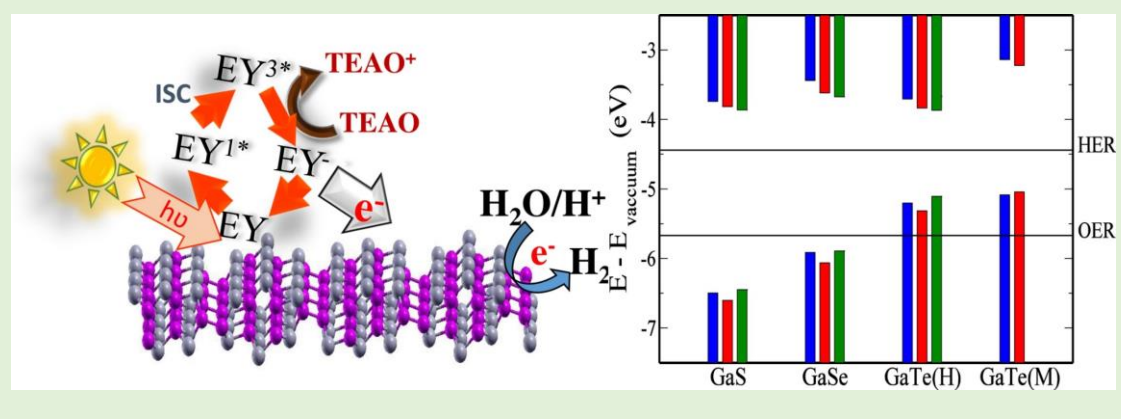
1. Introduction

Layer-dependent properties of 2D inorganic materials, especially transition metal dichalcogenides (TMDs) have been of vital interest in the last three to four years [1-4]. The property knows to have potential applications as well.
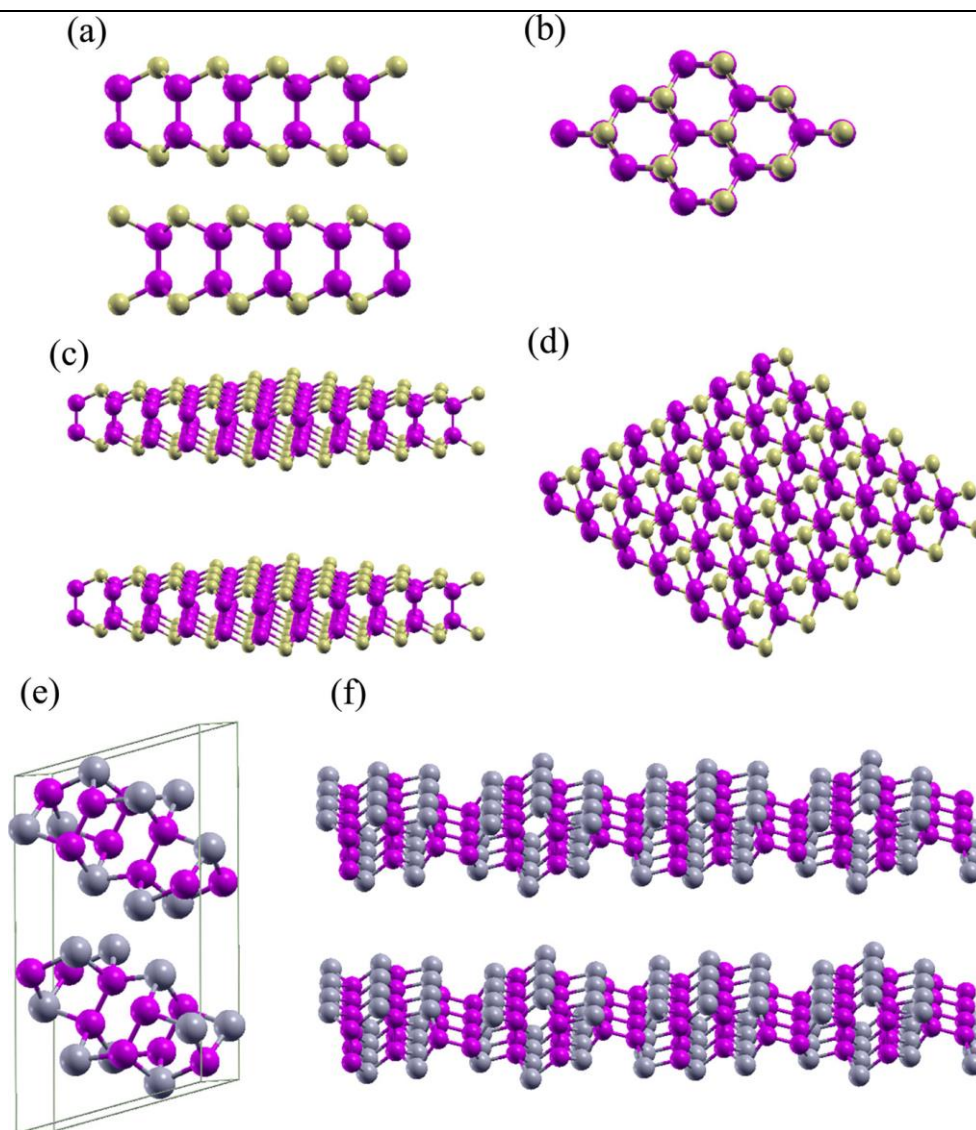

Figure 1. Structure of GaX, showing layers stacked on one another (a) side view and (b) top view of bulk; perspective views of (c) bulk and (d) monolayer hexagonal form; (e) bulk form and (f) stacking of layers of monoclinic GaTe. [Pink atoms represent Ga, yellow atoms represent X = S, Se or Te, grey atoms represent Te.]

Atomically thin layered 2D semiconductors of group III-VI (GaS, GaSe, GaTe and InSe) have received attention due to their 2D properties [5-9]. These materials may find applications in optoelectronics [6], non-linear optics [7] and terahertz devices [10]. All the three GaX materials (X= S, Se, Te) occur in layered hexagonal structures belonging to the $P6_3/mmc$ space group (No. 194), with each layer comprising of four X-Ga-Ga-X triangular lattice planes stacked along the c-axis **(Figure 1).** The primitive unit cell for the bulk structure of hexagonal GaX consists of two layers of X-Ga-Ga-X, containing 8 atoms per unit cell. GaTe also crystallizes in the monoclinic system belonging to the $C2/m$ space group (No. 12). Its unit cell consists of two layers containing 12 atoms each. In this structure, only two third of the Ga-Ga dimers are oriented perpendicular to the layers, while the remaining one third lie almost in the plane of the layer. The local coordination of hexagonal and monoclinic GaX are similar with the Ga atom coordinated to three X atoms and one Ga atom, while X atom coordinated to three Ga atoms.

The bulk mobilities of GaS and GaSe are ~80 and 215 cm^2 V^{-1} s^{-1} while those of few-layers is 0.1 and 0.6 cm^2 V^{-1} s^{-1} respectively exhibiting p-type characteristics [9-14]. These chalcogenides generally have a direct band gap slightly higher in energy with than indirect bandgap [6, 10]. In spite of the indirect band gap, few-layer of GaS and GaSe exhibit photoresponsivity of 2.8 AW^{-1} and 19.2 AW^{-1} respectively [15, 16]. Recently GaS is reported to split water photochemically [17]. In the high-temperature form of GaTe, the individual layers are held together by van

der Waals forces [18]. There are two types of Ga-Ga bonds two-thirds perpendicular and one-third parallel to the layer. Unlike GaS and GaSe, with indirect band gaps above 2.0 eV [19], bulk GaTe appears to have a direct band gap of 1.65 eV in bulk and as well as in single layer forms [20-22]. GaTe nanoflakes have been used for photodetection by Liu et al. with a photo-response of 10^4 A/W which is superior compared to MoS_2 and graphene [20]. A detectivity of ~10^{12} Jones is reported for GaTe nanosheets [22]. This suggests that GaTe may possess interesting photoelectronic and photocatalytic properties considering that single layers of other TMDs generally have direct band gaps. Additionally, GaTe nanosheets seem to possess high carrier mobility and long carrier lifetimes [23]. The present study includes photocatalytic hydrogen evolution from water and results of first-principles calculations of layer-dependent electronic structure and properties of GaTe.

2. Scope of the present investigations

In view of the exciting properties with potential applications in water splitting and other areas [23-26], we considered it essential to investigate layer- dependent electronic structure and properties of Gallium chalcogenides by carrying out first-principles calculations. Based on the theoretical calculations we carried out experimental photochemical hydrogen evolution for gallium chalcogenides and studied their properties.

3. Experimental section

3.1 Computational details

First-principles Density Functional Theoretical (DFT) calculations were performed to determine the electronic structure of layered gallium chalcogenides using Quantum Espresso package [27]. The exchange-correlation energy functional was approximated with a Generalized Gradient Approximation (GGA) with a parametrized form of Perdew, Burke, and Erzenhoff (PBE) [28]. Calculations were also performed using exchange-correlation functional approximated with a Local Density Approximation (LDA) with parametrization of Perdew and Wang (PW) [29]. The interactions between the ionic cores and valence electrons were represented using ultrasoft pseudopotentials for GGA and norm-conserving pseudopotentials for LDA calculations. Energy cutoffs of 50 Ry and 400 Ry were used to truncate the plane wave basis for representing wavefunctions and charge density respectively. In the case of norm-conserving pseudopotential, plane wave basis for representing wave functions was truncated with energy cut off of 60 Ry and charge density with a cutoff of 240 Ry. Since the band gaps are underestimated within GGA or LDA based DFT, HSE-06 hybrid functional was used to estimate band gaps accurately. Grimme term was used to capture the van der Waals interaction between the layers [30]. Integrations over the Brillouin-zone were sampled with a 12X12X1 uniform grid of k-points for hexagonal and 4X13X1 k-grid for monoclinic structures. A vacuum of 12 Å was used to keep the magnitude of interactions between periodic images low. Structures

were relaxed until the Hellman-Feynman force on each of the atoms was 0.01 eV/Åor less, and the unit cell parameters were relaxed until stresses were within 1 kbar.

3.2 Experimental details

3.2.1 Synthesis of GaTe(Se) crystals:

Ga and Te of 5N purity were loaded in a quartz tube at a pressure 10-5 Torr. The sealed quartz tube was placed in a vertical high-temperature furnace. The hot upper part and lower cooler part of the furnace was maintained at 1143 and 1108 K respectively. It was slowly heated till it attains the above melting point (>1208 K) required temperature. The ampoule was kept for 24 hrs to yield continuous mix. It was lower into the condensation zone at 1108 K at 1mm/hr. The ampoule was kept in condensation zone for one week and cooled to room temperature. The products obtained were single crystals of good quality. Similarly, GaSe crystals were synthesized with Se metals as Se-source. GaS crystals were procured from an external supplier.

3.2.2 Photocatalytic hydrogen evolution:

The bulk samples (GaTe, GaSe, and GaS) was dispersed in 15% v/v solution of triethanolamine in water in a cylindrical vessel. The sample was thoroughly purged with N_2, and 0.014 mm of Eosin Y dye was added to it. The hydrogen evolution studies were done with 100 W halogen lamp under constant stirring. The evolved gas analyzed over a period of time in Perkin Elmer 580C Clarus GC-TCD.

Turnover frequency (TOF) was calculated for each catalyst using the following equation,

$$TOF\ (h^{-1}) = \frac{Activity\ of\ the\ catalyst}{Moles\ of\ the\ catalyst\ used} \quad (1)$$

4. Results and discussion

4.1. Theoretical results

(Theoretical calculations were carried out by Dr. Sandhya U. Shenoy and Prof. U.V. Waghmare of the Theoretical Sciences Unit)

Table 1 reports the lattice constants of bulk and monolayered GaX obtained using calculations with GGA and LDA functionals.

Table 1. Comparison of lattice constants obtained from calculations with different exchange-correlation energy functionals with experimental values.

	Bulk			Monolayer	
	GGA (Å)	LDA (Å)	Experimental (Å)	GGA (Å)	LDA (Å)
GaS (Hexagonal)	a = 3.57 c = 15.51	a = 3.44 c = 14.50	a = 3.59 c = 15.49	a =3.57	a = 3.44
GaSe (Hexagonal)	a = 3.74 c = 15.95	a = 3.60 c = 15.13	a = 3.74 c = 15.89	a = 3.74	a = 3.60
GaTe (Hexagonal)	a = 4.04 c = 16.62	a = 3.89 c = 15.87	a = 4.06 c = 16.96	a = 4.04	a = 3.88
GaTe (Monoclinic)	a = 17.22 b = 3.92 c = 10.39	a = 16.33 b = 4.06 c = 9.91	a = 17.44 b = 4.07 c = 10.46	a = 23.14 b = 4.05	a = 22.03 b = 3.89

The GGA based estimates are in agreement with the experimental lattice parameters of all the structures, while they are significantly under-estimated using LDA. The electronic structures of bulk hexagonal GaS, GaSe, and GaTe, calculated using GGA and LDA functionals, are given in **Figures 2a and b**, respectively. The GGA results show that hexagonal GaS and GaTe exhibit an indirect band gap between Γ and M, while GaSe has a direct band gap at Γ (which is about the same as its indirect band gap between Γ and M). In contrast, LDA results reveal that GaS and GaSe have an indirect band gap between Γ and K, while GaTe is metallic in nature.

Figure 2. *Electronic structure of bulk GaX (hexagonal) determined with (a) GGA and (b) LDA functionals [black triangles – GaS; red squares – GaSe; purple circles – GaTe]; (c) bulk GaTe (monoclinic) determined with GGA [black open circles] and LDA [red closed triangles] functionals.*

For hexagonal GaX, it is clear that as the chalcogen X changes from S to Se and to Te, the conduction band drops lower towards the Fermi level

causing a decrease in the band gap. In monoclinic GaTe, the valence band maximum (VBM) appears between Γ and Z while the conduction band minimum (CBM) appears at Γ within the GGA description. The CBM appears close to X when LDA functional is used **(Figure 2c)**. Details of the electronic structures depend sensitively on the device of DFT-functional, and hence a hybrid functional seems essential to estimate gaps quantitatively.
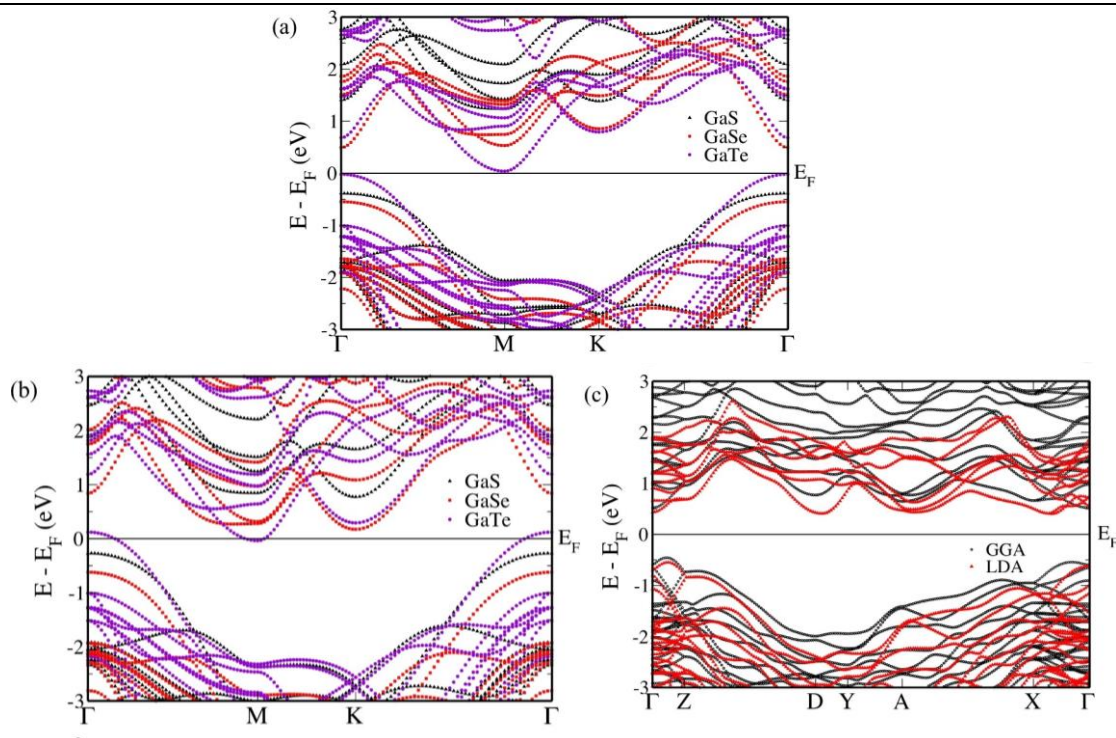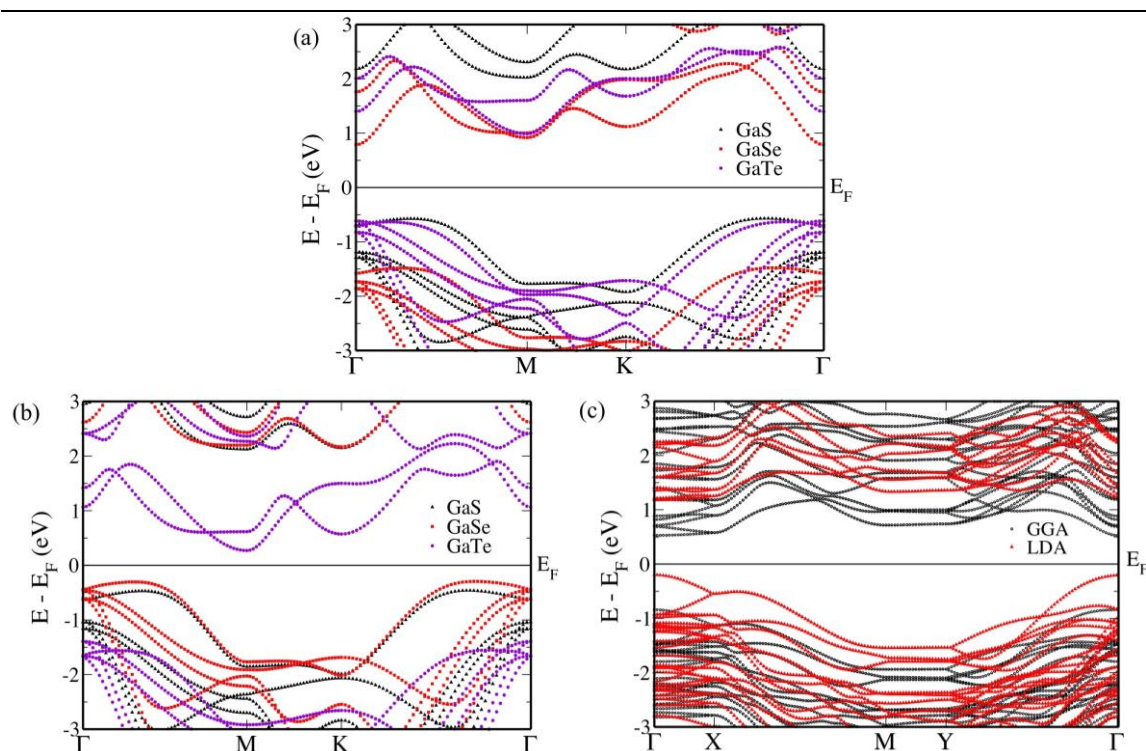

Figure 3. *Electronic structure of monolayered GaX (hexagonal) determined with (a) GGA and (b) LDA functionals. [Black triangles – GaS; red squares – GaSe; purple circles – GaTe]; (c) monolayered GaTe (monoclinic) determined with GGA [black open circles] and LDA [red closed triangles] functionals.*

Electronic structures of monolayered hexagonal GaS, GaSe, and GaTe obtained from GGA and LDA calculations **(Figures 3a and 3b)**, reveal that they possess an indirect band gap. The VBM of GaS is located between

Γ and M points, and the CBM at the M point. In GaSe, the VBM is located between K and Γ points, and the CBM is at the Γ point (within the GGA description). The electronic structure of GaSe based on the LDA functional shows the VBM between K and Γ points and the CBM at the K point. The VBM and CBM for a monolayer of hexagonal GaTe appear at Γ and M respectively. The electronic structure of a monolayer of GaTe with the monoclinic structure reveals a direct bandgap at the Γ point **(Figure 3c)**. Thus, the indirect bandgap changes to direct band gap as the structure change from hexagonal to monoclinic. The band gap of bulk GaX estimated using GGA is generally greater than that estimated using the LDA functional, while in the case of monolayered GaX the band gaps estimated with both the functionals are in agreement. As the band gaps are typically underestimated in DFT, the Heyd-Scuseria-Ernzerhof (HSE-06) hybrid functional was used to estimate band gaps accurately. **Table 2** compares the band gaps calculated using different functionals. We find a reduction in the gap as the chalcogen species changes from S to Te, consistent with the decrease in ionicity. The GGA and LDA functionals underestimate the band gaps in comparison to the HSE functional by 0.5-1.0 eV, and the HSE gaps are closer to experimental band gaps. The band gap of GaTe estimated with the HSE-06 functional falls within the visible spectrum, indicating that these materials could be used to harness solar energy. Our results of the many VBMs and CBMs suggest that GaX systems are expected to have good thermoelectric properties such as Seebeck coefficient due to band convergence.

Table 2. **Comparison of band gaps of GaX obtained using different exchange-correlation functionals.**

	Bulk			Monolayered		
	GGA (eV)	LDA (eV)	HSE (eV)	GGA (eV)	LDA (eV)	HSE (eV)
GaS (Hexagonal)	1.620	1.042	1.939	2.599	2.594	3.528
GaSe (Hexagonal)	1.040	0.793	1.639	2.267	2.463	3.319
GaTe (Hexagonal)	0.059	-0.158	0.497	1.604	1.663	2.456
GaTe (Monoclinic)	0.979	0.951	1.620	1.370	1.377	2.063

To determine whether the Ga chalcogenides can be useful in photocatalytic water splitting, we aligned their bands with respect to vacuum and the redox potentials of water **(Figure 4)**. The redox potentials of water are straddled by the VBM and CBM of monolayers of GaX (hexagonal). The VBM and CBM of a monolayer of GaTe (monoclinic) straddle only the HER (hydrogen evolution reaction) potential. The band gaps of 2, 4 and 8-layered GaX (hexagonal) and 2, 4-layered GaTe (monoclinic) were determined **(Table 3)** using the HSE-06 functional, and band alignment **(Figure 4b)** was carried out with respect to the vacuum and the redox potentials of water. With the increase in the thickness of GaX layers, the band gap reduces and falls within the visible spectrum indicating that its efficient for harvesting solar light. While 2, 4 and 8-layered GaS and GaSe are useful for overall water splitting, few-layered

GaTe can be used primarily in the hydrogen evolution reaction using a sacrificial agent as its valence band maximum occurs above the OER (oxygen evolution reaction) potential.
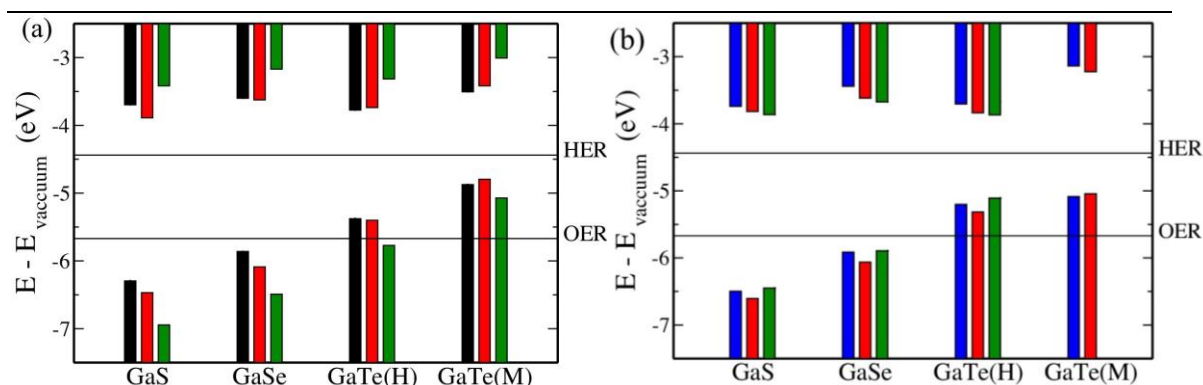
Figure 4. *Conduction and valence band edges of (a) monolayered GaX determined with GGA [black], LDA [red] and HSE [green] functionals; and (b) 2-layered [blue], 4-layered [red], 8-layered [green] GaX determined with HSE functional, and aligned with HER and OER.*

Table 3. Comparison of band gaps of different layers of GaX determined with HSE functional.

Number of layers	2	4	8
GaS (Hexagonal)	2.954	2.788	2.587
GaSe (Hexagonal)	2.473	2.445	2.220
GaTe (Hexagonal)	1.497	1.479	1.240
GaTe (Monoclinic)	1.948	1.821	-

4.2. Experimental results

(Since GaSe was unstable for water splitting we did not characterize the samples).

The single crystals of Gallium chalcogenides (GaS and GaTe) were characterized using X-Ray diffraction. From the diffraction pattern, we confirm that GaS has hexagonal structure while GaTe possessed monoclinic structure **(Figure 6a)**. The diffused UV spectra for GaTe and GaSe sample are shown in **Figure 6b and c**. The band gap of this GaTe and GaS is 1.6 eV and 2.3 eV respectively.

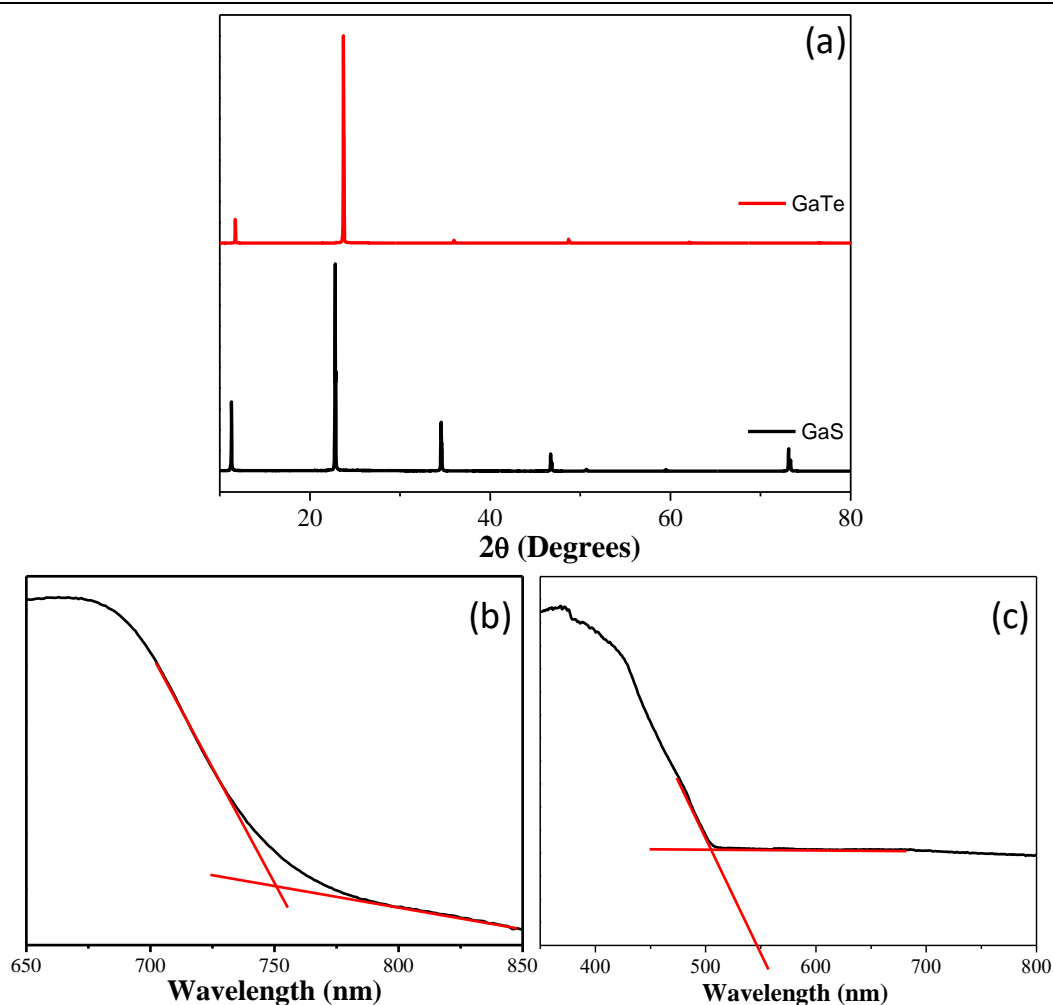**Figure 6:** *X-ray diffraction pattern of single crystals of (a) GaS and GaTe. The diffused reflectance UV-vis spectra of (b) GaTe and (c) GaS.*

We carried out hydrogen evolution for these semiconductors in 0.1M Na_2S and Na_2SO_3 and 10 % v/v aqueous solution of lactic acid. The samples are not stable in that solution, and therefore their HER properties could not be studied. We, therefore, carried out the photochemical generation of hydrogen from water with layered gallium chalcogenides (GaX) in the presence of triethanolamine with eosin Y (EY) dye as the photosensitizer. The plausible mechanism for hydrogen evolution from bulk GaX is shown in **Figure 7**. Eosin Y absorbs light, and from the singlet state excited light, and goes from singlet to the triplet state. The triplet state takes up an electron from the amine present and becomes negatively charged. The electron from the anion of eosin is transferred to GaTe and then channeled to H_2O for H_2 evolution [34, 35].
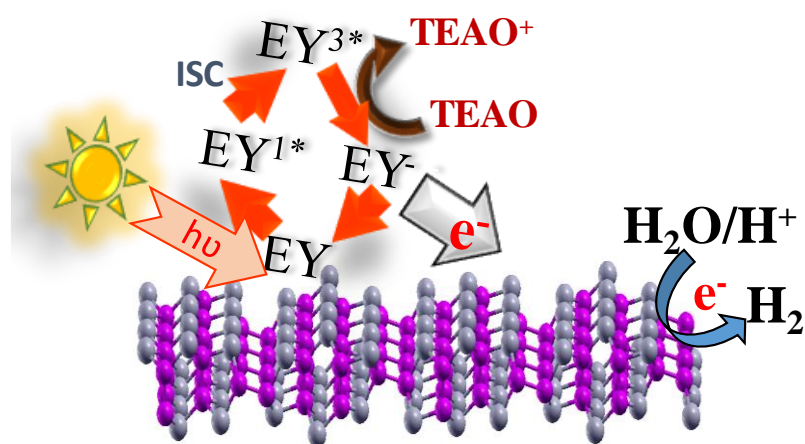
Figure 7. *The plausible mechanism in dye-induced hydrogen evolution in gallium chalcogenides.*

From the results of theoretical calculations, we find that all the chalcogenides of GaX have favorable band alignment for photocatalytic HER. However, we find that both GaS and GaSe are inactive in the dye-sensitized photochemical process, GaSe being unstable under the reaction conditions. On the other hand, GaTe is active and stable during

photocatalytic hydrogen evolution. The activity of layered GaTe was found to be 600 mmol h^{-1} g^{-1}. The hydrogen evolution property of GaTe is compared with GaS **(Figure 8)**.
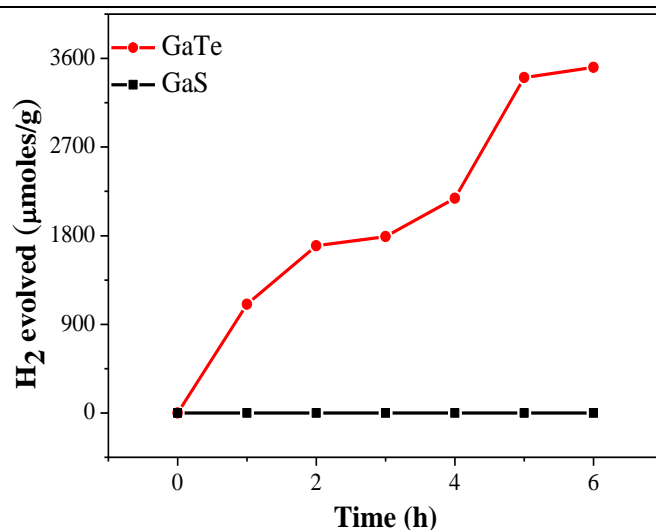
Figure 8. *Time course of hydrogen evolution of dye-sensitized photochemical H$_2$ evolution on GaTe and GaS.*
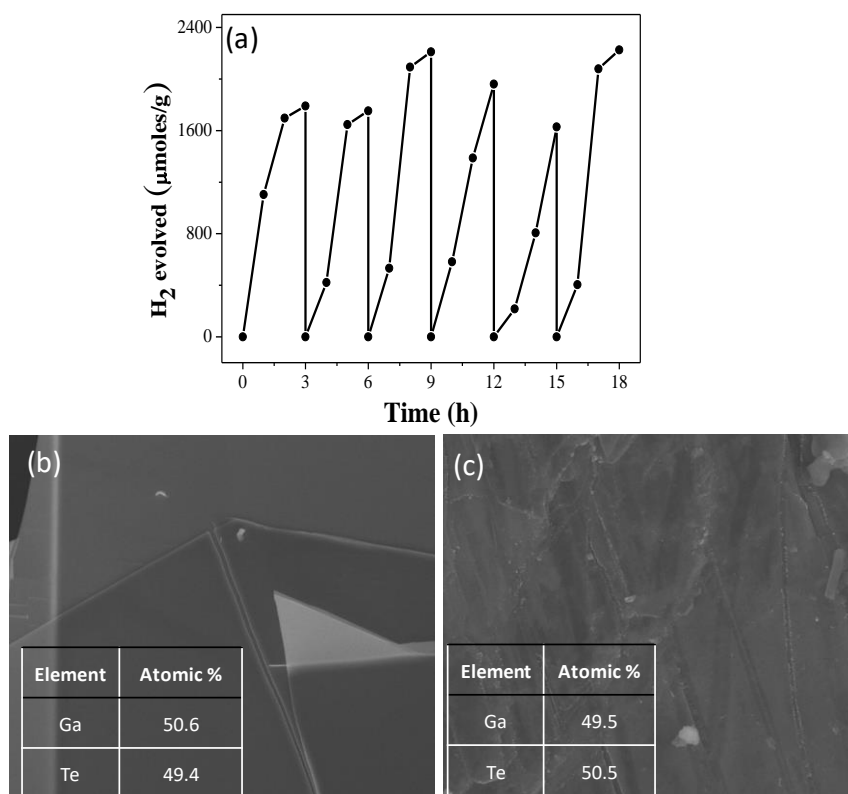
Figure 9. *Cycling HER studies of GaTe in the presence dye. The EDS analysis and SEM images of GaTe (b) before and (c) after HER.*

Cycling studies were performed to check the stability of GaTe during the photocatalytic cycles. The activity decreases only slightly on cycling but is regained upon sonication the activity is regained thereby confirming the stable photocatalytic HER activity of GaTe **(Figure 9a)**. SEM images and EDS data of the sample are shown in **Figure 9 b and c** before and after hydrogen evolution.

5. Conclusions

First-principles calculations of band gaps and band edge positions reveal that as the thickness of GaX (X = S, Se, Te) increases, the band gap decreases and approaches the bulk limit. In the case of GaTe (hexagonal and monoclinic) though the VBM position relative to OER becomes unfavorable, use of sacrificial agents is seen to support the photocatalytic water splitting, as the CBM lies above the HER potential. Experimental studies of hydrogen evolution properties show that layered GaTe is an active and stable catalyst in the Eosin Y dye-sensitized process.

6.   References

1.   M. Chhowalla, H. Suk Shin, G. Eda, L. Li, K.P. Loh, H. Zhang, Nat. Chem., 2013, 5, 263.

2.   C.N.R. Rao, U. Maitra, U.V. Waghmare, Chem. Phys. Lett., 2014, 609, 172.

3.   C.N.R. Rao, H.S.S. Ramakrishna Matte, U. Maitra, Angew. Chem. Int. Ed., 2013, 52, 13162.

4.   C.N.R. Rao, U. Maitra, Annu. Rev. Mater. Res., 2015, 45, 29.

5.   H. Wang, H. Feng and J. Li, Small, 2014, 10, 2165.

6.   M. Xu, T. Liang, M. Shi and H. Chen, Chem. Rev., 2013, 113, 3766.

7.   P. Hu, L. Wang, M. Yoon, J. Zhang, W. Feng, X. Wang, Z. Wen, J.C. Idrobo, Y. Miyamoto, D.B. Geohegan, K. Xiao, NanoLett., 2013, 13, 1649.

8.   X. Li, M. Lin, A.A. Puretzky, J.C. Idrobo, C. Ma, M. Chi, M. Yoon, C. M. Rouleau, I.I. Kravchenko, D.B. Geohegan and K. Xiao, Sci. Rep., 2014, 4, 5497.

9.   Z. Wang, K. Xu, Y. Li, X. Zhan, M. Safdar, Q. Wang, F. Wang and J. He, ACS Nano, 2014, 8, 4859.

10.   Y. Zhou, Y. Nie, Y. Liu, K. Yan, J. Hong, C. Jin, Y. Zhou, J. Yin, Z. Liu and H. Peng, ACS Nano, 2014, 8, 1485.

11.   D.J. Late, B. Liu, J. Luo, A. Yan, H.S.S.R. Matte, M. Grayson, C.N.R. Rao and V.P. Dravid, Adv. Mater., 2012, 24, 3549.

12.   P. Hu, Z. Wen, L. Wang, P. Tan and K. Xiao, ACS Nano, 2012, 6, 5988.

13.   X. Li, L. Basile, B. Huang, C. Ma, J. Lee, I.V. Vlassiouk, A.A. Puretzky, M. Lin, M. Yoon, M. Chi, J.C. Idrobo, C.M. Rouleau, B.G. Sumpter, D.B. Geohegan and K. Xiao, ACS Nano, 2015, 9, 8078.

14.   S. Yang, S. Tongay, Y. Li, Q. Yue, J. Xia, S. Li, J. Li, S. Wei, Nanoscale, 2014, 6, 7226.

15.   P.A. Hu, Z.Z. Wen, L.F. Wang, P.H. Tan, K. Xiao, ACS Nano, 2012, 6, 5988.

16. P.S. Hu, L.F Wang, M. Yoon, J. Zhang, W. Feng, X.N. Wang, Z.Z. Wen, J.C. Idrobo, Y. Miyamoto, D. B. Geohegan, K. Xiao, Nano Lett., 2013, 13, 1649.

17. S. Kouser, A. Thannikoth, U. Gupta, U.V. Waghmare, C.N.R. Rao, Small, 2015, 11, 4723.

18. M. Gauthier, A. Polian, J.M Besson, A.A. Chevy, Phys. Rev. B., 1989, 40, 3837.

19. A. Yamamoto, A. Syouji, T. Goto, E. Kulatov, K. Ohno, Y. Kawazoe, K. Uchida, N. Miura, Phys. Rev. B: Condens.Matter., 2001, 64, 035210.

20. F.C. Liu, H. Shimotani, H. Shang, T. Kanagasekaran,V. Zolyomi, N. Drummond, V. I. Fal'ko, K. Tanigaki, ACS Nano, 2014, 8, 752.

21. Y.L. Cui, D.D. Caudel, P. Bhattacharya, A. Burger, K.C. Mandal, D. Johnstone, S.A. Payne, J. Appl. Phys., 2009, 105, 053709.

22. D.N. Bose, S. Pal, Phys. Rev. B., 2001, 63, 235321.

23. A. Segura, J. Bouvier, J.M.V Andrés, F.J Manjón, V. Muñoz, Phys. Rev. B., 1997, 56, 4075.

24. K.C. Mandal, R.M Krishna, T.C Hayes, P.G Muzykov, S. Das, T.S Sudarshan, S.G. Ma, IEEE Trans. Nucl Sci., 2011, 58, 1981.

25. C. Julien, I. Ivanov, C. Ecrepont, M. Guittard, Phys. Statu. Solidi (A), 1994, 145, 207.

26. B. Radisavljevic, A. Radenovic, J. Brivio, V. Giacometti, A. Kis, Nat. Nanotechnol., 2011, 6, 147.

27. P. Giannozzi, S. Baroni, N. Bonini, M. Calandra, R. Car, C. Cavazzoni, D. Ceresoli, G. L. Chiarotti, M. Cococcioni, I. Dabo, A. L Corso, S. De Gironcoli, S. Fabris, G. Fratesi, R. Gebauer, U. Gerstmann, C. Gougoussis, A. Kokalj, M. Lazzeri, L. Martin-Samos, N. Marzari, F. Mauri, R. Mazzarello, S. Paolini, A. Pasquarello, L. Paulatto, C. Sbraccia, S. Scandolo, G. Sclauzero, A. P. Seitsonen, A. Smogunov, P. Umari, R. M. Wentzcovitch, J. Phys. Condens. Matter., 2009, 21, 395502.

28. J.P. Perdew, K.P Burke, M. Ernzerhof, Phys. Rev. Lett., 1996, 77, 3865.

29. J.P. Perdew, Y. Wang, Phys. Rev. B., 1992, 45, 13244.

30. S.J. Grimme, Comput. Chem., 2006, 27, 1787.

31. A. Aydinli, N.M. Gasanly, A. Uka, H. Efeoglu, Cryst. Res. Technol., 2002, 37, 1303.

32. F.C. Liu, H. Shimotani, H. Shang, T. Kanagasekaran, V. Zolyomi, N. Drummond, V.I. Fal'ko, K. Tanigaki, ACS Nano, 2014, 8, 752.

33. J.F. Sánchez-Royo1, G. Muñoz-Matutano1, M. Brotons-Gisbert, J.P. Martínez-Pastor1, A. Segura1, A. Cantarero1, R. Mata, J. Canet-Ferrer1, G. Tobias, E. Canadell, J. Marqués-Hueso, B.D. Gerardot, Nano Research, 2014, 7, 1556.

34. U. Maitra, U. Gupta, M. De, R. Datta, A. Govindaraj, C.N.R. Rao, Angew. Chem. Int. Ed., 2013, 52, 13057.

35. U. Gupta, B.S. Naidu, U. Maitra, A. Singh, S.N. Shirodkar, U.V. Waghmare, C.N.R. Rao, APL Mater., 2014, 2, 092802.

Part 2

Photochemical H_2 evolution reaction based on Weyl semimetals and topological insulators
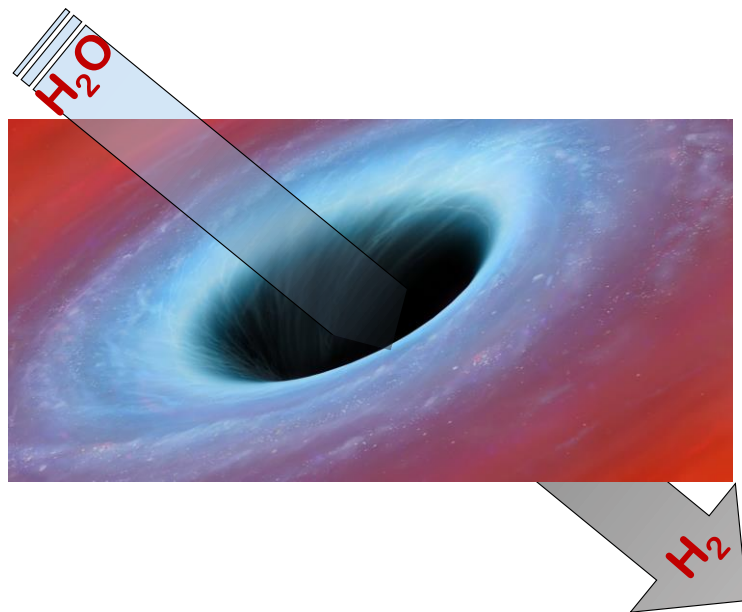
Summary

The highly efficient and low-cost catalysts are the main driving forces in catalytic chemistry. Current strategies for catalyst design focus on increasing the number and the activity of local catalytic sites, such as the edge-sites of molybdenum disulfide in the hydrogen evolution reaction (HER). Here, we propose and demonstrate a different principle that goes beyond local site optimization by utilizing topological electronic states to spur catalytic activity. For HER, we have explored topologically non-trivial material like Weyl semimetals (transition-metal monopnictides-NbP, TaP, NbAs, and TaAs) and topological insulators (Bi_2Te_3, Bi_2Te_2Se and Bi_2Se_3). We have found excellent catalysts among the Weyl semimetals. Here we show that a combination of robust topological surface states and large room temperature carrier mobility, both of which originate from bulk Dirac bands of the Weyl semimetal, is a recipe for high activity HER catalysts. This approach has the potential to go beyond graphene based composite photocatalysts where graphene simply provides a high mobility medium without any active catalytic sites that we find in these topological materials. Thus, our work provides a guiding principle for the discovery of novel catalysts from the emerging field of topological materials.
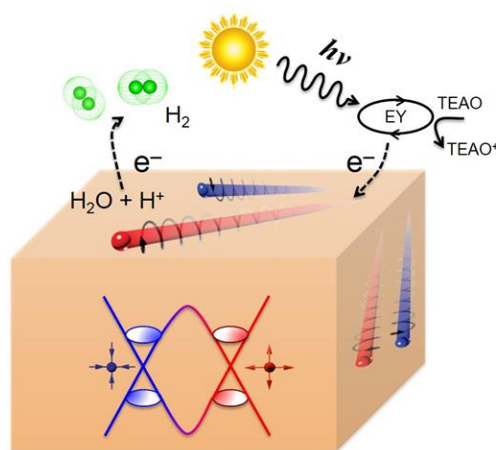
1. Introduction

Heterogeneous catalysis plays a major role in organic and inorganic chemistry. The high complexity of the catalytic process is a major challenge [1-4]. One important catalytic process, of increasing importance, is the harvesting of solar energy to produce hydrogen (H_2) from water: one of the major challenges in the supply of "green energy" [5, 6]. Educts, products and the surface of the catalyst have to be taken into account in heterogeneous catalysis. Many conventional metals and semiconductors are under investigation as potential catalysts [7-9]. A stable supply of itinerant electrons at the surface is important for catalytic processes involving redox reactions. Materials with high mobilities of electrons and holes reduces the probability of recombination of the electron-hole pairs that are created in the redox process. Here we introduce a new concept based on the use of unconventional topological materials as catalysts. Whilst these materials have drawn significant attention from the condensed matter community, their unique properties have not yet been considered by chemists. But the high carrier mobilities that are realized from the linear bands of a Dirac cone and which are thereby a fundamental property of Weyl- and Dirac-semimetals [10, 11] suggest that these materials could be excellent catalysts, as we show here. Moreover, the problem of surface contamination, which is a major bottleneck in the field of catalysis, can be diminished to a great extent in topological materials because of their robust topologically-protected surface states [12, 13]. We have explored the behaviour of

topological materials in catalysis, primarily in the hydrogen evolution reaction.

1.1 Topology

Topology by definition is study of properties of matter unperturbed by the dynamic change in shape or size of the body. The properties remain intact under physical stress or strain (bending, stretching, twisting and so on) but on breaking the body the properties changes.
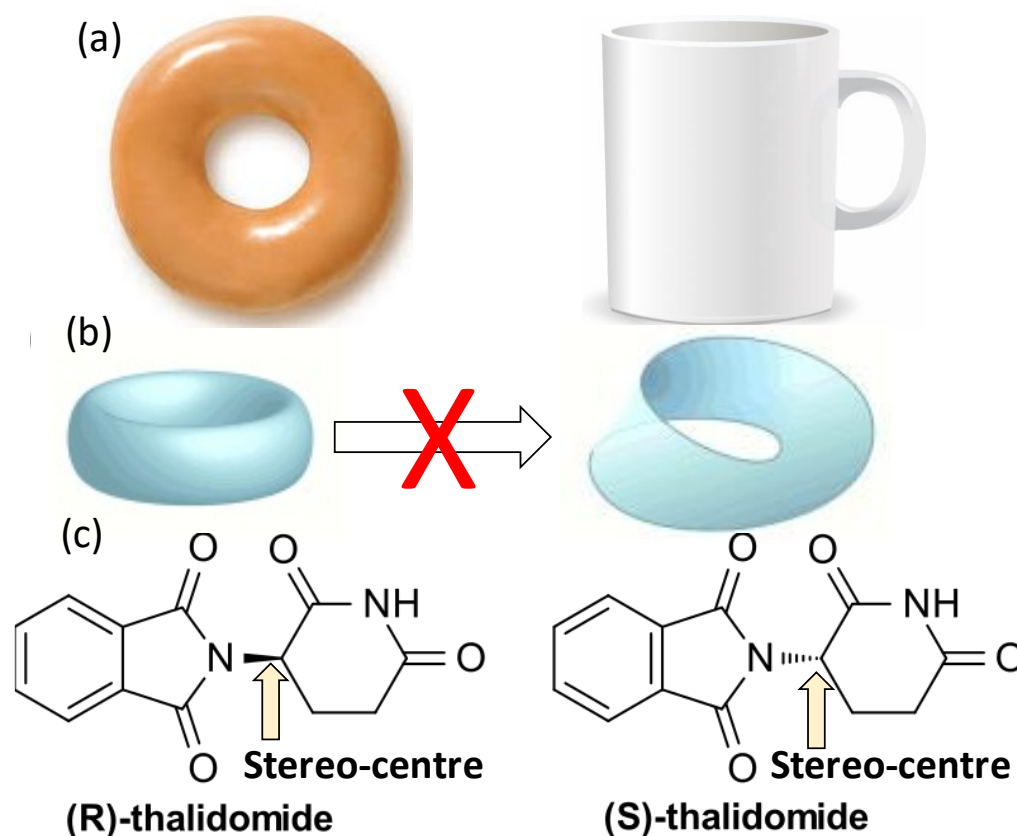
Figure 1. (a) Topologically identical materials which can be transformed from one to another by physical forces like stretching and so on. The material may look different but topologically are same. (b) The rings look same but are topologically different. To transform from one ring to another one need to break or cut the ring and re-join them to convert from one form to another. (c) Enantiomers of thalidomide have same chemical formula but different biological functions. To convert one enantiomer to another we need to break the bond in the stereo-centre of the compound.

Figure 1a shows that donut and coffee mug although look different but are topologically same since, they can be changed into each other from on application of physical strain. A ring and a Möbius ring although may appear similar but topologically different since one has to tear and glue back to get interchange one form to another **(Figure 1b)**.

Topology allows the classification of fundamental intrinsic properties of the large number of diverse chemical compounds, modelling out the distinctive topographies of a class of materials with different complexity. Chemists encounter the notion of topology with respect to chirality, since, molecules with different chiralities can exhibit different physical and chemical properties **(Figure 1c)**. On an abstract level, isolobal concept is a topological principle where grouping compounds with similar properties independent of their composition. For example, topologically interesting compounds are 4n aromatics which possess Möbius geometry while normal 4n compounds are anti-aromatic [14]. Approaches discussed earlier mentions the topology of molecules in the real-space. Beginning with the work of Chern, in physics, the topology of the underlying mathematical space has been explored for topological materials, [15–17] and it has been calculated in the framework of high-energy extensions of the standard model using quantum field theory [18]. Topological materials have been identified as new class of compounds, which bring together solid-state chemistry and condensed matter physics. Topological materials can be understood with concept of bonds, symmetry, bands structure and nuclear charges and phase of orbitals. These chemical principles motivate for the

search for new topologically nontrivial materials by chemists and materials scientists with new applications.

The prerequisite to a Weyl semimetal or a topological insulator (TI), is an energy band inversion. Many compounds containing heavy metals show such a band inversion, more commonly referred to as inert pair effect [19]. In a relativistic band structure, band crossing is forbidden such that, in topological insulators, a new band-gap opens, and a surface-state with a Dirac cone electronic structure appears. Dirac and Weyl semimetals appear at the borderline between topological and trivial insulators. Topological surface states of exhibit robust transport against scattering and against environmental perturbations. The first feature promises fast and low-dissipation electron transport channels with high mobility, which may improve the conductivity of electrodes in electrochemical reactions. The second feature serves stable supply of itinerant electrons at the interface, which may serve as a robust electron bath for the charge transfer for the chemical reaction [20]. Therefore, we expect that topological states may demonstrate interesting catalytic properties.

1.2   Topological Weyl semimetals

Topological Weyl semimetals (TWSs) are topologically non-trivial materials which possess Fermi arcs on the surface and magnetic effects in the bulk [21, 22]. They possess the massless fermions known as Weyl fermions, named after Hermann Weyl in 1929 [23-25]. The band structure of TWSs is formed due band inversion, where bands disperse linearly in 3D-momentum space through points called Weyl points [26]. At Weyl points the Berry curvature (the relationship between the conduction band and

valance band which is equivalent to magnetic field in momentum space) becomes singular and acts like a monopole with chirality of source as '+' and sink '-' occurring as pairs **(Figure 2a and b)** [27].
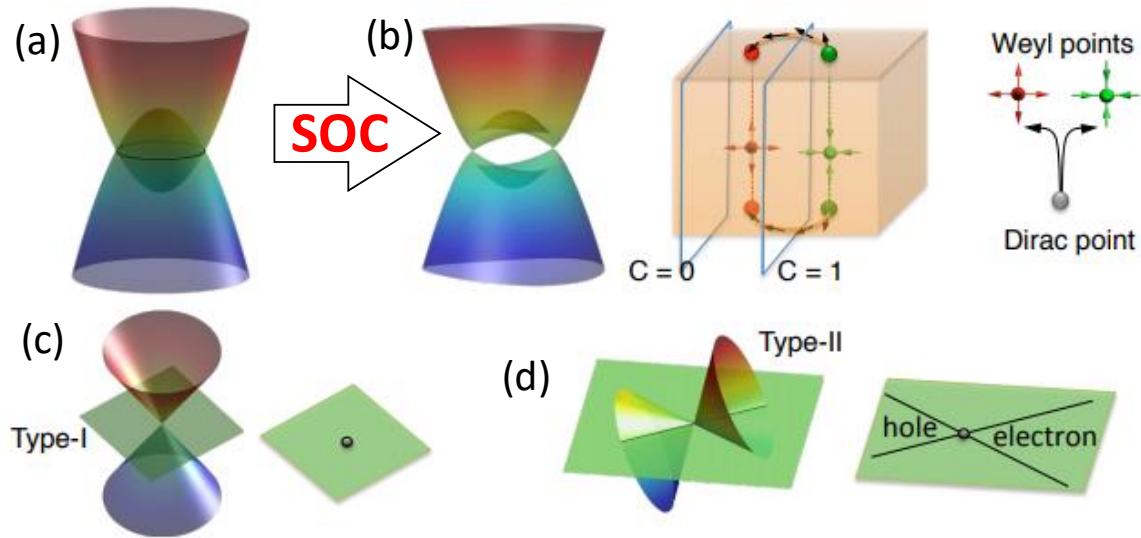
Figure 2. *(a) and (b) The spin-orbit coupling (SOC) in a Weyl semimetals (WSMs), the bulk bands are gapped in the 3D momentum space except at some isolating linearly crossing points, known as Weyl points, like in 3D analogue of graphene. Due to the topology of the bulk bands, topological surface states appear on the surface and form exotic Fermi arcs. are WSMs the degeneracy is lifted due to the breaking of the inversion symmetry or time-reversal symmetry, or both. (c) The type-I WSM. The Fermi surface (FS) shrinks to zero at the Weyl points when the Fermi energy is sufficiently close to the Weyl points. (d) The type-II WSM. Due to the strong tilting of the Weyl cone, the Weyl point acts as the touching point between electron and hole pockets in the FS.*

In a Weyl semimetal, pairs of Dirac cones are formed in the bulk of the material where the number of pairs depends on the detailed symmetry of the particular metal. The TWSs phase can only be realized with breaking of either inversion symmetry or time reversal symmetry. For example, samples studied in this these are transition metal pnictides (NbP, TaP,

NbAs and TaAs) have preserved time reversal symmetry but have broken inversion symmetry due to the crystal structure or symmetry [28]. Further, TWS can be classified into Type-I (Tilt parameter (ω/ν) = 0.5; Fermi surface contracts to a point) **(Figure 2b)** or Type-II (Tilt parameter (ω/ν) = 1.2; Fermi surface tilts to a greater extent) with respect to the Lorentz symmetry [29, 30] **(Figure 2 c)**.

1.3 Topological insulators

Topological insulators (TI) possess insulating bulk with a conducting surface or edges. TIs possess an energy gap similar to that of a trivial insulator in the bulk with a metallic surface states [31]. The surface state of TIs is different compared to bulk and from trivial metallic states as they arise from the non-trivial topology of the bulk bands. The non-trivial topology of a TI arises due from the and inversion wherein the bulk a gap opens due to spin orbit coupling (SOC). The conducting electrons align themselves in a spin non-degenerate fashion which causes spin-current **(Figure 3a)**. The non-triviality allows for spin-up and spin-down currents to flow in separate channels, which protects the surface states from back scattering. The electronic bulk-band structure of TIs is very similar to that of traditional insulators except for gapless/ conducting states on the boundary for 2D and the surface for the 3D that are protected by time reversal symmetry **(Figure 3b and c)** [32]. Topological insulators were first observed in bismuth chalcogenides [33, 34]. Topologically different from Fermi surfaces of a TI or an ordinary material, their surface states present unclosed Fermi surfaces, called Fermi arcs, which connect the surface projections of WPs with opposite chiralities [3].
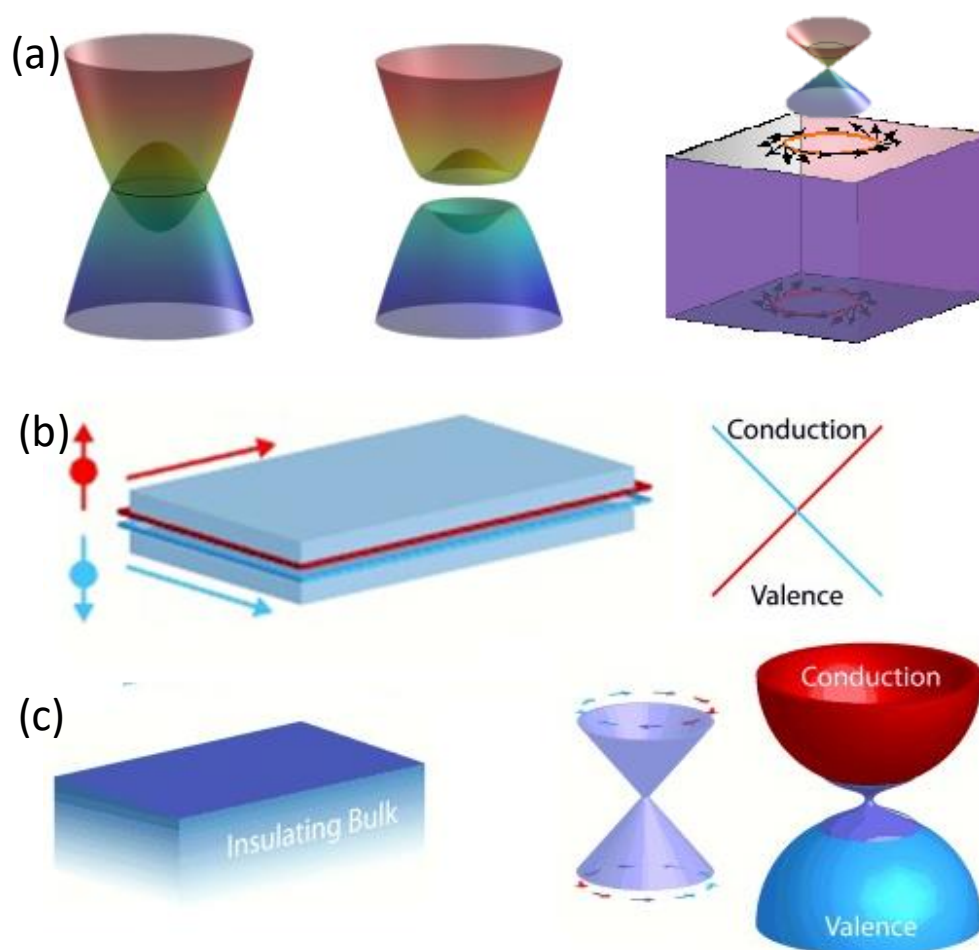
Figure 3. (a) The topological insulator originates from similar inverted band structure.due to spin-orbit coupling (SOC) opens a full gap after the band inversion giving rise to metallic surface states on the surface. (b) A two-dimensional topological insulator (2D TI). Only one of the one-dimensional counter-propagating edge states is shown for each surface. (c) 3D TI and schematic band structure with a Dirac cone.

2. Scope of the present investigations

To verify our hypothesis that the new topological materials with superior electronic properties can also be highly efficient in catalysis, we have tested them for dye-sensitized hydrogen evolution reaction (HER). Topological insulators (TIs) are insulating in the bulk, but conducting on all sides of the outer surface [1-2]. Since backscattering is forbidden, topological

surface states are expected to be ideal conducting channels for electric transport. Recently, the first four WSM materials ever to be identified, namely, the transition-metal mono-pnictides (TaAs, TaP, NbAs and NbP), were predicted in theory [4] and later confirmed by observation of the Fermi arcs in ARPES (angle resolved photo-emission) [5-8]. MoTe$_2$ and WTe$_2$ are also predicted to be WSM candidates [9, 10]. There has been a good deal of experimental and theoretical effort devoted to their transport properties [11-13, 19, 35-37]. For example, giant positive magnetoresistance and ultrahigh mobility are reported in NbP [11], which is believed to be a manifestation of the linear bulk bands and the Berry curvature.

The topological surface states of TIs and WSMs and bulk linear bands of WSM exhibit two common appealing features: the robust transport against scattering and the robust existence against environment perturbations. The first feature promises fast and low-dissipation electron transport channels with high mobility (as found in NbP), which may improve the conductivity of electrode in electrochemical reactions. The second feature serves stable supply of itinerant electrons at the interface, which may serve as a robust electron bath [38, 39] for charge transfer in the process of chemical reaction. Therefore, we expect that topological states, the new concept in physics community, may help improve the catalyst behavior in chemistry. Except above two features, it is still a tantalizing question whether the spin polarized topological states can interfere with the catalysis process directly. We have explored photocatalysis by Weyl semi-metals as well as topological insulators in the light of the recent

reports that metallic $1T\text{-}MoS_2$ and $1T\text{-}MoSe_2$ exhibit excellent performance in generating H_2 from H_2O by dye-sensitized photochemical means [37, 40].

The stable 2H-form of MoS_2 yields H_2 from water on sensitization with a dye and, the metallic form 1T-phase, is far superior in be better for the H_2 generation, yielding 600 times more hydrogen than 2H- MoS2 [37]. Similar results have been found with $1T\text{-}MoSe_2$ [40]. Metallic surface along the basal planes of $1T\text{-}MoS_2$ and $1T\text{-}WS_2$ are catalytically active along with the edge and the metallicity of the basal planes determines the activity and stability of the catalyst [38]. In the present study, we have investigated dye-sensitized photocatalytic hydrogen generation by type I Weyl semimetals NbP, TaP, NbAs, and TaAs as well as $1T\text{-}MoTe_2$ which is type II Weyl semimetal. We have also investigated hydrogen generation by the topological insulators Bi_2Te_3 and Bi_2Te_2Se. For the purpose of comparison, we have examined H_2 generation by $1T\text{-}TaS_2$ which is trivial metallic system.

3. Experimental section

(Synthesis and characterization of the material has been carried out in Max Planck Institute for Chemical Physics of Solids by Prof. Claudia Felser and co-workers in Dresden, Germany)

3.1 Weyl semimetals

3.1.1   Materials synthesis

$1T'\text{-}MoTe_2$ and $2H\text{-}MoTe_2$ crystals were grown via chemical vapour transport using polycrystalline $MoTe_2$ powder and $TeCl_4$ as a transport additive.(*1*) $1T\text{-}TaS_2$ was grown from its elements via solid state route. Stoichiometric quantities of Ta (Alfa Aesaer 99.999%) and S (Alfa Aesar

99.99%) were sealed in a quartz ampoule and heat treated at 900°C for one week and quenched. Single crystals of NbP, TaP, NbAs and TaAs were grown via chemical vapour transport. Stoichiometric quantities of Nb (Alfa Aesar, 99.99%) and P (Alfa Aesar, 99.999%) were weighed in accurately in a quartz ampoule, flushed with Ar, sealed under vacuum and tempered in two consecutive steps of 600 °C and 800 °C for 24 h each prior to crystal growth. Crystal growth was carried out in a two-zone furnace between 850 – 950 °C for 2 weeks using I_2 (8 mol/ml) as the transport agent. Stoichiometric quantities of Nb (Alfa Aesar, 99.99%) and As (Chempur, 99.9999%) were tempered in a similar manner prior to crystal growth. Crystal growth was carried out in a two-zone furnace between 900 – 1000 °C for 4 weeks using I_2 (8 mol/ml) as the transport agent. Stoichiometric quantities of Ta (Alfa Aesar, 99.97%) and P (Alfa Aesar, 99.999%) were tempered in a similar manner prior to crystal growth. Crystal growth was carried out in a two-zone furnace between 900 – 1000 °C for 2 weeks using I_2 (12 mol/ml) as the transport agent. Stoichiometric quantities of Ta (Alfa Aesar, 99.97%) and As (Chempur, 99.9999%) were also tempered in a similar manner prior to crystal growth. Crystal growth was carried out in a two-zone furnace between 900 – 1000 °C for 4 weeks using I_2 (12 mol/ml) as the transport agent.

3.1.2 Characterization

The crystals obtained have been characterized by powder X-ray diffraction using an image-plate Huber G670 Guinier camera with a Ge (111) monochromator and Co K_α radiation. Indexing was done with the

program WINX POW19 and PowderCell.20. The diffraction pattern is in good agreement with the calculated pattern. The FESEM images were recorded using Nova Nano FESEM 600 FEI. The surface area of samples was determined using a BET surface area technique using Quantachrome Adsorption instrument.

3.1.3 Computational details:

Electronic structures were calculated by the density functional theory (DFT) method as implemented in the Vienna *ab initio* Simulation Package (VASP). The exchange–correlation was considered in the revised Perdew-Burke-Ernzerhof (rPBE) parameterized generalized gradient approximation (GGA) [41] and spin–orbital coupling (SOC) was included. While calculating the adsorption energies, the van der Waals interaction using DFT-D2 method of Grimme was included [42].

3.2 Topological insulators

3.2.1   Materials synthesis and characterization

Single crystals of Bi_2Te_3, Bi_2Te_2Se and Sb_2Te_2Se were synthesised using the flux method. Nanosheets of Bi_2Te_3 have been synthesized according to ref. [43] All materials have been characterized by powder X-ray diffraction using an image-plate Huber G670 Guinier camera with a Ge (111) monochromator and Cu K_α radiation. FESEM images were recorded using Nova Nano FESEM 600 FEI. The surface area of samples was determined using a BET surface area technique using Quanta Chrome Adsorption instrument.

3.2.2. Computational details

Our first-principles calculations are based on density functional theory as implemented in the Quantum Espresso code [44] which uses pseudopotentials to model the interaction between core and valence electrons. We used norm-conserving pseudoptentials generated [45] from the solutions of fully relativistic Dirac equation for an atom to take into account the effect spin-orbit coupling in our calculations. Exchange-correlation energy of the electrons was treated within a generalized gradient approximated (GGA) functional as parametrized by Perdew, Burke and Ernzerhof [46]. We truncated the plane-wave basis used in representation of the Kohn-Sham wavefunctions and charge density with cut-off energies of 60 Ry and 240 Ry, respectively. Discontinuity in the occupation numbers of the electrons at the Fermi level were smeared with a broadening of k_{BT}= 0.003 Ry in the Fermi-Dirac function. We determined work functions of Bi_2Se_3 and Bi_2Te_3 from calculations on their slabs with (001) surface orientation taking 15 and 30 atomic layers respectively. While constructing the periodic cell with a slab, we used optimized atomic coordinates of the bulk at their experimental lattice structures [47], and included a vacuum of length 10 Å along the c-direction to keep the interaction between the periodic images of the slab low. We estimated the work function (Φ) [48] by taking the difference between the constant potential in the vacuum (V_{vac}) and the Fermi energy of the slab ($E_{F,slab}$), i.e., $\Phi = V_{vac} - E_{F,slab}$. We find that the effect of van der Waals interactions (at the level of Grimme dispersion correction (DFT-D2) [17]) on the calculated

work functions is not significant [42]. Hence, we present here the results of calculations that do not include van der Waals interaction. To study the optical absorption spectra, we obtained the frequency dependent dielectric tensor of both these compounds in their bulk as well as slab forms taking into account the effect of spin-orbit coupling. We used uniform grid of 9x9x1 k-points in our calculations on the slab.

3.3 Hydrogen evolution measurements

Single crystals of topological insulators (Bi_2Se_3, Bi_2Te_3, Bi_2Te_2Se) and Weyl semimetals (NbP, NbAs, TaP, TaAs, 1T'-$MoTe_2$), Sb_2Te_2Se, 2H-$MoTe_2$ and 1T-TaS_2 were dispersed in 48 ml of triethanolamine (15% v/v) aqueous solution with 14 μmole of Eosin Y dye and was sonicated for 30 mins. The vessel was placed on a magnetic stirrer and thoroughly purged with N_2 gas for 5 minutes to free the surface of the catalyst by previously adsorbed gas and also to remove dissolved O_2 from the solution. The flask was then sealed with a rubber septum and irradiated with 100 W halogen lamp with constant stirring. The evolved gases were manually collected from the headspace of the vessel and analysed with a thermal conductivity detector TCD in PerkinElmer Clarus ARNEL 580GC gas chromatograph.

Turn over frequency (TOF) was calculated as follows:

$$TOF\ (h^{-1})\ ) = (Activity\ of\ the\ catalyst)/(Moles\ of\ the\ catalyst\ used)\ (1)$$

4. Results and discussion

(Synthesis and characterization of the material has been carried out in Max Planck Institute for Chemical Physics of Solids by Prof. Claudia Felser and co-workers, Dresden, Germany)

4.1 Weyl semimetals

4.1.1 Structural characterization

The samples studied to understand the role of Weyl-surface in photocatalytic hydrogen evolution. The X-ray diffraction of transition metal dichalcogenides (1T-TaS$_2$, 1T'-MoTe$_2$ and 2H-MoTe$_2$) used for hydrogen evolution are shown in **Figure 4**.
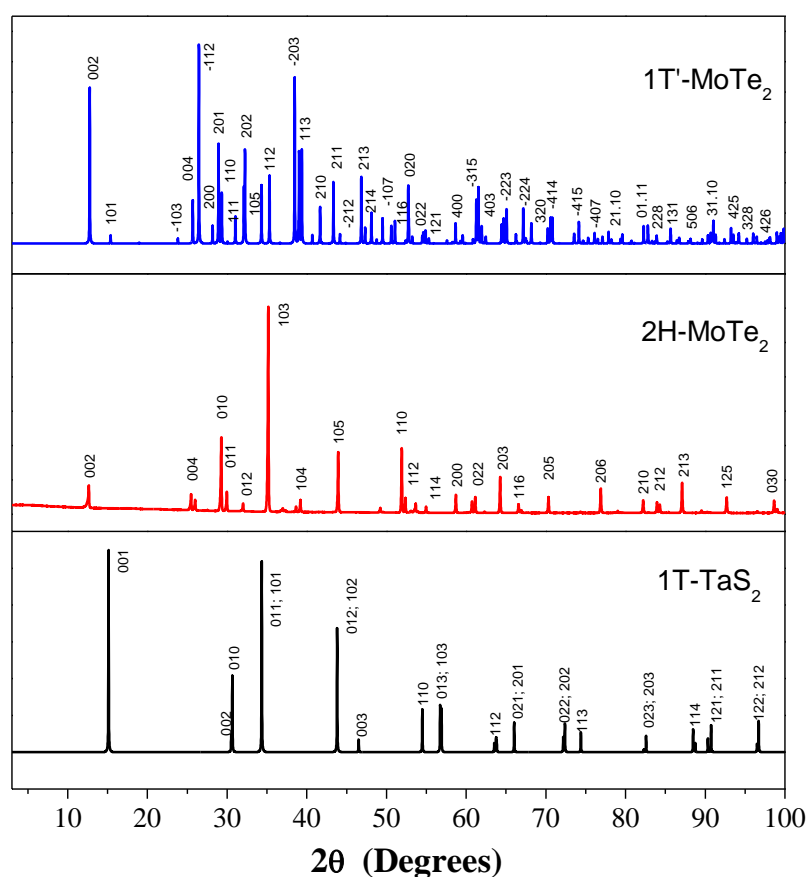

Figure 4. *The powder X-ray diffraction patterns of 1T'-MoTe$_2$, 2H-MoTe$_2$ and 1T-TaS$_2$. 1T'-MoTe$_2$ is monoclinic with space group P12/m (no. 11); 2H-MoTe$_2$ is hexagonal with space group P6$_3$/mmc (no. 194) 1T-TaS$_2$ is with space group P-3m1 (no. 164).*

1T'-MoTe$_2$ crystallizes in P2$_1$/m (space group 11). 2H-MoTe$_2$ crystallizes in space group P6$_3$/mmc (space group 194) while 1T-TaS$_2$ crystallizes in space group P-3m1 (no. 164). The crystal structure of transition metal phosphides is shown in **Figure 5a**. The X-ray diffraction is shown in the **Figure 5b**. NbP, TaP, NbAs and TaAs crystallize in the space group I4$_1$md (no. 109).
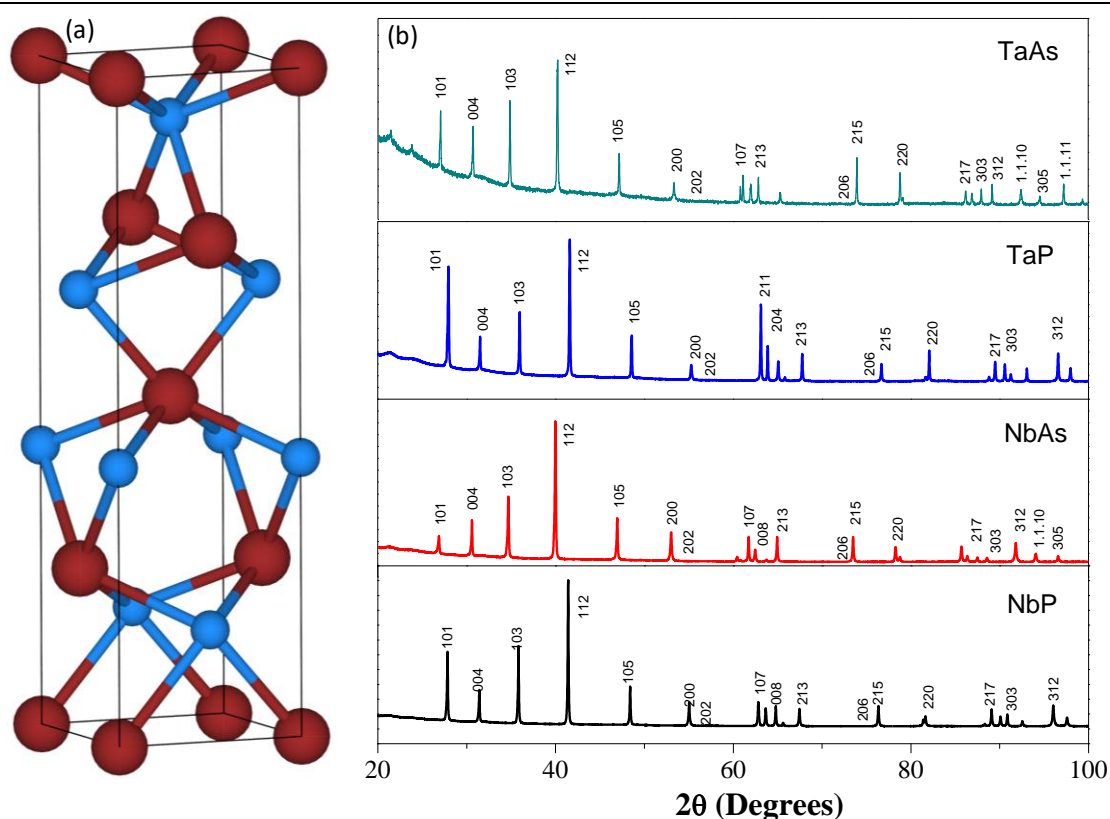
Figure 5. *(a) The representative crystal structure of transition metal pnictides which crytallize in space group I4$_1$md (no. 109). (b) The powder X-ray diffraction patterns of transition metal monopnictides are tetragonal and share the same space group.*

4.1.2 Hydrogen evolution studies

To verify our hypothesis that the new topological materials with superior electronic properties can also be highly efficient in catalysis we have tested them for dye-sensitized hydrogen evolution reaction (HER). In

the HER, solar light is absorbed by photon capture systems, such as the dye Eosin Y (EY). The resultant excited electrons can be transferred to the catalyst, on which H^+ in the water is reduced to form H_2. A schematic representation of the HER process is shown in **Figure 6**.

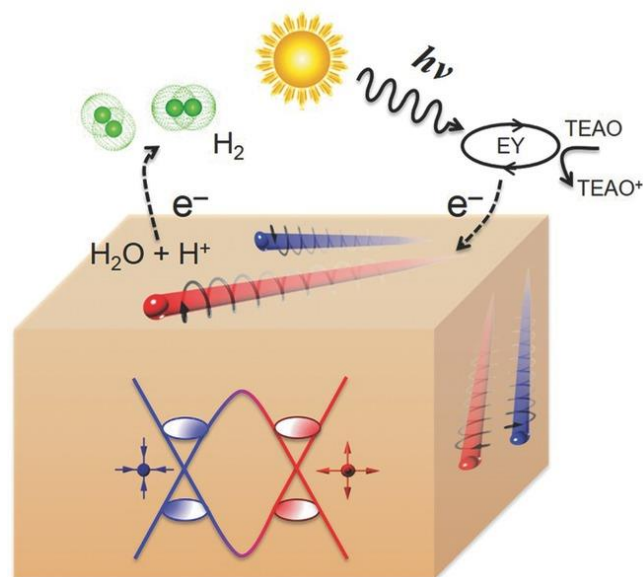**Figure 6.** *Schematic diagram of a TWS for catalyzing the dye-sensitized hydrogen evolution. When light falls upon EY it is excited and, in the presence of the sacrificial agent triethanolamine (TEAO), the dye transfers an electron to the surface of the TWS, leading to charge separation, and, thereby, reducing water to hydrogen. In a TWS the bulk bands are gapped by spin–orbit coupling in momentum space, except for some isolated linear-crossing points, namely, the Weyl points/Dirac points.*

The HER activity of 1T'-MoTe$_2$, 2H-MoTe$_2$ and 1T-TaS$_2$ powdered single crystals are compared in **Figure 7a**. 1T'-MoTe$_2$ exhibits a H_2 evolution reaching a value of 1294 µmoles g^{-1} in 6 hours. However, semiconducting 2H-MoTe$_2$ evolves only 28.14 µmoles g^{-1} in the same period. Surprisingly, metallic 1T-TaS$_2$ is completely inactive, even though it was predicted to be an active and stable metallic transition metal catalyst based on conventional free energy considerations [38]. In **Figure 7b**, we

show a histogram of the rate of H_2 evolution of the three compounds where we can clearly see that the topologically nontrivial 1T'-MoTe$_2$ is the most active catalyst.
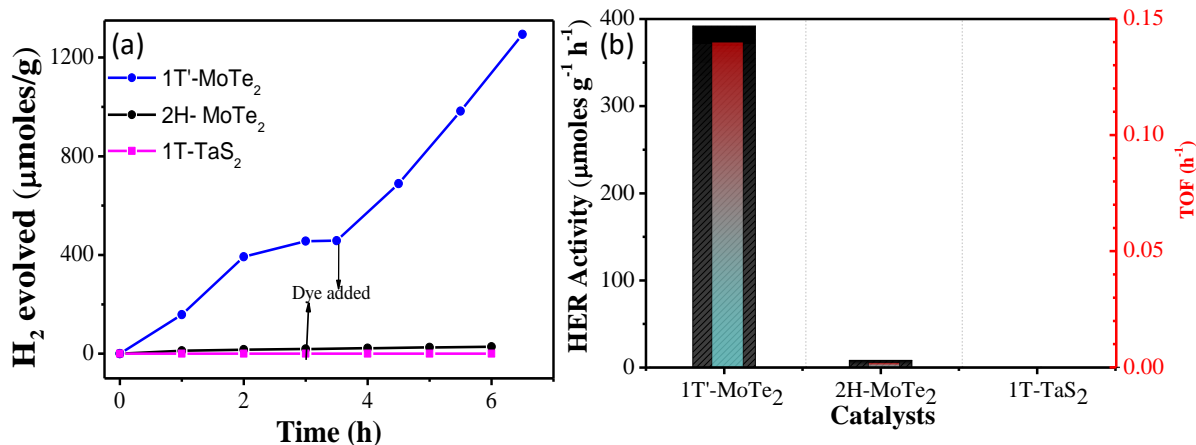

Figure 7. *Hydrogen evolution in TMDs. (a) Comparison of the rate of H$_2$ evolution using 1T'-MoTe$_2$, 2H-MoTe$_2$, and 1T-TaS$_2$. 1T'-MoTe$_2$ shows a higher activity compared to its 2H polymorph. (b) Histogram of rate of H$_2$ evolution rate using 1T'-MoTe$_2$, 2H-MoTe$_2$, and 1T-TaS$_2$.*

We are convinced that the electronic structure of Weyl semimetals favors catalysis. To test whether the metallicity alone is sufficient or rather it is the topology that is at work, we have compared the catalytic performance of several different TMDs for HER: topologically trivial semiconducting 2H-MoTe$_2$; topologically trivial metallic 1T-TaS$_2$; and topologically nontrivial 1T'-MoTe$_2$. Note that Ta has a d^1 configuration (octahedral coordination) in 1T-TaS$_2$ and Mo has a d^2 configuration (trigonal prismatic coordination) in 2H-MoS$_2$, which makes the first system metallic and the latter semiconducting. Additionally, bulk orthorhombic MoTe$_2$ is type-II Weyl semimetal [39, 49-52] while the monolayer [53] and few layers 1T'-MoTe$_2$ have non-trivial Z2 topological invariants. We show the calculated band structure of the three TMDs in **Figure 8**.
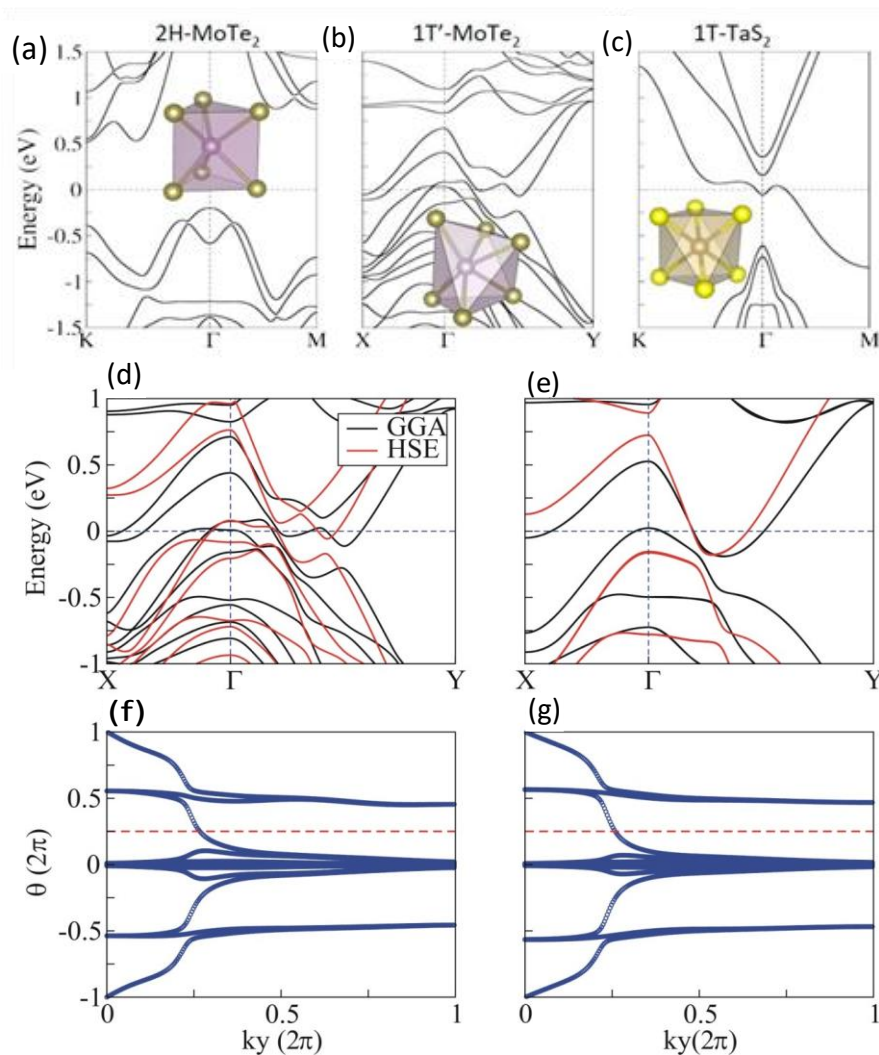
Figure 8. *Electronic band structure of transition metal dichalcogenides (TMDCs). Electronic band structure of a) semiconducting 2H-MoTe₂, b) semimetallic 1T'-MoTe₂, and, c) metallic 1T-TaS₂. The comparisons of band structures of 1T'-MoTe₂ between GGA and HSE approximations for both (d) bulk and (e) monolayer. (f, g) Wannier center evolutions for the band structure monolayer. The reference lines cross the evolution lines odd times for both (f) GGA and (g) HSE approximations, which present the non-trivial Z2 invariant. Though the band structures from GGA and HSE calculations are a little different, (such as the direct band gap is larger in HSE calculations), they predict the same topology.*

In a Weyl semimetal, the conduction and valence bands cross each other linearly through nodes **(Figure 9a)**, called the Weyl points, near the

Fermi energy. As a three dimensional analogue of graphene, TWSs are expected to exhibit very high mobility in their charge transport [11]. Similar to TIs, TWSs also present robust metallic surface states [54] that are stable against defects, impurities, and other surface modifications. Analogous to the role of graphene, in the MoS_2 catalyzed HER, we believe that the highly mobile TWS bulk states help electrons diffuse freely and quickly.

Furthermore, the topological surface states may cause the surface to act as stable active planes for catalysis. The first family of TWSs that was experimentally discovered, from direct observations of their topological surface states, were the transition metal monopnictides: NbP, TaP, NbAs, and TaAs [55-59] These materials are semimetals wherein Weyl points are located near the Fermi level with a total of 12 pairs of Weyl nodes in the first Brillouin zone. For this reason, we have investigated the HER activity in these TWS compounds **(Figure 9b)**.
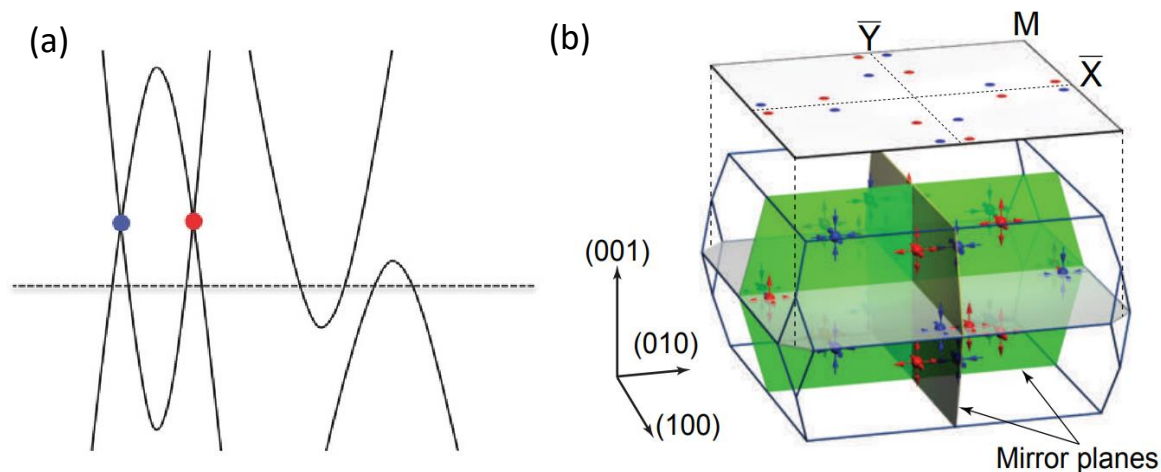

Figure 9. Schematic band structure of the transition metal monopnictide TWS family, revealing semimetallic character. The first Brillouin zone with twelve pairs of Weyl points. The red and blue spheres represent the Weyl points with "+" and "-" chirality, respectively. The arrows surround a Weyl point stand for the monopole-like distribution of the Berry curvature.

The HER activities of NbP, TaP, NbAs, and TaAs were studied over a period of 6 hours. Our studies show that all four TWSs are highly HER active and NbP, being the lightest among all, performs the best as an HER catalyst with the highest value of H_2 evolved per gram of the catalyst (3520 µmoles g-1) **(Figure 10a)**. We show the activity and turnover frequency (TOF: the number of moles of H_2 evolved per mole of catalyst used) as histograms for all four compounds in **Figure 10 b**
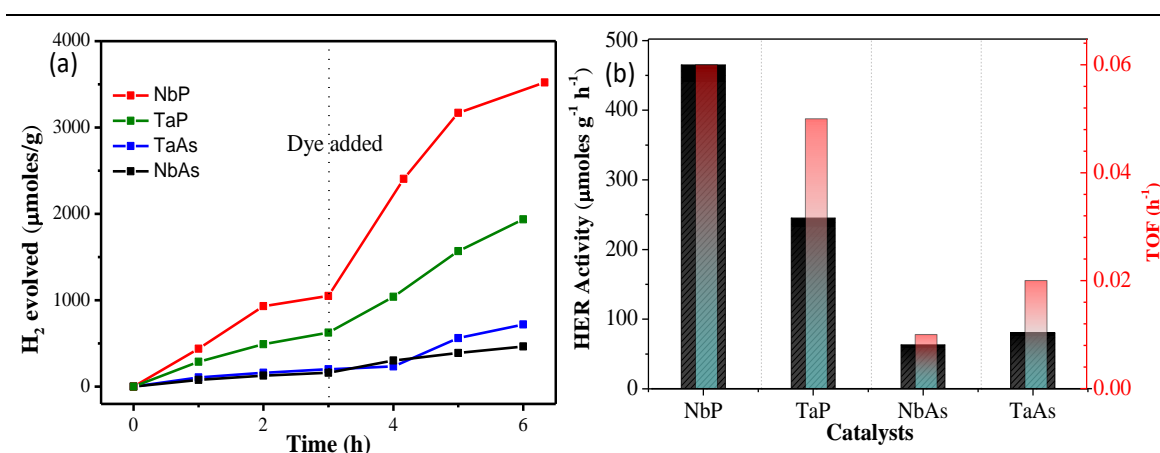
Figure 10. *Comparison of hydrogen evolution activity of various TWSs (NbP, TaP, NbAs, and TaAs) powdered single crystals with an intermediate dye addition. c) Histogram of hydrogen evolution rate and TOF, shown on left and right axes, respectively, for all four compounds.*

. In general, phosphides are better HER catalysts than arsenides. We note that all 4 compounds are WSMs with well- defined and distinct Weyl points and each has very high mobilities from the linearly dispersed bands at the Weyl points, which accounts for their high catalytic activities. We compare and summarize the activity of Weyl semimetals in **Table 1.** WSMs was further explored for HER to understand their role in catalysis. We studied effect of their size, recyclability and hydrogen evolution sites were examined using theoretical calculations.

Table 1: Summary of HER activity and TOF of WSMs

Catalyst	H$_2$ Evolution (µmoles g^{-1} h^{-1})	TOF (h^{-1})
1T'-MoTe$_2$ crystal	392	0.14
2H-MoTe$_2$ crystal	8	0.002
1T-TaS$_2$ crystal	0	0
NbP polycrystal	1140	0.14
NbP crystal	465	0.06
TaP crystal	245	0.05
TaAs crystal	80	0.02
NbAs crystal	63	0.01

Since water splitting is surface phenomenon, increasing the surface area would increase the activity of the catalyst. We sonicated 1T'-MoTe$_2$ single crystals for equal duration of time and studied their HER activity over the period of time. The activity of both single crystals and polycrystalline samples of 1T'-MoTe$_2$ did not exhibit much change **(Figure 11 a)**.
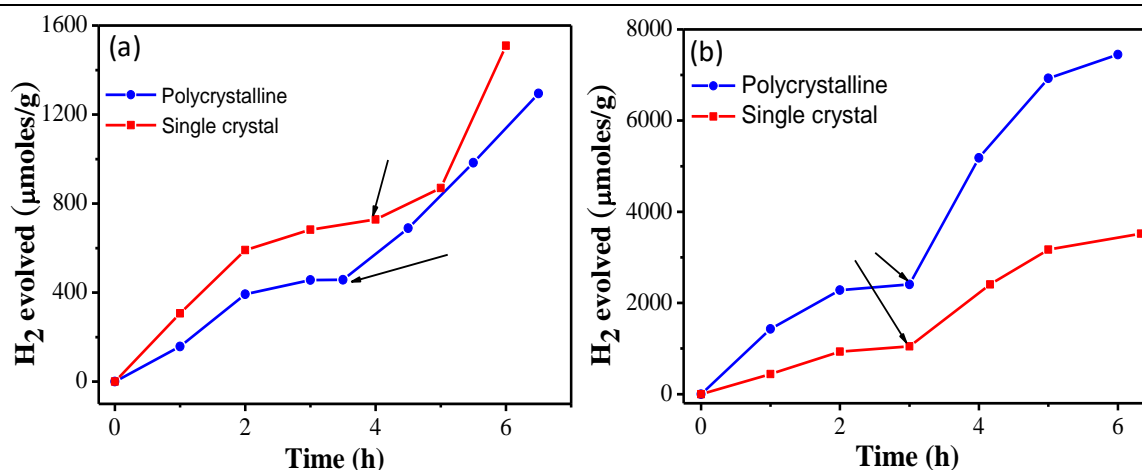

Figure 11. *(a) Comparison of H$_2$ evolution of (a) polycrystalline 1T'-MoTe$_2$ with single crystalline 1T'-MoTe$_2$ and (b) polycrystalline NbP with single crystal NbP.*

The following observation could be attributed to the nature of the single crystals which can be exfoliated upon sonication. The total surface

area of single crystals on exfoliation can be comparable to that of polycrystals and thereby exhibiting comparable activities. Unlike $MoTe_2$, NbP polycrystalline samples do not break upon sonication. We compare the activity of crushed single crystals (few μm in size) with polycrystalline one (sub-micron (150-300 nm) in size) obtained by solid state reaction. We observe 2-fold increase in the activity for polycrystalline samples due to larger surface area of the latter. Thus, the increase in surface area will increase the activity of the samples due to more active sites **(Figure 11 b)**.The compounds can undergo many cycles of HER without activity fading as can be seen in **Figure 12**, where we show three cycles of HER in NbP and $MoTe_2$ with a comparable catalytic performance each time. The activity was stable and robust.

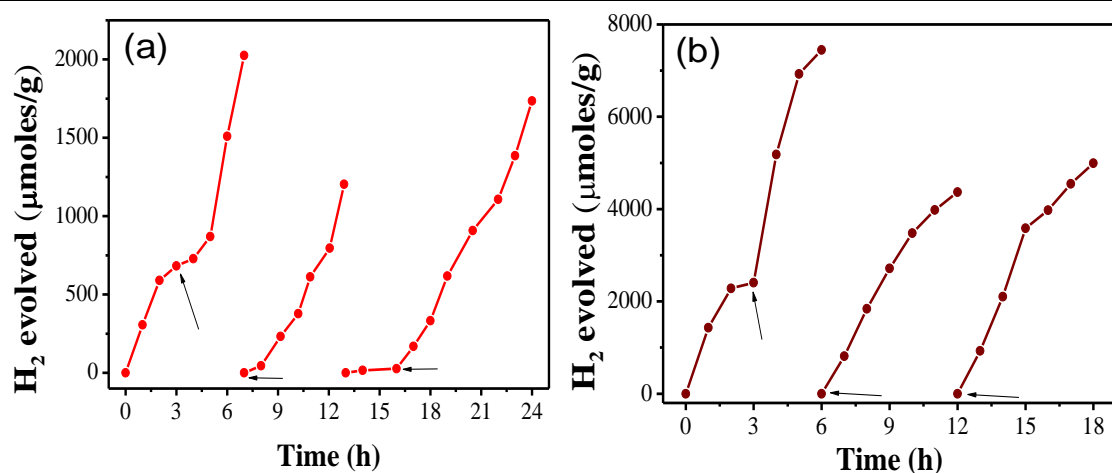**Figure 12.** *(a) Cycling Studies of polycrystalline (a) 1T'-MoTe$_2$ and (b) NbP powder in the presence of dye. indicating the stability of H$_2$ evolution. The addition of dye is marked with* arrows *and the mixture was purged with nitrogen to regenerate the surface after 6 h, 12 h and 24 h.*

Chemical analysis shows no observable changes in chemical composition of our catalysts **(Figure 13)** after several HER cycles.
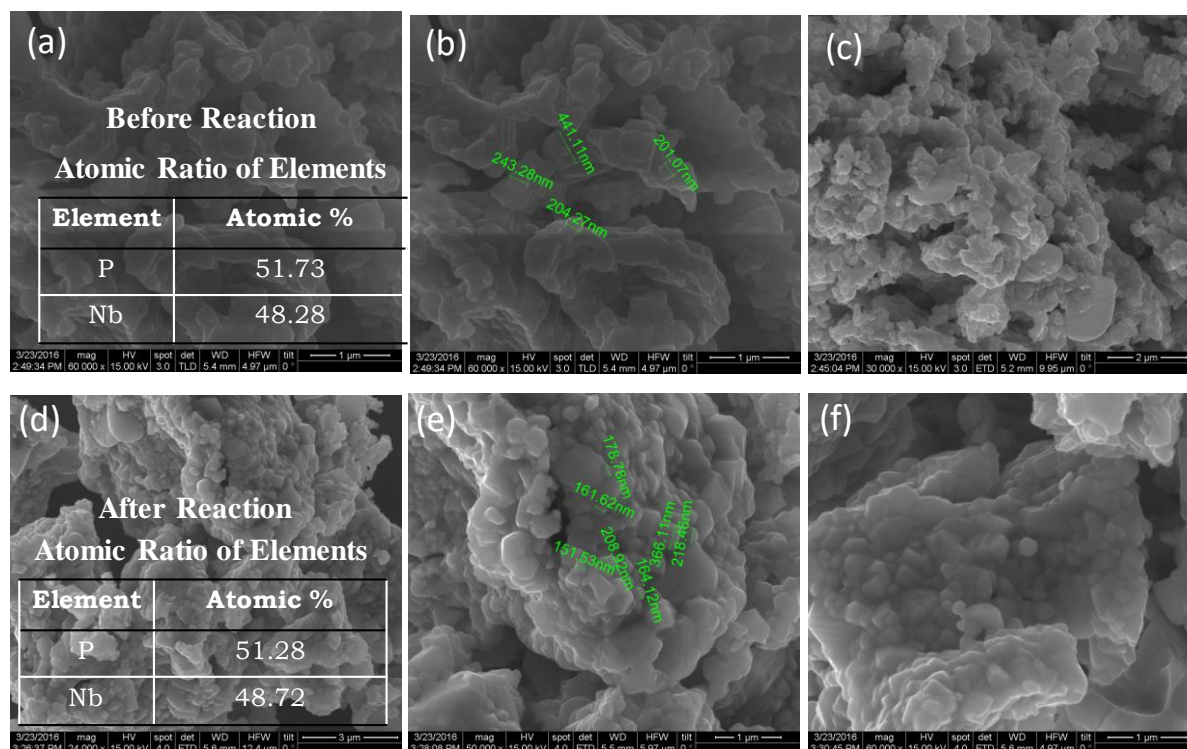
Figure 13. *(a), and (b) FESEM of polycrystalline NbP before catalysis; d) and e) FESEM of polycrystalline NbP after catalysis. The atomic percentages of Nb are 48.27 and 48.72 respectively before and after catalysis and the atomic percentages of P are 51.73 and 51.28 respectively before and after catalysis. The chemical composition of the NbP remains unaltered within the limits of experimental error. (e) and (f) FESEM images of powdered NbP single crystals*

4.1.3 Comparison with some highly active catalyst for HER

We compare the activity in terms of per gram of the catalyst and TOF is comparable to catalysts such as Ni metal nanoparticles [60] and highly active platinum decorated TiO_2 nanoparticles, [61] under similar experimental conditions. In order to draw any conclusive effect of the kinetics we must scale the activity per surface area of the catalyst **(Figure 14)** (The surface area of NbP was 12.3 m^2/g via N_2 adsorption using BET method). Interestingly, here NbP performs much better than the Ni nanoparticles with an activity that is one order of magnitude higher,

despite the fact that the latter has a ΔG_H value closer to zero. Moreover, the HER activity of NbP is also higher compared to Pt–TiO$_2$ (Pt-P25), where the catalytic sites mostly reside at the metallic surface of Pt. The titania nanoparticles used were a mixture of anatase and rutile, and the interfaces of these two polymorphs have been identified as an excellent medium for electron and hole separation. For SrNbO$_3$, a well-known visible light absorbing metallic oxide, the activity per unit surface area is two orders of magnitude smaller than for NbP [62].
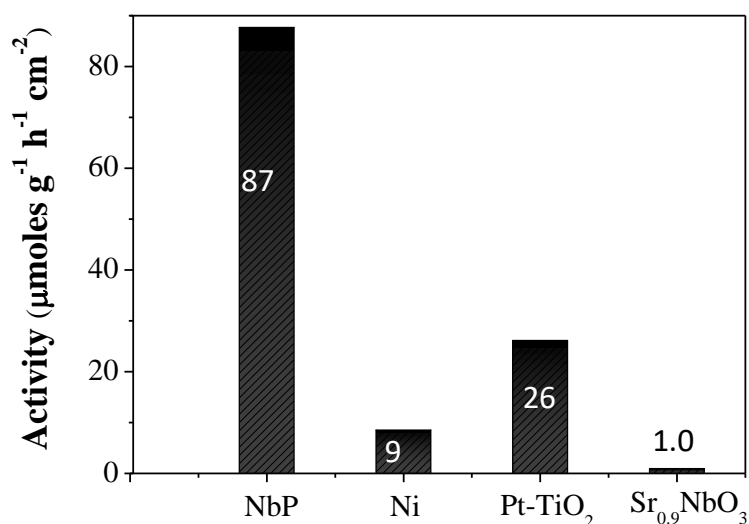
Figure 14. *Histogram of HER activity of polycrystalline NbP, Ni-metal nanoparticles, Pt-TiO$_2$ and Sr$_{0.9}$NbO$_3$ scaled to the surface are of the catalysts.*

We compare the electronic properties of NbP and Ni in order to gain insights into the higher HER activity of NbP compared to Ni, when conventional considerations would suggest the opposite (ΔG_{H*} is more favorable for Ni than NbP). We note that Ni is highly metallic with a room temperature conductivity of $\approx 10^7$ S m^{-1}; on the other hand, NbP is semimetallic ($\approx 10^6$ S m^{-1} at room temperature). As the conductivity σ is related to the mobility through the density of charge carriers ($\sigma = \mu n e$,

where μ is the mobility, n is the carrier density, and e is the electronic charge), the carriers are much more mobile in NbP as compared to Ni, because of the much smaller carrier density in NbP. The average mobility of NbP is of the order of 10^3 cm^2 V^{-1} s^{-1} as compared to $\approx$10 cm^2 V^{-1} s^{-1} in Ni at room temperature [11]. The effect of mobility on the hydrogen evolution reaction has been discussed in the literature, however, has mostly been focused on composite catalysts where graphene is used as a medium to provide for a high mobility of the carriers since graphene has no active catalytic sites [63]. Such a material requirement can be overcome in systems where catalytic active sites, as well as high carrier mobility, can be integrated together, for example, the Weyl semimetals studied herein. A large electronic mobility facilitates the rapid transfer of carriers for the catalytic reactions, thereby enhancing the kinetics of HER. It also helps for the rapid separation of electrons and holes. Recent studies on TaAs shows that the bulk Weyl nodes and, therefore, the states close to the projected Fermi arcs on the surfaces, predominantly carry Ta-orbital character [64]. This implies that the As states, as well as the surface states from the trivial bands, are prone to delocalize into the bulk, whereas the Ta states are comparatively more robust on the surface. We, therefore, speculate an important role for transition metal states on the hydrogen evolution activity in our catalysts.

4.1.4 Theoretical analysis

(Theoretical calculations were carried out by Dr. Binghai Yan and co-workers in Max Planck Institute for the Physics of Complex Systems, Dresden, Germany)

To compare the catalysis activity, we have further calculated the Gibbs free energy of H adsorption in the most stable sites of each material. The data was collected and listed in **Table 2**. The Gibbs free energy ΔG_{H*} of H adsorption on the basal surface of each material are calculated to describe the trends of hydrogen evolution reaction. It was calculated as

$$\Delta G_H = \Delta E_H + \Delta E_{ZPE} - T\Delta S \quad (2)$$

Here, ΔE_{ZPE} and ΔS are the difference in zero-point energy and entropy between the adsorbed species and the gas phase molecule, respectively. For the adsorbed species, they can be determined from the vibrational frequencies of the adsorbed species using normal mode analysis with DFT calculation [65]. While for the gas phase molecule, the zero-point energy of H_2 and the TS at room temperature (300K) can be looked up from standard molecular tables [66]. ΔE_H is the hydrogen binding energy which was calculated as

$$\Delta E_H = E_{(surface+H)} - E_{(surface)} - 1/2 \; E_{(H2)} \quad (3).$$

The $E_{(surface+H)}$, $E_{(surface)}$ and $E_{(H2)}$ are the total energy of respective parts.

The Gibb's free energy (ΔG_{H*}) of adsorption of hydrogen at the catalyst surface is very often used to predict the activity of an HER catalyst. The closer this value is to zero the better is the performance. We therefore

expect that the catalytic HER properties within this series will be determined by the chemical bonding of hydrogen at the surface, which is reflected in the value of ΔG_{H*}. Indeed, we find that their HER activity is correlated with the ΔG_{H*} values for these compounds. The ΔG_{H*} (on abscissa) and the activity (on ordinate) hence make a so-called volcano diagram **(Figure 15)**.
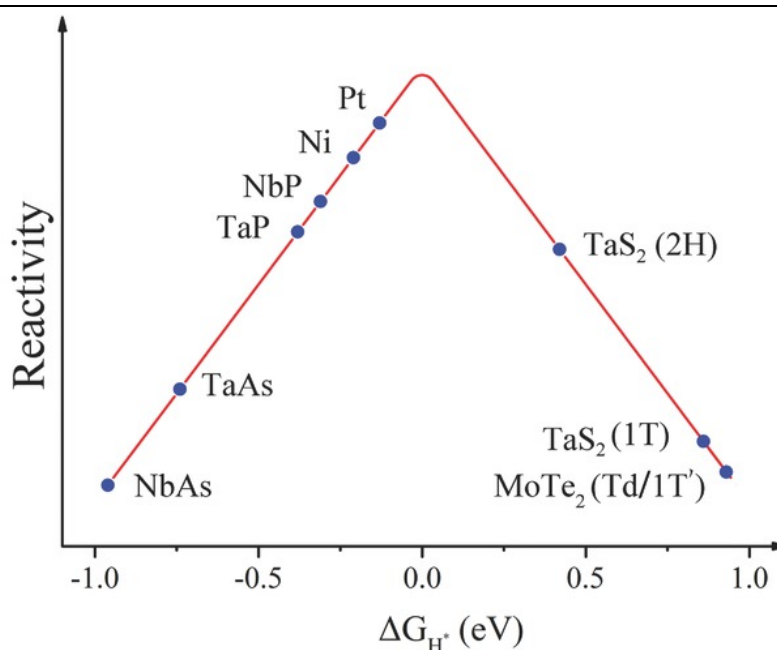
Figure 15. *Predicted relative activities of various HER catalysts following the volcanic scheme as a function of calculated free energy of adsorption of hydrogen on the surface of the catalyst.*

We consider below the recently discovered Weyl semimetals, NbAs, TaAs, NbP and TaP. To model H adsorption on the basal surface, a 2×2 supercell of NbP, TaP, NbAs, and TaAs (001) surface with 24 atom layers in thick was used in our calculation. For the transition metal dichalcogenides, since they are layer structures, a single molecular layer of $4 \times 2\sqrt{3}$ orthogonal supercell with 4 metal atoms in each direction are

used. For Ni and Pt, the (111) surface with 4×4 supercell and 6 atom layers thick was used. The vacuum layer was larger than 10 Å in all the calculation. NbP has the lowest ΔG_{H^*} among all these compounds followed by TaP, TaAs and NbAs and TOF also follows a similar trend.

Notwithstanding that both 1T-TaS$_2$ and 1T'-MoTe$_2$ are metallic with comparable ΔGH^* values, the HER activity of these two compounds is quite different. As mentioned earlier, 1T-TaS$_2$ shows almost no HER activity whereas 1T'-MoTe$_2$ shows a very high activity. Since few layer 1T'-MoTe$_2$ rather exhibits topological features in its band structure, this has encouraged us to consider the possible role of topological effects. The Gibbs free energy of Weyl semimetals is listed in **Table 2**.

Table 2. Gibbs Free energy of the most stable structure in different materials.

Materials	Gibbs free energy (eV)
NbAs	-0.96
TaAs	-0.74
TaP	-0.38
NbP	-0.31
Ni	-0.22
Pt	-0.12
MoTe$_2$(2H phase)	1.89
MoTe$_2$(1T' phase)	0.93
TaS$_2$(1T phase)	0.86

Notwithstanding that both 1T-TaS$_2$ and 1T'-MoTe$_2$ are metallic with comparable ΔG_{H^*} values, the HER activity of these two compounds is quite different. As mentioned earlier, 1T-TaS$_2$ shows almost no HER activity whereas 1T'-MoTe$_2$ shows a very high activity. Since few layer 1T'-MoTe$_2$ rather exhibits topological features in its band structure, this has encouraged us to consider the possible role of topological effects.

Further, we have identified preferred catalytic sites numerically. From the free energy calculations, we find that the bridge sites in the Nb/Ta terminated surface are the most active catalytic sites (**Figure 16** in the Supporting Information). In the case of P/As terminated surface, hollow sites are comparatively more active. The details of active catalytic sites for other catalysts are discussed in **Figures 17-19**.

As/P-terminal

(a) top-site (b) top-site (c) hollow-site (d) hollow-site (e) bridge-site (f) bridge-site

Ta/Nb-terminal

(g) top-site (h) top-site (i) hollow-site (j) hollow-site (k) bridge-site (l) bridge-site
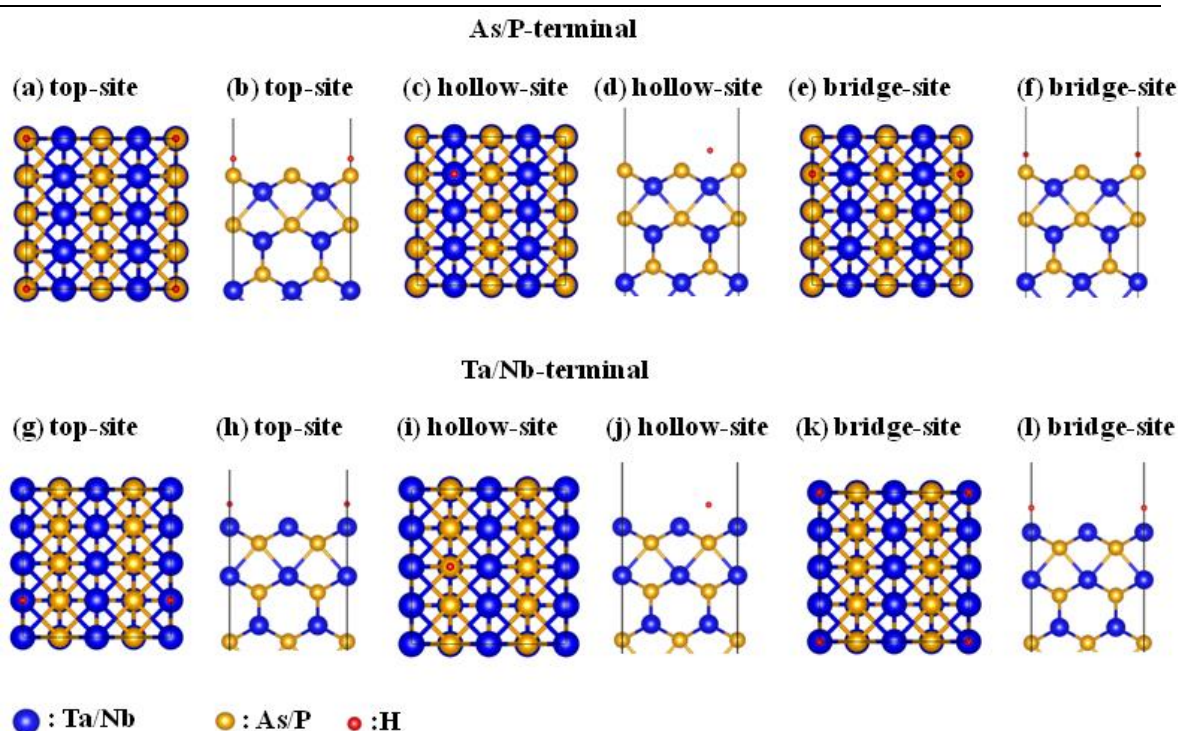
● : Ta/Nb   ○ : As/P   ● : H

Figure 16. *Three possible reaction sites were checked for both (a-f) As/P and (g-l) Ta/Nb terminals. Both top-view and side-view are given for each site.*

We have tried the top, hollow, and bridge sites to identify the most reactive surface sites. For the four transition metal monoarsenides/phosphides Weyl semimetals, we have performed the check for both As/P and Ta/Nb terminals, as shown in **Figure 17**, and the absorption energy for hydrogen is summarized in **Table 3**, from which we can see that the most active sites for As/P terminal is the hollow site and that for Ta/Nb terminal is bridge site. Therefore, the most active sites were used for the simulations of the catalysis. Further analysis of the Gibb's energy, we found that the Ta/Nb terminal is more preferred for the catalyst progress.

Table 3. Absorption energy of H on different sites for both As/P and Ta/Nb terminals in transition metal monoarsenides/phosphides Weyl semimetals.

Catalysts	Absorption energy for As/P terminal (eV)			Absorption energy for Ta/Nb terminal (eV)		
	Top site	Hollow site	Bridge site	Top site	Hollow site	Bridge site
NbAs	--	0.13560	0.43406	--	--	-1.33874
TaAs	--	0.89027	0.89162	--	0.06317	-0.73334
TaP	--	0.41192	0.88421	--	-0.00477	-1.00938
NbP	--	0.77633	0.94563	--	0.10277	-0.84421

The "--" means the atom H cannot be stable on corresponding sites in the simulation progress.

Different configuration of H atoms on Ni and Pt (111) surface are shown in **Figure 17**. To better describe the adsorption sites, different atom layers are distinguished by different atom sizes. For fcc configuration, the

atom below the adsorbed H atom is the third layer Pt atom, while for hcp configuration, the atom below the adsorbed H atoms is the second layer Pt atom. For Pt the most energy preferable adsorption sites is top site, while for Ni, the fcc sites is most stable sites.
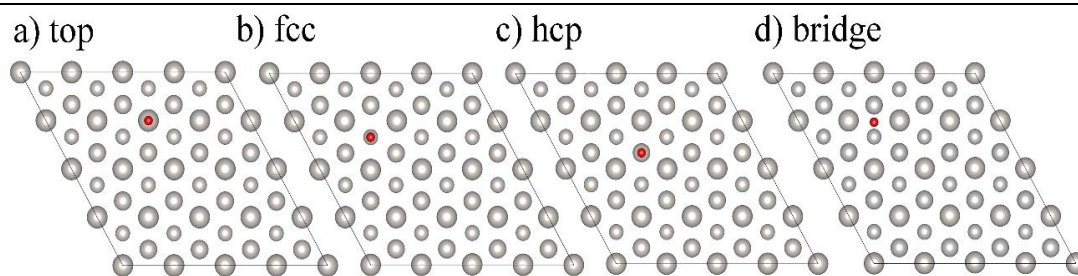
Figure 17. *Four possible reaction sites were checked for both Ni and Pt. The biggest, middle and smallest white atoms represent first, second and third layer of atoms, respectively.*

The corresponding adsorption energies are shown in **Table 4**.

Table 4. Adsorption energy (in eV) for Ni and Pt (111) surface.

Catalyst	top	fcc	hcp	bridge
Ni	0.07	-0.45	-0.44	--
Pt	-0.48	-0.43	-0.38	-0.40

We have also checked several possible sites both for 1T'-MoTe$_2$ and 2H-MoTe$_2$ phase. For 2H-MoTe$_2$, one top (t1), one bridge (b1) and two hollow sites (h1 and h2) has been considered as shown in **Figure 18 (a-c)**. The results indicate that H tend to be adsorbed in hollow sites (h1 and h2). If it was putted in other sites, it will transfer to h1 site automatically after

relaxation. The adsorption energy of H in h1 and h2 sites are 1.69 eV eV and 1.80 eV, respectively. While for 1T'-MoTe$_2$, which can be regarded as distorted 1T phase, three bridge (b1, b2, b3), two top (t1, t2) and a hollow sites (h1) were calculated. Among these possible adsorption sites, only t1 and t2 can be obtained after relaxation as shown in **Figure 18 (e-f)**. The adsorption energies of t1 and t2 configuration are 1.48 and 0.62 eV, respectively.
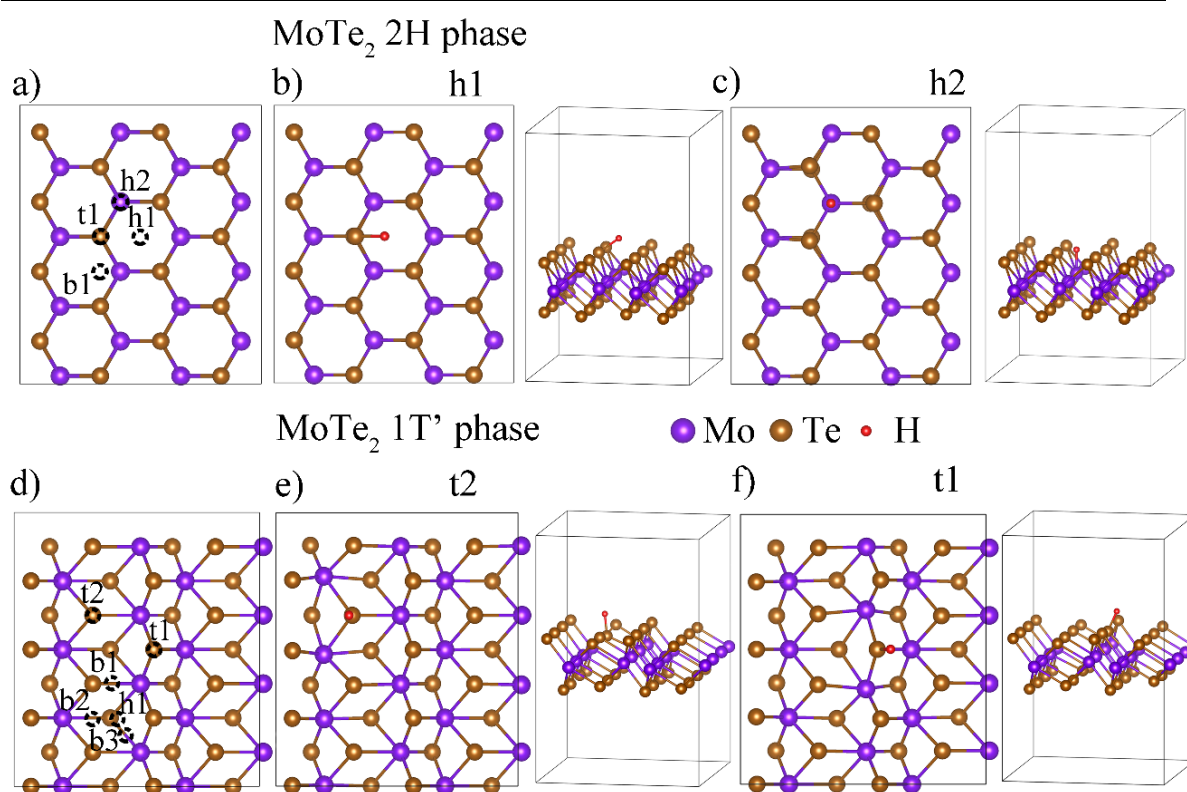
Figure 18. *a, d) Possible adsorption sites for 2H -MoTe$_2$ and 1T'-MoTe$_2$, respectively. The most stable and metastable adsorption configuration for 2H-MoTe$_2$ (b, c) and 1T'-MoTe2 (e, f), respectively.*

Comparing to 1T'-MoTe$_2$, 1T-TaS$_2$ has higher symmetry, therefore we have only considered one top (t1), one bridge (b1) and two hollow sites (h1 and h2). Finally, two adsorption configuration was obtained as in **Figure 19**, with the adsorption energy of 0.58 eV for t1 and 0.72 eV for h2,

respectively. For other sites, H atom will transfer to t1 sites, further verified the stability of H in t1 site.

Figure 19. *(a) Different sites were checked for 1T-TaS₂. (b, c) The most stable and metastable adsorption configuration, respectively.*

TWSs serve as excellent candidates for catalysis. We have shown that inherent metallicity alone in a material does not improve catalytic activity, and that the most important factors that one must consider are electronic p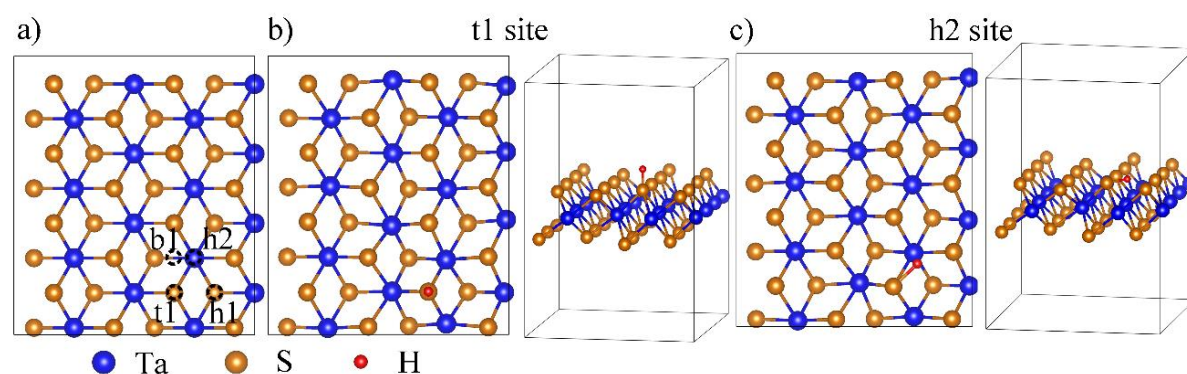roperties as well as the mobility of carriers. Among the transition metal monopnictides, the phosphides are better for HER compared to the arsenides. These catalysts are also robust and therefore can be used long term. They are also durable and have no significant changes in chemical composition after the catalytic procedure. We already observe an improvement in the HER activity with the size reduction when we compare the single crystals and the polycrystalline material. Size reduction plays a more important role in topological materials because the surface states are protected by topology compared to trivial metals. Hence, the effect of disorder will be minimized in topological materials. The activities of TWSs can further be improved significantly by reducing the

particle size, for example, by forming them as nanoparticles until the bulk remains metallic.

We further explore another class of topologically non-trivial compound, topological insulators (TIs). The catalyst studied were bismuth chalcogenides based topological insulators.

4.2   Topological insulators

4.2.1   Structural Characterization

Bi_2Se_3, Bi_2Te_3, Bi_2Se_2Te and Sb_2Te_2Se are layered materials with X-M-X-M-X layers comprising of quintuple layer comprising of a unit cell. The crystal structures of these compounds are shown in the **Figure 20 a**. The powder X-ray diffraction (PXRD) pattern of these compounds studied are shown in **Figure 20 b**. The compounds crystallize in the space group R-3m (no. 166).
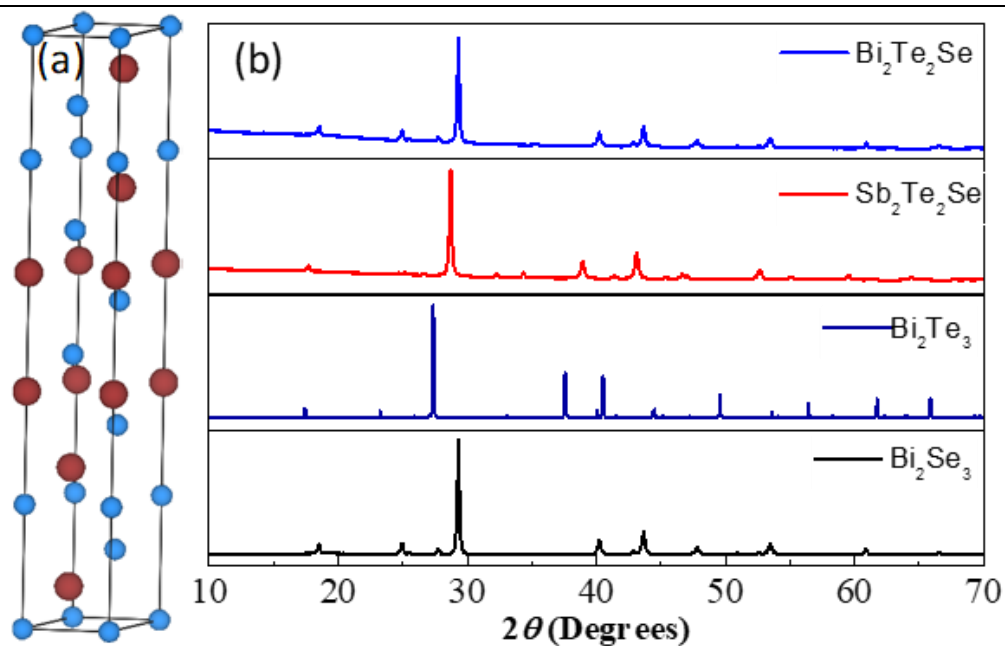
Figure 20. *(a) Representative crystal of bismuth chalcogenides. (b) Powder X-ray diffraction patterns of Bi_2Se_3 Bi_2Te_3, Sb_2Te_2Se and Bi_2Te_2Se.*

The nanosheets of Bi_2Te_3 were synthesized and characterized using PXRD. The nanosheets of Bi_2Te_3 were synthesized and characterized using PXRD. The X-ray diffraction pattern was similar to that of bulk form, except less intense (006) basal reflection **(Figure 21 a)**. The surface area of the nanosheets was around 14.6 m^2 g^{-1} as calculated from N_2 adsorption via BET method **(Figure 21 b)**. The High resolution transmission reflection microscopy (TEM) and selected area electron diffraction for the nanosheets is shown in **Figure 21 c and d**.

Figure 21. *(a) The X-ray diffraction pattern of Bi2Te3 nanosheets. (b) N_2 Adsorption isotherm of Bi_2Te_3 nanoparticles. The surface area of the nanosheets are determined to be 14.6 m^2 g^{-1}. (c) HRTEM images of Bi_2Te_3 nanosheets had an average flake size of ~400 nm (inset of TEM). The SAED exhibit high crystallinity of the sample*

4.2.2 Hydrogen evolution studies

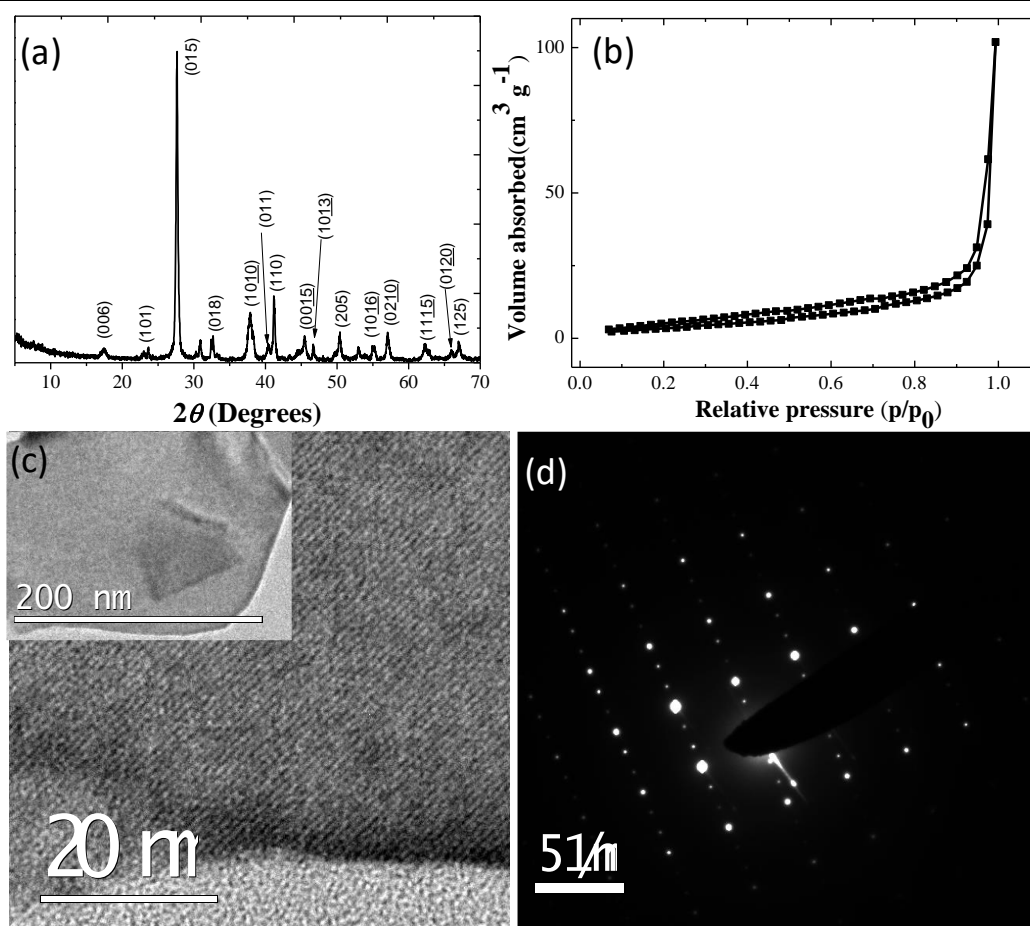Photocatalytic HER study was carried out with single crystals of Bi_2Te_3, Bi_2Se_3, Bi_2Se_2Te and Sb_2Te_2Se over a period of 6 hours. The hydrogen evolution was studied via same technique we studied for Weyl semimetals **(Figure 6)**. The hydrogen evolved after three hours in Bi_2Te_3 was 192 µmoles g^{-1} which increases to 627 µmoles g^{-1} on further addition of 14 µmol of dye after 3 hours shown in figure 3. Hydrogen evolved after three hours in Bi_2Te_2Se was 152 µmoles g^{-1} which increases to 447 µmoles g^{-1} on further addition of dye **(Figure 22 a)**.
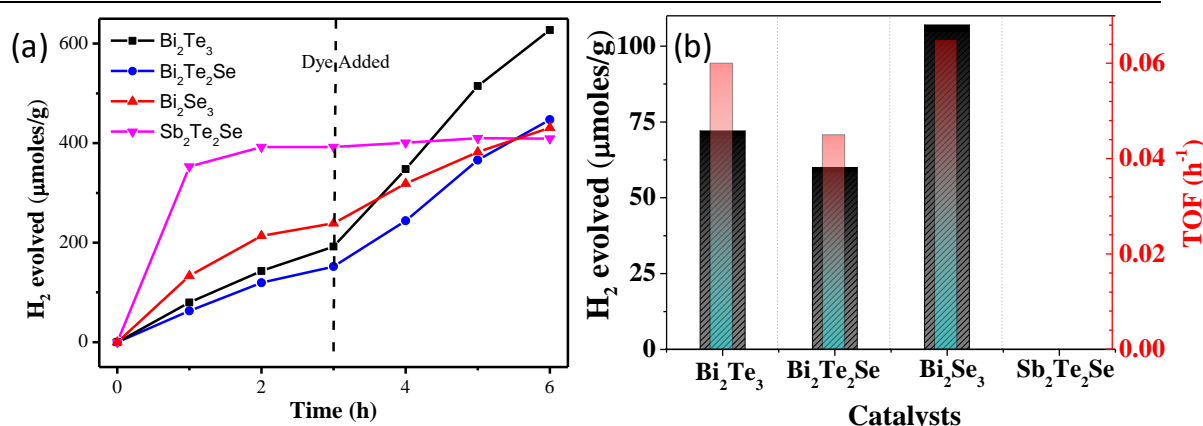
Figure 22. *(a) Catalytic behavior of the topological insulators under study. 3 is the most active among the series. (b) Histogram of hydrogen evolution rate and TOF, shown on left and right axes, respectively, for all four compounds.*

The hydrogen evolved after three hours in Sb_2Te_2Se was 395 µmoles g^{-1} which does not show significant increase on further addition of dye. The photocatalytic activity of Bi_2Te_3 and Bi_2Te_2Se was 72 and 60 µmoles h^{-1} g^{-1} with TOF of 0.06 and 0.045 h^{-1} and further increase to 161 and 107 µmoles h^{-1} g^{-1} with TOF of 0.13 and 0.08 h^{-1} **(Figure 22 b)**. The Sb_2Te_2Se a topologically trivial material does not exhibit with an activity for an hour

(196 µmoles h^{-1} g^{-1}) and TOF of 0.11 h^{-1} with no activity in the later 5 hours even on further on addition of dye **(Figure 22 a)**. We observed superior photocatalytic hydrogen evolution in Bi$_2$Se$_3$, but it was not as robust as Bi$_2$Te$_3$, decomposing in the reaction mixture during HER further increase to 161 and 107 µmoles h^{-1} g^{-1} with TOF of 0.13 and 0.08 h^{-1}. We observe that the activity of Bi$_2$Te$_3$ and Bi$_2$Te$_2$Se is comparable but over the period the activity of the selenium substituted Bi$_2$Te$_3$ decreases significantly with respect to Bi$_2$Te$_3$. In Bi$_2$Te$_2$Se the Se-sites are passivated over the period which leads to decrease in number of active sites thereby overall decrease in the activity. Thus, activity of Bi$_2$Te$_2$Se is lower with respect to Bi$_2$Te$_3$ in long period of observation. Similarly, we observe that activity of Bi$_2$Se$_3$ decrease considerably due to passivation of the catalyst surface. We observed superior photocatalytic hydrogen evolution in Bi$_2$Se$_3$, but it was not as robust as Bi$_2$Te$_3$, decomposing in the reaction mixture during HER.

The hydrogen evolution activity of Bi$_2$Te$_3$ was also tested with nanosheets. The hydrogen evolved in Bi$_2$Te$_3$ nanosheets after 3 hours was 2018 µmoles g^{-1} which increases to 5521 µmoles g^{-1} after 6 hours, with no further addition of dye shown in **Figure 23 a**. The surface area of these nanosheets was 14.6 m^2 g^{-1} **(Figure 21 b)**. The activity of nanosheets is clearly better in comparison to single crystals due to the high surface area and greater active sites available for water reduction. Bi$_2$Te$_3$ crystals can be cycled for the hydrogen evolution whereas the activity of the nanosheets is lower in the second cycle, not so remarkable and needs improvement **(Figure 23 b and c)**.
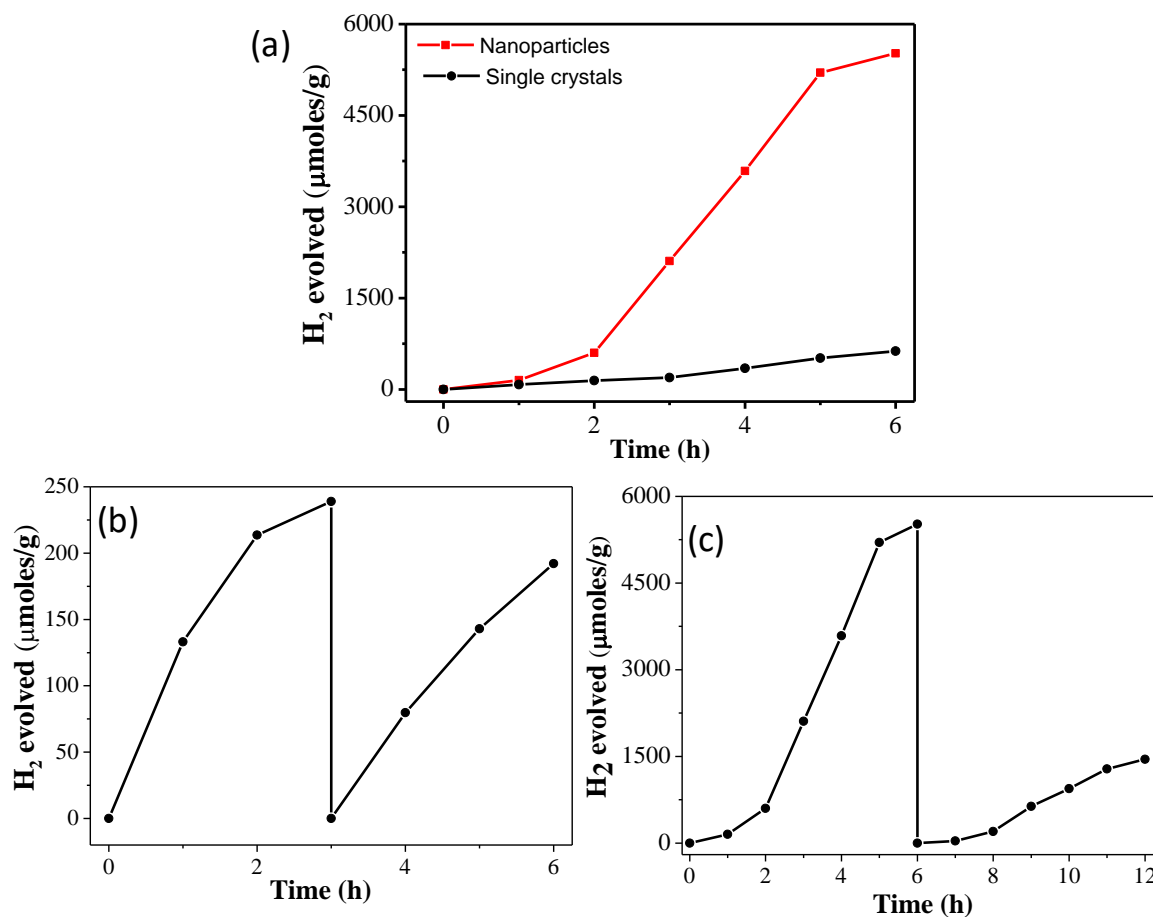
Figure 23. *(a) Comparison of HER activity of single crystals of Bi_2Te_3 with nanosheets of Bi_2Te_3. Cycling studies to check the stability of the: **(b)** Bi_2Te_3 single crystals and **(c)** nanosheets in solution.*

Figure 24. *SEM images of Bi_2Te_3 before and after HER studies. We observe morphology changes after HER.*

The stability of Bi_2Te_3 was tested by soaking them in the reaction mixture for 24 h and performing EDX study before and after catalysis **(Figure 24)**. The morphology of Bi_2Te_3 changes after HER. The atomic percentage before and after catalysis for Bi: 37.51; 29.84 and Te: 62.49; 70.15 respectively. The change in morphology may be attributed to slow decomposition of the compound which result in reduced activity as observed in **Figure 23 c**.

4.2.3   Absorbance Studies

The steady state absorption spectra of the dye recorded with and without catalyst is shown in **Figure 25 a**. The topological surface can protect the electrons on the surface and assist the HER by increasing the life time of the excited electron. The following concept was probed by Transient absorption (TA) spectroscopy. The dye was taken in (15 % v/v) triethanolamine solution and was excited at various wavelengths (480, 520, 560 and 600 nm) as shown in **Figure 25 b**. The maximum intensity was obtained at 560 nm. The catalyst was then added to the solution and was excited at 560 nm. Interestingly, we observe increase in the intensity of the peak in the presence of the catalyst. The concentration of the catalyst was maintained as it was in the HER. The TA-curve indicates that electron on the surface of the catalyst stayed for a longer time as compared to the dye **(Figure 25 c)**. The TA spectra recorded at 200 ps time pulse for 5 fs clearly indicates that the electron decay occurs immediately on the dye in the absence of the dye whereas in the presence of the catalyst occurs much

slowly (Figure 25 d). Therefore, electron on the surface of the catalyst is protected from decaying faster comparatively.
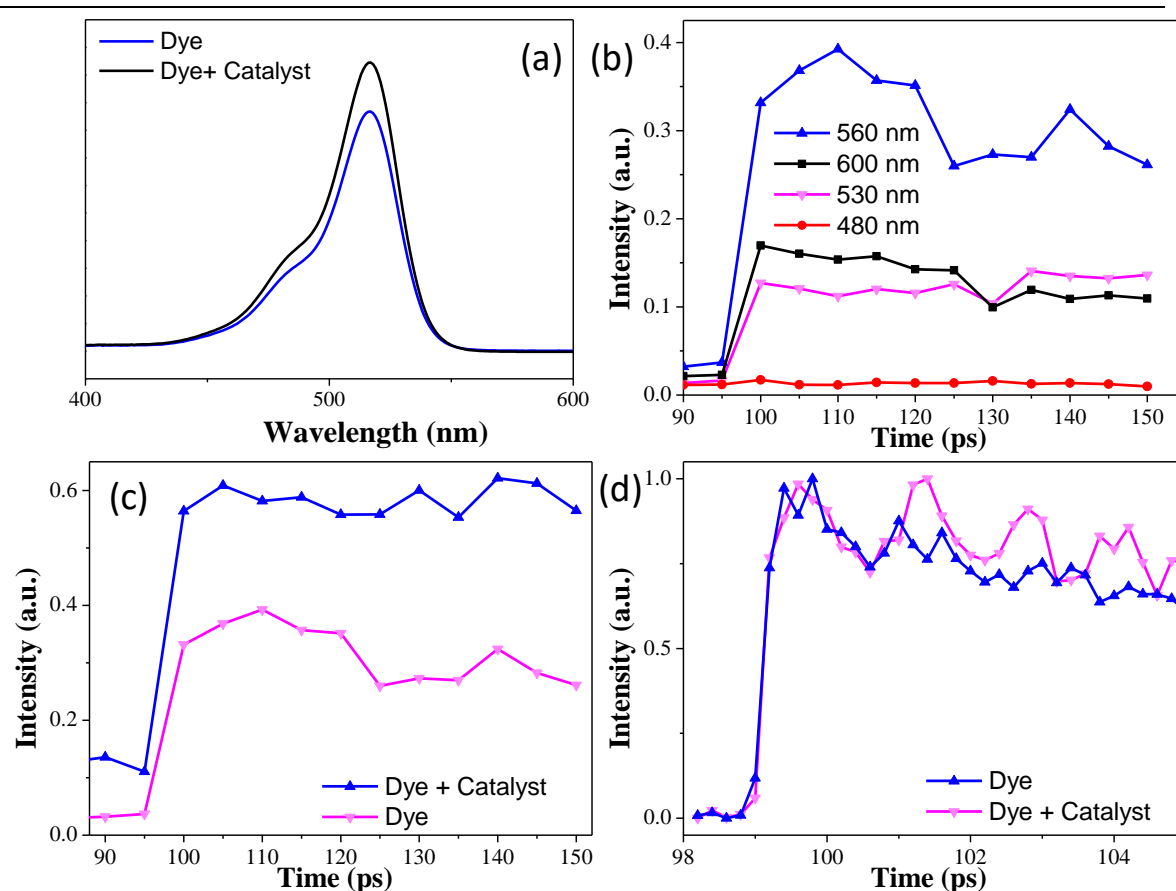
Figure 25. *(a) Steady state absorption spectra of dye and dye with catalyst in triethanolamine solution (15 % v/v) (b) Transient state absorption of dye in triethanolamine excited at various wavelengths (480, 530, 560 and 600 nm). The comparison of transition absorption spectra of dye and catalyst in triethanolamine: c) at 5 ps pulse and d) 200 fs pulse at 560 nm excitation.*

4.2.4 Electrochemical studies

Mott–Schottky analysis of the sample was done at the onset potential of the sample under the reaction conditions similar to those in photocatalytic hydrogen evolution. The dye is replaced by the electrochemical potential. The polarization curve is given in **Figure 26 a**. The frequency chosen for Mott–Schottky analysis was obtained from the frequency corresponding to phase angle change in the Bode plot **(Figure**

26 b). The Mott–Schottky curve shows that the charge carrier type is n-type with a donor density of 1.3×10^{22} m^{-3} for Bi2Te3 nanosheets. The flat band potential is estimated to be −0.36 V (vs. Ag/AgCl) as derived from **Figure 26 c**.
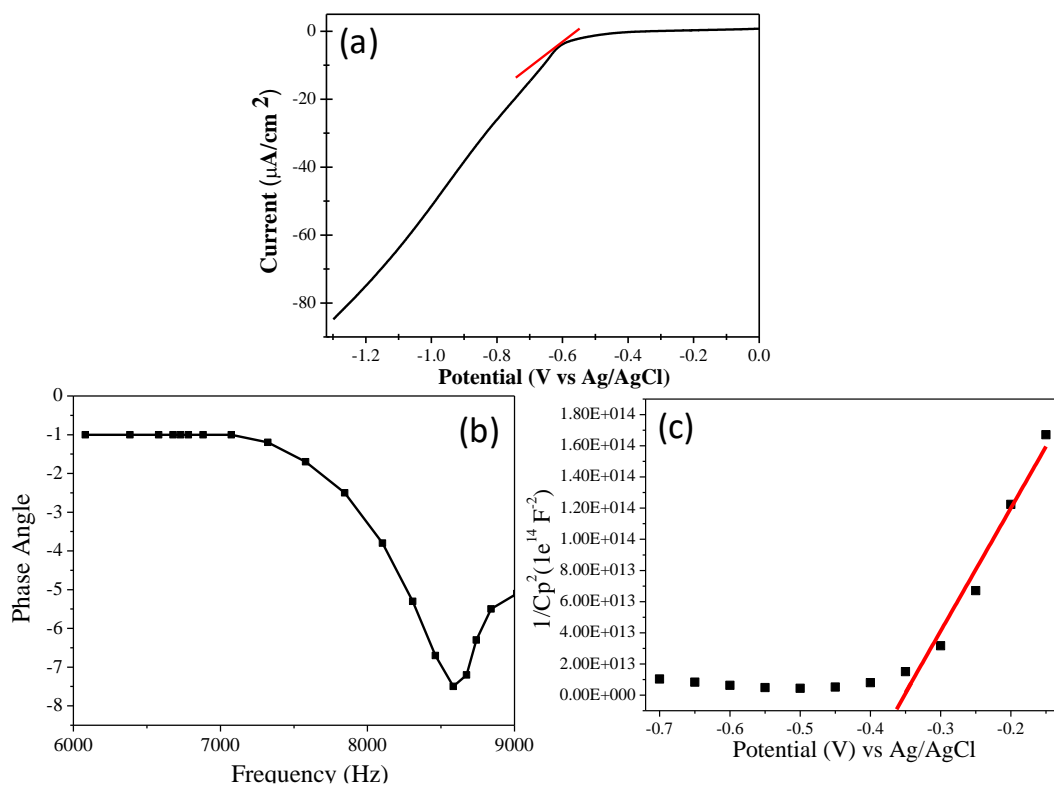
Figure 26. *(a) The linear sweep voltammetry curve of Bi$_2$Te$_3$ nanosheets at pH ~10. The Bode plot indicate impedance (Z) dependence on frequency. (c) Mott–Schottky plot of Bi$_2$Te$_3$ nanosheets.*

4.2.5 Theoretical analysis

(First-principle analysis was carried out by Dr. K. Pal and Prof. U.V. Waghmare in Theoretical Sciences Unit, JNCASR)

Bi$_2$Se$_3$ and Bi$_2$Te$_3$ are strong topological insulators (TIs) in three dimensions (3D) with quintuple layers of their formula unit stacked along the z-direction. Nontrivial topology of the bulk electronic wavefunctions of a topological insulator manifests as the gapless topological states in the

surface electronic structure. In the slab geometry, Bi_2Se_3 and Bi_2Te_3 exhibit topological metallic states (Dirac cone appears at Γ point) when their slab unit cells contain 15 and 30 atomic layers, respectively **(Figures 27 a,b)**.
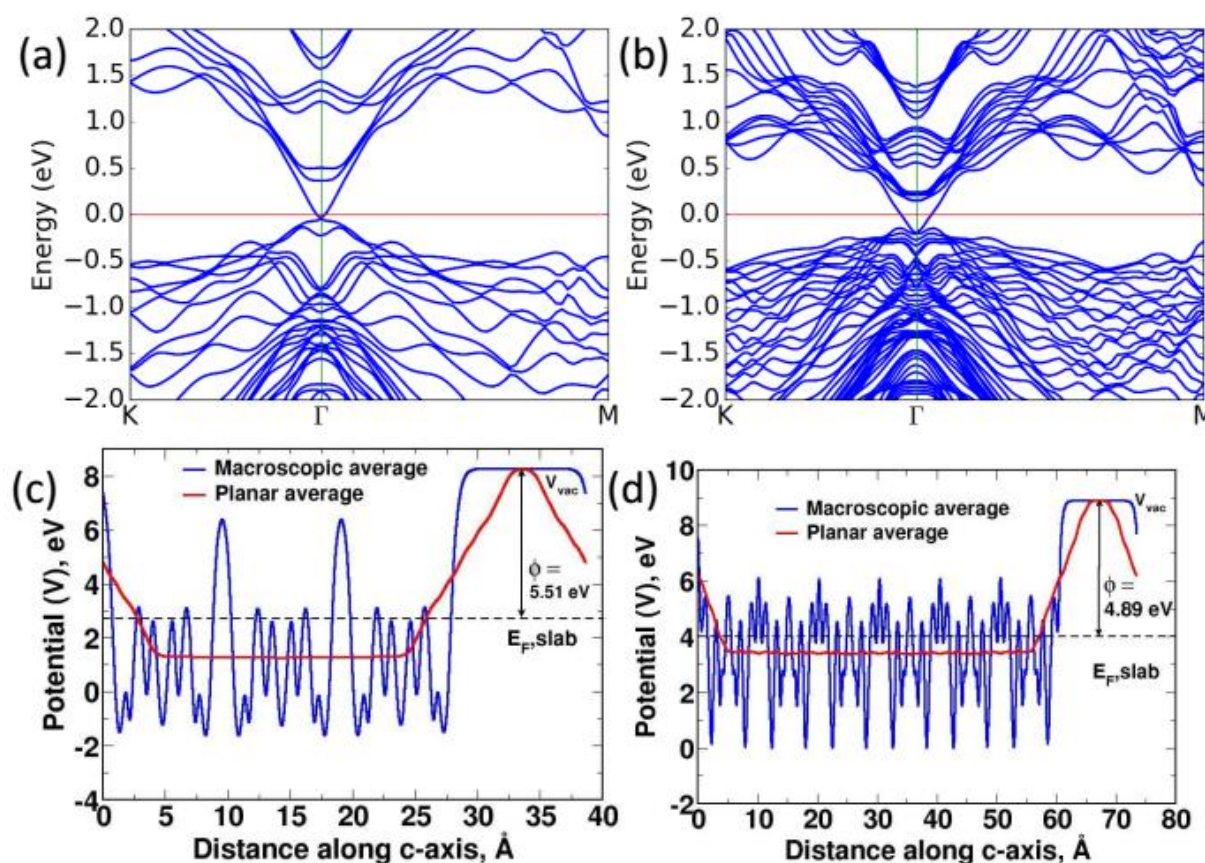
Figure 27. *Electronic structures of the (001) surfaces of: a) Bi_2Se_3 and b) Bi_2Te_3 showing gapless Dirac cones at the Γ point. Planar and macroscopic average of the electrostatic potentials of: c) Bi_2Se_3 and d) Bi_2Te_3 slabs calculated as functions of distance along the c-axis of the unit cell (layered direction in their crystal structures). The estimates of work functions (φ) of Bi_2Se_3 and Bi_2Te_3 are 5.51 and 4.89 eV, respectively. Vvac is the vacuum potential energy.*

Hence, to take the effect of topological surface states on the catalytic activity into account, we have performed calculations of Bi_2Se_3 and Bi_2Te_3 slabs containing 15 and 30 atomic layers, respectively. To assess

the activity of these 3D TIs in the hydrogen evolution reaction, we have calculated work functions of these compounds with (001) surface orientation with Se or Te termination. The work functions of Bi_2Se_3 and Bi_2Te_3 calculated without the inclusion of van der Waals interaction are 5.51 eV and 4.89 eV respectively.

To assess the activity of these 3D TIs in the hydrogen evolution reaction, we have calculated work functions of these compounds with (001) surface orientation with Se or Te termination. The work functions of Bi_2Se_3 and Bi_2Te_3 calculated without the inclusion of van der Waals interaction are 5.51 eV and 4.89 eV respectively. The corresponding energies of the Fermi level (when the vacuum potential is set to 0 eV) of the slabs of Bi_2Se_3 and Bi_2Te_3 are at −5.51 eV and −4.89 eV, respectively. These values are clearly below the standard redox potential (−4.44 eV) of HER. Inclusion of van der Waals interaction and an increased thickness of the slab do not alter the values of the work functions of Bi_2Se_3 and Bi_2Te_3 significantly **(Table 5).**

Table 5: Summary of the effects of van der Waals interaction and thickness of the slab on the calculated work functions of Bi_2Se_3 and Bi_2Te_3.

	Bi_2Se_3 (Work function in eV)		Bi_2Te_3 (Work function in eV)	
	Without van der Waals interaction	With van der Waals interaction	Without van der Waals interaction	With van der Waals interaction
15 atomic layers	4.83	--	5.51	5.53
30 atomic layers	4.89	4.91	--	5.52

Since, surface metallicity is two-dimensional in nature and is associated with a Dirac point, the corresponding density of states vanishes at the Fermi level. To explain the observed photocatalytic activity of the Bi_2Se_3 family of topological insulators, we have determined the frequency-dependent optical dielectric tensor (i.e. optical absorption spectrum) of Bi_2Se_3 **(Figure 29 a)** and Bi_2Te_3 **(Figure 29 b)** in their bulk as well as slab geometries.
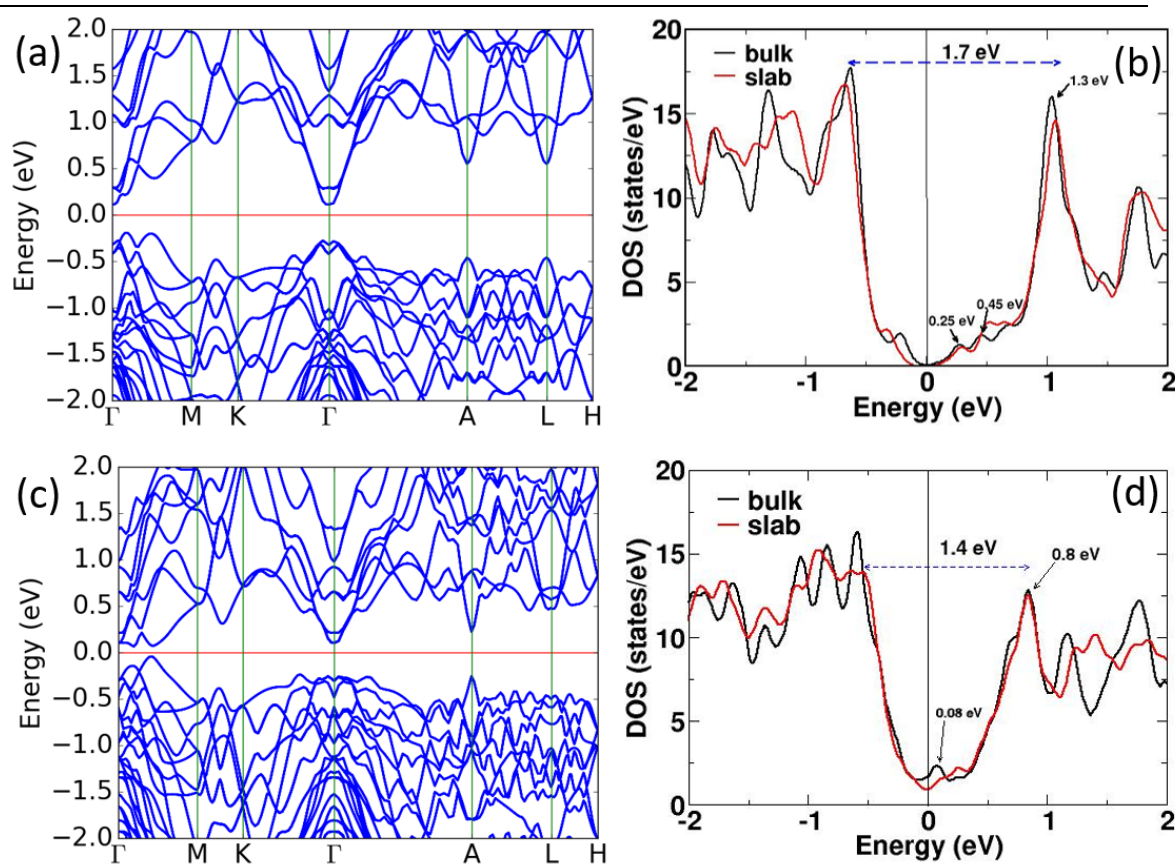
Figure 28. *Electronic structures of the bulk: a) Bi_2Se_3 and c) Bi_2Te_3. The density of states (DOS) for the bulk and slab unit cells of: b) Bi_2Se_3 and d) Bi_2Te_3.*

In Bi_2Se_3, the topological surface states give rise to new infra-red (IR) peaks (marked with blue arrows in **Figure 29 a**) in the absorption spectrum. Looking at the electronic structure of the bulk (**Figure 28 a**) and the surface **(Figure 29 a)** of Bi_2Se_3 and the corresponding density of states

(Figure 29 b), it becomes clear that the electrons from the metallic surface states as well as from the bulk valence bands get photo-excited to the empty conduction bands.

The strongest peak in the density of states of the conduction band (i.e. corresponding to the peak at 1.3 eV) has the highest population of photo-excited electrons. Comparing the peaks in the DOS in **Figure 29 b** (see the blue dashed arrow) and absorption spectrum in **Figure 29 a** (i.e. the peak corresponding to 1.7 eV), we confirm that the photo excitation of the electrons from the valence to this (1.7 eV) conduction band is quite feasible.
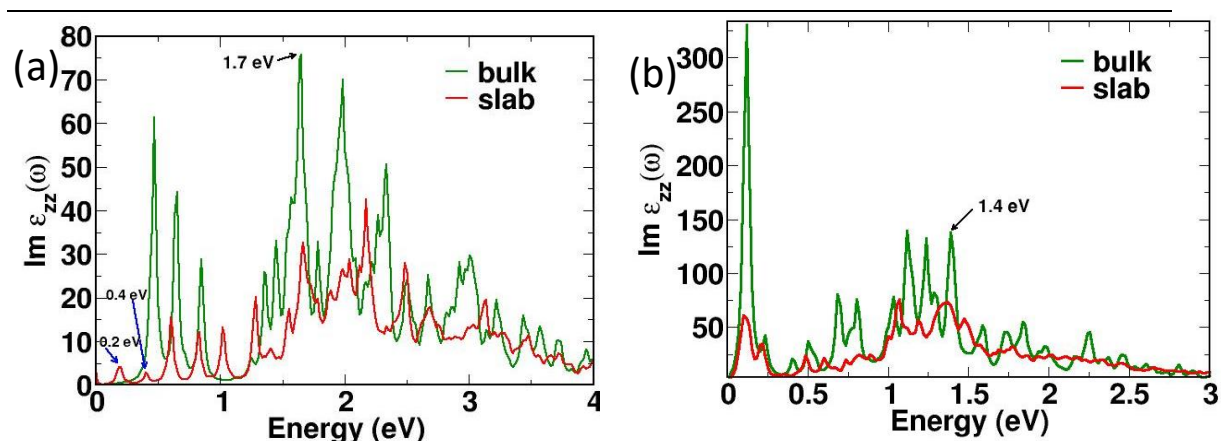
Figure 29. *Frequency-dependent optical dielectric function for the bulk and slab unit cells of: a) Bi2Se3 and b) Bi2Te3.*

Thus, the photoelectrons of Bi_2Se_3 populate states at (-5.51 eV $+1.3$ eV$=$) -4.21 eV with respect to vacuum that lies just above the standard redox potential (-4.44 eV) of the HER. Thus, H^+ ions receive these photo-excited electrons from the conduction band at -4.2 eV and get reduced to H_2. A similar mechanism holds for Bi_2Te_3. The electronic structure of the bulk **(Figure 28 c)**, and the surface **(Figure 27 b)** of Bi_2Te_3 and their DOS **(Figure 27 d)** reveal that similar to Bi_2Se_3, this material also facilitates

transition of electrons from the metallic surface states and the bulk valence band to the empty conduction band in the bulk. Comparing **Figure 28 d** and **Figure 29 a**, we see that the photo-excited electrons largely populate the conduction band at 0.8 eV. Hence, the photo-electrons of Bi_2Te_3 are in the states at (-4.89 eV $+0.8$ eV$=$) -4.09 eV, which readily supplies electrons to H^+ ions for HER (at -4.44 eV).

In **Figure 30** we present a schematic diagram for the density of states to explain the mechanism of photocatalysis in Bi_2Se_3.When light shines on this material, electrons from the surface and the bulk valence bands get excited to the conduction band and largely populate the bands associated with the strongest peak in DOS. This peak lies slightly above the redox potential of the hydrogen evolution reaction, and donates electrons to H^+ ions to produce H_2. Due to their topology, the parity of these bands is opposite, which permits optical transitions.
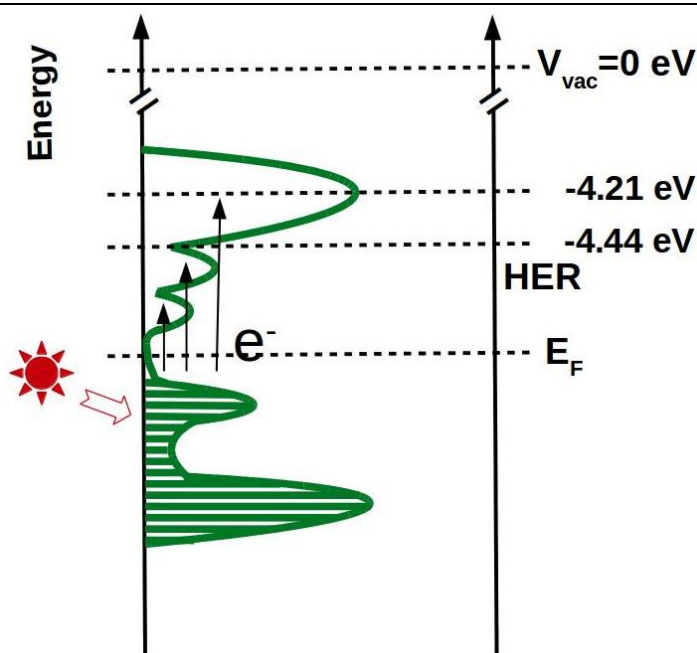
Figure 30. *Schematic diagram of the density of states and mechanism for the photocatalytic activity of Bi_2Se_3.*

5.Conclusion

To conclude, we have shown that the topological electronic structure strongly influences the catalysis of the redox reaction with regard to H_2 evolution from water fin two distinct families of Weyl semimetals. We have identified 1T'-MoTe$_2$, and NbP and related monopnictides as excellent catalysts for the H_2 evolution reaction. Our findings suggest that topological metals or semimetals with high mobilities, robust surface states, and a stable supply of itinerant electrons are promising candidates for catalysis, and thus provide a new route to the discovery of efficient catalysts. In particular, we show that the catalytic activity is several times high per surface area of catalyst compared to well-known catalysts under the same experimental conditions. Moreover, we propose that the chiral surface state of topological materials may pave the path for asymmetric catalysis. We have observed that magnetic fields strongly influence the HER activity of Weyl semimetals*.

Bismuth chalcogenide-based topological insulators such as Bi_2Te_3 exhibit robust photocatalytic hydrogen evolution. The activity decreases with the substitution of Se in Te and increases in nanosheets. From theory, we find that the photo-catalytic activity of the topological insulators arises from the photoexcitation of the electrons from: a) bulk valence to the bulk conduction bands, and b) topological surface states to the conduction band of the bulk. We also find that the topological surface states give rise to new IR bands in the absorption spectra of these materials that slow down the decay of photoelectrons to lower energy states.

*** Patent Pending**

6.   References

1.   G. C. Bond, Oxford University Press 1987.

2.   R. Schlögl, Angew. Chem. Int. Ed. 2015, 54, 3465.

3.   P. B. Weisz, Annu. Rev. Phys. Chem. 1970, 21, 175.

4.   J. K. Norskov, T. Bligaard, J. Rossmeisl, C. H. Christensen, Nat. Chem. 2009, 1, 37.

5.   E. Borgarello, J. Kiwi, E. Pelizzetti, M. Visca, M. Gratzel, Nature 1981, 289, 158.

6.   X. Wang, K. Maeda, A. Thomas, K. Takanabe, G. Xin, J. M. Carlsson, K. Domen, M. Antonietti, Nat. Mater. 2009, 8, 76.

7.   M. Zeng, Y. Li, J. Mater. Chem. A 2015, 3, 14942.

8.   M. G. Walter, E. L. Warren, J. R. McKone, S. W. Boettcher, Q. Mi, E. A. Santori, N. S. Lewis, Chem. Rev. 2010, 110, 6446.

9.   X. Zou, Y. Zhang, Chem. Soc. Rev. 2015, 44, 5148.

10.   T. Liang, Q. Gibson, M. N. Ali, M. Liu, R. J. Cava, N. P. Ong, Nat. Mater. 2015, 14, 280.

11.   C. Shekhar, A. K. Nayak, Y. Sun, M. Schmidt, M. Nicklas, I. Leermakers, U. Zeitler, Y. Skourski, J. Wosnitza, Z. Liu, Y. Chen, W. Schnelle, H. Borrmann, Y. Grin, C. Felser, B. Yan, Nat. Phys. 2015, 11, 645.

12.   M. Z. Hasan, C. L. Kane, Rev. Mod. Phys. 2010, 82, 3045.

13.   X.-L. Qi, S.-C. Zhang, Rev. Mod. Phys. 2011, 83, 1057.

14.   D. Ajami, O. Oeckler, A. Simon, R. Herges, Nature, 2003, 426, 819

15.   S. S. Chern, Ann. Math. 1946, 47, 85.

16.   C. N. Yang, Phys. Today 2012, 65, 33.

17.   E. Bick, F. D. Steffen in Topology and Geometry in Physics, Lect.Notes Phys. 65 (Eds.: R. Beig, W. Beiglbock, W. Domcke, B.-G.Englert, U. Frisch, P. Hanggi, G. Hasinger, K. Hepp, W.Hillebrandt, D. Imboden, R. L. Jaffe, R. Lipowsky, H. v. Loh-neysen, I. Ojima, D. Sornette, S. Theisen, W. Weise, J. Wess, J.Zittartz), Springer, Berlin, 2005, DOI: 10.1007/b10063

18.   E. Witten, Prog. Math. 1995, 133, 637, arXiv:hep-th/9207094v2

19. L. M. Schoop, L. Müchler, C. Felser, R. J. Cava, Inorg. Chem. 2013, 52, 5479.

20. J. Xiao, L. Kou, C.-Y. Yam, T. Frauenheim, B. Yan, ACS Catal. 2015, 5, 7063–7067

21. X. Wan, A. M. Turner, A. Vishwanath, S. Y. Savrasov, Phy. Rev. B, 2011, 83, 205101

22. L. Balents, Physics, 2011, 4, 36.

23. H. Weyl, Proc. Natl. Acad. Sci. USA, 1929, 15, 323.

24. S. Y. Xu, I. Belopolski, N. Alidoust, M. Neupane, G. Bian, C. Zhang, R. Sankar, G. Chang, Z. Yuan, C. Lee, S. Huang, H. Zheng, J. Ma, D. S. Sanchez, B. K. Wang, A. Bansil, F. Chou, P. P. Shibayev, H. Lin, S. Jia, M. Z. Hasan, Science, 2015, 349, 613

25. B. Q. Lv, H. M. Weng, B. B. Fu, X. P. Wang, H. Miao, J. Ma, P. Richard, X. C. Huang, L. X. Zhao, G. F. Chen, Z. Fang, X. Dai, T. Qian, and H. Ding, Phy. Rev. X, 2015, 5, 031013

26. S. Murakami, New J. Phys., 2008, 10, 029802

27. H. B. Nielsen, M. Ninomiya Nucl. Phys. 1981,185, 20.

28. B. Yan, C. Felser, Annu. Rev. Condens. Matter Phys., 2017, 8, 337

29. A. Soluyanov, D. Gresch, Z. Wang, Q. Wu, M. Troyer, X. Dai, A. B. Bernevig, Nature, 2015, 527, 495.

30. G. E. Volovik and M. A. Zubkov, 2014, 881, 514.

31. K. Charles, M. Joel, Physics World, 2011, 84, 035443

32. K. I. Imura, Y. Takane and A. Tanaka, Phy. Rev. B, 2011, 84, 3, 035443.

33. D.Hsieh, D. Qian, L. Wray, Y. Xia, Y.S Hor, R. J. Cava, M. Z. Hasan, Nature, 2008, 452, 970.

34. L. Fu, C. Kane Phy. Rev. Lett., 2008, 100, 096407.

35. H. Li, C. Tsai, A. L. Koh, L. Cai, A. W. Contryman, A. H. Fragapane, J. Zhao, H. S. Han, H. C. Manoharan, F. Abild-Pedersen, J. K. Norskov, X. Zheng, Nat. Mater. 2016, 15, 48.

36. D. Voiry, M. Salehi, R. Silva, T. Fujita, M. Chen, T. Asefa, V. B. Shenoy, G. Eda, M. Chhowalla, Nano Lett. 2013, 13, 6222.

37.   U. Maitra, U. Gupta, M. De, R. Datta, A. Govindaraj, C. N. R. Rao, Angew. Chem. Int. Ed. 2013, 52, 13057.

38.   C. Tsai, K. Chan, J. K. Nørskov, F. Abild-Pedersen, Surf. Sci. 2015, 640, 133.

39.   Y. Sun, S.-C. Wu, M. N. Ali, C. Felser, B. Yan, Phys. Rev. B 2015, 92, 161107.

40.   U. Gupta, B. S. Naidu, U. Maitra, A. Singh, S. N. Shirodkar, U. V. Waghmare, C. N. R. Rao, APL Mater. 2014, 2, 092802.

41.   B. Hammer, L. B. Hansen, J. K. Nørskov, Phys. Rev. B, 1999, 59, 7413.

42.   S.   Grimme, J Comp. Chem., 2006, 27, 1787.

43.   Y. Zhang, L. P. Hu, T. J. Zhu, J. Xie, X. B. Zhao, Cryst. Growth Des., 2013, 13, 645.

44.   P. Giannozzi, et al., J. Phys. Condensed Matter, 2009, 21, 395502.

45.   A. Dal Corso, Comput. Mater. Sci., 2014, 95, 337.

46.   J. P. Perdew, K. Burke, M. Ernzerhof, Phys. Rev. Lett.,1996, 77, 3865.

47.   A. Belsky, et al., Acta Crystallogr. Sect. B, 2002, 58, 364.

48.   N. E. Singh-Miller, N. Marzari, Phys. Rev. B, 2009, 80, 235407.

49.   K. Deng, G. Wan, P. Deng, K. Zhang, S. Ding, E. Wang, M. Yan, H. Huang, H. Zhang, Z. Xu, J. Denlinger, A. Fedorov, H. Yang, W. Duan, H. Yao, Y. Wu, S. Fan, H. Zhang, X. Chen, S. Zhou, Nat. Phys. 2016, 12, 1105.

50.   Y. Xu, F. Zhang, C. Zhang, Phys. Rev. Lett., 2015, 115, 265304.

51.   L. Huang, T. M. McCormick, M. Ochi, Z. Zhao, M.-T. Suzuki, R. Arita, Y. Wu, D. Mou, H. Cao, J. Yan, N. Trivedi, A. Kaminski, Nat. Mater. 2016, 15, 1155.

52.   J. Jiang, Z. K. Liu, Y. Sun, H. F. Yang, C. R. Rajamathi, Y. P. Qi, L. X. Yang, C. Chen, H. Peng, C. C. Hwang, S. Z. Sun, S. K. Mo, I. Vobornik, J. Fujii, S. S. P. Parkin, C. Felser, B. H. Yan, Y. L. Chen, Nat. Commun. 2017, 8, 13973.

53.   X. Qian, J. Liu, L. Fu, J. Li, Science 2014, 346, 1344.

54. X. Wan, A. M. Turner, A. Vishwanath, S. Y. Savrasov, Phys. Rev. B 2011, 83, 205101.

55. H. Weng, C. Fang, Z. Fang, B. A. Bernevig, X. Dai, Phys. Rev. X 2015, 5, 011029.

56. S.-Y. Xu, I. Belopolski, N. Alidoust, M. Neupane, G. Bian, C. Zhang, R. Sankar, G. Chang, Z. Yuan, C.-C. Lee, S.-M. Huang, H. Zheng, J. Ma, D. S. Sanchez, B. Wang, A. Bansil, F. Chou, P. P. Shibayev, H. Lin, S. Jia, M. Z. Hasan, Science 2015, 349, 613.

57. Z. K. Liu, L. X. Yang, Y. Sun, T. Zhang, H. Peng, H. F. Yang, C. Chen, Y. Zhang, Y. F. Guo, D. Prabhakaran, M. Schmidt, Z. Hussain, S. K. Mo, C. Felser, B. Yan, Y. L. Chen, Nat. Mater. 2016, 15, 27.

58. B. Q. Lv, H. M. Weng, B. B. Fu, X. P. Wang, H. Miao, J. Ma, P. Richard, X. C. Huang, L. X. Zhao, G. F. Chen, Z. Fang, X. Dai, T. Qian, H. Ding, Phys. Rev. X 2015, 5, 031013.

59. L. X. Yang, Z. K. Liu, Y. Sun, H. Peng, H. F. Yang, T. Zhang, B. Zhou, Y. Zhang, Y. F. Guo, M. Rahn, D. Prabhakaran, Z. Hussain, S. K. Mo, C. Felser, B. Yan, Y. L. Chen, Nat. Phys. 2015, 11, 728.

60. W. Zhang, Y. Li, X. Zeng, S. Peng, Sci. Rep. 2015, 5, 10589.

61. R. Abe, K. Hara, K. Sayama, K. Domen, H. Arakawa, J. Photochem. Photobiol., A 2000, 137, 63.

62. X. Xu, C. Randorn, P. Efstathiou, J. T. S. Irvine, Nat. Mater. 2012, 11, 595.

63. G. Xie, K. Zhang, B. Guo, Q. Liu, L. Fang, J. R. Gong, Adv. Mater. 2013, 25, 3820.

64. H. Inoue, A. Gyenis, Z. Wang, J. Li, S. W. Oh, S. Jiang, N. Ni, B. A. Bernevig, A. Yazdani, Science 2016, 351, 1184.

65. E. Skúlason et al., J. Phys. Chem. C, 2010, 114, 18182.

66. P. W. Atkins, Physical Chemistry, 6th ed.; Oxford University Press: Oxford, UK, 1998; pp 1485, 1925, and 1942.

Part 3

Electrochemical H_2 generation from water splitting using doped MoS_2 fullerenes
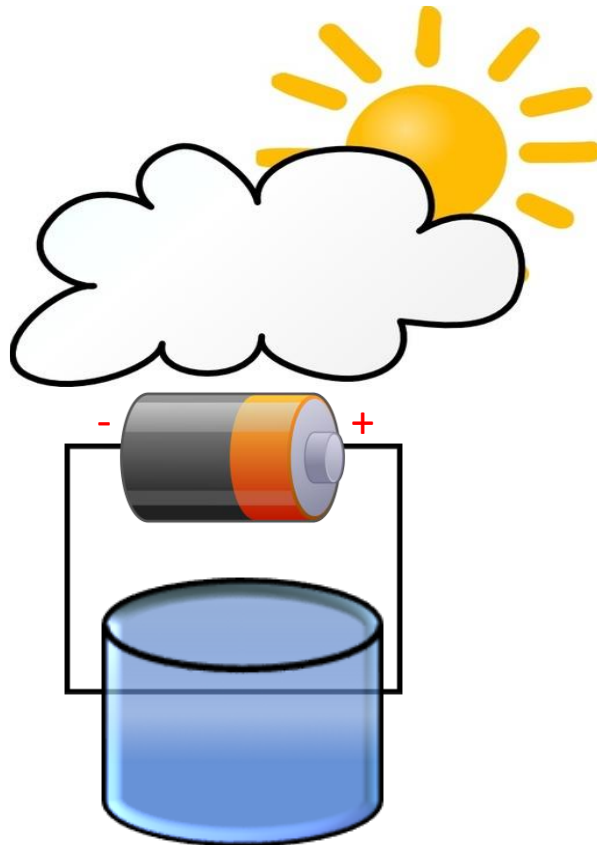
*Effects of p- and n-type doping in the MoS$_2$ fullerene (IF) on the hydrogen evolution reaction**

Summary

In this chapter, we describe a systematic study of the effects of p- and n-type doping on the hydrogen evolution reaction (HER) of Inorganic Fullerene (IF) MoS$_2$. Active edge site enriched IF-MoS$_2$ further promoted by strategically introducing Nb (p-type), and Re (n-type) dopants (below 500 ppm) enable facile HER over a range of pH values of electrolytes. Experimental results suggest that while Nb doping on IF-MoS$_2$ leads to better electrocatalytic HER activity in the alkaline medium with an onset potential difference of 40 mV, Re doping gives excellent activity in the acidic medium. The present work gives a systematic study in designing the strategy to improve the HER activity. Method to fine-tune the activity in different electrolyte medium in different pH values by the deliberate doping of parent substrate catalyst with p- and n-type materials. The doped IF-MoS$_2$ catalyst exhibits excellent catalytic activity even with sea water as an electrolyte.
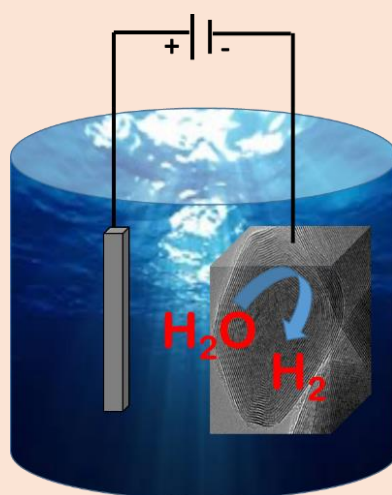
1. Introduction

From the previous parts, we have found that the photochemical potential from dye or semiconductor can be used to split water to generate hydrogen. Electricity (electrochemical) or light and electricity (photoelectrochemical) can be employed for water splitting with the use of suitable catalysts. Electrochemical hydrogen evolution method is efficient, flexible, and can produce hydrogen or oxygen with high-purity ($\approx$100%). Electrochemical cells based on platinum are efficient, but their industrial scalability is limited due to the high cost and scarcity of the metal. It is, therefore, the opportunity for material chemists to develop low-cost catalysts for water splitting systems with high efficiency and long-term durability. Considerable efforts have been made in both electrodes and electrolyte systems to develop inexpensive, environmentally-safe and durable electrocatalysts. System like borides [1], carbides [2], nitrides [3], phosphides [4], metal alloys [5-6], metal oxides [7-8], metal dichalcogenides [8], enzymes [10] and bioinspired electrocatalysts [11-13]. The hydrogen evolution reaction (HER) occurs at the cathodes while at the anodes oxygen evolution reaction (OER) take place. The half reactions at the electrodes are shown in **equations 1 and 2.**

Reduction: $2H^+ + 2e^- \rightarrow H_2$; E_o vs NHE = 0 (1)

Oxidation: $2H_2O + 4e^- \rightarrow O_2 + 4H^+ + 4e$- ; E_o vs NHE = 1.23 V (2)

(NHE= Normal hydrogen electrode).

The reaction generally does not occur at 0 V but at a potential <0 V known as the onset overpotential or namely as onset potential. It refers to the minimum potential where the HER/OER process begins on the catalyst surface. An optimal HER catalyst should provide catalytic surfaces (C) that exhibit a Gibbs free energy of adsorbed hydrogen at thermo-neutral position ($\Delta G_H \approx$ 0). Thus, an efficient catalyst lies at the top of the curve **(Figure 1)**, which indicates neither binding with the intermediate C-H$_{ads}$ is too weak nor too strong [14].
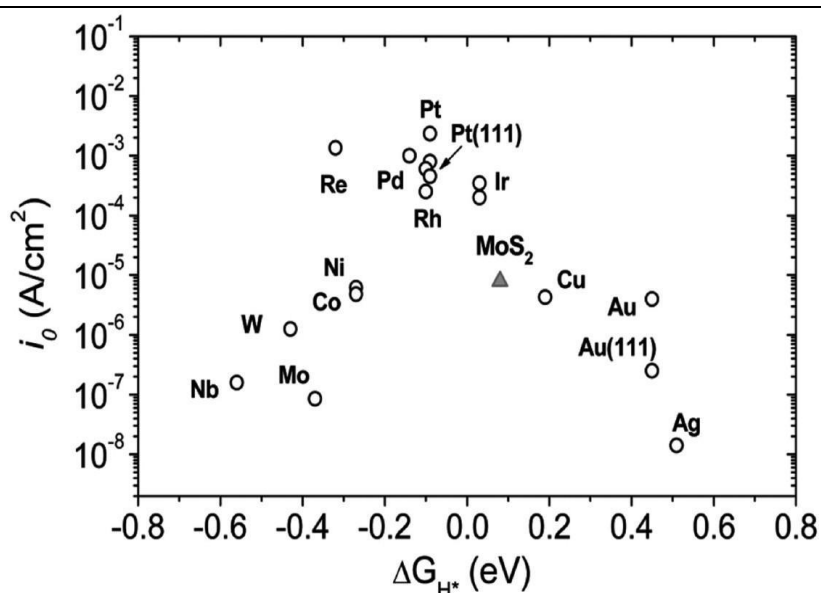
Figure 1. *Sabatier (Volcano) plot of the exchange current density with respect to calculated Gibbs free energy of adsorbed atomic hydrogen for MoS$_2$ with metals. Reproduced with permission from ref 15. Copyright 2007 American Association for the Advancement of Science.*

The HER activities of various catalysts can be summarized in the Sabatier Plot, as shown in **Figure 1** [15], where the exchange-current density for different catalysts in acids are plotted as a function of the Gibbs free energy of adsorbed atomic hydrogen on these catalysts [16]. Pt is a commonly chosen catalyst for the HER because of low ΔG_H and high current density.

MoS$_2$ just lies below those of the noble Pt group metals (by comparison of the exchange-current densities of the common metals at their corresponding free energy of adsorbed H, ΔG$_H$~0), suggesting the vast potential of MoS$_2$-based materials as an alternative to Pt for the HER **(Figure 1)** [15].

The HER process can occur via two mechanisms and three possible reaction steps on the electrocatalysts in acidic or alkaline media [17]. The initial step is the Volmer step involving adsorption of hydrogen on the catalyst surface:

$H_3O^+ + e^- + C \rightarrow C\text{-}H_{ads} + H_2O$ (3); (acidic medium)

$2H_2O + e^- + C \rightarrow C\text{-}H_{ads} + OH^-$ (4); (alkaline medium)
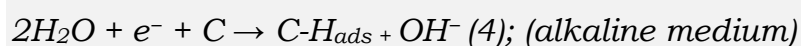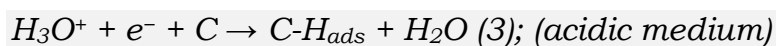
this is followed either by the Heyrovsky step (electrochemical desorption):

$C\text{-}H_{ads} + e^- + H^+ \rightarrow C + H_2$ (5); (acidic medium)

$C\text{-}H_{ads} + H_2O + e^- \rightarrow C + H_2 + OH^-$ (6); (alkaline medium)
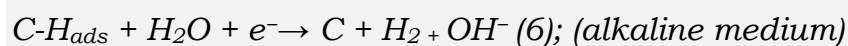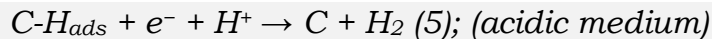
or the Tafel step (chemical desorption)

$2C\text{-}H_{ads} \rightarrow 2C + H_2$ (7), (for both acidic and alkaline medium)

where C represents an empty active catalyst site, and C-H$_{ads}$ represents an adsorbed H intermediate [18].

In electrochemical reaction kinetics, the rate of the reaction, or the current density, depends on overpotential, and the relationship is described by Butler-Vomer equation**(Equation 8)**;

$$I = I_o\left[e^{(1-\alpha)nf} - e^{-\alpha nf}\right] \text{ (8)};$$

where I is the current density, I_o is the exchange-current density, n is the overpotential, α is known as transfer coefficient and f = F/RT (F is the Faraday constant, R is the gas constant, and T is the temperature in Kelvin). At given electrode in the working condition, overpotential (n) at a specified apparent current density is used. Overpotential (lies in the range of 0.1–0.5 V for the HER) vary between cells and operational conditions even for the same reaction and is specific to cell design [19]. At high overpotential ($\eta >$ 0.05 V), the Butler–Volmer equation can be simplified to Tafel equation **(Equation 9);**

$$n = a + b \log i \ (9)$$

Electrochemical evaluation for HER on various catalytic materials is represented by the kinetic values of the constants a and b of the Tafel equation [20]. The constant b, defined as Tafel slope, is an inherent property of the catalysts and is related to the reaction mechanism of a catalyst which is determined by the rate-limiting step of the HER. The value depends on several factors, including the reaction pathway and the adsorption conditions of the active site [20]. Because of a high H_{ads} coverage ($\theta_H \approx 1$), HER proceeds via the Volmer–Tafel mechanism **(equations 3 and 7)**, and the Tafel step is the rate-limiting step at low overpotential, as attested by the measured Tafel slope of 30 mV/dec [20]. Tafel slopes >120 mV generally occurs via a Volmer-Heyrovsky mechanism, while with values in between 30<b<120 mV/dec can co-occur via both mechanisms. It is, therefore, necessary to design materials possessing onset potentials near the thermo-neutral potentials and with a low Tafel-slope. Important strategies to

increases the activity of the MoS$_2$ as a standalone material has been discussed in the next section.

1.1 Literature survey of the strategies to improve the activity of MoS$_2$

The Sabatier plot shows, MoS$_2$ to be a promising material for industrial scale electrochemical hydrogen production due to low hydrogen binding energy, good current density, and cost-effectiveness **(Figure 1).** MoS$_2$, similar to graphene, has a two-dimensional (2D) hexagonal layered structure. The S-Mo-S intra-layers are covalently-linked while the interlayers are held together by weak van der Waals force. Bulk MoS$_2$ studied as a catalyst for electrochemical HER in 1977 exhibited poor activity [21].The inherent problem of MoS$_2$ is the low electronic conductivity between two nearby S-Mo-S layers which is ~2200 times more reduced as compared to that through the basal planes [21]. This suggests that a single layer of MoS$_2$ would be ideal for high current density and electrochemical applications. Joo and coworkers studied layered dependent electrochemical HER activity of MoS$_2$ and found that that activity both on the size and number of layers [22] as well as edge sites [23]. Few (2-4)-layers MoS$_2$ exhibited lower onset potential compared to a monolayer or bulk MoS$_2$ **(Figure 2 a).** The Tafel slope of a monolayer is different from that of bi- or tri-layers layers **(Figure 2 b).** This indicates that interlayer electron transport along the edges is an important process for HER. The rate of hydrogen evolution decreases with the number of layers probably due to poor electron transport across the layers **(Figure 2 c)**.
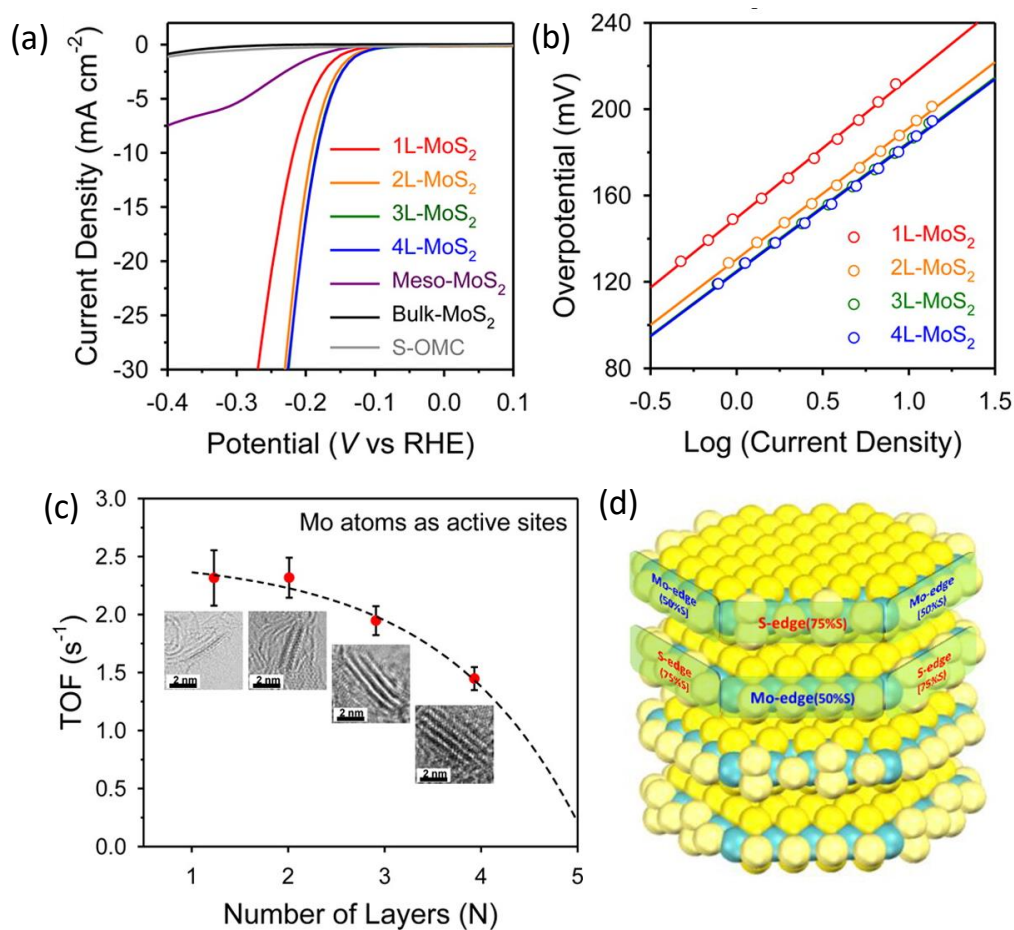
Figure 2. *HER activity of MoS₂ is dependent on the number of layers seen from the (a) linear sweep voltammetry, (b) Tafel slope, calculated linear sweep voltammetry and (c) TOF calculated at 200 mV. TOF was calculated with the assumption that (d) Mo-edge is the active site as shown. Adapted with permission from ref. 22. Copyright 2015 American Chemical Society.*

The Mo-edge is identified as an active site from calculations which also indicates that the interlayer electron transfer is important than intralayer electron transport **(Figure 2 d)**. The edge site is active catalytic sites instead of the basal planes for HER for electrochemical is inferred from numerous theoretical [24-26] and experimental studies [23]. Chorkendoff and co-workers have shown that the electrocatalytic activity has a linear relationship with the length of edge sites and is independent of the MoS₂

area coverage which they quantified from scanning tunneling microscopy [23]. The general strategy employed to improve the electrocatalytic performance of MoS_2 is by increasing the number of edge site density. One of the straightforward approaches is by introducing defects into the crystal structure of MoS_2 which adds edge sites originating from the cracks [27]. The cracking of the basal planes, borne out of disordered atomic arrangement forms new edges, which results in excellent HER performance. MoS_2 single-crystal nanobelts synthesized by Yang and co-workers exhibited a current density of 20 mA cm^{-2} at an overpotential of 170 mV in an acid electrolyte (0.5 M H_2SO_4) [28]. The upper surface of the nanobelt is vertically placed basal plane edges. The exposure of edges makes the material optically active and reduces all the indirect bandgap excitons. Vertically grown MoS_2 as grown by Lewis et al. maximize the exposure of active edge sites which enhances the activity. This observation directly correlates with the previous study which suggests that increasing the number of edge sites of MoS_2 increases the activity of the catalyst [29, 30]. Enlarged spaces in MoS_2 can be achieved by adjusting the interlayer spacing as reported by Sun and co-workers. The strategy proposes that the electronic structures of the edge-terminated MoS_2 colloids can be modified, which results in improved performance. The increased interlayer spacing of MoS_2(9.4 Å) **(Figure 3 a)** had the onset potential was 103 mV (with respect to RHE) **(Figure 3b)** with a Tafel slope of 49 mV/dec **(Figure 3c)** with stable catalytic activity up to 3000 cycles **(Figure 3d)** [31]. Nanostructuring in MoS_2 can increase the activity of MoS_2 by increasing the number edge sites which provide additional sites for HER.
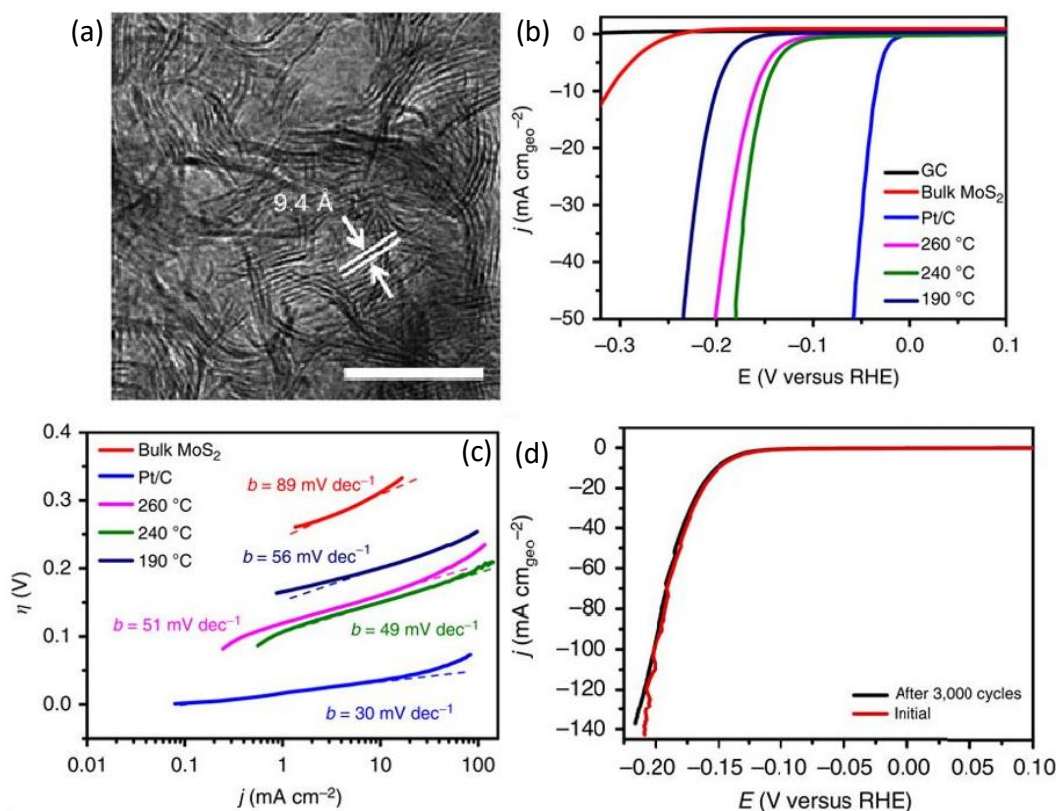
Figure 3. *(a) HRTEM highlight the expanded interlayer-spacing with 9.4 Å with (b)The linear sweep curves, (c) Tafel slope of MoS₂ nanosheets compared with bulk MoS₂ as well as commercial Pt/C catalyst. The expanded sheets exhibited a superior activity which is comparable to Pt/C commercial catalyst with (d) stability up to 3000 cycles as adapted with permission from ref 31. Copyright 2015 Nature Publishing Group.*

Increasing the number of edge sites by introducing crystal defects, growing exposed edges sheets on a substrate, or nanostructuring are some of the important strategies to maximize active edge sites and thereby, increasing the electrochemical activity.The reduction in onset potential of MoS₂ to thermo-neutral value can be achieved by modifying the intrinsic character. Since Mo-edge are the active sites, introducing S-vacancy in MoS₂ activate the basal plane on a monolayer of 2H-MoS₂ [33]. S-vacancies act as new catalytic sites on the basal plane as inferred from experimental and

theoretical results. Hydrogen atom binds directly to exposed Mo-atoms as allowed by gap states around the Fermi level. The hydrogen binding energy was further tuned by applying strain using an Au-substrate. The onset potential and Tafel slope of vacancy induced (12.5 ± 2.5%) and strained (1.35 ± 0.15%) MoS₂ were 170 mV and 60 mV/dec respectively. The unstrained MoS₂ in comparison had the onset of 300 mV and Tafel slope of 60 mV/dec. Substitution with another chalcogen element in MoS₂ introduces the possibility of tuning the composition and altering the electronic structure [33-36]. For example in $MoS_{2x}Se_{2(1-x)}$, exhibited improved performance compared to the binary equivalents. Free energy (ΔG_H) of H-adsorption onMo-Se edges (−140 meV) is stronger than (80 meV) on Mo-S edges. Similarly, nanoflakes of $MoS_{2(1-x)}Se_{2x}$ synthesized by a solution method by Gong et al. showed better activity than both MoS₂ or MoSe₂ [33]. Doping Co in MoS₂have also shown to improve the catalytic activity of MoS₂ by decreasing the ΔG_H from the S-edge [37]. Introducing Co-atoms also changes the shape of MoS₂ crystal from truncated triangle to hexagonal which gives rise to catalytically more active Co-binding S-edges [37]. Doping of the catalyst with a suitable atom can reduce the binding energy of hydrogen adsorption (ΔG_{H*}). In order to modify the surface and electronic structure of MoS₂, the metallic phase 1T-MoS₂, **(Figure 4 a)** has been used as the electrocatalyst by Chhowalla and co-workers [2]. The metallic phase of MoS₂ provides facile electron kinetics, due to excellent electrical transport and spread of active catalytic sites. The HER performance of metallic 1T-MoS₂ is superior semiconducting 2H phase due to increased metallicity and more catalytically active sites **(Figure 4 b and c)** [38]. The edge sites are not the only active sites in

1T phase unlike in the 2H-phase. The edges become highly disordered on oxidation, while the basal plane of the nanosheets is unaffected. Electrochemical oxidation of the edges reduces the catalytic activity for 2H nanosheets, but the catalytic performance 1T- nanosheets are unaffected by oxidation **(Figure 4 b and c)**. The overall performance of oxidized 2H-MoS$_2$, improved after volumetric cycling signifying that the catalytic activity from the edges of 2H-MoS$_2$ was partially re-established.
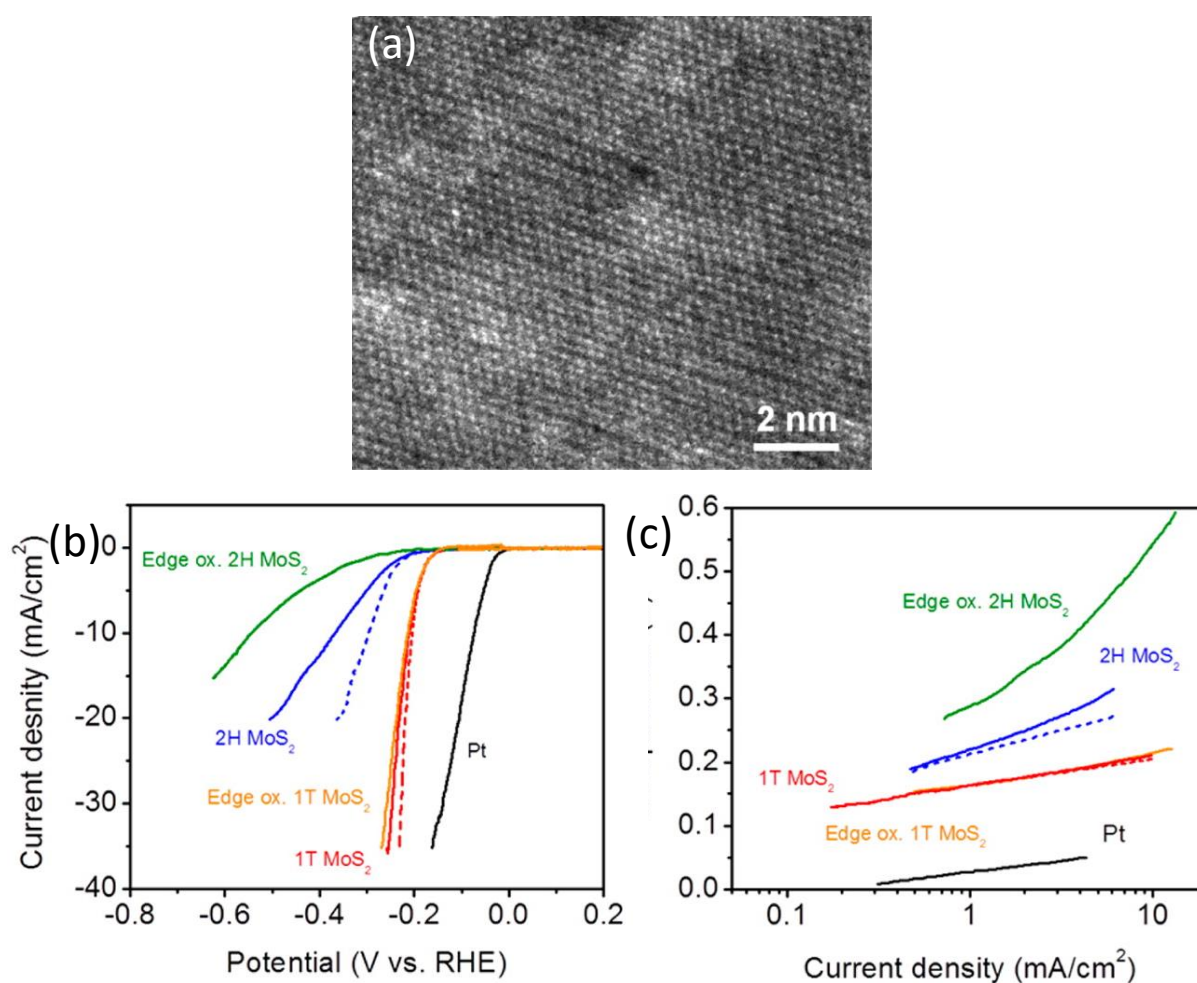

Figure 4. *(a) HAADF STEM image of the chemically exfoliated MoS$_2$ composed of distorted regions of zigzag chains, with octahedral coordination. (b) The linear sweep voltammetry curve (LSV) and (b) Tafel slopes obtained from the LSV curve of edge oxidized 2H-MoS$_2$, 2H-MoS$_2$, 1T-MoS$_2$ and edge oxidized 1T-MoS$_2$. Adapted with permission from ref. 38.*

We observe that creating a vacancy or doping with a suitable atom can lower the onset potential of MoS$_2$. However, systematic investigation of the effect of dopants on HER with MoS$_2$ is not adequately investigated. An increase in the number of active sites can also be achieved by modifying the intrinsic activity of the catalyst by doping it with an atom which optimizes the H$^+$ ion adsorption/desorption process, thereby reducing the ΔG_{H*}. We have integrated the dual strategy of maximizing the number of edge sites by synthesizing inorganic fullerene (IF-MoS$_2$) combined with the nature of dopants and studied it's HER activity over all pH ranges. The present study shows how electrochemical activity can be tuned at different pH by introducing p- and n-type dopants in IF-MoS$_2$. We observe that at low pH n-doped IF- MoS$_2$ has shown better activity then p-type and vice versa.

2. Scope of the present investigations

Niobium is located to the left of molybdenum in the periodic table and would, therefore, induce p-type doping. In mixed Mo$_{1-x}$Nb$_x$S$_2$ (x< 1 wt%), the bottom of the valence band corresponds to 3p-S and 4d-Mo(Nb) hybrid states and the upper part of the 4d$_z{}^2$ Mo (Nb) states [39-41]. The number of valence electrons in MoS$_2$ is sufficient to fill the valence band completely, rendering MoS$_2$ a semiconductor with an indirect bandgap of 1.23 eV and a direct bandgap at the Gamma point of 1.92 eV. However, NbS$_2$ has one electron less per metal atom so that the top of its valence band is half filled with metallic behavior.Consequently, substituting molybdenum by niobium is expected to lead to p-type doping of the nanoparticles[39, 40], which would acquire a positive charge on their surface. To control the position of the

Fermi level, exquisite control of the doping level below 1000 ppm is necessary, which is not trivial. The concept of n-type Re-doping in IF-MoS$_2$ and its achievement is already reported [42-43]. For example, doping of MoS$_2$ with Re atoms at 10–100 ppm can increase the free charge carriers by 10^{16}–10^{17} cm^{-3} in the conduction band. These charge carriers lie on the surface of inorganic fullerenes (IF) or nanotubes of MoS$_2$, and increase the n-type character and conductivity of the pristine IF-MoS$_2$ and of rhenium-doped analogs [42]. We found that Re-doping increased the free charge carriers by 10^{16} -10^{17} cm^{-3} in the conduction band of MoS$_2$. These free charge carriers lie close to the surface of MoS$_2$ fullerene (IF) and increase the n-type character and electrical conductivity [42, 43]. Due to this difference in the dopant nature of Nb and Re, we observe different activities of modified MoS$_2$.

3. Experimental section

3.1 Synthesis of undoped and doped IF-MoS$_2$

(Synthesis was carried out by Prof. Reshef Tenne and co-workers at the Weizmann Institute of Science. Israel)

The mixed oxides of Mo and Nb were prepared using high purity grade precursors from Aldrich. Thoroughly ground weighted and mixed powders of MoO$_3$ (99.5%) and Nb$_2$O$_5$ (99.9%) were heated in nitrogen flow in quartz crucibles, for 18 hours at a temperature of 973°C. The boat with crucibles was then moved out of the furnace and cooled naturally to room temperature in a nitrogen flow. The subsequent conversion of the Nb-Mo oxide cake into the Nb-doped IF-MoS$_2$ nanoparticles (Nb: IF-MoS$_2$) possesses some similarity to that of pure (undoped) IF-MoS$_2$ or Re: IF-

MoS$_2$ NP: The synthesis of the undoped IF-MoS$_2$ was performed in a quartz reactor at 800-830 ^{o}C. Here evaporated MoO$_3$ powder was reacted with H$_2$S gas in a reducing atmosphere. Subsequently, a final annealing step was carried out for 25-35 h at 870 ^{o}C. The synthesis may be separated into four consecutive steps: Evaporation of the Nb-Mo oxide cake at temperature about 810 °C, Partial reduction of the oxide vapor with consequent condensation into Nb-doped MoO$_3$nanoparticles, Fast sulfidization of the first few layers of the oxide nanoparticles in the volume of the reactor, Further sulfidization of the nanoparticles proceeding on the collecting quartz wool filter and subsequent annealing in the presence of H$_2$S /H$_2$ at 870-900 °C for 35-40 h. The Re-doped IF-MoS$_2$was prepared from the pre-prepared densified oxide mixture similarly to Nb-doped IF-MoS$_2$. Re concentration was varied from 0.02 to 0.7 at-% initially taken is much higher than the actual dopant concentration in the Re: IF-MoS$_2$ product.

3.2 Characterization

The sample was characterized using high-resolution transmission electron microscopy (HRTEM) using FEI Tecnai F30-UT microscope equipped with a field-emission gun operating at 300 kV. Scanning electron microscope (SEM) was done using LEO model Supra 55VP equipped with EDS detector (Oxford model INCA).

3.3 Electrochemical studies

The electrochemical HER activity of the electrocatalysts, FL-MoS$_2$, IF-MoS$_2$, Re-doped IF-MoS$_2$ and Nb-doped IF-MoS$_2$ was studied by cyclic

voltammetry (CV), linear sweep voltammetry (LSV), and electrochemical impedance spectroscopy (EIS). Electrochemical workstation (CHI760E) fitted with a three-electrode system: a glassy carbon electrode (GCE) (3 mm in diameter) as working electrode, a platinum coil electrode as the counter and Ag/AgCl (3 M NaCl) as the reference electrode was used for all the measurements. Before the measurements, GCE was cleaned by sequential polishing using alumina powders and a polishing pad (CHI120 electrode polishing kit). 1 mg of catalyst dispersed in 200 µL of Nafion solution (5 wt% Nafion: IPA: H_2O = 0.05:1:4 (v/v/v)) is named as the catalyst ink here. 2.5 µL of this ink was drop-casted on the polished GCE and was allowed to dry. The Electrolytes used (different pH solutions) was saturated with N_2 gas by purging for 30 minutes prior to measurements. To remove any impurities from the electrode surface, initially, the electrode was scanned between 0 V to 0.8 V for 10 cycles. A similar measurement was done with few-layer MoS_2 for comparison. The potentials with respect to RHE was converted by the following formula from the Nernst equation.

$$E \ (RHE)= E_{(Ag/AgCl)} + E°_{(Ag/AgCl)} + 0.059 \times pH \ (10)$$

3.4 Calculation of turnover frequency (TOF)

The Turn over Frequency of hydrogen evolution reaction was assessed by the estimation of a number of active sites on the surface of the electrode. The extrapolations from these calculations are an approximation because of the assumptions made.

(1) The origin of the active site for HER is not precisely known but assumed.

(2) The calculations of sites do not account for the loss of the surface area upon the attachment of the particles on the electrode and among themselves.

[Using the current density at an overpotential of 5 mA/cm² (vs Ag/AgCl, 3 M NaCl).]

Theoretical calculation of active sites of the IF-structure,

Assume that Nb-, Re-doped and undoped IF-MoS₂ nanoparticles (NPs) have a radius of 70 nm with the hollow core of 6 nm.

Thus, the surface area of the (spherical) IF-MoS₂ is:

$$S = 4\pi r^2 = 4\pi \times 70^2 nm^2 = 6.16 \times 10^4 \ nm^2 = 6.16 \times 10^{-10} \ cm^2$$

The volume of the IF nanoparticle (V$_{IF}$):

$$V = \frac{4}{3}\pi\left(r_{sphere}^3 - r_{core}^3\right) = 4.18 \times (70^3 - 3^3) \ nm^2 = 1.44 \times 10^{-15} \ cm^2$$

The mass of the single IF calculated from the density of bulk MoS₂ (4.8 g/cm³). Supposing that packing density IF is 75% of bulk MoS₂, the weight of IF is 5.2 x10⁻¹² mg.

$$m_{np} = \rho V = 4.8 \times 0.75 \times 1.44 \times 10^{-15} cm^3 = 5.18 \times 10^{-15} \ g = 5.18 \times 10^{-12} \ mg$$

In the experiment 1 mg of the IF were dispersed in 200 µL solution of which 2.5 µL were used, i.e., 0.0125 mg of the IF were used for each electrode. The number of IF-MoS₂ in the electrode is 0.0125/(5.2x10⁻¹²) = 2.4x10⁹ ≈ 10⁹ IF nanoparticles in each electrode. The volume of the 2H-MoS₂ unit cell is 0.10699nm³. Thus the number of the 2H cells can be derived by dividing the

volume of the IF by volume of the cell and is 1.3×10^7. The number of atoms can be derived by multiplying the number of cells by 2 for Mo and 4 for S.

$$N_{cells} = \frac{V_{IF}}{V_{cells}} = 1.3 \times 10^7$$

$$N_{Mo\_atoms\_in\_IF} = 1.34 \times 10^7 \times 2 = 2.68 \times 10^7$$

$$N_{S\_atoms\_in\_IF} = 1.34 \times 10^7 \times 4 = 5.36 \times 10^7$$

Molar Volume (M_v) = 44.46 cm³/mol

Molar Mass (M_m) = 160.07 g/mol

Surface area of the nanoparticle: S_{IF} = 6.16 x 10^{-10} cm²

Volume of the IF nanoparticle: V_{IF} = 1.43 x10^{-15} cm³

The mass of catalyst deposited on the electrode per cm² = 0.177 mg/cm²

The density (d) of IF-MoS$_2$ 3.6g/cm³,

Surface area per mg of 70 nm of diameter (S_A)= S_{IF} x $1/V_{IF}$ x $1/d$

S_A = 6.16 x 10^{-10} cm² x 1/1.43 x 10^{-15} cm³x 1cm³/3.6 g = 119.7 cm²/mg

The average number of surface atoms (A_S) per cm² for 4H-MoS$_2$ = (n x 6.022 x 10^{23} atoms x $1/M_v$)$^{2/3}$

= 0.177 x (6 x 6.022 x 10^{23} atoms x (1/44.46 cm³))$^{2/3}$ = 1.32 x 10^{14} cm^{-2}

The number of surface atoms per testing area (S_t) = S_A x A_S

= 119.7 x 1.32 x 10^{15}= 3.98 x 10^{16}

TOF (s^{-1}) per cm² = (1/2) e$^-$ x Current Density x (1/ F) x 6.022x10^{23} e$^-$ x (1/S$_t$); (F= Faradays Constant =96485 C)

Equation used for TOF calculation

$$TOF *= \frac{1}{2e-} * Current\ density * \frac{1}{F} * 6.022 * 10^{23} * \frac{1}{Surface\ site\ per\ cm*cm} \ (11)$$

4. Results and Discussion

4.1 Synthesis and characterization

(Synthesis was carried out by Prof. Reshef Tenne and co-workers at the Weizmann Institute of Science. Israel
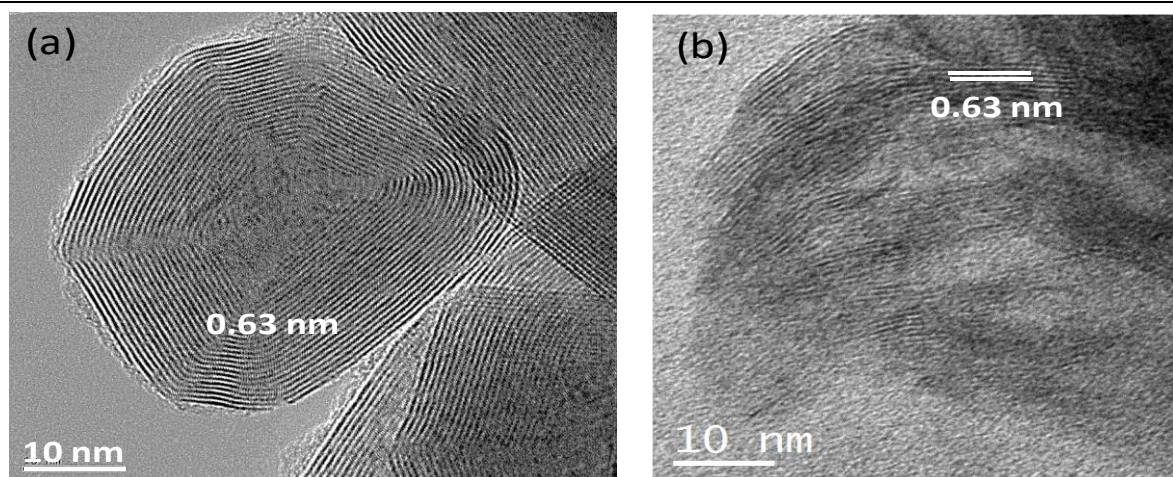
Figure 5. *HRTEM of (a) Re-doped IF-MoS$_2$ and (b) FL-MoS$_2$. (spacing between fringes is 0.63nm.)*

The inorganic fullerene structure of MoS$_2$ imparts it a higher density of active edge sites in comparison to few-layer (FL) MoS$_2$ [42]. The morphology of Nb-doped IF-structures was examined by the TEM and HRTEM. In **Figure 5** we show a typical HRTEM image of the fullerenes. Because of the onion-like morphology, active edge sites in the catalyst increases and hence higher electrocatalytic activity is anticipated. p- and n-type doping were induced on IF-MoS$_2$ by in-situ doping of fullerene-like nanoparticles of MoS$_2$ with Niobium and Rhenium atoms respectively. Nb-doped IF-MoS$_2$ were

synthesized by using Nb_2O_5 and MoO_3 as Nb and Mo precursors respectively. The critical point of the present approach is the development of a particular composition of the mixture Nb:Mo oxide precursor. The preparation of this complex oxide includes several stages and results in the formation of a solid solution of molybdenum and niobium oxides. Unlike the case of rhenium doping of IF-MoS_2, Nb_2O_5 is not volatile at the reactor temperatures of 800-900°C needed to sulfidize the MoO_3 nanoparticles. Therefore, congruent evaporation of the minor phase (Nb_2O_5), like the case of Re-Mo is not possible [42, 43]. A new strategy for the Nb doping of IF-MoS_2 nanoparticles was, therefore, developed[42] to ensure uniform doping density in the MoS_2 of nanoparticles through careful control of the reaction conditions. The analysis of minute amounts of the dopant atoms (<500 pm) in the nanoparticles is a difficult task. The Re- and Nb- doping level in the IF-MoS_2 nanoparticles was determined using inductive coupled plasma mass spectrometry (ICP-MS) analysis.

4.2 Hydrogen evolution studies

Electrocatalytic hydrogen evolution activity was studied by linear sweep voltammetry (LSV) by sweeping the working electrode in the cathodic direction to overcome the innate overpotential in the process of hydrogen ion reduction. The potentials reported here are with respect to the reversible hydrogen electrode (RHE) unless mentioned otherwise. The onset potential gives the measure of overpotential involved in the process of HER. A comparative analysis of the onset potentials for the three electrocatalysts shows that the activity of Re and Nb-doped IF-MoS_2 differ at different pH of

the electrolyte. The inference and the detailed discussion of this observation are given in the latter part of the chapter. In acidic pH, the overpotential is less for Re-doped IF- MoS₂ than the undoped and Nb-doped counterparts. The onset potential being 0.30 V (vs Ag/AgCl, 3M NaCl) close to the value exhibited by the commercial Pt/C electrode (0.24 V vs Ag/AgCl).The onset potential difference (OPD) between Re- and Nb-doped IF-MoS₂ is ~170 mV at pH-0.3. As the pH of the electrolyte increases (7.2, 9.2 and 13), the overpotential for Nb-doped IF-MoS₂ becomes less than that of the Re-doped IF-MoS₂ (OPD of ~ 0-70 mV) **(Figure 6)**.
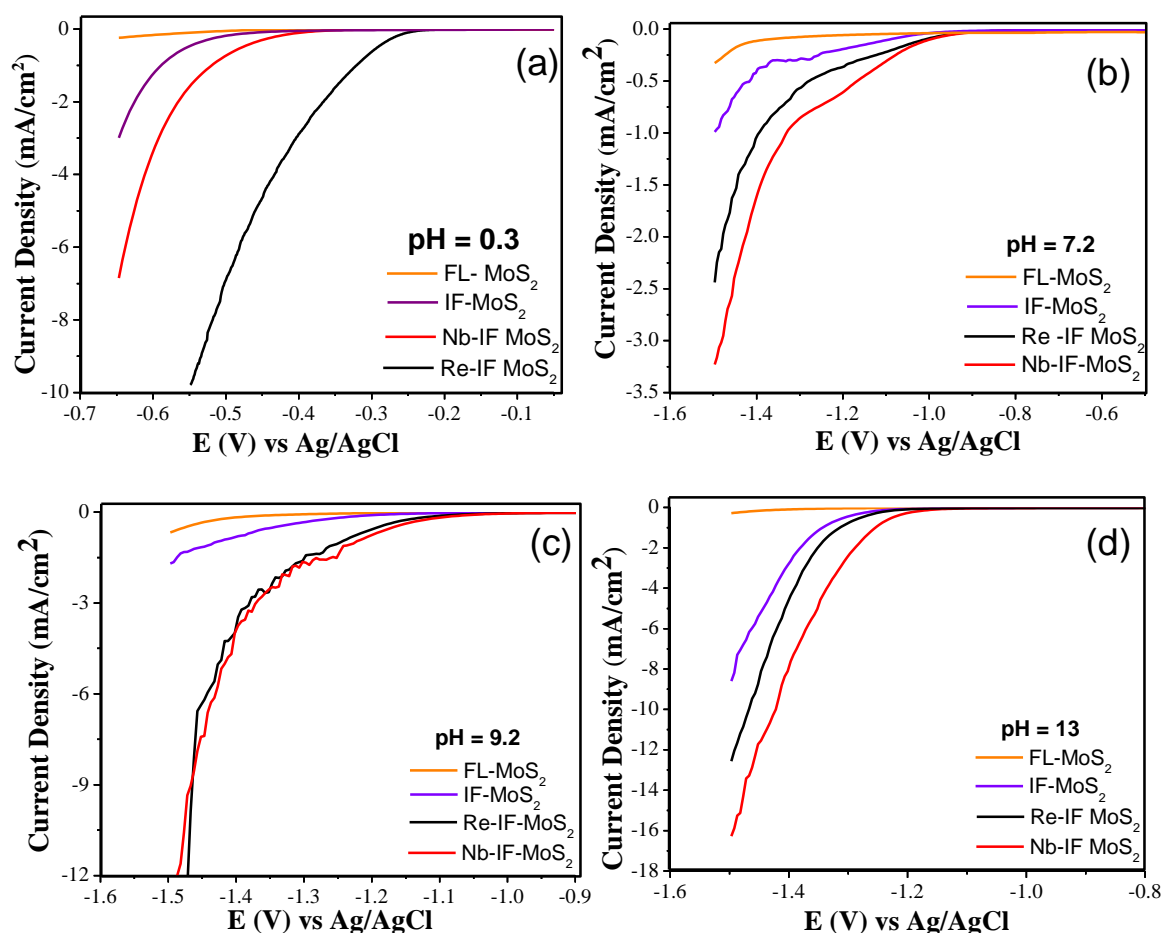

Figure 6. *The LSV polarization curves for the various catalysts (FL-, IF-, Re-doped and Nb-doped MoS₂) measured at 5 mV s-1 at pH (a) 0.3, (b) 7.2 (c) 9.2, and (d) 13 of the electrolyte.*

The features in the trend in activity suggest improvement in HER activity in both acidic and basic media by the modification in MoS$_2$ (from few-layer (FL) to IF structure) and doping with Re and Nb atoms. Modification of the properties of MoS$_2$ by doping can lead to changes in the electronic structure which are necessary for HER. From earlier reports of Trassatti [44] and Norskov [45] on the volcano plot for hydrogen evolution, one can predict the higher activity of Re in comparison to Nb in the acidic medium as observed in the present study. However, the effect of nanoclusters or low doping of metals on the substrate was not considered, and there would be additional effects caused by local strain on the adsorption-desorption process in HER [46]. The dopant sites act as active sites for catalysis. If the volcano plot (Sabatier's principle) is considered, the activity of the metals, which lie in the ascending region is controlled by desorption of the product whereas those lying in the descending region is limited by the activation of the reactant [45]. It is important to note that the descending region of volcano plot is mainly occupied by metals which form oxide films during the evolution of hydrogen. This implies that by changing the experimental condition, the activity of Nb for HER can be enhanced, and hence we propose that this is why the activity of Nb-doped IF-MoS$_2$ is higher than that of the Re-doped counterpart in the basic medium.

At pH-7.2, the onset potential for Nb- and Re-doped samples is -0.36 V whereas that for the undoped sample it is -0.44 V suggesting an improvement in overpotential difference (OPD) by 80mV. The improvement in the onset overpotential difference with Nb-doped MoS$_2$ fullerene over Re-

doped and undoped IF-MoS$_2$ samples is 10 mV and 130 mV at pH-9.2; 73 mV and 93 mV at pH-13 respectively **(Figure 6 and Figure 10a)**. The question of the activity of Nb-doped sample being better than that of Re doped counterpart in the basic medium is worth investigating. The same observation of the difference in HER activity was encountered in previous studies by Markovic et al. [47]. However, the investigation was based on transition metals and the relationship between the type of electrode and the HER activity at higher pH was addressed. The HER activity at higher pH is not only dictated by the HBE but also by its correlation with the kinetic energy necessary for the dissociation of water [47,48]. In this study, we have encountered a similar observation which gives insight about the relation between the type of electrode and the HER activity at different pH. The exact prediction of the activity as a function of pH would, therefore, be ambiguous due to the absence of a correct descriptor of activity for the study.

The reduction of hydrogen ion at the cathode is a function of pH of an electrolyte and usually follows Nernst equation **(equation 10)**,

$$E \ (RHE) = E \ _{(Ag/AgCl)} + E° \ _{(Ag/AgCl)} + 0.059 × pH \ (10)$$

Here, E_o is the standard reduction potential of hydrogen. The cathodic potential increases with the pH, but shows a deviation from the Nernstian trend due to the effects on minute dopants on the MoS$_2$ matrix. The values of the overpotential at a current density of 5 mA/cm^2 with a turnover frequency (TOF) of 0.11s^{-1} is listed in **Table 1**. The trend in the values as a function of pH of the electrolyte was found to be the same as that of the onset potentials. The improvement in the overpotential towards the less

cathodic potential indicates the enhancement in activity due to modification of MoS$_2$ through structural alteration as in the case of the fullerenes and through doping. The Nb-doped IF-MoS$_2$ shows improved performance in HER at higher pH values while the Re doped sample shows at the lower pH. The activity comparison is further manifested by Tafel slope analysis obtained from the LSV curves. To understand the mechanism involved in hydrogen evolution mechanism, we have examined the Tafel slopes **(equation 9)**;

$$n = a + b \log i \ (9)$$
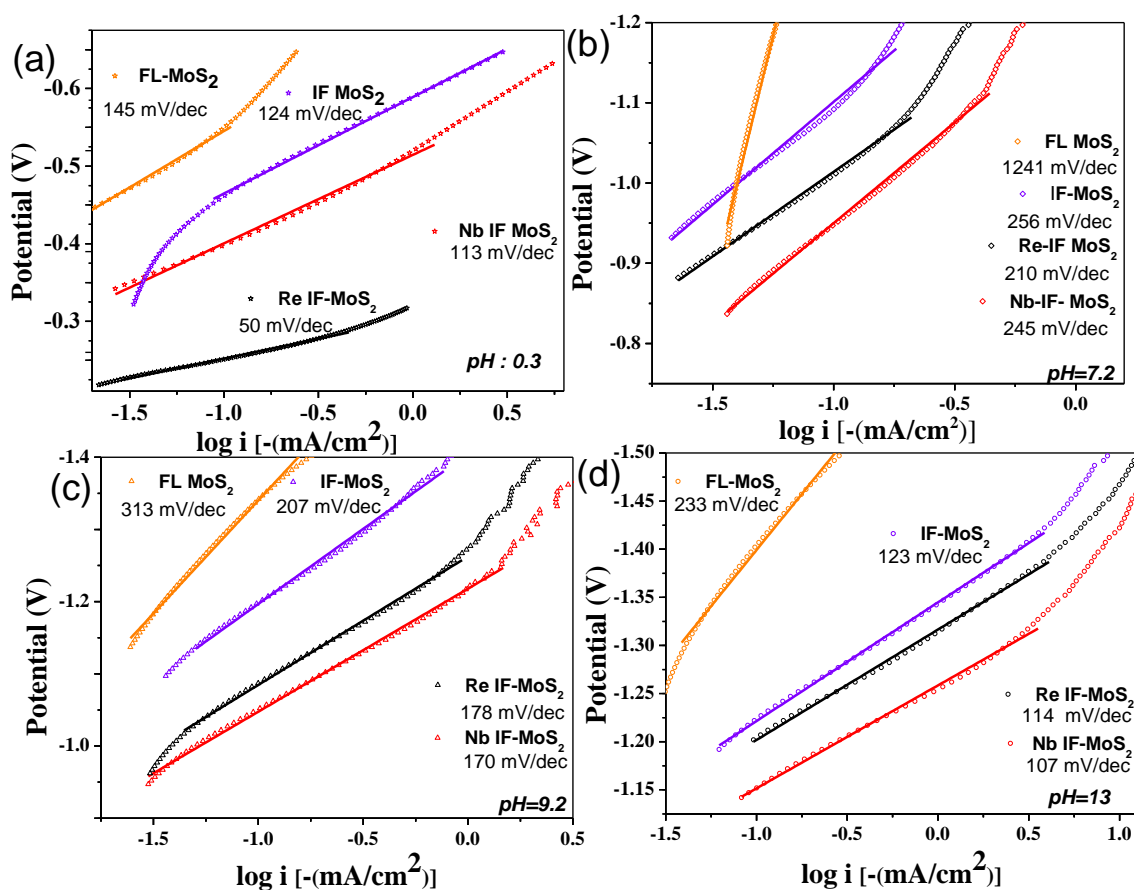
Figure 7. *pH-dependent Tafel slope analysis of various catalyst (FL-, IF-, Re-doped and Nb-doped MoS2) in HER at pH (a) 0.3, (b) 7.2 (c) 9.2, and (d) 13. (the potential here is w.r.t Ag/AgCl, 3 M NaCl).*

The results obtained clearly indicates that by Nb-doping we have further enhanced the HER activity in basic medium. The values of the Tafel slope are 107 mV/dec, 170 mV/dec and 245 mV/dec at pH 13, 9.2 and 7.2 respectively for Nb-doped IF-MoS$_2$ **(Figure 7, Figure 9b and Table 1).**
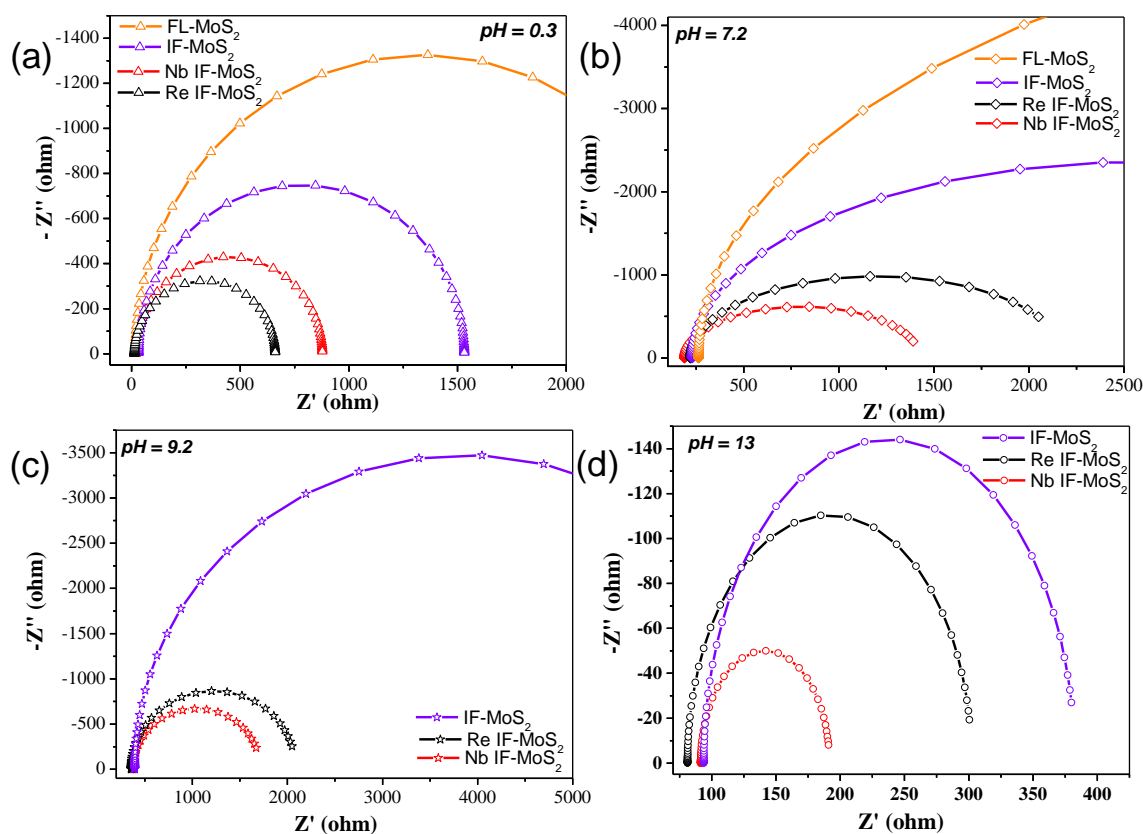
Figure 8. Electrochemical impedance spectroscopy (Nyquist plot) of various catalyst (FL-, IF-, Re-doped and Nb-doped MoS$_2$) at onset potential at different pH (a) 0.3, (b) 7.2 (c) 9.2 and (d) 13.

The hydrogen evolution by cathodic reduction of H$^+$ ion from the electrolyte occurs as **(equation 1)**, $2H^+ + 2e^- \rightarrow H_2-$ (1). In this process, the electrode encounters a significant charge transfer resistance (Rct) at the electrode-electrolyte interface, which also depends on the electrolyte used. This hinders HER activity of the electrocatalyst. With increases in pH of the electrolyte, the Rct increases at the electrolyte/electrode interface changes

for both the catalysts. The lower Rct values for Nb-doped IF-MoS$_2$ in comparison to the Re-doped counterpart at higher pH explain the better activity of Nb-doped sample **(Figure 8, Figure 9c and Table 1)**.

Table 1: Comparison of onset, Tafel slope, charge transfer resistance (R$_{ct}$)and overpotential (η) to obtain a current density of 5 mA cm^{-2} and TOF of 0.11 s^{-1} for doped and undoped IF-MoS$_2$.

Sample	pH	Onset (V) vs Ag/AgCl	η @5 mA/cm^2 (V) vs Ag/AgCl	Tafel (mV/dec)	R$_{ct}$ (ohm)
Nb-doped IF-MoS$_2$	13	-1.21	-0.36	107	100
	9.2	-1.13	-0.66	170	1348
	7.2	-1.00	--	245	1320
	0.3	-0.43	-0.38	113	860
Re-doped IF-MoS$_2$	13	-1.26	-0.43	114	220
	9.2	-1.16	-0.67	178	1712
	7.2	-1.00	--	210	2055
	0.3	-0.29	-0.23	50	649
IF-MoS$_2$	13	-1.297	-0.47	123	288
	9.2	-1.284	--	207	7172
	7.2	-1.118	--	256	4801
	0.3	-0.510	--	124	1525

The mechanism of hydrogen evolution in acidic and basic media are given below,

$$H^+ + e^- \rightarrow H_{ads} \text{ (acidic)- (4)}$$

$$H_2O + e^- \rightarrow H_{ads} + OH^- \text{ (alkaline) - (5)}$$
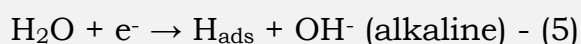
H$_{ads}$ is the surface adsorbed hydrogen which leads to H$_2$ in further steps (Tafel and Heyrovsky) depending upon the particular mechanism followed.
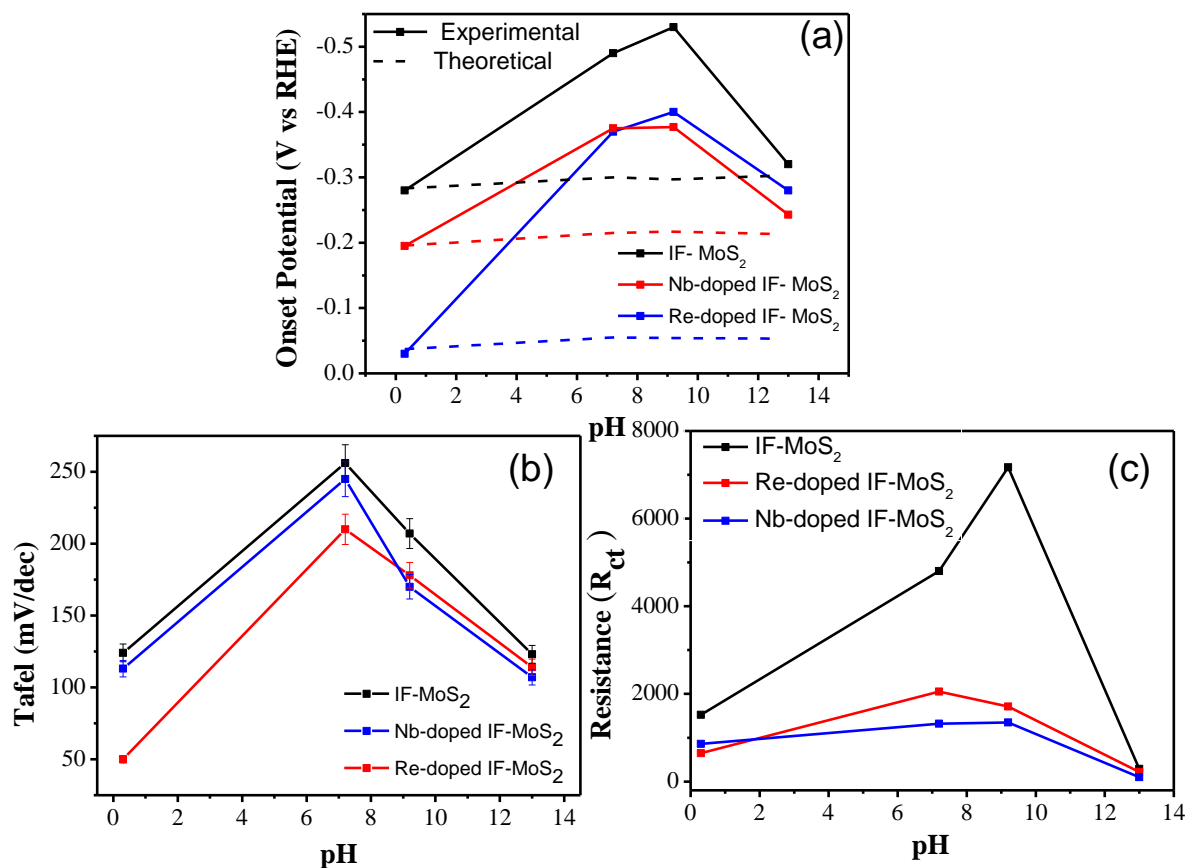
Figure 9. *Comparative analysis of p and n-type of dopant in IF-MoS$_2$ for HER as a function of pH of the electrolyte (a) onset overpotential (b) Tafel slope and (c) charge transfer resistance (R_{ct}).*

Unlike the case of Re, the 4d orbitals in Nb are compact, and hence interaction with H^+ ions fall off quickly with distance. The electron transfer rate at the electrode/electrolyte interface is therefore sluggish (which is also due to the presence of an oxide layer in the acidic medium during hydrogen evolution reaction). In alkaline medium, on the other hand, H_2O interacts with the catalyst in the electrode/electrolyte interface; due to the p-type nature of the Nb, interaction with H_2O is expected to lead to enhanced charge transfer and activity in alkaline medium in comparison to Re-doped IF-MoS$_2$ (n-type dopant). Nb has more vacant d-orbitals compared to that of Re. Additionally, Nb forms an oxide layer in an acidic medium that hinders

the activity of hydrogen production resulting in low exchange current density.

The trends in activity and the Rct value, therefore, is expected to reverse as the pH increases. Another factor to note is the low concentration of dopant and its effect on the electronic properties and local strain at the dopant site of IF-MoS$_2$. The concentration of free charge carriers in the conduction band can be increased by Re- and Nb- doping at 10–500 ppm (by 10^{16}–10^{17} cm−3) [42, 43]. As a result, the surface of IF- MoS$_2$ consists of n-type or p-type carriers, which improve the conductivity of pristine MoS$_2$ and reduces the charge-transfer resistance in electron transfer reactions. The Tafel slope and charge transfer resistance (Rct) at varying pH values suggests that the Nb-doped fullerene is better than the Re-doped one at alkaline pH while the reverse holds at acidic pH **(Figures 9b and c)**. With this strategy of doping, it appears that one should be able to tune HER activity of MoS$_2$ fullerenes over a range of pH values.
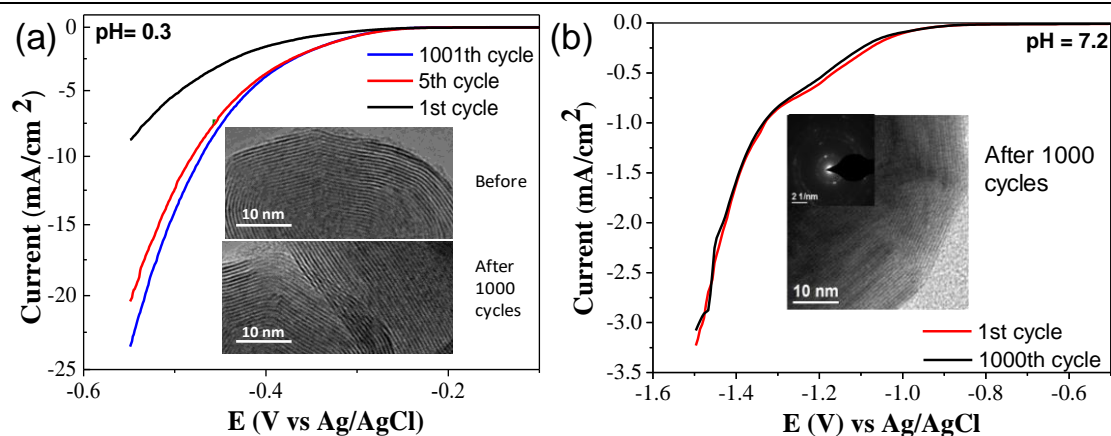

Figure 10. *Stability test of from linear sweep voltammetry (LSV) curves (a)for Re-doped IF-MoS$_2$: the 1st, 5th and 1001st cycles; the inset shows an HRTEM image of the Re-doped IF-MoS$_2$ after 1000 cycles at pH= 0.3. (b) for Nb-doped IF-MoS$_2$ at pH=7.2 before and after 1000 accelerated CV cycling.*

Another crucial parameter for the practical applicability of a catalyst is the stability test. The stability of the catalyst under study was tested by CV in the potential range of −0.3 to 0 V at a scan rate of 100 mV s⁻¹ **(Figure 10a)**. The HER activity of Re-doped IF-MoS₂ was found to be as good as the initial value after 1000 cycles The stability of the catalyst in nearly neutral pH (~7.2) was studied by accelerated cyclic voltammetry test (-0.25 to -1 V) for 1000 cycles **(Figure 10b)**.

Sample	Nb-IF	Re-IF
Onset (V)	-1.281	-1.302
η @ 5 mA/cm^2	-1.475	-1.438
Tafel (mV/dec)	254	241
R_{ct} (ohm)	2476	2080
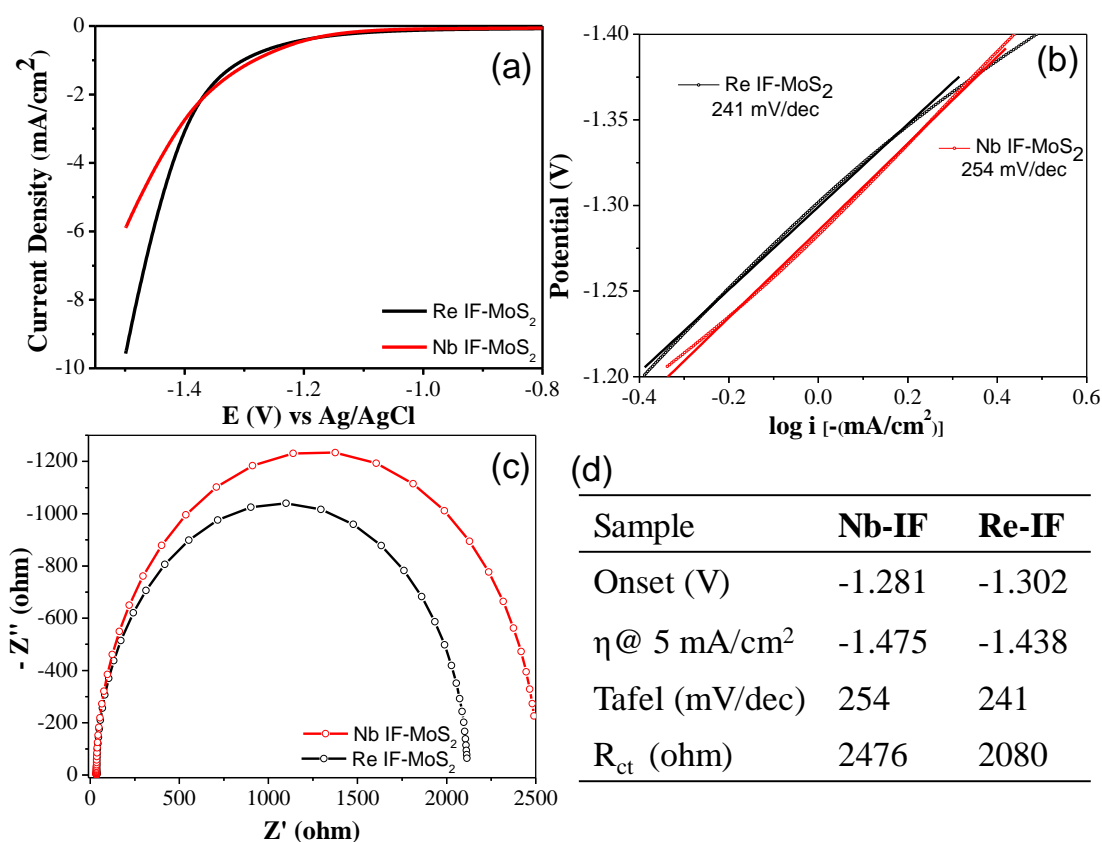
Figure 11. *HER activity of Nb and Re doped IF-MoS₂ in sea coast water (pH~6.75) as an electrolyte-(a) LSV polarization curve, (b) Tafel plot (potential wrt to Ag/AgCl) and (c) Nyquist plot and (d) comparison summary of these parameters.*

The activities before and after these cycles remained the same which suggests high stability of the catalyst. Over a period of time, the catalyst loses its activity, due to corrosion under the harsh experimental conditions or due to

agglomeration and Ostwald ripening of the catalytic particles, thereby decreasing the active surface area. In the case of IF-MoS$_2$, the stability is attributed to the structural morphology of the IF structure, which is retained even after 1000 cycles. A principal focus in the design of catalysts for hydrogen production is the practical application and its economic viability. A realistic catalyst must be efficient in the practical situation. One way to look into the problem is by using abundant seawater (1/3 abundance in the earth) as the electrolyte. The bottleneck to this idea is the presence of other cations and anions and their possible effects on the kinetics of HER at the cathode. This happens because the incipient adatoms can be adsorbed on the active sites thereby reducing the activity. We have examined hydrogen production from seawater (Arabian Sea coast) by these two catalysts. Interestingly, with Re-doped and Nb-doped IF-MoS$_2$ catalysts are very specific for hydrogen production at pH close to 7 (~6.8) **(Figure 11)**. A comparative study of other types of modifications in MoS$_2$-based catalysts and the present study is given in **Table 2.**

Table 2: Comparison of other MoS$_2$ catalysts with the present study.

Catalyst [Ref]	Overpotential (V vs RHE)	Tafel slope (mV/dec)
1-T MoS$_2$ [49]	0.19	43
Ultrathin MoS$_2$ (4.18% O) [50]	0.12	67
Vertically aligned MoS$_2$ [51]	0.22	86
2H-MoS$_2$ [49]	0.20	117
Re-doped IF-MoS$_2$ [a]	0.03	50
Nb-doped IF-MoS$_2$[a]	0.2	113
IF-MoS$_2$[a]	0.27	124

[a]Present Work

5. Conclusions

The present study demonstrates how doping MoS$_2$ based fullerene with minute concentrations of p- and n-type dopants (~500 ppm) gives rise to excellent electrochemical catalytic activity in HER. It is noteworthy that Nb- and Re-doped IF-MoS$_2$ catalysts are active in both acidic and basic media, with Nb-doping being superior to Re-doping in alkaline media. Similar studies can be performed with IF-sulfides of W, Ti, Ta, etc. and understand their role in HER. We propose this study will help in better designing strategies of electrocatalysts for various practical applications like PEM electrolyzers, PEMFC, etc. that can operate in wide range of pH values depending on the need of the situation.

6. References

1.   H. Vrubel and X. L. Hu, Angew. Chem. Int. Ed., 2012, 51, 12703.

2.   W. F. Chen, K. Sasaki, C. Ma, A. I. Frenkel, N. Marinkovic, J. T. Muckerman, Y. M. Zhu and R. R. Adzic, Angew. Chem. Int. Ed., 2012, 51, 6131.

3.   W. F. Chen, C. H. Wang, K. Sasaki, N. Marinkovic, W. Xu, J. T. Muckerman, Y. Zhu and R. R. Adzic, Energy Environ. Sci., 2013, 6, 943.

4.   D. Merki and X. Hu, Energy Environ. Sci., 2011, 4, 3878.

5.   J. Greeley, T. Jaramillo, J. Bonde, I. Chorkendorff and J. K. Nørskov, Nat. Mater., 2006, 5, 909.

6.   C. Lupi, A. Dell'Era and M. Pasquali, Int. J. Hydrogen Energy, 2009, 34, 2101.

7.   Y. Okamoto, S. Ida, J. Hyodo, H. Hagiwara and T. Ishihara, J. Am. Chem. Soc., 2011, 133, 18034.

8.   S. Cobo, J. Heidkamp, P. A. Jacques, J. Fize, V. Fourmond, L. Guetaz, B. Jousselme, V. Ivanova, H. Dau, S. Palacin, M. Fontecave and V. Artero, Nat. Mater., 2012, 11, 802.

9.   E. J. Popczun, J. R. McKone, C. G. Read, A. J. Biacchi, A. M. Wiltrout, N. S. Lewis and R. E. Schaak, J. Am. Chem. Soc., 2013, 135, 9267.

10.   D. J. Evans and C. J. Pickett, Chem. Soc. Rev., 2003, 32, 268.

11.   M. L. Helm, M. P. Stewart, R. M. Bullock, M. R. DuBois and D. L. Du Bois, Science, 2011, 333, 863.

12.   H. I. Karunadasa, C. J. Chang and J. R. Long, Nature, 2010, 464, 1329.

13.   E. S. Andreiadis, P.-A. Jacques, P. D. Tran, A. Leyris, M. Chavarot-Kerlidou, B. Jousselme, M. Matheron, J. Pécaut, S. Palacin, M. Fontecave and V. Artero, Nat. Chem., 2013, 5, 48.

14.   B. Hinnemann, P. G. Moses, J. Bonde, K. P. Jørgensen, J. H. Nielsen, S. Horch, I. Chorkendorff and J. K Nørskov J. Am. Chem. Soc., 2005, 127, 5308.

15.   T. F. Jaramillo, K. P Jørgensen, J. Bonde, J. H Nielsen, S. Horch, I. Chorkendorff, Science, 2007, 317, 100.

16.   B. E. Conway, X. Angerstein, H. Kozlowska and F. C Ho J. Vac. Sci. Technol., 1977, 14, 351.

17.   H. Tributsch and J. C. Bennett J. Electroanal. Chem., 1977, 81, 97.

18.   S. J Trasatti, Electroanal. Chem., 1972, 39, 163.

19.   A. B. Laursen, S. Kegnaes, S. Dahl and I. Chorkendorff, I. Energy Environ. Sci., 2012, 5, 5577.

20.   B. E. Conway and B. V. Tilak Electrochim. Acta, 2002, 47, 3571.

21.   H. Tributsch, Berichte der Bunsengesellschaft für physikalische Chemie, 1977, 81, 361.

22.   B. Seo, G.Y. Jung, Y.J. Sa, H.Y. Jeong, J.Y. Cheon, J.H. Lee, H.Y. Kim, J.C. Kim, H.S. Shin, S.K. Kwak, S.H. Joo, ACS Nano, 2015, 9, 3728.

23.   T.F. Jaramillo, K.P. Jørgensen, J. Bonde, J.H. Nielsen, S. Horch, I. Chorkendorff, Science, 2017, 317, 100.

24.   B. Hinnemann, P.G. Moses, J. Bonde, K. P. Jorgensen, J.H. Nielsen, S. Horch, I. Chorkendorff and J. K. Norskov, J. Am. Chem. Soc., 2005, 127, 5308.

25.   H. Vrubel, D. Merki and X. L. Hu, Energy Environ. Sci., 2012, 5, 6136.

26.   J. Bonde, P. G. Moses, T. F. Jaramillo, J. K. Norskov and I. Chorkendorff, Faraday Discuss., 2008, 140, 219.

27.   J. Xie, H. Zhang, S. Li, R. Wang, X. Sun, M. Zhou, J. Zhou, X.W. Lou, Y. Xie, Adv. Mater., 2013, 25, 5807.

28.   L. Yang, H. Hong, Q. Fu, Y. Huang, J. Zhang, X. Cui, Z. Fan, K. Liu, B. Xiang, ACS Nano, 2015, 9, 6478.

29.   L. Yang, H. Hong, Q. Fu, Y. Huang, J. Zhang, X. Cui, Z. Fan, K. Liu, B. Xiang, ACS Nano, 2015, 9, 6478.

30.   Z. Lu, W. Zhu, X. Yu, H. Zhang, Y. Li, X. Sun, X. Wang, H. Wang, J. Wang, J. Luo, X. Lei, L. Jiang, Adv. Mater., 2014, 26, 2683.

31.   M.-R. Gao, M.K.Y. Chan, Y. Sun, Nat. Comm., 2015, 6, 7493.

32.   H. Li, C. Tsai, A.L. Koh, L. Cai, A.W. Contryman, A.H. Fragapane, J. Zhao, H.S. Han, H.C. Manoharan, F. Abild-Pedersen, J.K. Norskov, X. Zheng, Nat. Mater., 2016, 15, 48.

33.   Q. Gong, L. Cheng, C. Liu, M. Zhang, Q. Feng, H. Ye, M. Zeng, L. Xie, Z. Liu, Y. Li, ACS Catalysis, 2015, 5, 2213.

34.   L. Yang, Q. Fu, W. Wang, J. Huang, J. Huang, J. Zhang, B. Xiang, Nanoscale, 2015, 7, 10490.

35.   V. Kiran, D. Mukherjee, R.N. Jenjeti, S. Sampath, Nanoscale, 2014, 6, 12856.

36.   C. Xu, S. Peng, C. Tan, H. Ang, H. Tan, H. Zhang, Q. Yan, J. Mater. Chem. A, 2014, 2, 5597.

37.   D. Merki, H. Vrubel, L. Rovelli, S. Fierro, X. Hu, Chem. Science, 2012, 3, 2515.

38.   D. Voiry, M. Salehi, R. Silva, T. Fujita, M. Chen, T. Asefa, V.B. Shenoy, G. Eda, M. Chhowalla, Nano Lett., 2013, 13, 6222.

39.   V. V. Ivanovskaya, A. Zobelli, A. Gloter, N. Brun, V. Serin, C. Colliex, Phys. Rev. B, 2008, 78, 134104.

40.   V. V. Ivanovskaya, G. Seifert, A. L. Ivanovskii, Russ. J. Inorg. Chem., 2006, 51, 320.

41.   F. L. Deepak, R. Popovitz-Biro, Y. Feldman, H. Cohen, A. Enyashin, G. Sei-fert, R. Tenne, Chem. Asian J., 2008, 3, 1568.

42.   L. Yadgarov, D. G. Stroppa, R. Rosentsveig, R. Ron, A. N. Enyashin, L. Houben, R. Tenne, Z. Anorg. Allg. Chem., 2012, 638, 2610.

43.   L. Yadgarov, R. Rosentsveig, G. Leitus, A. Albu-Yaron, A. Moshkovich, V. Perfilyev, R. Vasic, A. I. Frenkel, A. N. Enyashin, G. Seifert, L. Rapoport and R. Tenne, Angew. Chem. Int. Ed., 2012, 51, 1148.

44.   S. Trasatti, J. Electroanal. Chem., 1972, 39, 163.

45.   J. K. Nørskov, T. Bligaard, J. Rossmeisl, C. H. Christensen, Nat. Chem., 2009, 1, 37.

46.   J. K. Nørskov, T. Bligaard, A. Logadottir, J. R. Kitchin, J. G. Chen, S. Pande-lov, U. Stimming, J. Electrochem. Soc., 2005, 152, J23.

47.   N. Danilovic, R. Subbaraman, D. Strmcnik, V. R. Stamenkovic, N. M. Markovic, J. Serb. Chem. Soc., 2013, 78, 2007.

48.   W. Sheng, M. Myint, J. G. Chen, Y. Yan, Energy Environ. Sci., 2013, 6, 1509.

49. M. A. Lukowski, A. S. Daniel, F. Meng, A. Forticaux, L. Li, S. Jin, J. Am. Chem. Soc., 2013, 135, 10274.

50. J. Xie, J. Zhang, S. Li, F. Grote, X. Zhang, H. Zhang, R. Wang, Y. Lei, B. Pan, Y. Xie, J. Am. Chem. Soc., 2013, 135, 17881.

51. D. Kong, H. Wang, J. J. Cha, M. Pasta, K. J. Koski, J. Yao, Y. Cui, Nano Lett., 2013, 13, 1341.

Part 4

Hydrazine as a hydrogen carrier in the photocatalytic generation of H_2

Summary

The need for safe storage and transportation of H_2 has made liquid-phase materials safer H_2-carriers with a high gravimetric and volumetric hydrogen density. Unlike thermal or electrocatalytic decompose on precious metal catalysts, a photocatalytic route to decomposing these liquid-phase materials can offer triggered on-board production of H_2 and help mitigate the safety issues concerned with H_2 storage. We have investigated visible-light induced H_2 evolution from aqueous hydrazine using CdS quantum dots (QDs) as metal-free photocatalysts. Hydrazine acts as a H_2 carrier as well as a donor, giving rise to a visible-light induced H_2 evolution activity as high as 34.7 mmol g^{-1} h^{-1}. This has been achieved by the use of CdS-QDs capped with S^{2-} ligands. The use of larger ligands such as mercaptopropionic acid (MPA) hinders the adsorption of hydrazine onto CdS-QDs and significantly decreases the activity. The effect of pH on the hydrogen yield in aqueous hydrazine has also been examined.
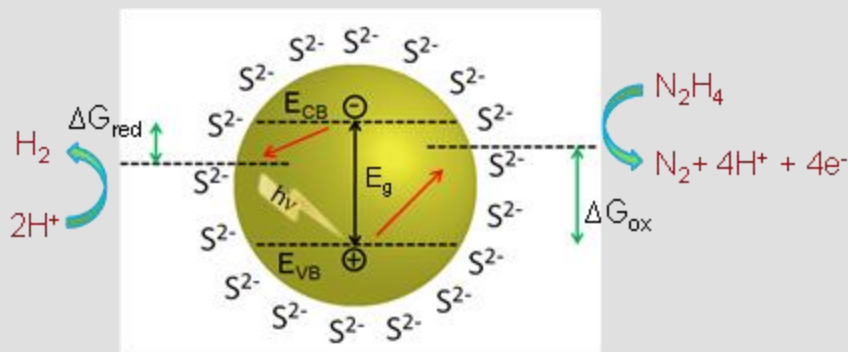
1. Introduction

Hydrogen as an alternative energy carrier has attracted serious attention due to its renewability and zero carbon footprint. Hydrogen is primarily stored as water, fossil fuels, and in living organism. These hydrogen carriers are thermodynamically stable and possess low H_2 density. We need high-density H_2 carriers to store, transport and use them at time of need. Liquid hydrogen (with a volumetric density of 71 kg m^{-3}) is difficult to store and transport due to safety issues. In order to replace the present gasoline system, the new system should be safe, easily transportable and workable at ambient room temperature and pressure. Therefore, large-scale synthetic hydrogen carriers need to be manufactured which possess high gravimetric and volumetric storage capacity with moderate stability. Decomposition of these chemical storage materials generates hydrogen that can be directly channelled into fuel cells and for on-board applications.

Solid-state hydrogen storage such as metal hydrides, borohydrides or boron-nitride has shown promising results [1]. However, most of the solid hydrogen storage materials have high decomposition temperature, slow kinetics in H_2 release and unusable by-products with irreversible H_2 storage in some cases. In this context, liquid-phase chemical hydrogen storage materials have emerged as an efficient, safe hydrogen-carriers with a high gravimetric and volumetric hydrogen density [2]. Water has a volumetric and gravimetric density of 111 Kg (of H_2) m^{-3} and 0.111 Kg (of H_2) m^{-1} respectively with an enthalpy of

formation of 143 MJ for per kg of H_2. The heat of combustion of H_2 gas is 143 MJ, which implies that theoretical turn around efficiency of H_2O is ~0%. A commercially available H_2 carrier like liquid ammonia or hydrazine has higher volumetric and gravimetric density as compared to water with better turn around efficiency **(Table 1)** [3]. The theoretical turn around efficiency of liquid ammonia is ~90% (For instance, 15.4 MJ are necessary todissociate enough ammonia to produce 1 kg of hydrogen-a theoretical turnaround efficiency of 90%, [143-15.4 (net energy gain) MJ/143 MJ (energy from hydrogen combustion)] and can be a suitable choice for a large-scale H_2 carrier. However, liquid ammonia (NH_3) requires high temperature such as 400 °C to decompose on a catalytic surface. Although, electrocatalytic decomposition of ammonia at room temperature is known on metal electrodes assisted by alkali metal amides as supporting catalysts [4-6]. It is still difficult to handle liquid ammonia under ambient conditions without special set-ups. Hydrazine (N_2H_4), a liquid-phase chemical hydrogen storage material, possesses high volumetric and gravimetric density and can be easily transported and handled at room temperature **(Table 1)**.

Table 1. Comparison of packing densities of common liquid H_2 carriers with an enthalpy of formation.

H_2 Carrier	Kg (H_2) m^{-3}	Kg (H_2) m^{-1}	Enthalpy of formation (kg $^{-1}$ of H_2) MJ
Water (H_2O)	111	0.111	143
Ammonia (NH_3)	113	0.147	15.4
Hydrazine (N_2H_4)	126	0.125	-12

Hydrazine on complete decomposition **(equation 1)** on a catalyst gives H_2 and N_2

$$N_2H_4 \rightarrow N_2(g) + 2H_2(g) \quad \Delta H = -95.4 \text{ kJ mol}^{-1} \quad (1)$$
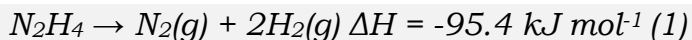
while on incomplete decomposition **(equation 2)** N_2 and NH_3 are the products.

$$3N_2H_4 \rightarrow 4NH_3 + N_2(g) \quad \Delta H = -157 \text{ kJ mol}^{-1} \quad (2)$$
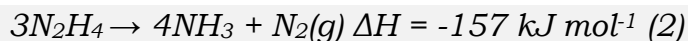
Thermocatalytic decomposition [7-9] and electro-oxidation of hydrazine over metal catalysts [10-12] are extensively studied. In thermocatalytic hydrazine decomposition, the reaction takes place on the surface of a catalyst-assisted by temperature. At temperatures below 300 °C, most of the reported catalysts exhibit high activity with reaction-pathway which follows **equation 2** [13-20]. At a high temperature above 400 °C, the hydrogen selectivity tends to increase (~100%) due to the decomposition of NH_3 over these catalysts. Catalysts such as SiO_2-supported Ni, Pd, and Pt catalysts have shown activity near room temperature with the Ni/SiO_2 catalyst with 90% selectivity for hydrogen at 50°C [13]. However, explosive nature of anhydrous hydrazine (>98%) upon exposure to metal catalysts surface limits its application.

Hydrazine monohydrate, $N_2H_4.H_2O$, with a relatively high thermogravimetric and volumetric density can be used for hydrogen generation [21]. H_2 generation is accompanied by only nitrogen as a by-product which does not need onboard collection for recycling and can be used for generation of starting material. These advantages of $N_2H_4.H_2O$ make it a promising hydrogen carrier. To effectively exploit the hydrogen-storage properties of hydrazine, it is

neccessary to develop efficient and selective catalysts for H_2 generation from $N_2H_4.H_2O$ [22-29]. The catalytic activity of metals like Fe, Co, Ni, Cu, Ru, Rh, Pd, Ir and Pt nanoparticles exhibit hydrazine decomposition at room temperature **(Figure. 1)** [30]. Among the various NPs examined, the Rh NPs were found to be the most selective (~44%) for hydrogen release from $N_2H_4.H_2O$ decomposition. Other metal NPs, such as Co, Ru, and Ir, exhibited only 7% selectivity for hydrogen, and Fe, Cu, Ni, Pt, and Pd are totally inactive under the described reaction condition [30].
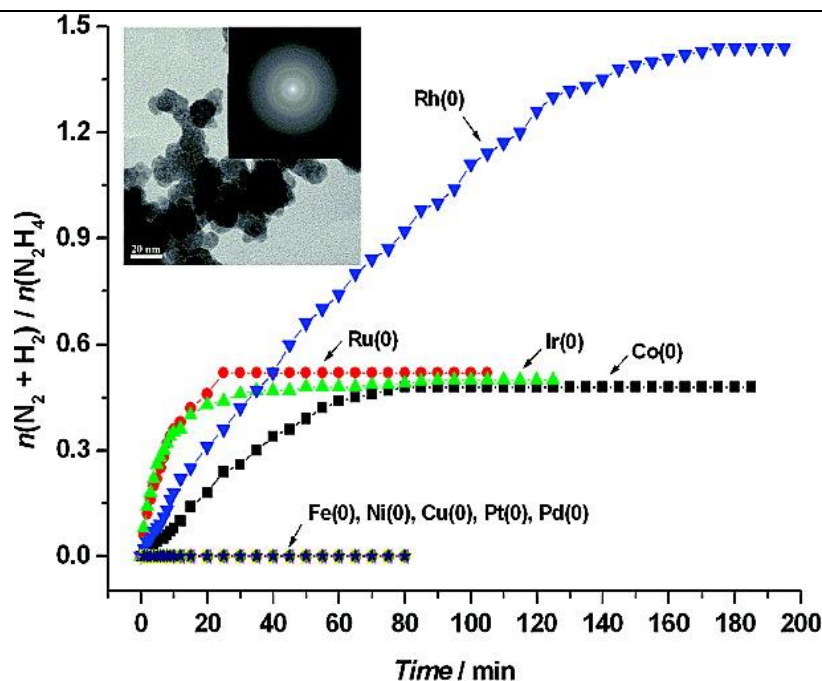
Figure 1. *Time-course plots for the decomposition of hydrazine in aqueous solutions in the presence of different metal NPs at room temperature. Adapted with permission from ref. 30. Copyright 2009 American Chemical Society.*

In thermocatalytic decomposition of $N_2H_4.H_2O$, selectivity is a major issue as most of the catalyst used are noble metals which limit the scalability of the process. For the high performance of this catalyst, we need elevated temperature.

Another process is the electro-oxidation of N_2H_4 over a metal surface assisted. The use of N_2H_4 in fuel cells has attracted immense importance in the field of electrocatalysis. A major challenge lies mainly in the developing catalysts which are capable of decreasing the oxidation overpotential for hydrazine reduction [31]. Ag, Au and Pt electrodes are active in hydrazine anodic oxidation. However, these materials are also quite expensive which creates the opportunity for the development of cheaper catalysts. Unfortunately, carbon electrodes are inactive to this reaction, and its direct use for detection and quantification of this analyte is not possible [32]. In this regard, many materials like cobalt hexacyanoferrate, cobalt tetraphenylporphyrin, quinizarin, and chlorogenic acid assist present electrodes (with high electrocatalytic activity towards hydrazine electro-oxidation of hydrazine) by reducing overpotential of the reaction [33]. Therefore, overpotential required for hydrazine reduction depends on the electrode material. Eletro-oxidation of hydrazine is still under research with emphasis on developing low-cost highly active material to industrialize the method.

Different from the well-studied thermocatalytic decomposition and electro-oxidation of hydrazine using metal-based catalysts, we have explored a photocatalytic route. We explored semiconductor-based catalysts for the controlled generation of hydrogen from aqueous hydrazine under ambient conditions. Photocatalytic decomposition of N_2H_4 over precious metal/anatase (under UV-light) [34] and photoelectrochemical decomposition of N_2H_4 over a fullerene-based organocatalyst (under visible-light) [35] have been reported to date. Visible-light-induced decomposition of N_2H_4 over semiconductor QDs has

not been investigated hitherto. We have explored the use of hydrazine (N_2H_4) as a proton-source as well as the donor for the visible-light-induced H_2-evolution over CdS QDs. The hydrogen evolution reaction (HER) based on hydrazine exhibits an activity as high as 33 mmol g^{-1} h^{-1} at pH 8 with CdS-S^{2-} QDs under visible-light illumination. Hence the key is to develop high-performance catalysts with long-term stability.

2. Scope of the present investigations

Colloidal semiconductor quantum dots (QDs) have been at the forefront of solar energy applications such as photovoltaics and photocatalysis owing to their high quantum efficiency and tunability of optical and electronic properties [36-41]. According to the Marcus theory, quantum confined semiconductors favor higher rates of interfacial charge transfer due to the increased thermodynamic energy of confined electron-hole pairs, an attribute of importance to solar energy conversion. In heterogeneous photocatalysis, photon absorption is followed by the migration of photogenerated carriers to the semiconductor surface to participate in redox reactions. Though electron-transfer is a faster process especially when conjugated with metal chalcogenides or electron sinks such as Pt and Pd as co-catalysts, hole-transfer rates and the subsequent oxidation by holes are sluggish, limiting the overall efficiency of H_2 generation [42]. Hole-scavenging has to be assisted to confer photostability to the catalyst against self-oxidation by the photoexcited holes. In the case of CdS-Pt nanorods, the formation rate of H_2 and photostability are found to increase with donors having

a high oxidation potential [43]. An efficient donor should possess a high oxidation potential and offer high rates of hole-scavenging without limiting the net energy storage capacity.

In the present study, we demonstrate visible-light induced hydrogen evolution from the photocatalytic oxidative decomposition of N_2H_4 using metal-free all-inorganic CdS QD based photocatalysts. We have examined the effect of the ligand-size by studying the HER from aqueous hydrazine over CdS QDs capped with sulfide ions (S^{2-}) as well as mercaptopropionic acid (MPA). We find that former to be a suitable ligand for the HER owing to the shorter diffusion lengths involved in the adsorption of hydrazine molecules on the CdS surface. We have further examined the effect of pH on the HER in aqueous hydrazine, containing CdS-S^{2-} QDs.

3. Experimental section

3.1 Synthesis

3.1.1 Synthesis of nanoparticles and quantum dots (QDs)

CdS nanoparticles were synthesized by dropwise addition of 50 mM aqueous Na_2S into 50 mM aqueous $Cd(CH_3COO)_2$ under stirring. The precipitate was washed successively with water and ethanol and dried at 60 °C for 12 hours. We have obtained CdS QDs as follows. 1M sulfur-trioctylphosphine (TOP-S) stock solution was prepared by dissolving elemental sulfur in a TOP solvent with stirring at room temperature (RT). A mixture containing 128 mg of CdO, 8 ml of octadecene and 0.8 ml of oleic acid was degassed under evacuation in a 50 ml

(Round bottom flask) RBF for 60 min at 120 ^{o}C after which the temperature was increased and maintained at 220 ^{o}C under N_2 flow. After a clear transparent solution of cadmium oleate was formed, 0.5 ml of 1M TOP-S solution was injected under N_2 flow. Aliquots were taken at different intervals for monitoring the growth of nanoparticles through photoluminescence and UV-Vis absorption spectroscopy. After nanoparticles reached the desired size, the reaction mixture was quenched in water kept at room temperature. The nanoparticles were purified by washing the contents thrice with 30 ml of a hexane-methanol mixture (1:1 by vol.), coagulated with excess ethanol and centrifuged to obtain a pellet. The pellet was dissolved in 6 ml of toluene or hexane and stored in the dark. CdS QDs of 4.2 nm diameter were chosen for the photocatalytic experiments. The size was inferred from the first exciton peak position (λ = 423 nm) using a sizing curve for CdS QDs established by Peng et al. [44].

3.1.2 Ligand exchange of CdS quantum dots (QDs): Sulfide ion (S^{2-})-capped CdS QDs were prepared by adding 2 ml of 25 mg/ml solution of Na_2S in formamide to 2 ml of QD stock solution in a 15 ml vial and stirred for 30 min under dark condition. After the completion of ligand exchange, the contents of the vial were centrifuged at 1500 rpm for 3 min. After separating both the phases, 4 ml of acetonitrile was added to the formamide phase and centrifuged to precipitate the QDs. The precipitate was finally dispersed in 5 ml of N_2-degassed millipore water and stored in the dark. To obtain CdS QDs capped with mercaptopropionic acid (MPA), the above procedure was repeated with 2 ml of formamide solution of 50µl of MPA and 80mg of NaOH.

3.2 Characterization

Powder X-ray pattern was recorded on Bruker D8 Advance diffractometer using Cu-K$_\alpha$ source (λ = 1.541 Å). Transmission electron microscope (TEM) images were obtained by using a JEOL TEM 3010 instrument fitted with a Gatan CCD camera operating at an accelerating voltage of 300 kV. Absorption spectra were recorded on Agilent-8453 UV-Vis spectrophotometer. Raman spectra were recorded on a Jobin Yvon LabRam HR spectrometer using Ar-laser (514.5 nm) excitation in a backscattering configuration. The concentrations of CdS QDs used in the photocatalytic experiments were determined by inductively coupled plasma-optical emission spectroscopy (ICP-OES) using Perkin Elmer Optima 7000 DV instrument. Samples were digested in 1:1 HNO_3: HCl mixture and diluted to 10 ml solutions with Millipore water before the analysis.

3.3 Photocatalytic measurements

Photocatalytic activities of CdS nanoparticles and CdS QDs capped with sulfide ligands (CdS/S^{2-}) and mercaptopropionic acid (CdS-MPA) in 1 % or 0.2 % (v/v) aqueous solution of $N_2H_4.H_2O$. CdS NCs (5 mg) or CdS QDs (0.21 mM or 0.42 mM) were dispersed in 50ml of deionized water along with the sacrificial donor (pH of the medium is maintained between 7 and 10) taken in a custom-built quartz flask with flat surfaces being exposed to the light. The solution was degassed with N_2 for 15 min before initiating the photocatalytic reaction. The control experiments were done under similar conditions. The solution was illuminated with 400 W Xenon arc lamp (New Port-6280) fitted with infrared and

399 nm cut-off filters. We carried out similar experiments with bulk gallium sulfide (GaS). The H_2 gas evolved was detected and quantified using Perkin Elmer-Clarus 580C gas chromatograph equipped with thermal conductivity detector by manually injecting 2 ml of sample headspace at regular intervals of time. Cycling studies were performed by degassing the flask with N_2 for 15 min at regular intervals. Turn over frequency (TOF) was calculated as follows:

$$TOF\ (/h) = \frac{Activity\ of\ the\ Catalyst}{Moles\ of\ the\ catalyst}$$

3.4 Electrochemical measurements

Working electrodes were fabricated by drop casting an aqueous dispersion of CdS/S^{2-} QDs on ITO substrates pre-cleaned by ultra-sonication in acetone, isopropanol, and deionized water successively and drying overnight in an evacuated desiccator under dark condition. Electrochemical dark scans were performed on ITO: CdS QD films in 1M KCl and 0.1 M Na_2SO_3 aqueous solution at pH 9.7, 12.1 and 12.9 at a scan rate of 10 mV S^{-1}. pH was adjusted by the addition of 1M NaOH.

4. Results and discussion

4.1 Synthesis and characterization

Neat CdS nanoparticles were synthesized by the reaction of $Cd(CH_3COO)_2$ and Na_2S in aqueous media at room temperature. Oleate-capped CdS quantum dots (QDs) of the desired size were synthesized by the reaction of cadmium oleate and a sulfur-trioctylphosphine (TOP-S) complex in a mixture of octadecene and oleic acid at 220 °C. Water-soluble sulfide- and MPA-capped CdS-QDs were obtained by a ligand-exchange procedure.

The X-ray diffraction pattern of CdS nanoparticles in **Figure. 2a** shows broad reflections due to the small particle size. The TEM image in **Figure. 2b** reveals the size of CdS nanoparticles to be in the 5–10 nm range. **Figure. 2c** shows the absorption spectra of CdS QDs before and after ligand-exchange with water-soluble S^{2-} and MPA ligands. The first excitonic peak appears at 423 nm for the oleate-capped CdS QDs indicating a mean diameter of 4.2 nm (ref. 44) which is consistent with the corresponding TEM image given in **Figure 2d**. After the ligand-exchange, the first exciton peak is red-shifted to 437 nm for CdS-S^{2-} QDs while the shift is negligible in the case of CdS-MPA QDs. The observed redshift can result from strong coupling of QD energy levels with the molecular orbitals of adsorbed S^{2-} ligands [45-46]. The effective radius of CdS QDs increases due to the outer S^{2-} ligands on the QD surface leading to a red-shift in the first excitonic peak [47]. Besides, S^{2-} can reduce surface-traps in CdS QDs generating

an electric field inside the QD, which perturbs the excitonic electron/hole wave functions and their optical transitions through the Stark effect [48].
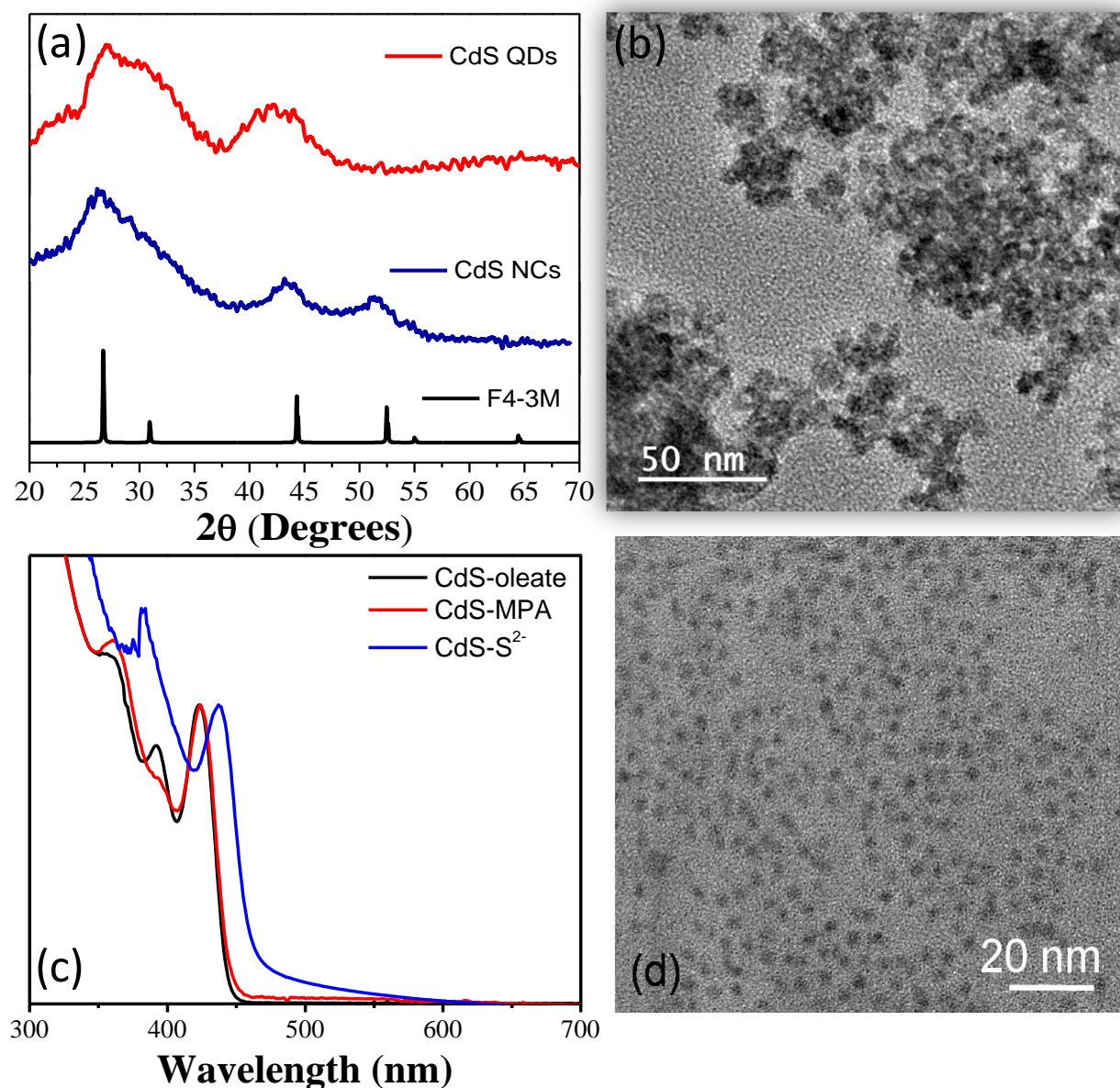

Figure 2. *(a) Powder XRD patterns of CdS nanoparticles (NCs) and QDs along with a reference, (b) TEM image of CdS nanoparticles; (c) UV-Vis absorption spectra of oleate-capped CdS QDs in toluene (before ligand exchange) and CdS QDs capped with MPA and S²⁻ ligands in water (after ligand exchange) and (d) TEM image of oleate-capped CdS QDs.*

4.2 Hydrazine decomposition

Aqueous dispersions of CdS nanoparticles and CdS QDs were used for HER-studies with N_2H_4 as the electron donor as well as the proton-source. The photocatalytic HER activity with CdS nanoparticles in 1% (v/v) aqueous hydrazine (pH 9.3) in the first cycle of illumination was 8.8 mmol g^{-1} h^{-1} which increases up to 14.7 mmol g^{-1} h^{-1} in the subsequent cycles **(Figure 3a)**. Similarly, we have studied photocatalytic HER in aqueous hydrazine using CdS-QDs. With 0.21 mM CdS-S^{2-} QDs in 1% (v/v) $N_2H_4 \cdot H2O$ in water (pH 8), the HER activity in the first cycle is 25 mmol g^{-1} h^{-1} which increases up to 33 mmol g^{-1} h^{-1} in the 4th cycle **(Figure 3b)**. Control experiments in the absence of light or the CdS catalyst yielded no H_2 indicating that the HER in aqueous hydrazine is indeed photocatalytic listed in **table 2**.
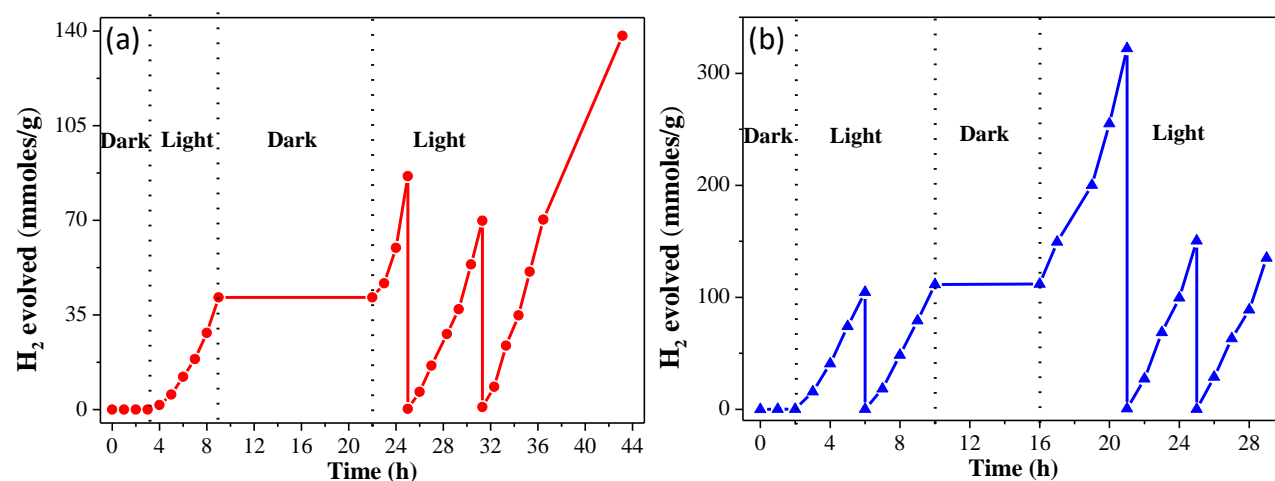

Figure 3. *(a) HER studies in 1% (v/v) aqueous hydrazine containing CdS nanoparticles; (b) HER studies in 1% (v/v) aqueous $N_2H_4 \cdot H_2O$ at pH 8 with CdS-S^{2-} QDs.*

Table 2: Control Experiments to determine the hydrogen evolution

Experiments	Results	Reactant solution	Remarks
Hydrazine+ water (In presence of Light)	No H_2 evolution	Water + $N_2H_4.H_2O$ (1%)	---
Hydrazine + water + Catalyst (In Dark for 12 hours)	No H_2 evolution	Water + $N_2H_4.H_2O$ (1%)	Catalyst dispersion is stable
Hydrazine (1%)+ water + Catalyst at 50^oC for 6 hours (in dark)	A trace amount of H_2 evolution for initial 1 hour	Water	Coagulates, no H_2 production
Hydrazine (1%)+ water + CdS (ppt) (In presence of light for 40 hours)	Continuous H_2 evolution	Water + $N_2H_4.H_2O$ (1%)	Stable, continuous H_2 production
Hydrazine (1%)+ D_2O + CdS (QDs) (In presence of light)	No D_2 Observed	$D_2O + N_2H_4.H_2O$ (1%)	Hydrogen source is N_2H_4

The experimental conditions employed along with our observations are tabulated in **table 2.** We observe no hydrogen evolution from aqueous N_2H_4 in the dark at ambient temperature (monitored for 12 hours) or at 50^oC (monitored over 6 hours) in the presence or absence of the CdS catalyst. We can thus rule out the thermocatalytic decomposition of N_2H_4 to generate H_2. Profuse evolution of H_2, however, occurs upon illumination with visible-light in the presence of the CdS catalyst. Dispersions of CdS nanoparticles and CdS-QDs in aqueous hydrazine remain stable against photocorrosion with no apparent decomposition of the catalyst as evidenced by Raman spectra and energy dispersive X-ray analysis **(Figure 4)**. In the absence of N_2H_4, anodic photo-corrosion of the CdS

catalyst occurs with negligible H_2 evolution confirming the hole-scavenging (electron-donating) role of N_2H_4. When we replaced H_2O by D_2O, keeping the other conditions the same, only hydrogen evolution was observed, and no D_2 was detected in the mass spectrometer. This observation establishes N_2H_4 to be the proton source for hydrogen evolution. The consumption of N_2H_4 during the reaction was also monitored using the Nessler's reagent before and after the reaction to confirm this observation further.
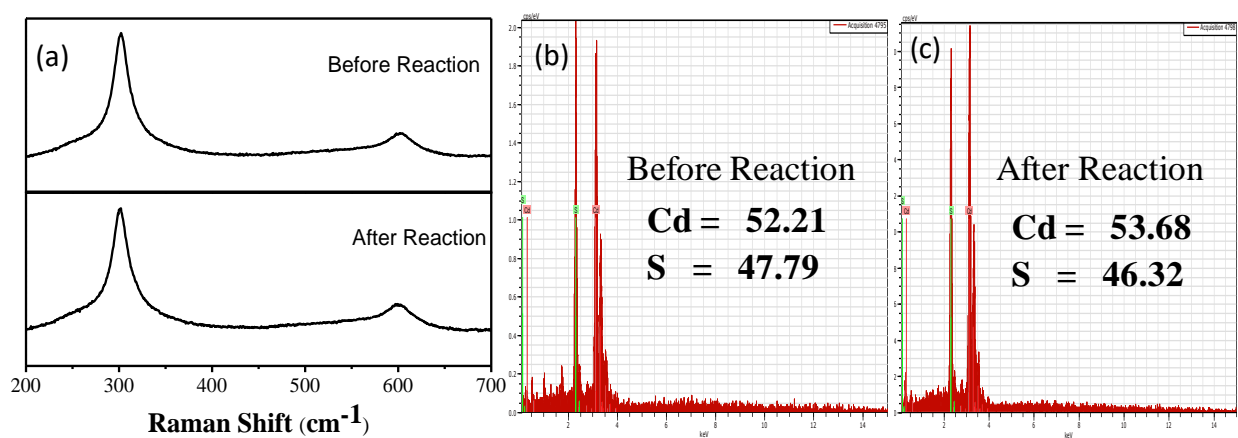

Figure 4. *(a) Raman spectra and energy dispersive spectra of CdS nanocrystals before and after photocatalytic decomposition of hydrogen.*

According to Gerischer [49], the rate of electron transfer at the semiconductor/electrolyte interface is enhanced upon widening the semiconductor bandgap due to the increased thermodynamic potential of photogenerated electron-hole pairs. Quantum confinement results in band gap widening as conduction band (E_{cb}) and valence band (E_{vb}) levels become more reducing and oxidizing respectively leading to increasing thermodynamic driving force and kinetics associated with the charge transfer. The enhanced HER

activity with the CdS-QDs as compared to the larger CdS nanoparticles is ascribed to high ΔG associated with the reduction and oxidation processes in addition to higher surface to volume ratio in the former.

HER activity with N_2H_4 over CdS QDs can be understood in terms of the thermodynamic driving force, $\Delta G_{ox} = nF_{\{E-EVB\}}$ where E is the reduction potential of the donor and E_{vb}, the valence band level of semiconductor catalyst. Oxidation of N_2H_4 involves a four-electron transfer and is described by the following **equations 3 and 4**: [35, 50].
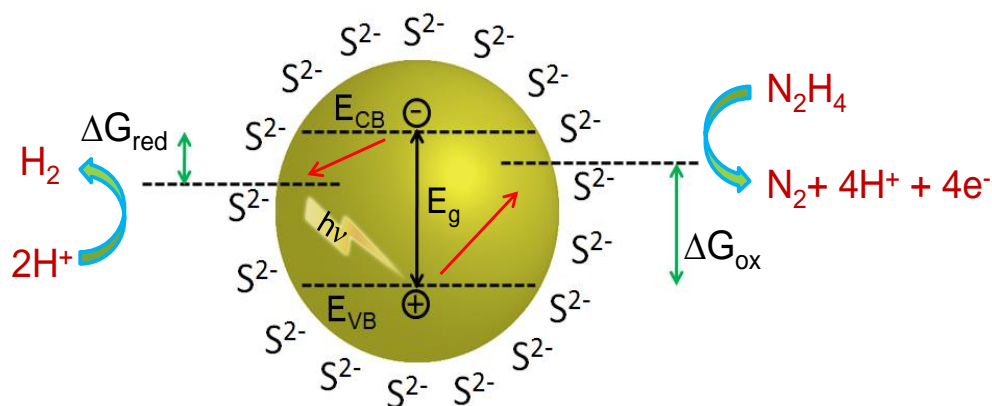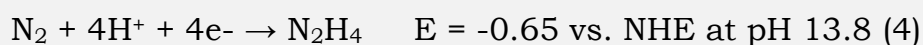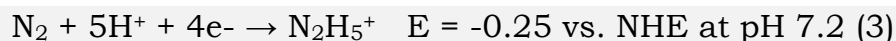
$$N_2 + 5H^+ + 4e- \rightarrow N_2H_5^+ \quad E = -0.25 \text{ vs. NHE at pH 7.2 (3)}$$

$$N_2 + 4H^+ + 4e- \rightarrow N_2H_4 \quad E = -0.65 \text{ vs. NHE at pH 13.8 (4)}$$

Figure 5: *Schematic of a plausible mechanism of H_2 evolution with $N_2H_4.H_2O$ as a sacrificial hole-scavenger.*

The reduction potential of N_2/N_2H_4 redox couple ($E_{[N2/N2H4]}$) under basic conditions is -0.65 vs. NHE. The suitable reduction potential of N_2/N_2H_4 and the large thermodynamic driving force, ΔG_{ox} (= $nF\{E_{[N2/N2H4]}-E_{VB}\}$) for filling the

photogenerated holes in the valence band of CdS catalyst leads to spontaneous oxidation of N_2H_4 upon irradiation with visible-light. The resulting protons from the oxidation of N_2H_4 are reduced by the photoexcited electrons at the conduction band (CB) edge of CdS to generate H_2. A plausible mechanism for H_2 generation from aqueous hydrazine is shown as a schematic in **Figure 5.**

4.2.1 Ligand-dependent H_2 generation

Given the detrimental effects of large insulating organic ligands capping the semiconductor QDs on the charge transport, it is appropriate to use shorter inorganic ligands to achieve efficient electronic conduction with high mobilities in QD arrays [51. 52]. The often used long chain thiol-based carboxylate ligands form a steric barrier for the diffusion and adsorption of hole-scavenging molecules to the QD surface and inhibit an efficient electron-transfer. The photocatalytic HER activity of nickel-decorated CdS nanorods has been shown to enhance significantly at a high pH of 14 via redox- shuttling of electrons by smaller OH- species across nanorods and ethanol [53]. The possible effect of the ligand-size on the performance of the catalyst, we have carried out HER in aqueous hydrazine using CdS-S^{2-} QDs and CdS-MPA QDs. The rate of hole-filling by hydrazine molecules is indeed affected by the size of capping ligand as reflected from the decreased activity of MPA-capped CdS QDs compared to that of sulfide-capped CdS QDs. The HER activity and turn over factor (TOF) are 34.7 mmol g^{-1} h^{-1} and 5.0 h^{-1} respectively for CdS-S^{2-} QDs and 4.2 mmol g^{-1} h^{-1} and 0.7 h^{-1} respectively for CdS-MPA QDs **(Figure 6)**. The use of shorter S^{2-} ligands

apparently facilitates the adsorption of hydrazine molecules on the QD surface and the subsequent reduction of protons.
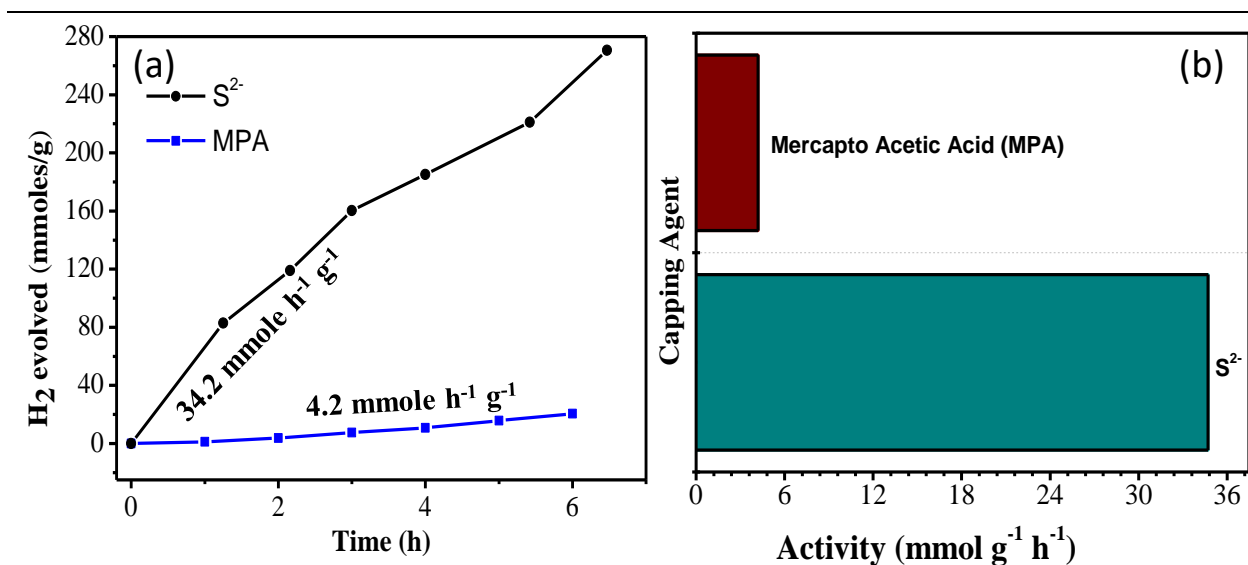

Figure 6. *(a) H₂ evolution over a period of time with CdS-S²⁻ QDs and CdS-MPA QDs in the presence of 1% (v/v) N₂H₄.H₂O as the sacrificial donor. (b) The comparison of respective HER activities of CdS capped quantum dots with different ligands.*

4.2.2 pH-dependent H₂ generation

We have examined the effect of pH on the HER activity of CdS-S²⁻ QDs in aqueous hydrazine. In **Figure. 7**, we present the photocatalytic activity of 0.42 mM CdS QDs in 50 ml solution of 0.2% (v/v) $N_2H_4.H2O$ at pH 7, 9.8 and 12.4. The HER activity during the first four hours and the TOF of the CdS-S²⁻ QDs are found to be 24.5 mmol g^{-1} h^{-1} and 3.54 h^{-1} respectively at pH 12.4 which decrease to 19.5 mmol g^{-1} h^{-1} and 2.8 h^{-1} respectively at 9.8 pH and further to 14.9 mmol g^{-1} h^{-1} and 2.15 h^{-1} respectively at pH 7 (**Table 3**).
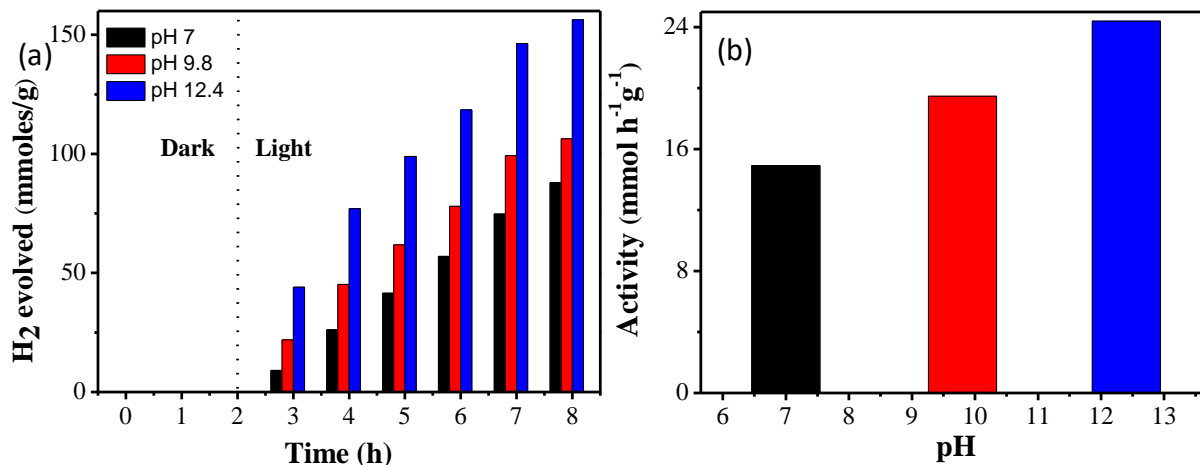
Figure 7. (a) *H_2 evolution over a period of time with CdS-S^{2-} QDs at pH 7, 9.8 and 12.4 in the presence of 0.2% (v/v) $N_2H_4.H_2O$ as the sacrificial donor. (b) Comparison of the HER activity at pH 7, 9.8 and 12.4 with CdS-S^{2-} with 0.2% (v/v) $N_2H_4.H_2O$ as the sacrificial donor.*

The value of E_{cb} can be approximated to the Cd^{2+} lattice reduction peak potential which was determined by dark electrochemical scans on CdS QD films coated on an ITO substrate in 1M KCl and 0.1 M Na_2SO_3 aqueous electrolyte at pH 9.7, 12.1 and 12.9. E_{cb} values of CdS-S^{2-} QDs are about -0.67, -0.84 and -0.98 V vs. NHE at pH 9.7, 12.1 and 12.9 respectively **(Figure 8).**

In the pH range used, E_{cb} of CdS QDs is more negative compared to $E_{[N2/N2H4]}$ **(Equations. 3 and 4)** so that the reduction of CdS QDs by hydrazine is not thermodynamically feasible. As seen in **Figure 7** and **Table 3**, the HER activity increases with pH. At higher pH, hydrazine exists in the highly basic unprotonated form ($N_2H_4 + H_2O \leftrightarrow N_2H_5^+ + OH^-$, $pK_b \sim 5.9$ and $pK_a \sim 8.1$ see **equations 3 and 4**) and gives rise to the enhancement in photocatalytic HER activity. The lower activity at pH 7 can also arise from the slight coagulation of

CdS QDs induced by partial stripping of the sulfide ligands ($H_2S \leftrightarrow H^+ + HS^-$, pK_{a1}=7, and pK_{a2} =12.8).
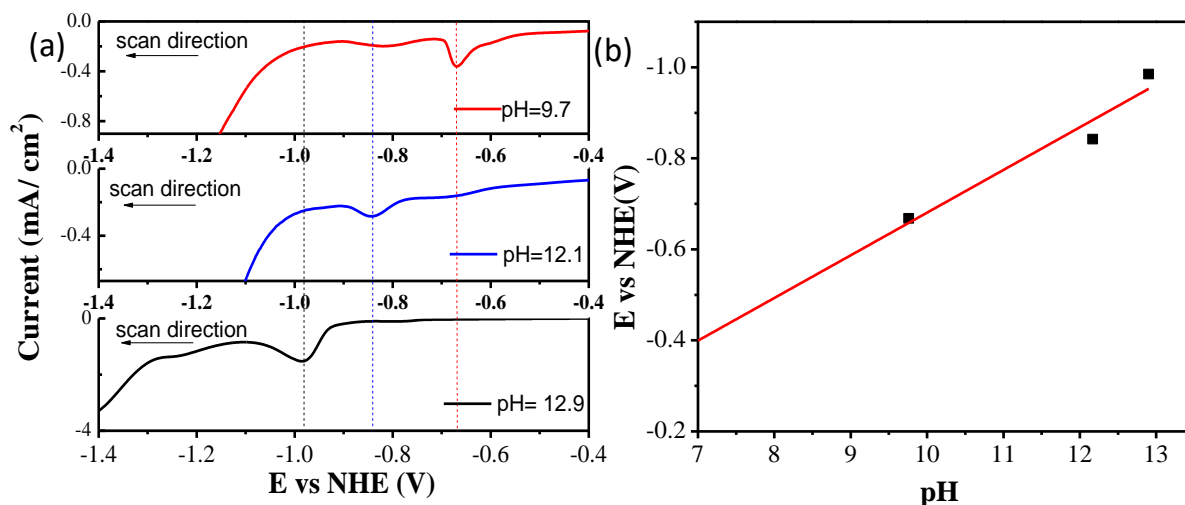

Figure 8. *(a) Dark electrochemical scans of CdS-S^{2-} QDs: ITO in 1M KCl and 0.1 M Na_2SO_3 aqueous electrolyte at pH 9.7, 12.17 and 12.9 recorded at a scan rate of 10mVs^{-1}. Dotted lines intersect the minima of lattice Cd^{2+} reduction peaks at different pH. (b) The Cd^{2+} reduction potential vs. pH shows that Cd is stable against chemical reduction due to hydrazine.*
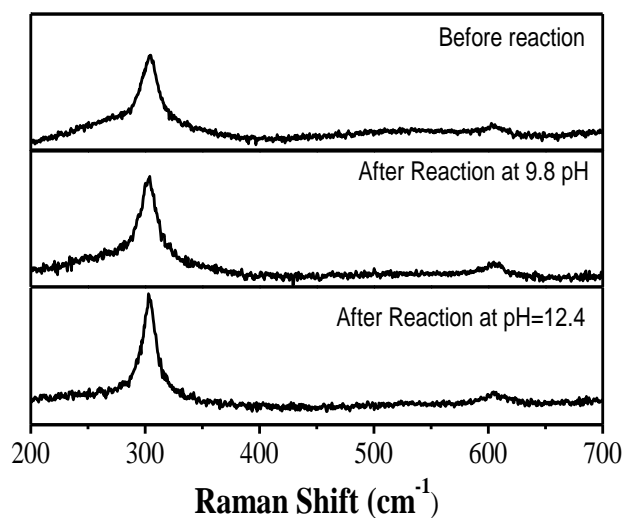

Figure 9. *Raman Spectra of CdS-S^{2-} QDs shows that quantum dots are stable against both photo- and chemical corrosion.*

The dispersions of CdS-S^{2-} QDs were stable against photocorrosion throughout the reaction as also evidenced by Raman spectra recorded at pH 9.8 and 12.4 **(Figure 9).**

The summary of the experiments conducted with $N_2H_4.H_2O$ under various conditions is highlighted in **Table 3**.

Table 3: The summary of the experiments conducted with N₂H₄.H₂O under various conditions using CdS-S^{2-} quantum dots

Experiments	Activity (mmole g^{-1} h^{-1})	Reactant Solution	Remarks
Hydrazine (0.2%)+ water + Catalyst [a]	pH 12.4=24.5 pH 9.8= 19.5 pH 7.0= 14.5	Water+ N₂H₄.H₂O (0.2%)	Increases with pH
Varying Hydrazine (0.2 and 1%)+ water + Catalyst [b]	0.2%=19 1%=25	Water+ N₂H₄.H₂O (0.2% and 1%)	Increases with hydrazine mount
Hydrazine (1 %)+ water + Varying Catalyst concentration [b]	0.5 ml=34 1.0 ml= 25 2.0 ml= 19	Water + (1ml) N₂H₄.H₂O (1%)	Vary with varying catalyst amount with optimal result at low concentration

CdS-S^{2-} QD concentration of [a] 0.21 mM [b] 0.415 mM.

The hydrogen evolution from the photocatalytic decomposition of hydrazine using CdS can be controlled and tuned by modifying the condition. We observed at higher pH rate of H$_2$ evolution increases. The dependence of H$_2$ evolution with a concentration of catalyst shows that quantum dots at higher concentration decreases the activity. This is probably due to scattering of light by quantum dots and unavailability of active sites for hydrazine.

4.3 Decomposition of hydrazine with gallium sulfide (GaS)

Gallium sulfide, like CdS, is a visible light absorbing semiconductor with a band gap of 2.3 eV **(Part 1, Chapter 6 Figure 2).** Gallium sulfide (GaS) single crystals were sonicated in 1 % v/v hydrazine solution and was illuminated with light.
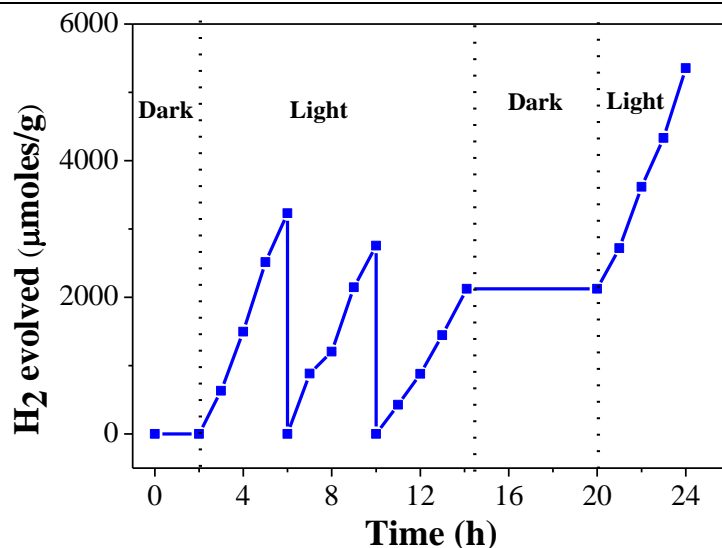

Figure 10. *Hydrogen evolution in hydrazine (1% v/v) and sulfide (0.1 m), and b) light and dark cycle in hydrazine (1% v/v) for GaS over a period of time in the visible light.*

The HER studies were done in both dark and light to make sure that H_2 evolution is light-induced. There was no hydrogen evolution in the dark, which implies that H_2 evolution is light-induced. The activity in the first cycle was 0.89 mmol g^{-1} h^{-1}, followed by a decrease in the activity in the further cycles. When GaS sheets were exfoliated by sonication before the reaction, they appear to restack during the course of reaction blocking the surface sites and making them inaccessible for the photocatalytic HER, leading to the observed reduction in activity (0.57 mmol g^{-1} h^{-1} in the third cycle). In the second dark cycle (for 6 h),

there was no HER evolution. This further confirms that HER occurs only in the presence of light. In the last cycle, the compound was sonicated before irradiating with light and the HER rate increase to 0.80 mmol g^{-1} h^{-1} compared to third cycle value of 0.57 mmol g^{-1} h^{-1} **(Figure 10)**.
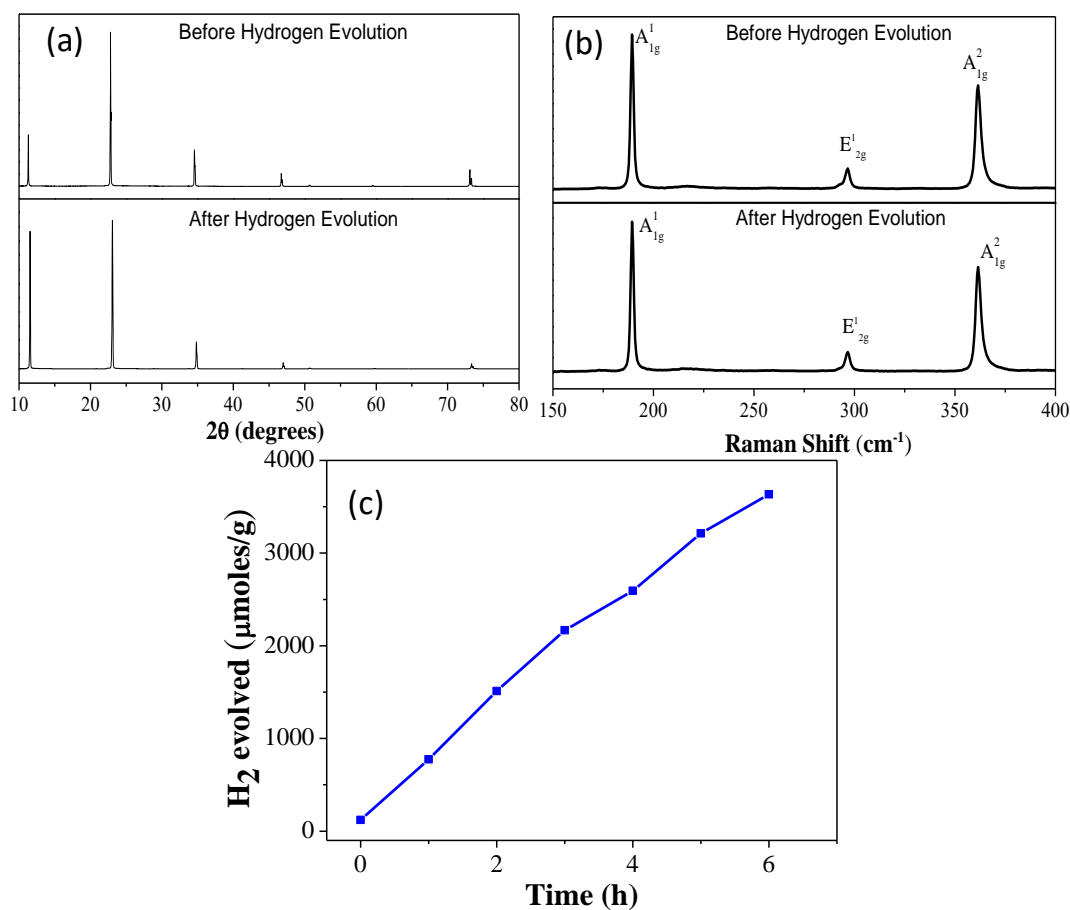

Figure 11. *(a) X-ray diffraction pattern and b) Raman spectra of GaS before (top) and after (bottom) photocatalytic hydrogen reaction. (c) Hydrogen evolution (790 μmol h^{-1} g^{-1}) in an aqueous solution of hydrazine (1% v/v) for the same GaS sample after 7 days.*

Stability of GaS after visible light–induced HER was confirmed by both X-ray diffraction and Raman, i.e., no photocorrosion **(Figure 11 and b)**. The stability of sample was further confirmed by an observed activity of 0.80 mmol

g^{-1} h^{-1} of H_2 after 7 d with the same sample without the additional use of a sacrificial agent **(Figure 11 c)**.

The comparison of the HER activity using the present CdS catalysts with that reported earlier with noble/anatase catalysts is shown in **Table. 4.**

Table 4: Comparison of the HER activity observed with aqueous hydrazine using the CdS catalyst with the other catalysts reported in the literature

Catalyst	Reaction Condition	Activity (mmol g^{-1} h^{-1})	TOF (h^{-1})
CdS-NC[a]	1% (v/v) N_2H_4	8.8	1
CdS-QDs[a]	1% (v/v) N_2H_4	34.7	5
CdS-QDs[a]	0.2 % (v/v) N_2H_4	24.5	3.5
GaS [a]	1% (v/v) N2H4	0.89	0.09
TiO_2 [b, c]	0.7 % (v/v) N_2H_4	0	0
Pt/TiO_2 [b, c]	0.7 % (v/v) N_2H_4	9.2	0.7
Pd/TiO_2 [b, c]	0.7 % (v/v) N_2H_4	7.0	0.6
Ir/TiO_2 [b, c]	0. 7% (v/v) N_2H_4	3.6	0.3
Pt/TiO_2 [b, c]	0.7 % (v/v) N_2H_4	3.1	0.3

[a] Present work (λ > 400 nm, 400 W Xenon lamp); [b] 450 W Xe-arc lamp full range (including UV); [c] Inferred from reference 34.

5. Conclusions

We have studied the photocatalytic generation of H_2 from oxidative decomposition of N_2H_4 over CdS-S^{2-} QDs. The HER activity from aqueous hydrazine obtained with CdS QDs capped with sulfide ligands is stable over long periods and is as high as 33 mmol g^{-1} h^{-1} with a TOF of 4.76 h^{-1} at pH 8 under visible-light illumination. We attribute the high HER activity of CdS-S^{2-} QDs to the relatively larger ΔG_{ox} associated with the oxidation of hydrazine and as well as the rapid transfer of photo-generated carriers across the solid-electrolyte interface facilitated by the shorter S^{2-} ligands. CdS-S^{2-} QDs are found to be good metal-free inorganic semiconductor catalysts for efficient visible-light induced generation of hydrogen from N_2H_4.

Bulk Gallium sulfide (GaS), possesses all the suitable criteria for water splitting, but still does not reduce water to hydrogen. However, GaS efficiently oxidizes hydrazine to hydrogen on irradiation with visible light.

6. References

1. T. He, P. Pachfule, H. Wu, Q. Xu and P. Chen, Nat. Rev. Mats., 2016, 1, 16059(1).

2. R. Costi, A. E. Saunders and U. Banin, Angew. Chem. Int. Ed., 2010, 49, 4878.

3. Fundamentals of Renewable Energy Process (3rd Edition), Aldo da Rosa, 2012, Elsevier.

4. J. Graetz, Chem. Soc. Rev., 2009, 38, 73.

5. U. Eberle, M. Felderhoff and F. Schuth, Angew. Chem. Int. Ed., 2009, 48, 6608.

6. T. V. Choudhary, C. Sivadinarayana and D. W. Goodman, Catal. Lett., 2001, 72, 197.

7. S. K. Singh, A. K. Singh, K. Aranishi and Q. Xu, J. Am. Chem. Soc., 2011, 133, 19638.

8. J. Wang, Y. Li and Y. Zhang, Adv. Func. Mater., 2014, 24, 7073.

9. J. Wang, X.-B. Zhang, Z.-L. Wang, L.-M. Wang and Y. Zhang, Energy Environ. Sci., 2012, 5, 6885.

10. L. D. Burke and K. J. O'Dwyer, Electrochim. Acta, 1989, 34, 1659.

11. J. Sanabria-Chinchilla, K. Asazawa, T. Sakamoto, K. Yamada, H. Tanaka and P. Strasser, J. Am. Chem. Soc., 2011, 133, 5425.

12. L. Q. Ye, Z. P. Li, H. Y. Qin, J. K. Zhu and B. H. Liu, J. Power Sources, 2011, 196, 956.

13. M. Zheng, R. Cheng, X. Chen, N. Li, L. Li, X. Wang and T. Zhang, Int. J. Hydrogen Energy, 2005, 30, 1081.

14. M. Zheng, X. Chen, R. Cheng, N. Li, J. Sun, X. Wang and T. Zhang, Catal. Commun., 2006, 7, 187.

15. X. Chen, T. Zhang, P. Ying, M. Zheng, W. Wu, L. Xia, T. Li, X. Wang and C. Li, Chem. Commun., 2002, 288.

16. J. B. O. Santos, G. P. Valencia, and J. A. J. Rodrigues, J. Catal., 2002, 210, 1.

17.   X. Chen, T. Zhang, M. Zheng, Z. Wu, W. Wu, and C. Li, J. Catal., 2004, 224, 473.

18.   Y. K. Al-Haydari, J. M. Saleh and M. H. Matloob, J. Phys. Chem., 1985, 89, 3286.

19.   D. J. Alberas, J. Kiss, Z. M. Liu and J. M. White, Surf. Sci., 1992, 278, 51.

20.   J. Prasad and J. L. Gland, Langmuir, 1991, 7, 722.

21.   Hydrazine and Its Derivatives: Preparation, Properties, Applications (2nd Edn), E. W. Schmidt, 1984, John Wiley & Sons, New York, 2nd edn,

22.   S. J. Cho, J. Lee, Y. S. Lee and D. P. Kim, Catal. Lett., 2006, 109,181.

23.   S. K. Singh and Q. Xu, Inorg. Chem., 2010, 49, 6148.

24.   S. K. Singh and Q. Xu, Chem. Commun., 2010, 46, 6545.

25.   S. K. Singh, Y. Iizuka and Q. Xu, Int. J. hydrogen energy, 2011, 36, 11794.

26.   S. K. Singh, Z. H. Lu and Q. Xu, Eur. J. Inorg. Chem., 2011, 2232.

27.   S. K. Singh, A. K. Singh, K. Aranishi and Q. Xu, J. Am. Chem. Soc., 2011, 133, 19638.

28.   J. Wang, X. B. Zhang, Z. L. Wang, L. M. Wang, and Y. Zhang, Energy Environ. Sci., 2012, 5, 6885.

29.   L. He, Y. Huang, A. Wang, X. Wang, X. Chen, J. J. Delgado and T. Zhang Angew. Chem. Int. Ed., 2012, 124, 6295.

30.   S. K. Singh, X. B. Zhang and Q. Xu, J. Am. Chem. Soc., 2009, 131, 9894.

31.   M. M. Ardakani, P. E. Karami, P. Rahimi, H. R. Zare and H. Naeimi, Electrochim. Acta, 2007, 52, 6118.

32.   C. Canales, L. Gidi, R. Arce and G. Ramírez New J. Chem., 2016, 40, 2806.

33.   W. M. Costa, A. L. B. Marques, E. P. Marques Cicero, W. B. Bezerra, E. R. Sousa, W. S. Cardoso, C. Song and J. Zhang, J. Appl. Electrochem., 2010, 40, 375.

34.   Y. Oosawa, J. Chem. Soc. Faraday Trans., 1984, 80, 1507.

35.   T. Abe, N. Taira, Y. Tanno, Y. Kikuchi and K. Nagai, Chem. Commun., 2014, 50, 1950.

36.   X. Chen, C. Li, M. Gratzel, R. Kostecki and S. S. Mao, Chem. Soc. Rev., 2012, 41, 7909.

37.   R. Costi, A. E. Saunders and U. Banin, Angew. Chem. Int. Ed., 2010, 49, 4878.

38.   T. Hisatomi, J. Kubota and K. Domen, Chem. Soc. Rev., 2014, 43, 7520.

39.   M. R. Kim and D. Ma, J. Phys. Chem. Lett., 2015, 6, 85.

40.   F. E. Osterloh, Chem. Soc. Rev., 2013, 42, 2294.

41.   P. Wang, J. Zhang, H. He, X. Xu, and Y. Jin, Nanoscale, 2014, 6, 13470.

42.   K. Wu, Z. Chen, H. Lv, H. Zhu, C. L. Hill and T. Lian, J. Am. Chem. Soc, 2014, 136, 7708.

43.   M. J. Berr, P. Wagner, S. Fischbach, A. Vaneski, J. Schneider, A. S. Susha, A. L. Rogach, F. Jackel and J. Feldmann, Appl. Phys. Lett., 2012, 100, 223903.

44.   W. W. Yu, L. Qu, W. Guo and X. Peng, Chem. Mater., 2003, 15, 2854.

45.   M. V. Kovalenko, M. I. Bodnarchuk, J. Zaumseil, J.-S. Lee and D. V. Talapin, J. Am. Chem. Soc., 2010, 132, 10085.

46.   Y. Q. Zhang and X. A. Cao, Appl. Phys. Lett., 2011, 99, 023106.

47.   G. K. Grandhi, K. Swathi, K. S. Narayan and R. Viswanatha, J. Phys. Chem. Lett., 2014, 5, 2382.

48.   H. Zhu, N. Song and T. Lian, J. Am. Chem. Soc, 2013, 135, 11461.

49.   H. Gerischer, Electrochim. Acta, 1990, 35, 1677.

50.   L. Aldous and R. G. Compton, Phys. Chem. Chem. Phys., 2011, 13, 5279.

51.   M. V. Kovalenko, M. Scheele and D. V. Talapin, Science, 2009, 324, 1417.

52.   A. Nag, M. V. Kovalenko, J.-S. Lee, W. Liu, B. Spokoyny and D. V. Talapin, J. Am. Chem. Soc., 2011, 133, 10612.

53.   T. Simon, N. Bouchonville, M. J. Berr, A. Vaneski, A. Adrovic, D. Volbers, R. Wyrwich, M. Doblinger, A. S. Susha, A. L. Rogach, F. Jackel, J. K. Stolarczyk and J. Feldmann, Nat Mater, 2014, 13, 1013.

Part 5

Photochemical Water oxidation using Co and Mn based oxides

Visible light induced oxidation of water by rare earth manganites, cobaltites and related oxides and beneficial effect of platinum*

Summary

Oxidation of water is a challenging process with a positive free energy change and it is purposeful to find good catalysts to facilitate the process. A study of the visible light induced oxidation of water by perovskite oxides of the formula $LaMO_3$ (M = transition metal) has revealed the best activity with $LaCoO_3$ which contains Co^{3+} in the intermediate-spin state with one e_g electron. Among the rare earth manganites, only orthorhombic manganites with octahedral Mn^{3+} ($t_{2g}^3 e_g^1$) ions exhibit good catalytic activity, while hexagonal manganites are poor catalysts. Interestingly, not only the perovskite rare earth cobaltites, but also solid solutions of Co^{3+} in cubic rare earth sesquioxides exhibit catalytic activity comparable to $LaCoO_3$, the Co^{3+} ion in all these oxides also being in the intermediate-spin ($t_{2g}^5 e_g^1$) state. While the perovskite oxides, $LaCoO_3$ and $LaMnO_3$, are good electron transfer catalysts in artificial photosynthesis to produce oxygen by the oxidation of water, the electron transfer is further favoured by the presence of platinum nanoparticles, causing a substantial increase in oxygen evolution.
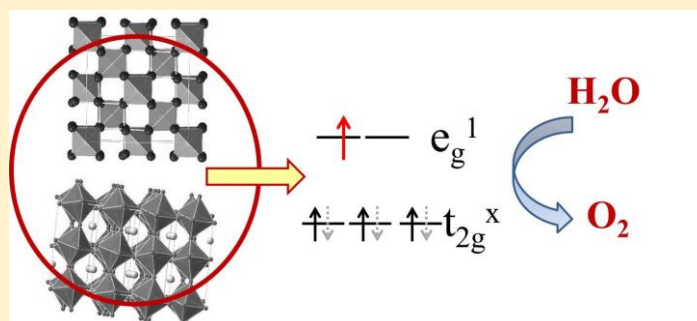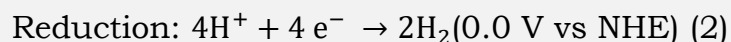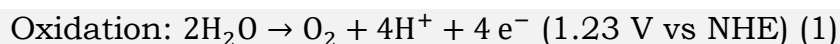
1. Introduction

As discussed in the previous parts, any strategy for solving the energy crisis would involve the generation of fuels through artificial photosynthesis, involving the sun as the only source of energy. In order to complete the solar cycle, water has to act as the source of electrons, either to generate liquid fuels by the reduction of CO_2 or to yield H_2 through a complete cycle of transfer of electrons. Photovoltaics have been used for the production of H_2, but the cost of photovoltaic solar cells marginalizes the use of this route for the purpose. Solar energy, an abundant source of energy can only be used by converting it into a useful form of energy [1, 2]. Solar stimulated catalytic water splitting to generate hydrogen has thus emerged to be a sustainable approach to solve the energy crisis [2]. The challenge is to develop a water splitting catalyst that is robust and is composed of earth-abundant non-toxic materials.

Since water splitting is an uphill reaction where major challenge lies in water oxidation **(Equation 1)**,

$$\text{Oxidation: } 2H_2O \rightarrow O_2 + 4H^+ + 4\,e^- \text{ (1.23 V vs NHE) (1)}$$

$$\text{Reduction: } 4H^+ + 4\,e^- \rightarrow 2H_2 \text{(0.0 V vs NHE) (2)}$$

Water oxidation is a 4-electron process **(Equation 1)** which makes it kinetically slower reaction compared to water reduction which is a 2-electron process **(Equation 2)**. In photocatalytic water splitting, oxidation of water involving the transfer of four electrons is the energy-intensive step and it, therefore, necessary to find good visible light active catalysts for water oxidation [3]. While IrO$_2$ and RuO$_2$ are good water oxidation

catalysts, they are expensive and scarce [4–8]. Any strategy to facilitate this process would also enhance the proton reduction ability of the photocatalytic system. Water oxidation takes place inside plants and can inspire to develop similar catalysts.

1.1 Natural photosynthesis

In **Figure 1**, we show a schematic demonstration of natural photosynthesis. Solar energy is absorbed by chlorophyll and other pigments of PSII, which is the center for light-reaction in photosynthesis. P680 (containing chlorophyll a) or PSII absorbs a photon and loses an electron to pheophytin (a modified form of chlorophyll) generating P680$^+$. The redox potential of P680 is highly oxidizing while that of pheophytin is -0.5V so that it is able to reduce H$^+$ to H$_2$ [9].
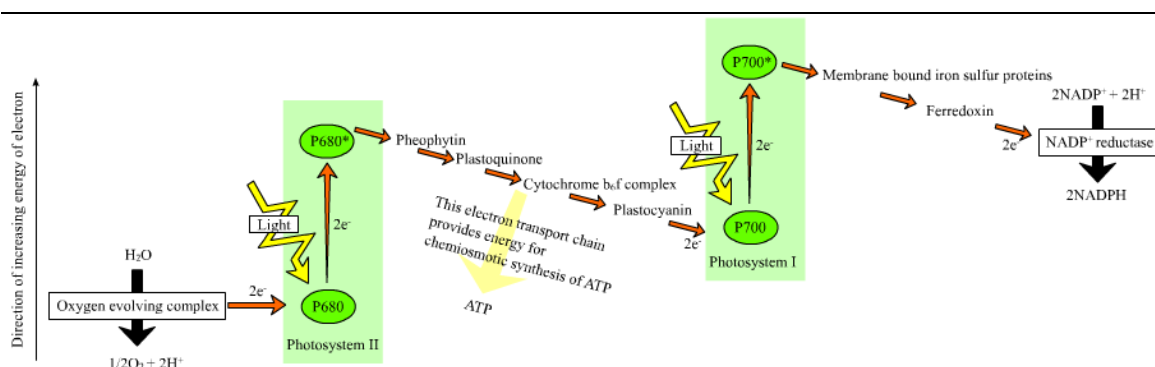

Figure 1. *Z-scheme of photosynthesis. PSI and PSII are photosystems I and II respectively, also known as P680 and P700. Adapted from Wikipedia.*

The probability of electron-hole recombination is minimized by the electron transport via pheophytin down, along with a chain of molecules to photosystem I (PSI). This process of electron transfer down a chain of potential gradients ensures that the charge separation quantum efficiency of nearly 100% since the electron transfer processes happen on a femtosecond timescale. The electrons (e$^-$) and holes (h$^+$) have lifetimes of

µsec before charge recombination. $P680^+$ regains its electron from water thereby oxidizing it to O_2 in a reaction catalyzed by the water oxidizing center (WOC) which is a cubic Mn_4O_5Ca cluster encapsulated in a protein environment **(Figure 2a)**. In the meantime, P700 or PSI absorbs light and loses an electron to reduce H^+ and convert $NADP^+$ to NADPH thereby generating $P700^+$. The electron that travels down the cascade of steps to PSI is used up by $P700^+$ [9].
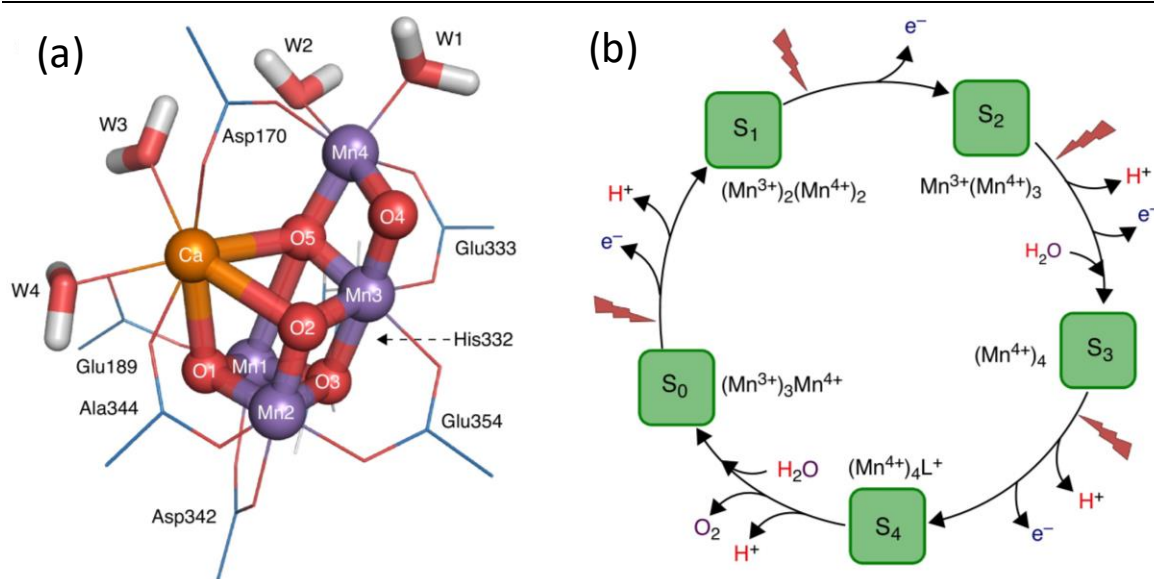

Figure 2. *(a) Structure of the water oxidation center (WOC) Mn_4CaO_5 and coordinating residues crystal structure. Mn (purple), Ca (orange) and O (red). (b) The intermediate "S" states of the Kok cycle, which shows the sequence of electron- and proton-removal steps. The probable oxidation states of the Mn ions in each metastable state is shown during the course of the cycle. Adapted with permission from reference 9. Copyright 2015 Elsevier.*

The reaction (Kok) cycle comprises of five distinct redox intermediates of Mn, the S_n (n= 0 to 4) states, where the n indicates the number of stored oxidizing equivalents required to split two water molecules **(Figure 2b)**. The cycle is successively driven by the photo-oxidant of PSII (P680). The

photochemistry of the reaction center is coupled to the reaction catalyzed by the Mn_4O_5Ca cofactor. The oxidation states of Mn changes over the different stages of the Kok cycle which helps in water oxidation **(Figure 2b)** [9].

The electron transport chain is commonly referred to as the **Z-scheme** of photosynthesis. Generation of O_2 from water is a 4 electron process as shown in reaction 1. PSII has to, therefore, absorb 4 photons to drive this half-reaction, and PSI also has to absorb 4 photons for the following reduction reaction. The natural photosynthetic system generates one electron and one hole on absorption of two photons which makes its efficiency to almost 50% (theoretical efficiency 100%). Considering that chlorophylls absorb nearly in the entire visible range but utilizes only the red part of the spectrum, the efficiency drops down to 20%. In practice, the efficiency of natural photosynthesis in an agricultural crop is nearly 1% over its entire life-cycle [10].

The natural system of water oxidation in plants occurs in the water oxidation complex (WOC) of the Photosystem II [11, 12]. The WOC is a Mn_4O_5Ca cluster housed in protein environment **(Figure2a)**. Mn is one of the most abundant transition metal found on earth while Ca is the fifth most abundant element on earth's crust. Understanding the WOC, therefore, paves the way to develop efficient water oxidation catalysts. A wide range of techniques has been applied to probe the molecular mechanism and investigate the structure of the catalytic center. X-ray absorption spectroscopy [13] and X-ray crystallography studies [14, 15], coupled with quantum mechanical analyses, have provided a refinement

of the structure of the WOC [16] and given detailed schemes for the water splitting chemistry leading to O–O bond formation [15, 17, 18]. These detailed investigations have revealed that WOC comprises three Mn ions and a Ca ion forming a cubane-like structure with the four metal ions linked by oxo-bridges **(Figure2a)**. A fourth Mn ion is linked to the cubane by two oxo-bridges and is adjacent to the Ca ion forming $CaMn_4O_5$ cubical core cluster [19, 20]. To study the principles governing photosynthesis, molecular systems with structures comparable to that of Mn_4O_5Ca cluster having a $[Mn_4O_4]$ core have been studied [21, 22].

1.2   Artificial photosynthesis

Artificial photosynthesis employs principles derived from natural photosynthesis. It involves a photon-absorbing center followed by a catalytic center with an electron and hole transfer pathway joining the two. This two processes can either be a single-step or a two-step process which can be employed in artificial photosynthesis **(Figure 3). Figure 3a** shows hydrogen and oxygen evolution reaction on a simple single semiconductor system. Light absorption and reaction takes places on the semiconductor. Since electron-hole recombination rate is faster than the reaction rate, suitable co-catalysts can be used to enhance the reaction rate over recombination **(Figure 3 a)**. A Schottky barrier (by using a semiconductor-metal heterojunction) increases charge separation across the interface. Sometimes a catalyst is inefficient in water oxidation a suitable reducing agent is used to facilitate the reaction which enhances the process **(Figure 3b)**. Dyes or photosensitizers can be used to harvest light which can assist the OER **(Figure 3c)**. Dye reduce itself or a sacrificial is used.
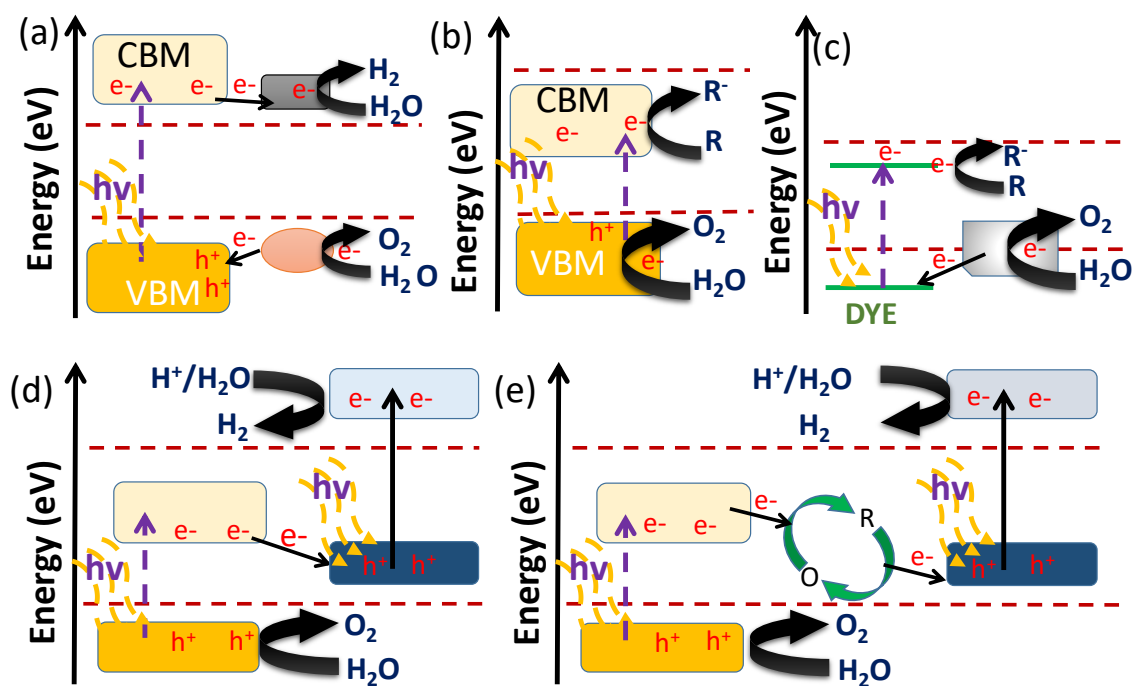
Figure 3. *(a) Overall water splitting, using on a single semiconductor. A co-catalyst is used to facilitate either or reduction or sometimes both. (b) Water oxidation in the presence of a sacrificial reagent. (c) Dye-sensitized oxygen evolution. Overall water splitting based on (d) Type II- and (e) Z-scheme based heterojunction catalysts.*

In the single-step process, a photon absorber is directly attached to an electron acceptor on one side and/or an electron donor on the other, or it can be the same species (catalyst). The light absorbing entity can either be a semiconductor or a dye which harvests light by generating an electron-hole pair. The wavelength of light absorbed is determined by the band gap of the semiconductor or the difference in the HOMO-LUMO gap of the dye **(Figure 3 a and c)**. The semiconductor or dye is generally used in conjugation with an electron accepter or an electron donor to enhance charge separation. An electron donor should possess an reduction potential more negative than that of excited state reduction potential of the semiconductor or the dye as well more facile than the water oxidation

potential **(Figure 3b)**. The electron acceptor would have an energy level more negative than the proton reduction potential and more positive than the excited state oxidation potential of the photon absorber. For fast electron transfer, acceptors and donors must be close to the photon absorber. Electron and hole transfer occurs directly from the energy levels of the semiconductor or the dye to either the electron acceptor or the electron donor or sometimes, neither of them are being used in the course of the reaction.

In the two-step process, two-photon absorbers are connected to each other by an electron transfer-relay material, the rest of the principles being similar to that of the single step process as shown in **Figure 3 (c and d)**. A redox couple is used as the electron transfer relay. The two-step process is analogous to the Z-scheme of natural photosynthesis and utilizes two photons to generate an electron and hole. The two components of the Z-scheme consisting of two inividual single-step process combined into one. The single-step process although easy, however, the disadvantage is that wavelength above <680 nm has to be used to initiate both the oxidation and reduction of water. The two-step process can be used for overall water splitting even with low excitation energy, as low as near-infrared wavelengths. The advantage is accompanied by the difficulty of maintaining the kinetics of the full electron-transfer process with minimal energy loss by charge recombination reactions. An ideal process of electron transfer is to have more than one electron acceptor or donor level closely spaced in energy as in natural photosynthesis. However, this increases the

complexity of the system and is somewhat difficult to achieve. Suitable electron acceptors like fullerenes [23, 24] have been coupled with chromophores to achieve up to 95% charge separation. A more straightforward but less effective strategy is to employ co-catalysts in semiconductor-based light harvesters. Pt, Pd, NiO (for H_2) and RuO_2, IrO_2 (for O_2) satisfy the required conditions for use as catalysts.

The mechanism of photosynthesis (artificial or natural) thus comprises three aspects: i) light-harvesting, ii) charge generation and separation and iii) catalytic reaction as shown in Figure 3 (a). The photosynthetic catalysts can be classified as:

- Semiconductor-based photocatalysts

- Catalysts used in photoelectrodes.

- Dye-sensitized catalysts

Inspired by natural photosynthesis, in the recent experiments, transition metal oxides have been used as WOCs in artificial photosynthesis. Catalysts based on Mn and Co oxides are inexpensive, and there have been efforts to investigate the photocatalytic properties of these oxides for the production of oxygen [25–35]. Several simple Mn and other transition metal oxides with structures similar to the Mn_4O_4 core have been studied to understand the process of natural photosynthesis utilizing simple inorganic oxides. Mn is not only an abundant element but also occurs in easily switchable oxidation states. Marokite type oxides, $CaMn_2O_4$ and $CaMn_2O_4.xH_2O$ exhibit good activity for water oxidation [25]. Based on X-ray spectroscopic studies, the mixed valency of Mn (III/IV) was considered to be a criterion for good catalytic activity [36]. Electrochemical

water oxidation by $Ca_2Mn_3O_8$ which is structurally analogous to the $CaMn_4O_5$ clusters has also been investigated [37]. Co_4O_4 based cubanes [38, 39], nanocrystalline Co_3O_4 [32] and Mn_2O_3 [40] as well as "Co-Pi" and Co-Phosphates [41, 42] have also been shown to be active for the oxygen evolution reactions(OER).

It has been shown recently that trivalency of Co and Mn ions, as well as the (e_g^1) electronic configuration, are crucial factors in determining the catalytic activity [43]. Catalytic activity for electrochemical oxygen evolution by lanthanide perovskites is also suggested to be dependent on the 3d-electron occupancy in the e_g orbitals of B site cations [44]. Thus, Mn_2O_3 and $LaMnO_3$ with Mn(III) in the $(t_{2g}^3 e_g^1)$ configuration as well as $Li_2Co_2O_4$ and $LaCoO_3$ with Co(III) in the $(t_{2g}^5 e_g^1)$ configuration are found to be an excellent catalyst for photocatalytic water oxidation [43]. We have examined the photocatalytic activity of these solid solutions containing Co(III) ions and found it to be comparable to that of the perovskites. In order to strictly compare the catalytic performance of the various oxide materials, we have measured the oxygen evolved per mole of transition metal per unit surface area. Of all the oxides, perovskites of Co^{3+} and Mn^{3+} with the (e_g^1) configuration are found to be most effective. The best results in the oxidation of water by reaction (1) have been obtained by $LaCoO_3$ and $LaMnO_3$. The OER activity is enhanced with Pt nanoparticles exhibiting synergistic effect between them.

2. Scope of the present investigations

We considered it to be of vital interest to explore the catalytic activity of a related series of perovskite cobaltites and manganites of the type $LnCoO_3$ and $LnMnO_3$ (Ln = rare earth) and also of related oxides. Careful photocatalytic water oxidation studies have indicated that cobaltites show better activity than manganites while nickelate and ferrites show reduced activity. Furthermore, orthorhombic manganites show much higher activity than the hexagonal manganites. In the case of cobaltites of the rare heavy earth such as Dy, Er, Yb and Y, the oxides obtained from the citrate gel decomposition depend on the reaction temperature, those prepared around or below 700°C generally exist as cubic solid solutions of Ln_2O_3 and Co_2O_3 (space group Ia).

We have carried out experiments to see whether platinum, a well-known co-catalyst for the hydrogen evolution reaction (HER) affects the rate of oxidation of H_2O in the oxygen evolution reaction (OER). For this purpose, we have used Pt nanoparticles and studied OER using $LaCoO_3$ and $LaMnO_3$ as the primary oxidation catalysts.

3. Experimental section

3.1 Synthesis

3.1.1 Synthesis of transition metal lanthanum oxides

All these materials were synthesized by citrate sol-gel method. $Mn(CH_3COO)_2.4H_2O$, $Co(CH_3COO)_2.4H_2O$, $Fe(NO_3)_3.9H_2O$, $Cr(NO_3)_3.9H_2O$, $Ni(NO_3)_2.6H_2O$, Li_2CO_3, anhydrous citric acid, urea, and conc. HNO_3 (70%) were used as starting materials. In a typical synthesis procedure, 5 mmol

of lanthanum nitrate and 5 mmol of transition metal nitrate were dissolved in 30 mL of distilled water. To this solution, 50 mmol of anhydrous citric acid was added and heated to 80 °C while stirring to form a gel and maintained at this temperature till dryness (around 9 h). This gel was kept in an electric oven at 200 °C for 12 h, and a small part of this gel was heated at required temperatures after grinding. For preparing lanthanide manganites, precursor citrate-gel was heated at 800 °C for 5h with a heating rate of 7 °C/min whereas for lanthanide ferrites and lanthanide nickelate heated at 700 °C for 5 h. In case of orthorhombic lanthanide cobaltates, the heating temperature was varied with lanthanides. In case of La, Pr, Nd, Sm; gel was heated at 500 °C for 8 h, for Gd at 700 °C and for Dy at 800 °C about 5 h.

3.1.2 Synthesis of Pt-LaMO$_3$ composites

Composites of LaCoO$_3$ with Pt nanoparticles were prepared with different weight percentages of Pt (0.5, 2, and 5). In a typical synthesis, 25mg of LaCoO$_3$ was dispersed in 10 ml of water, and to it, the corresponding amount of weight percent of H$_2$PtCl$_6$ was added and kept for overnight stirring. Then the excess of 50 mM solution of NaBH$_4$ was added to the dispersion of LaCoO$_3$ and H$_2$PtCl$_6$ while stirring and was left as it for 12 hours. The product was washed with water and ethanol and characterized.

3.2 Characterization

Powder X-ray diffraction (XRD) measurements were carried out with Bruker D8 Advance diffractometer using Cu K$_\alpha$ radiation. The average crystallite size was calculated by using Debye-Scherrer formula

$t = 0.9\lambda/(\beta Cos\theta)$, where β is the full width at half maxima in radians, λ is the wavelength of X-rays, θ is the Bragg angle. Particle size was also examined from transmission electron microscope (TEM) images obtained with a JEOL JEM 3010 operating at an accelerating voltage of 300 kV. Surface area was determined from N_2 adsorption measurements carried out in Quanta-chrome Autosorb instrument at 77K. Magnetic measurements were carried out with a vibrating sample magnetometer in the magnetic property measurement system (MPMS-SQUID VSM) of Quantum Design, USA.

3.3 Oxygen evolution studies

Oxygen evolution measurements were carried out using the oxygraph instrument, Hansatech Ltd, equipped with Clark type oxygen electrode. Calibration of the oxygen electrode was done with air saturated Millipore water and then deoxygenated by N_2 purging. Throughout all the measurements, the temperature of the reaction chamber was maintained at 25 °C by using Julabo F 25 pump. In the reaction chamber, 0.022 M Na_2SiF_6 and 0.028 M $NaHCO_3$ buffer, 1.5 mM $[Ru(bpy)_3]$ $Cl_2 \cdot 6H_2O$, 20 mM $Na_2S_2O_8$ and 80 mM Na_2SO_4 and 100 ppm catalyst was added. The total volume of the solution was 2 mL the solution was stirred continuously throughout the reaction with 100 rpm speed. The catalyst solution was sonicated for 5-10 min prior to adding into the reaction vessel. All the solutions were made fresh every day. This solution was purged with nitrogen until all the oxygen was purged out then the reaction chamber was closed with the airtight plunger and waited until the oxygen level was constant. Then the reaction vessel was illuminated with a 100 W halogen

lamp, and a small percentage of UV light was filtered with BG 38 filter. Light intensity was kept at 25,000 Lux. Oxygen evolution from these samples was further confirmed with Gas chromatograph (GC) by maintaining similar conditions for 50 ml reaction solution. Headspace gas was analyzed by using PerkinElmer Clarus 580 GC system.

4. Results and Discussion

4.1 Transition metal lanthanum oxides

Oxygen evolution property of the catalysts was studied under visible light in standard photoexcitation system [38] consisting of $[Ru^{III}(bpy)_3]^{2+}$ as photosensitizer and $Na_2S_2O_8$ as a sacrificial electron acceptor in a solution buffered at pH = 5.8. The singlet $[Ru(bpy)_3]^{2+}$ on photoexcitation goes to triplet state denoted as $[Ru(bpy)_3]^{2+*}$. The species transfers its electrons to the sacrificial oxidant $S_2O_8^{2-}$. The resulting $[Ru(bpy)_3]^{3+}$ takes an electron from the metal oxide catalyst which in turn oxidizes water to molecular O_2, as demonstrated in Scheme below **(Scheme 1)**.
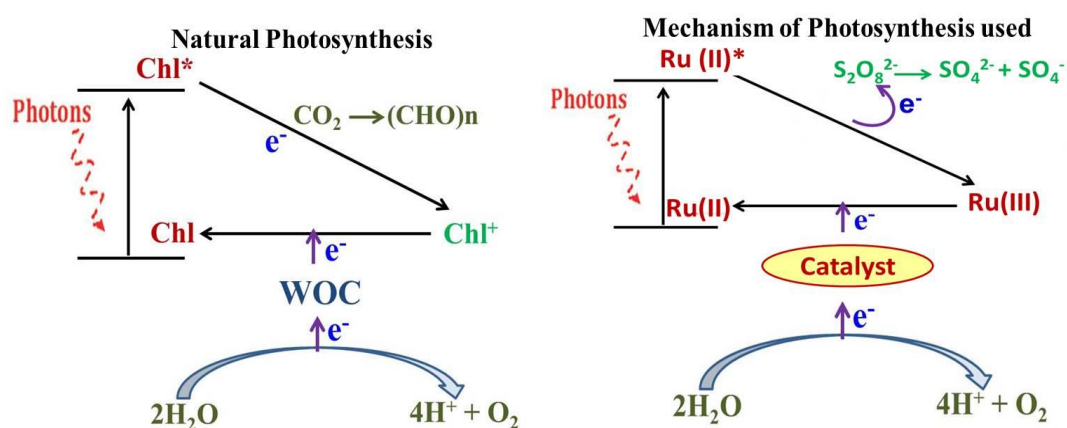
Scheme 1. *Comparison of the processes used for photosynthetic oxidation of water with that of natural photosynthesis.*

The process used to study water oxidation was designed similar to natural photosynthesis as shown in the Scheme below. While chlorophyll

acts as the photosensitizer in plants, $[Ru^{III}(bpy)_3]^{2+}$ was used in our processes, and the photoexcited electron instead of being used up by CO_2 is taken up irreversibly by $Na_2S_2O_8$. The catalyst thus plays the exact role as that of the WOC, donating electrons to regain the photosensitizer oxidizing water in the processes.

Oxygen evolved was quantified both by Clark type electrode and gas chromatography. To compare the catalytic performance of the various oxide materials strictly, we have measured the oxygen evolved per mole of transition metal and normalized it with respect to BET surface area of the catalyst. Turn over frequencies (TOF) for each catalyst was calculated from the initial slope of O_2 evolved per mole of transition metal vs. time plot.

4.1.1 LaMO$_3$ (M= Cr, Mn, Fe, Co, or Ni)

In order to establish the role of the electronic configuration of the transition metal ion on the photocatalytic water oxidation, we first examined the photochemical catalytic activity of lanthanum perovskites of the formula $LaMO_3$ (M= Cr, Mn, Fe, Co, and Ni).
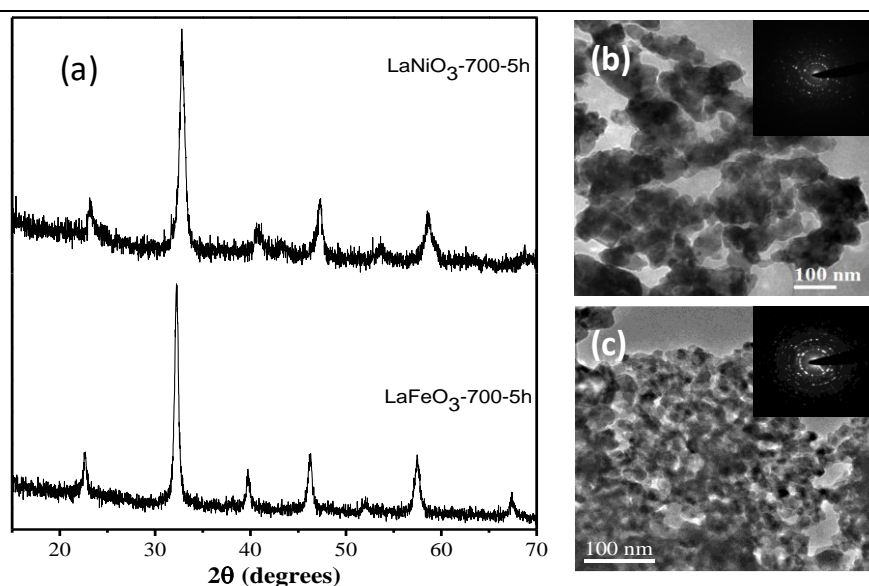

Figure 4. *(a), (b) XRD patterns and (c), (d) TEM images of LaNiO₃, LaFeO₃ respectively.*

The crystallite sizes of these oxides obtained from X-ray diffraction patterns **(Figure. 4 a)** as well as their BET surface areas are listed in **table 1**. The particle sizes obtained from TEM images are in the range 15-55 nm **(Figure 4 b and c)**.

Oxygen evolution properties of these materials per mole of the transition metal are shown in **Figure. 5(a)**. $LaCoO_3$ shows the best water oxidation activity with a TOF of 1.4×10^{-3} s^{-1} followed by $LaMnO_3$ (4.8×10^{-4} s^{-1}). $LaNiO_3$ (1.2×10^{-4} s^{-1}) and $LaFeO_3$ (8.9×10^{-5} s^{-1}) show poor activity. $LaCrO_3$ does not show any oxygen evolution catalytic activity under similar conditions.
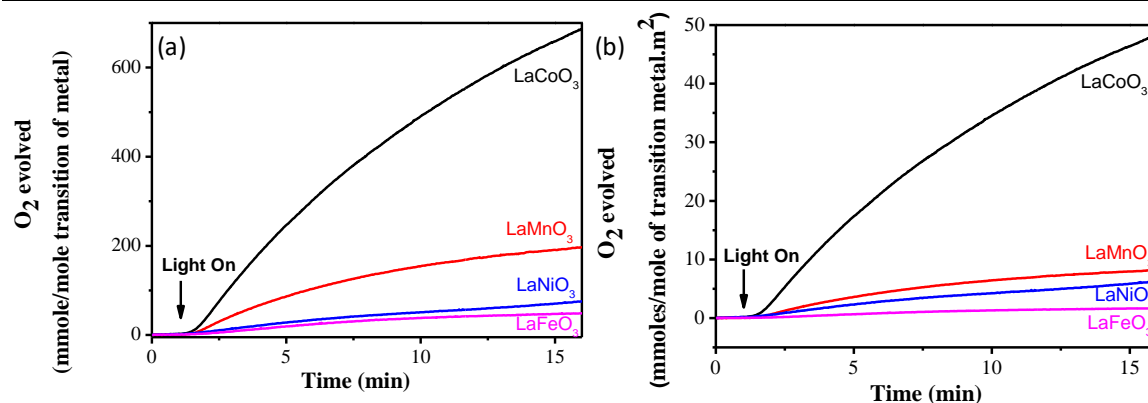

Figure 5. *O_2 evolved by $LaMO_3$ (M: Mn, Fe, Co, and Ni) (a) per mole of a transition metal, (b) per mole of transition metal per unit surface area.*

4.1.2 LnMnO₃ (Ln= La, Nd, Sm, Gd, Dy, Y or Yb)

The oxygen evolved per mole of transition metal per unit surface area is shown in **Figure. 5(b)** follows the same order as in **Figure. 5(a).** The oxygen evolved per mole of transition metal per unit surface area of $LaCoO_3$, $LaMnO_3$, $LaNiO_3$ and $LaFeO_3$ after 15 min are 48.3, 8.2, 6.3 and 1.7 mmol/mole of transition metal.m^2 respectively. We next studied the catalytic activity of the series of manganites $LnMnO_3$ with Ln= La, Nd, Sm,

Gd, Dy, Y and Yb for the oxidation of water, having prepared all the manganites by citrate gel decomposition at 800°C. The manganites of Nd, Sm, Gd, and Dy, crystallize in the orthorhombic structure (space group Pbnm) whereas those of yttrium and ytterbium crystallize in the hexagonal structure (space group P6$_3$cm). LaMnO$_3$ crystallizes in rhombohedral phase.
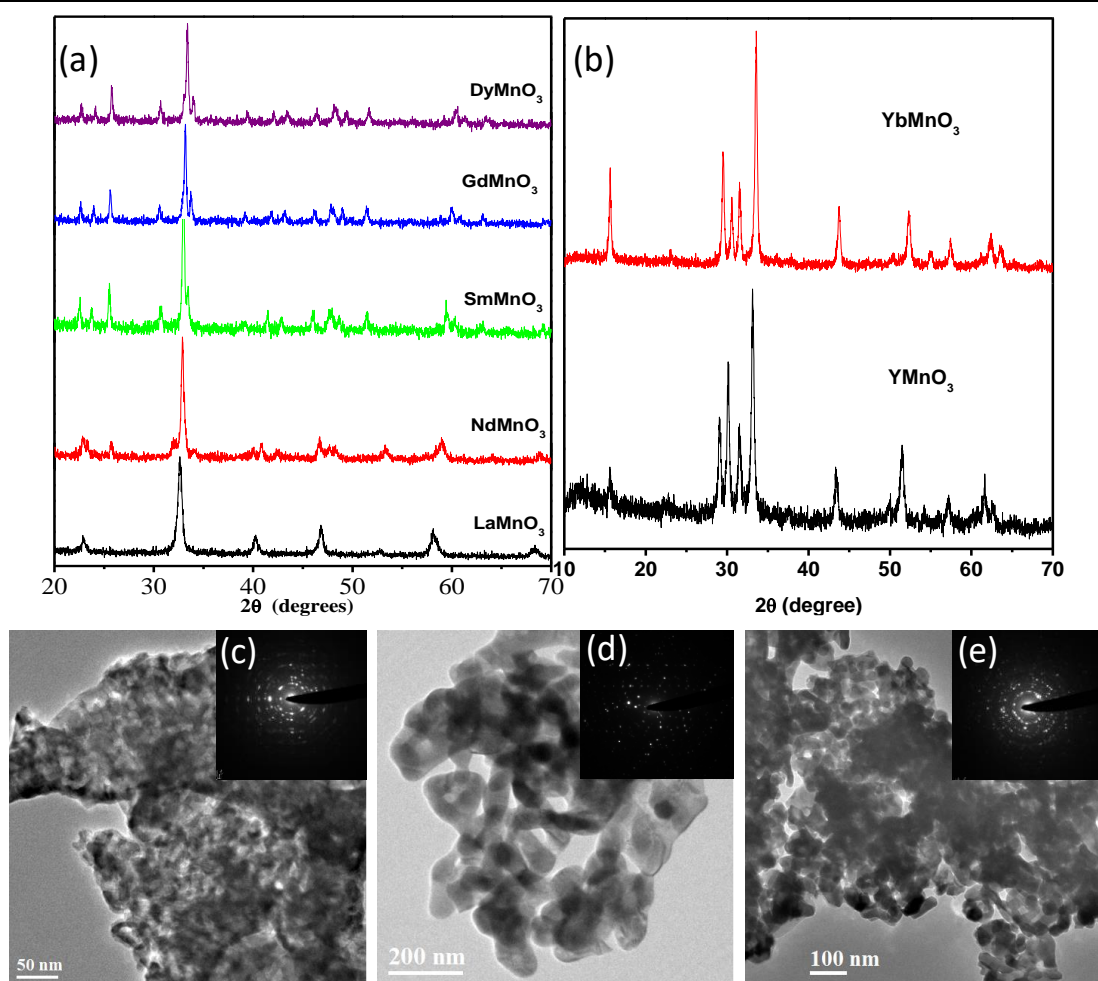

Figure 6. *XRD patterns of (a) orthorhombic (b) hexagonal lanthanide manganates prepared at 800 °C . TEM images of (c) LaMnO₃, (d) GdMnO₃, (e) YbMnO₃. In insets, corresponding SAED patterns were showed.*

The XRD patterns of the manganites are given in **Figure. 6 (a and b)**. TEM images showed that the oxide materials were composed of crystalline nanoparticles **(Figure. 6 c-e)**. The electron diffraction (ED) patterns shown

in the inset of **Figure. 6 (c-e)** confirm the crystalline nature of the catalysts. The crystallite size calculated from XRD patterns and the BET surface areas obtained from N_2 absorption at 77K are listed in **table 1.**

We have plotted the O_2 evolved per mole of manganese ion in **Figure 7 (a)**. Among the manganites, $LaMnO_3$ shows the highest catalytic activity with a TOF of 4.8×10^{-4} s^{-1}. All the other orthorhombic manganites (Ln= Nd, Sm, Gd, and Dy) have comparable catalytic activities with a TOF between 2.4×10^{-4} s^{-1} and 2.1×10^{-4} s^{-1} corresponding to 119 ± 7 mmole of O_2 per mole of Mn after 15 min of illumination. The hexagonal manganites (Ln= Y and Yb), on the other hand, show a much lower O_2 yield of 49 ± 10 mmole per mole of Mn after 15 min of illumination with a TOF of 5.2×10^{-5} s^{-1} for $YMnO_3$ and 9.2×10^{-5} s^{-1} for $YbMnO_3$.

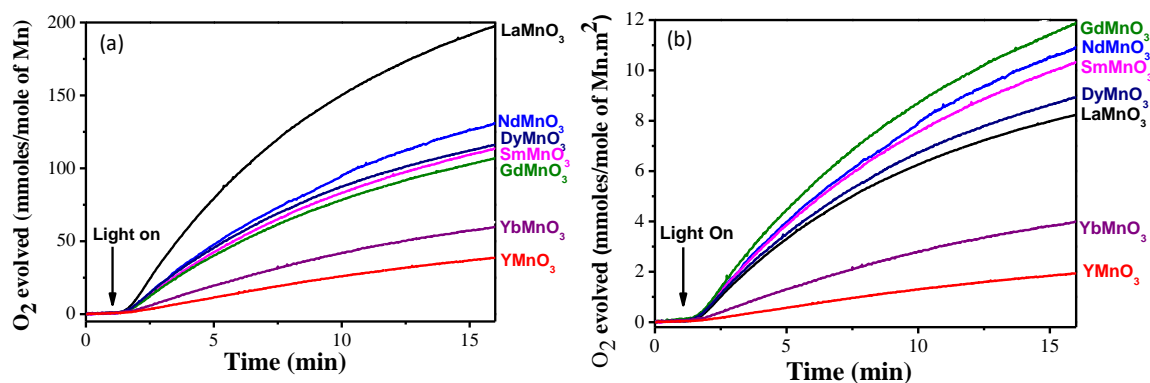**Figure 7.** *O_2 evolved by rare earth manganates (a) per mole of Mn, (b) per mole of Mn per unit surface area*

The data on oxygen evolved per mole of Mn per unit surface area are shown in **Figure 7 (b)**. The rare earth manganites with the orthorhombic structure, including $LaMnO_3$ show somewhat comparable oxygen evolution of 10 ± 1.8 mmol/mole of $Mn.m^2$. The hexagonal manganites show much lower values of O_2 evolved, in the range of 2.9 ± 1 mmol/mole of

Mn.m^2. Clearly, orthorhombic perovskite manganites show better catalytic activity as compared to hexagonal perovskites for photocatalytic water oxidation. It must be noted that in all these oxides, Mn is in +3 oxidation state. The difference in the oxygen evolution catalytic activity between the orthorhombic and hexagonal manganites is considered to depend on the electronic configuration of Mn^{3+} (d^4) ion which is determined by the nature of coordination. In the orthorhombic and rhombohedral manganites, Mn(III) exists in octahedral coordination and the electronic configuration is $t_{2g}^3 e_g^1$ which causes Jahn-Teller distortion of the octahedral [45]. In hexagonal manganites, Mn(III) exists in trigonal bipyramidal symmetry (MnO$_5$), the electronic configuration being $e''^2 e'^2 a_1'^0$ [45-47].

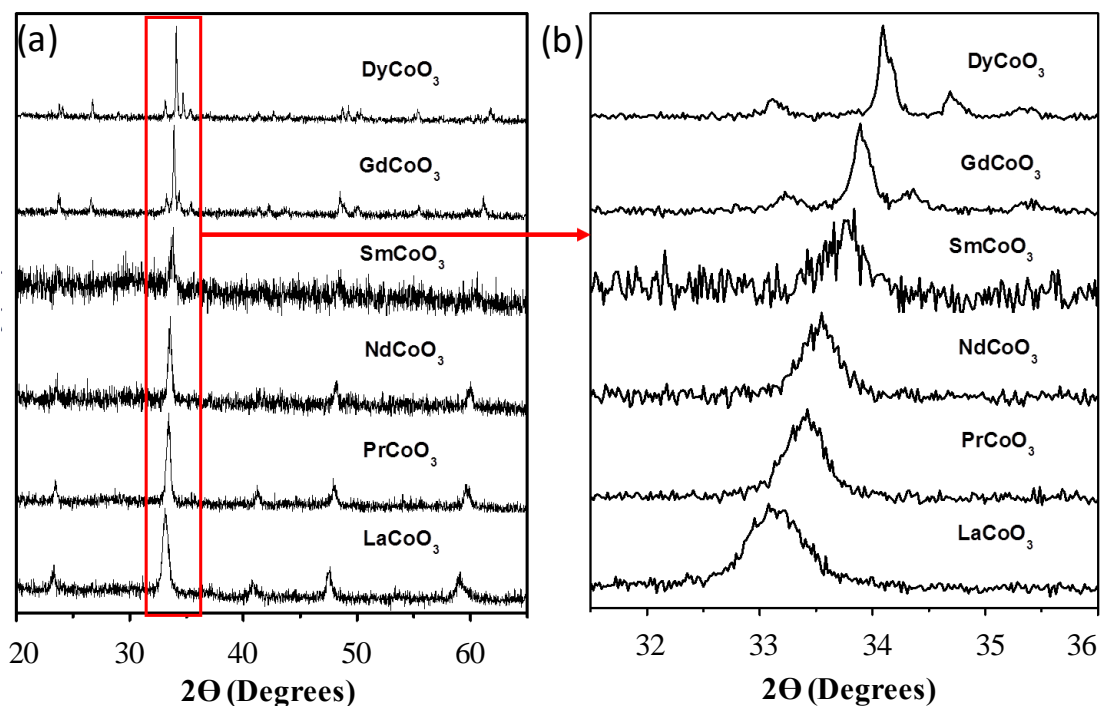### 4.1.3 LnCoO$_3$ (Ln: La, Pr, Nd, Sm, Gd, or Dy)

Figure 8. *XRD patterns of orthorhombic LnCoO$_3$ (Ln: La, Pr, Nd, Sm, Gd, and Dy).*

We have prepared several rare earth cobaltites, $LnCoO_3$ (Ln= Pr, Nd, Sm, Gd and Dy) with the orthorhombic crystal structure and $LaCoO_3$ with rhombohedral structure, by heating citrate gels to relatively high temperatures and examined their photocatalytic water oxidation properties. The XRD patterns of the cobaltites are shown in **Figure. 8**, and their crystallite size and BET surface areas listed in **table 1.**

The oxygen evolved by these orthorhombic cobaltites per mole of Co are presented in **Figure 9(a)**. $LaCoO_3$ exhibits the best oxygen evolution catalytic activity with a TOF of $1.4×10^{-3}$ s^{-1}. $DyCoO_3$ shows poor catalytic activity with a TOF $2.8×10^{-4}$ s^{-1}. All the other cobaltites show catalytic activity between these two. On calculating the O_2 evolution activity per unit surface area, $LaCoO_3$ (Rhombohedral, $R\bar{3}C$) remains the most active catalyst with the 49 mmol/mole of $Co.m^2$ while all orthorhombic cobaltites show comparable activities with a yield of 34.6±3.4 mmol/mole of $Co.m^2$ as shown in **Figure. 9(b)**.
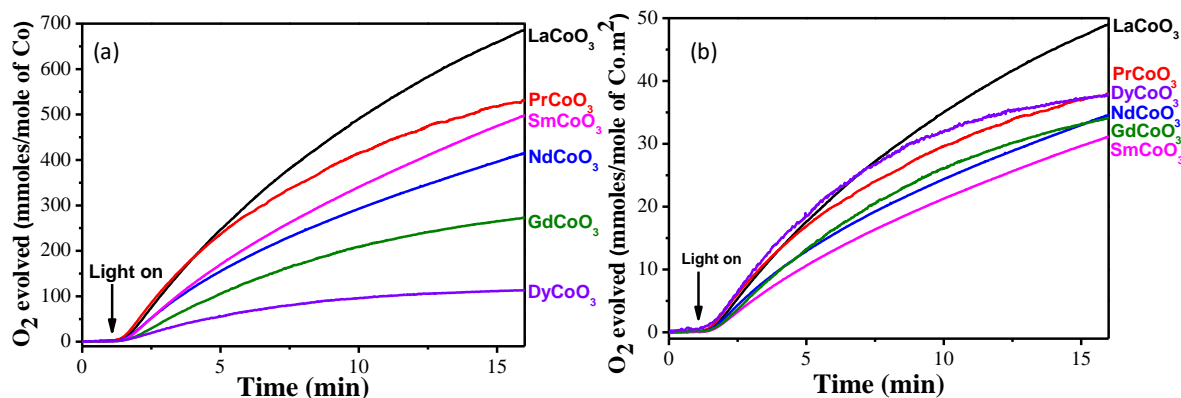

Figure 9. *O_2 evolved by rare earth cobaltates (a) per mole of Co, (b) per mole of Co per unit surface area.*

It is reported that monophasic orthorhombic $YbCoO_3$ cannot be prepared for heating the citrate gel even to high temperatures [48]. What one gets

instead is a solid solution of Co_2O_3 in Yb_2O_3 in the cubic rare earth oxide structure, with the cobalt in the +3 state. We prepared the solid solutions of the formula (Ln_2O_3) (Co_2O_3), $(Ln = Dy, Y, Er$ and $Yb)$ with the cubic structure by heating the citrate gels to 700°C or lower. The XRD patterns of the Dy-Co-citrate gel heated at different temperatures are shown in **Figure. 10 (a)** along with the XRD patterns of Dy_2O_3 **(Figure. 10(b))** prepared by the same method. The gel heated at 500°C and 700°C yields oxides crystallizing in the cubic structure similar to Dy_2O_3 and can be treated as the solid solutions (Dy_2O_3) (Co_2O_3). Samples heated at 800°C and 900°C, however, crystallize in the orthorhombic perovskite structure.
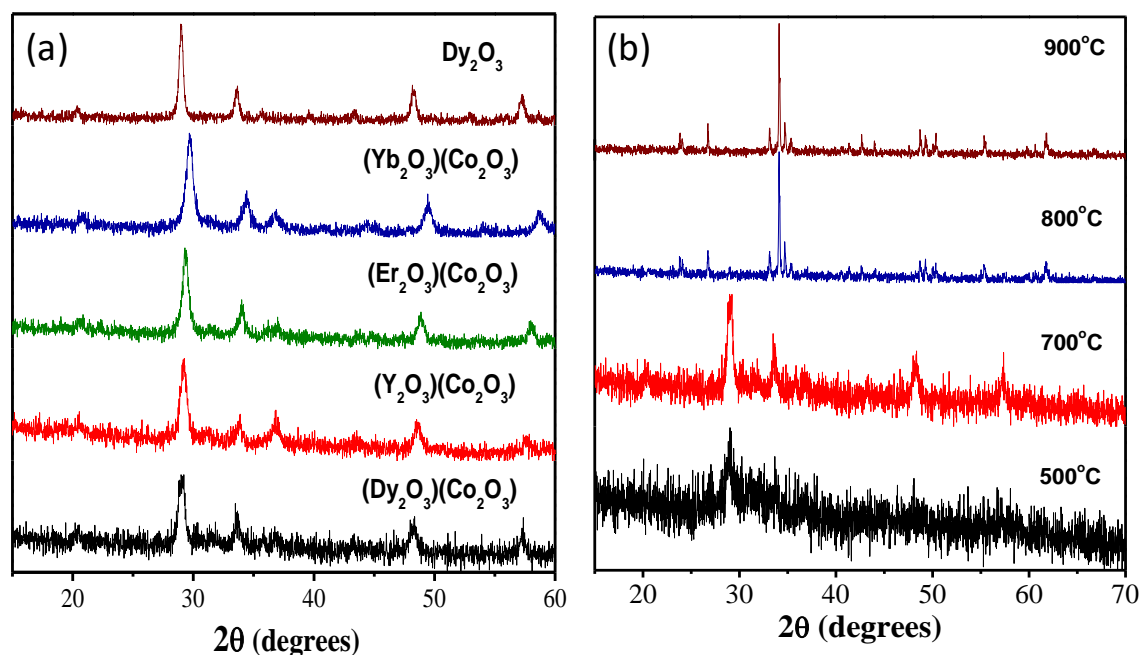
Figure 10. *XRD patterns of (a) Dy, Co citrate gel heated at 500°C, 700°C, 800°C, 900°C, (b) $(Ln_2O_3)(Co_2O_3)$ (Ln: Dy, Y, Er, Yb) solid solutions and Dy_2O_3 prepared at 700 °C.*

We found that in the case of yttrium the cubic phase occurs up to 700°C and a mixture of the cubic and orthorhombic phases above 700°C. We obtain only the cubic Ln_2O_3+Co_2O_3 solid solution up to 900°C in the

case of Er and Yb **(Figure. 11)**. Cubic C-type structures of Dy, Y, Er and Yb cobalt oxide derivatives prepared at 700°C are shown in **Figure.10 (b)**.
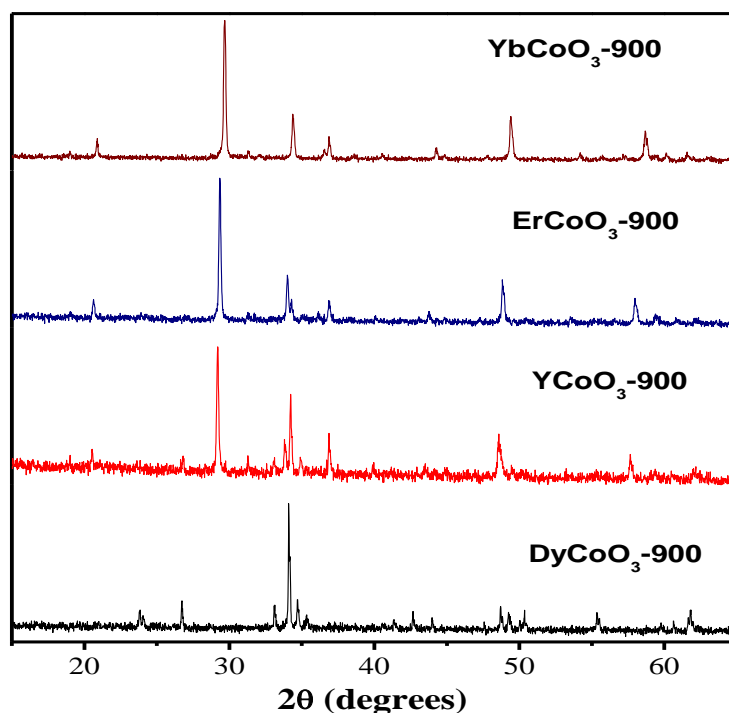
Figure 11. *XRD patterns of (Ln$_2$O$_3$) (Co$_2$O$_3$) (Ln: Dy, Y, Er, and Yb) solid solutions heated at 900 °C.*

All the cubic solid solutions of Co$_2$O$_3$ with Ln$_2$O$_3$ (Ln = Dy, Y, Er, and Yb) show excellent catalytic activity with TOF values between 7.9×10^{-4} and 1.3×10^{-3} s^{-1} **(Figure. 12(a))**.
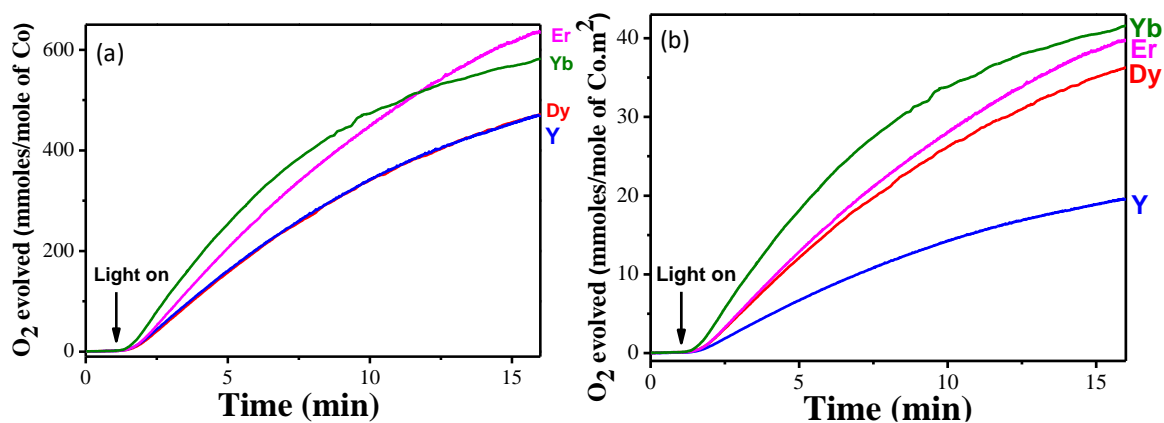
Figure 12. *O$_2$ evolved by (Ln$_2$O$_3$)(Co$_2$O$_3$) (Ln: Dy, Y, Er, and Yb) prepared at 500 °C (a) per mole of Co, (b) per mole of Co per unit surface area.*

The oxygen evolved per mole of Co per unit surface area is shown in **Figure. 12(b).** The cubic solid solution of Co_2O_3 with Y_2O_3 show somewhat lower catalytic activity of 19.5 mmol/mole of Co.m^2 after 15 min, but all the other solid solutions show a high activity of around 38.9±2.7 mmol/mole of Co.m^2 after 15 min. Having found good catalytic activity in solid solutions of Co_2O_3 and Ln_2O_3, we examined the electronic configuration of Co in these oxides by carrying out magnetic susceptibility measurements of the solid solution of Y_2O_3 and Co_2O_3. The plot of inverse magnetic susceptibility as a function of temperature **(Figure.13)** gives a magnetic momentum 2.41 μB, indicating that cobalt in the intermediate-spin state, $t_{2g}^5 e_g^1$. Interestingly, the yield of O_2 evolved by these solid solutions per mole of Co per unit surface area (38.9±2.7 mmol/mole of Co.m^2) is comparable to that of orthorhombic perovskite LnCoO$_3$ (34.6±3.4 mmol/mole of Co.m^2), the only commonality between the two is the electronic configuration of Co ($t_{2g}^5 e_g^1$).
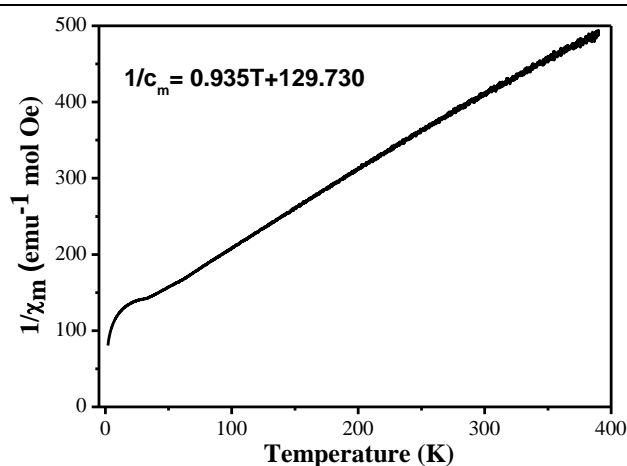

$$1/c_m = 0.935T + 129.730$$

Figure 13. *Magnetic susceptibility plot of (Y₂O₃) (Co₂O₃).*

We compare the activity of the catalyst studied scaled to their surface are and is listed in **table 1**.

Table 1. Calcination conditions, crystallite size calculated from XRD, BET surface area measured by N$_2$ adsorption at 77K, O$_2$ evolved per mole of catalyst, O$_2$ evolved per mole of catalyst per unit surface area of lanthanide manganites, cobaltites, ferrites, and nickelates.

Sample	Calcination temperature (°C) and duration (h)	Crystallite size (nm)	BET Surface area (m^2/g)	O$_2$ evolved (mmole/ mole of catalyst)$^\&$	O$_2$ evolved (mmole/ mole of catalyst. m^2)$^\&$
@LaMnO$_3$	800, 5h	18	24	197	8.2
@LaFeO$_3$	700, 5h	19	29	48	1.7
@LaCoO$_3$	500, 8h	16	14	687	49
@LaNiO$_3$	700, 5h	14	12	76	6.3
NdMnO$_3$	800, 5h	26	12	131	10.9
SmMnO$_3$	800, 5h	32	11	114	10.3
GdMnO$_3$	800, 5h	35	9	107	11.9
DyMnO$_3$	800, 5h	33	13	116	8.9
#YMnO$_3$	800, 5h	23	20	39	1.9
#YbMnO$_3$	800, 5h	27	15	59	3.9
PrCoO$_3$	500, 8h	23	14	532	38
NdCoO$_3$	500, 8h	24	12	415	34.5
SmCoO$_3$	500, 8h	29	16	498	31.2
GdCoO$_3$	700, 8h	47	8	273	34.1
DyCoO$_3$	800, 8h	67	3	114	38
!(Dy$_2$O$_3$)(Co$_2$O$_3$)	500, 8h		13	471	36.2
!(Y$_2$O$_3$)(Co$_2$O$_3$)	500, 8h		24	468	19.5
!(Er$_2$O$_3$)(Co$_2$O$_3$)	500, 8h		16	634	39.6
!(Yb$_2$O$_3$)(Co$_2$O$_3$)	500, 8h		14	582	41.6

 # Hexagonal Perovskite !Cubic (solid solution) Rest all are Orthorhombic Perovskites

$^\&$ After 15 min of illumination

We have compared the O_2 evolution activities (TOF values) of best reported manganese, cobalt based catalysts with our catalysts and shown in **Table 2.** The activities of some of our catalysts are comparable with best reported values.

Table 2. Comparison O_2 evolution activities (Turn of Frequencies, TOF) of our oxygen evolution catalysts with reported catalysts.

Catalyst	TOF/ s^{-1}	Reference
λ-MnO_2	3×10^{-5}	27
δ-MnO_2	1.56×10^{-5}	28
Mn_3O_4	1.6×10^{-4}	30
Mn_2O_3	5×10^{-4}	43
$MgMn_2O_4$	0.8×10^{-4}	43
$LaCoO_3$	1.4×10^{-3}	43
$Li_2Co_2O_4$	1.0×10^{-3}	33
$LaCoO_3$	1.4×10^{-3}	Present work
$LaMnO_3$	4.8×10^{-4}	Present work
$LaNiO_3$	1.2×10^{-4}	Present work
$LaFeO_3$	8.9×10^{-5}	Present work
$DyCoO_3$	2.8×10^{-4}	Present work
$YMnO_3$	5.2×10^{-5}	Present work
$YbMnO_3$	9.2×10^{-5}	Present work
$(Er_2O_3)(Co_2O_3)$	1.3×10^{-3}	Present work
$(Y_2O_3)(Co_2O_3)$	7.9×10^{-4}	Present work

4.2 Composites of Pt and LaMO₃ (M=Co or Mn)

Nanoparticles of LaCoO₃ and LaMnO₃ prepared by the citrate sol-gel method were examined by XRD patterns as shown in the previous section. energy dispersive spectra and TEM images of LaCoO₃ nanoparticles grafted with 5 wt% of Pt are shown in **Figure. 14**. **Figures 14 (a) and (b)** shows Pt nanoparticles residing on the LaCoO₃ particles. The amount of Pt is found to be ~ 5.3 wt % as confirmed from energy dispersion spectrum (EDS).
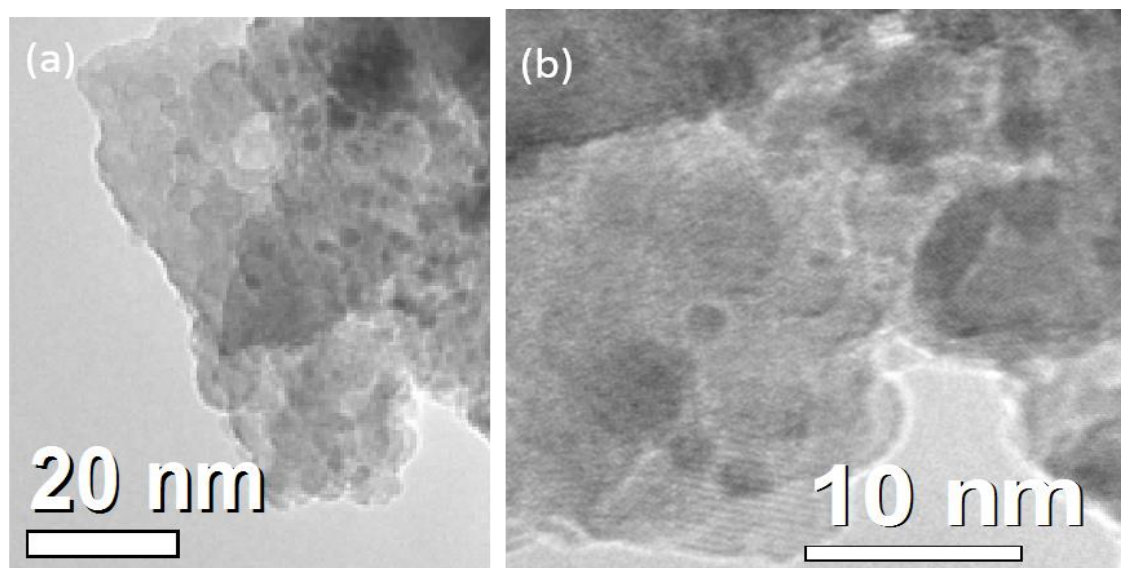

Figure.14. (a) and (b) TEM images (c) EDS spectrum of LaCoO₃: Pt (5wt %) composite.

To map out the distribution of Pt on the nanoparticles we performed elemental mapping via EDS. **Figure. 15** shows LaCoO₃ grafted with 5 and 2 wt % platinum, indicating a uniform distribution of the particles. From TEM and elemental mapping, we have observed that platinum grafting occurs on LaCoO₃ nanoparticles and not outside oxide nanoparticles. Oxygen evolution properties for the composites were examined.
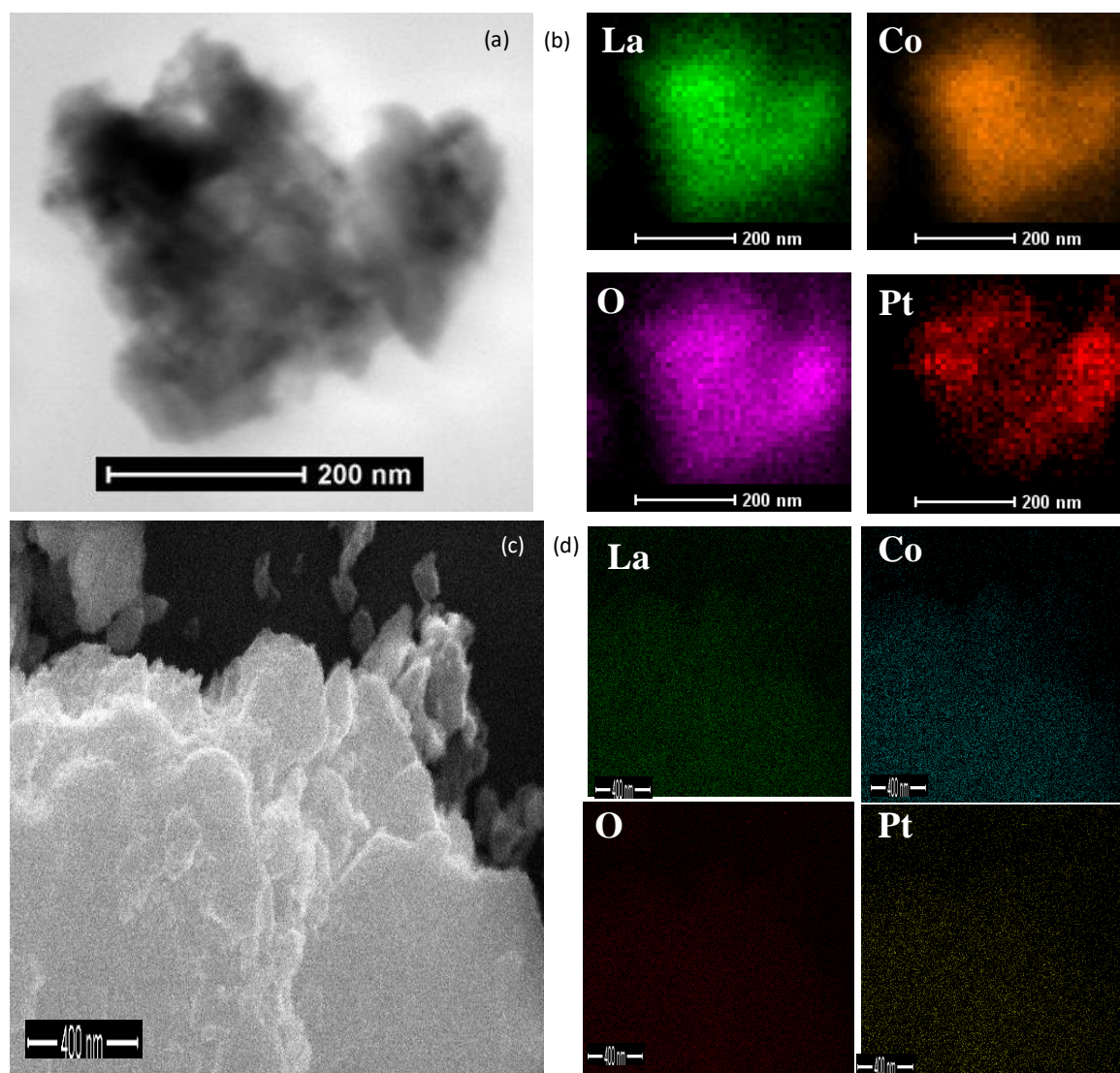
Figure. 15. *The elemental mapping of La, Co, O, and Pt of LaCoO₃: Pt (5wt%) composite.*

Oxygen evolution properties of $LaCoO_3$ and $LaMnO_3$ and their composites with Pt nanoparticles were studied, using $[Ru(bpy)_3]^{2+}$ as the sensitizer and $Na_2S_2O_8$ as the sacrificial agent. Oxygen in artificial photosynthesis resulting from the oxidation of water catalyzed by the perovskite oxides $LaCoO_3$ and $LaMnO_3$ is significantly enhanced by Pt nanoparticles. $[Ru(bpy)_3]^{2+}$ gets sensitized in the presence of light, this excited state oxidizes to $[Ru(bpy)_3]^{3+}$ via $Na_2S_2O_8$ reduction. Reduction of $[Ru(bpy)_3]^{3+}$ will go back to $[Ru(bpy)_3]^{2+}$ is facilitated by electrons which are

generated from water oxidation. $LaCoO_3$ is site of water oxidation and electron transfer site to $[Ru(bpy)_3]^{3+}$ which reduces to $[Ru(bpy)_3]^{2+}$. The rate of electron transfer can be facilitated by Pt nanoparticles which enhances the activity of the catalyst.
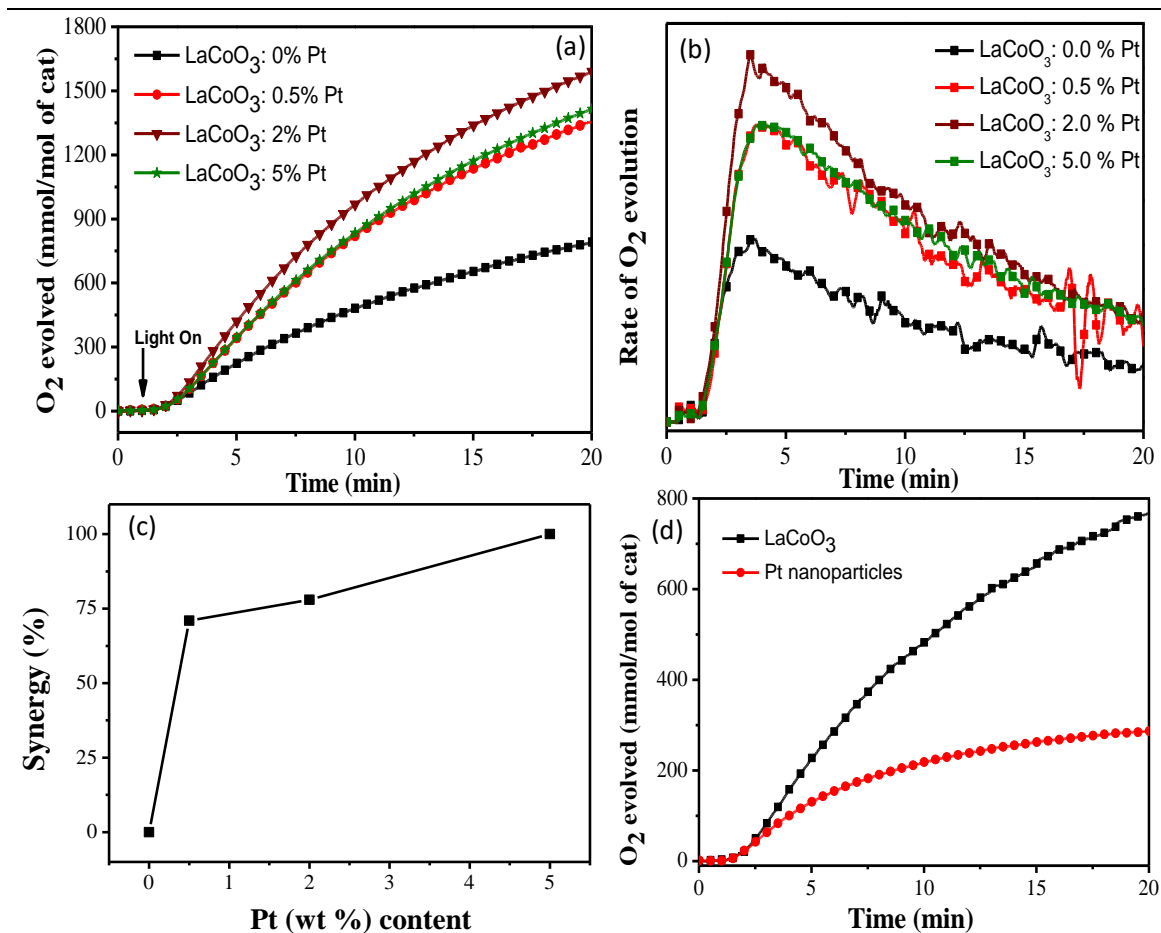
Figure. 16. *(a) O_2 evolution and (b) Rate of O_2 evolution with respect to time per mole of the catalyst of $LaCoO_3$ and composites of Pt with different wt percent (0.5,2,5 wt %) and (c) The synergy gain with respect to $LaCoO_3$. (d) O_2 evolution of Pt nanoparticles in comparison with $LaCoO_3$ nanoparticles.*

Figure. 16a shows the oxygen evolution activity (mmol/mol of the catalyst) of $LaCoO_3$ and its Pt composites with different weight percentages (0.5, 2, 5 wt %). The O_2 evolved from $LaCoO_3$ was 790 mmoles of O_2 per mole of the catalyst after 20 mins with a turn over frequency (TOF) 1.4x

10^{-3} s^{-1}. The $LaCoO_3$: Pt composite with 0.5wt% exhibits an evolution of 1352 mmoles of O_2 per mole of the catalyst with a TOF 2.33×10^{-3} s^{-1} having synergy of 71 % with respect to $LaCoO_3$ alone, with 2 wt% of Pt, 1588 mmole of O_2 per mole of the catalyst are evolved with TOF 2.82×10^{-3} s^{-1}, and having synergy of 100 % with respect to $LaCoO_3$ alone, with 5 wt% of Pt 1412 mmole of O_2 per mole of the catalyst were evolved with TOF 2.34×10^{-3} s^{-1} having synergy of 78 % with respect to $LaCoO_3$ alone. The synergy is shown in **Figure 16 c**. Thus, oxygen evolution increases with the increase of Pt loading content reaching a maximum value at 2wt%. Clearly, platinum acts as a co-catalyst and promotes electron the transfer process from $LaCoO_3$ to the dye. At high Pt loading, the activity decreases slightly due to the decrease in the availability of the $LaCoO_3$ sites for the OER [49-50]. In **Figure 16b**, we see that the rate of O_2 evolution is also higher for Pt composites compared to that of $LaCoO_3$ alone. The rate of O_2 evolution was higher for 2wt% Pt composite being more than two times that $LaCoO_3$ alone. In order to find out whether Pt nanoparticles act as a co-catalyst for reaction (1) or in reducing H^+ ions by reaction (2), we have carried out control experiments. The hydrogen evolution was studied under similar condition. We failed to find any H_2 as a reaction product, indicating that the Pt nanoparticles are not involved in the proton reduction by reaction (2). Pt nanoparticles alone show some O_2 evolution, but the amount is considerably less than $LaCoO_3$ (287 mmol of O_2 per mole of the Pt after 20 min **(Figure 16 d)**. We have studied the OER activity of Pt composites of $LaMnO_3$ in comparison with that of $LaMnO_3$. As the activity was maximum for 2wt% of Pt in the case of $LaCoO_3$, we synthesized a $LaMnO_3$: Pt with 2

wt% Pt. Oxygen evolution activity of $LaMnO_3$ was 212 mmol of O_2 per mole of the catalyst after 20 mins with a TOF $5x\ 10^{-4}$ s^{-1} and while that of the $LaMnO_3$: Pt composites was 313 mmol of O_2 per mole of the catalyst with TOF $6x10^{-4}$ s^{-1} as shown in **(Figure. 17 a)**. The rate of O_2 evolution activity was 1.6 times higher for Pt composite compared $LaMnO_3$ alone **(Figure 17 b)**.
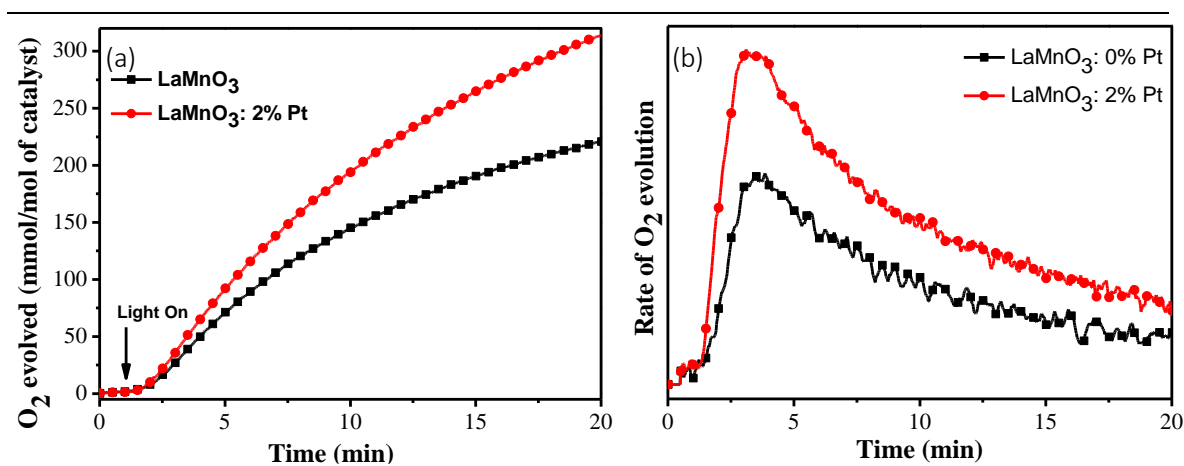

Figure 17. *(a) O_2 evolution (b) Rate of O_2 evolution with respect to time per mole of the catalyst of $LaMnO_3$ and composites of Pt with 2% wt percent.*

O_2 evolved in the presence of $LaCoO_3$: Pt composite was much more than the sum of the contributions of $LaCoO_3$/ $LaMnO_3$ and Pt, indicating synergy.

5. Conclusions

Orthorhombic rare earth manganites LnMnO$_3$ (Ln= La, Nd, Sm, Gd, and Dy) with the perovskite structure exhibit reasonably good photocatalytic properties for the oxidation of water unlike the hexagonal manganites, YbMnO$_3$ and YMnO$_3$. The presence of Mn^{3+} ions ($t_{2g}^3 e_g^1$) in the distorted octahedral environment in the orthorhombic manganites is clearly an important factor. In the rare earth cobaltites of perovskite structure LaCoO$_3$ (Rhombohedral, R$\overline{3}$C) shows the highest catalytic activity, while the other orthorhombic cobaltites LnCoO$_3$ (Ln= Pr, Nd, Sm, Gd and Dy) show comparable activity, although little lower than that of LaCoO$_3$. In all these cobaltites the Co^{3+} ion is in the intermediate spin ($t_{2g}^5 e_g^1$) states. The heavier rare earths (Dy, Er, Yb and Y) do not form orthorhombic perovskites readily and remain in the form of cubic solid solutions of Co^{3+} in Ln$_2$O$_3$ when prepared around 700°C or lower. These solid solutions with the cubic C-type rare earth oxide structure containing Co^{3+} present in the intermediate-spin configuration ($t_{2g}^5 e_g^1$) just as in LaCoO$_3$, interestingly exhibit catalytic activity for the oxidation of water comparable to LaCoO$_3$.

Pt nanoparticles act as good co-catalysts for the perovskite oxides LaCoO$_3$ and LaMnO$_3$ in the electron transfer reaction causing the oxidation of water. Thus 2% Pt enhances the amount of oxygen evolved 60-100 %, accompanied by an increase in the turn over factor. The increase in oxygen evolution is not due to the scavenging action of the Pt nanoparticles wherein they favor the reduction of protons.

6. References

1. N. Armaroli, V. Balzani, Angew. Chem. Int. Ed., 46, 2007, 52.

2. N.S. Lewis, D. G. Nocera, Proc. Natl. Acad. Sci. USA, 2006,103, 15729.

3. W. Ru¨ttinger, G. C. Dismukes, Chem. Rev., 1997, 97, 1.

4. N. D. Morris, M. Suzuki, and T. E. Mallouk, J. Phys. Chem. A., 2004, 108, 9115.

5. F.A. Frame, T.K. Townsend, R.L. Chamousis, E.M. Sabio, Th. Dittrich, N.D. Browning, F.E. Osterloh, J. Am. Chem. Soc., 2011, 133, 7264.

6. E. Tsuji, A. Imanishi, K. Fukui, Y. Nakato, Electrochim. Acta., 2011, 56, 2009.

7. Y. Lee, J. Suntivich, K.J. May, E.E. Perry, Y. Shao-Horn, J. Phys. Chem. Lett., 2012, 3, 399.

8. A. Harriman, I.J. Pickering, J.M. Thomas, P.A. Christensen, J. Chem. Soc., Faraday Trans., 1988, 1, 84, 2795.

9.   L. Vogt, D. J. Vinyard, S. Khan, G. W. Brudvig, Current Opinion in Chemical Biology, 2015, 25, 152.

10. R. Abe. J. Photochem. Photobio. C 2010, 11, 179.

11. V. Yachandra, V. DeRose, M. Latimer, I. Mukerji, K. Sauer and M. Klein. Science, 1993, 260, 675.

12. J. Penner-Hahn. in Metal Sites in Proteins and Models Redox Centres Vol. 90 Structure & Bonding (eds H. A. O. Hill, P. J. Sadler, & A. J. Thomson) Ch. 1, 1-36 (Springer Berlin Heidelberg, 1998).

13. J. Yano, J. Kern, K. Sauer, M. J. Latimer, Y. Pushkar, J. Biesiadka, B. Loll, W. Saenger, J. Messinger, A. Zouni and V. K. Yachandra. Science, 2006, 314, 821.

14. Z. Athina, W. Horst-Tobias, K. Jan, F. Petra, K. Norbert, S. Wolfram and O. Peter. Nature, 2001, 409, 739.

15. K. N. Ferreira, T. M. Iverson, K. Maghlaoui, J. Barber and S. Iwata. Science, 2004, 303, 1831.

16. E. M. Sproviero, J. A. Gascón, J. P. McEvoy, G. W. Brudvig and V. S. Batista. J. Am. Chem. Soc., 2008, 130, 3428.

17. J. P. McEvoy and G. W. Brudvig. Chem. Rev., 2006, 106, 4455.

18. P. E. M. Siegbahn. Chem Eur. J., 2006, 12, 9217.

19. Y. Umena, K. Kawakami, J.-R. Shen and N. Kamiya. Nature, 2011, 473, 55.

20. K. Kawakami, Y. Umena, N. Kamiya, and J.-R. Shen. J. Photochem. Photobio., B, 2011, 104, 9.

21. G. C. Dismukes, R. Brimblecombe, G. A. N. Felton, R. S. Pryadun, J. E. Sheats, L. Spiccia and G. F. Swiegers. Acc. Chem. Res., 2009, 42, 1935.

22. R. Brimblecombe, A. Koo, G. C. Dismukes, G. F. Swiegers and L. Spiccia. J. Am. Chem. Soc., 2010, 132, 2892.

23. D. González-Rodríguez, E. Carbonell, G. d. M. Rojas, C. A. Castellanos, D. M. Guldi and T. Torres. J. Am. Chem. Soc., 2010, 132, 16488.

24. G. Kodis, P. A. Liddell, A. L. Moore, T. A. Moore, and D. Gust. J. Phys. Org. Chem., 2004, 17, 724.

25.   M.M. Najafpour, T. Ehrenberg, M. Wiechen, P. Kurz, Angew. Chem., Int. Ed., 2010, 49, 2233.

26. A. Iyer, J. Del-Pilar, C.K. King'ondu, E. Kissel, H.F. Garces, H. Huang, A.M. ElSawy, P.K. Dutta, S.L. Suib, J. Phys. Chem. C, 2012, 116, 6474.

27.   D.M. Robinson, Y.B. Go, M. Greenblatt, G.C. Dismukes, J. Am. Chem. Soc., 2010, 132, 11467.

28. V.B.R. Boppana, S. Yusuf, G.S. Hutchings, F. Jiao, Adv. Funct. Mater., 2013, 23, 878.

29.   V.B.R. Boppana, F. Jiao, Chem. Commun., 2011, 47, 8973.

30.   D.M. Robinson, Y.B. Go, M. Mui, G. Gardner, Z. Zhang, D. Mastrogiovanni, E. Garfunkel, J. Li, M. Greenblatt, G.C. Dismukes, J. Am. Chem. Soc., 2013, 135, 3494.

31. D. Shevchenko, M.F. Anderlund, A. Thapper, S. Styring, Energy Environ. Sci., 2011, 4, 1284.

32.   F. Jiao, H. Frei, Angew. Chem., Int. Ed., 2009, 48, 1841.

33.   G.P. Gardner, Y.B. Go, D.M. Robinson, P.F. Smith, J. Hadermann, A. Abakumov, M. Greenblatt, G.C. Dismukes, Angew. Chem., Int. Ed. 2012, 51, 1616.

34. M.W. Kanan, Y. Surendranath, D.G. Nocera, Chem. Soc. Rev., 2009, 38, 109.

35. Y. Yamada, K. Yano, D. Hong, S. Fukuzumi, Phys. Chem. Chem. Phys., 2012, 14, 5753.

36. I. Zaharieva, M. M. Najafpour, M. Wiechen, M. Haumann, P. Kurz and H. Dau. Energy Environ. Sci., 2011, 4, 2400.

37. A. Ramírez, P. Bogdanoff, D. Friedrich and S. Fiechter. Nano Energy, 2012, 1, 282.

38. N. S. McCool, D. M. Robinson, J. E. Sheats and G. C. Dismukes. J. Am. Chem. Soc., 2011, 133, 11446.

39. M. D. Symes, D. A. Lutterman, T. S. Teets, B. L. Anderson, J. J. Breen and D. G. Nocera. Chem. Sus. Chem, 2013, 6, 65.

40. F. Jiao and H. Frei. Chem. Comm., 2010, 46, 2920.

41. M. W. Kanan, J. Yano, Y. Surendranath, M. Dincă, V. K. Yachandra and D. G. Nocera. J. Am. Chem. Soc., 2010, 132, 13692.

42. D. K. Zhong and D. R. Gamelin. J. Am. Chem. Soc., 2010, 132, 4202.

43. U. Maitra, B.S. Naidu, A. Govindaraj, C.N.R. Rao, Proc. Natl. Acad. Sci. USA, 2013, 110, 11704.

44. J. Suntivich, K.J. May, H.A. Gasteiger, J.B. Goodenough, Y. Shao-Horn, Science, 2011, 334, 1383.

45. J.-S. Zhou, J.B. Goodenough, J.M. Gallardo-Amores, E. Morán, M.A. Alario, Phys. Rev. B, 2006, 74, 014422

46. A. Filippetti, N.A. Hill, J. Magn. Magn. Mater., 2006, 236, 176

47. T.A. Betley, Y. Surendranath, M.V. Childress, G.E. Alliger, R. Fu, C.C. Cummins, D.G. Nocera Philos. Trans. R. Soc. B, 2008, 363, 1293

48. L.B. Farhat, M. Amami, E.K. Hlil, R.B. Hassen J. Alloys Compd., 2009, 479, 594

49. T. Uchihara, M. Matsumura, A. Yamamoto and H. Tsubomura, J. Phys. Chem., 1989, 93, 5870

50. N. Bao, L. Shen, T. Takata and K. Domen, Chem. Mater., 2008, 20, 110.

SUMMARY OF THE THESIS

Energy crisis is a severe problem of facing mankind due to the rapidly diminishing reserves of fossil fuels. Therefore, a new energy carrier needs to be found. Hydrogen is a suitable choice since it has high energy density and it can be generated from water which is earth-abundant. Water splitting is an uphill reaction and requires a significant amount of energy to split into its constituent elements H_2 and O_2. However, we can carry out this process with the help of suitable catalysts using light or light and electricity. In this thesis, we have explored various catalysts and strategies to split water into hydrogen and oxygen.

Part 1 consists of 6 chapters which explore the role of transition metal dichalcogenides as catalysts for the hydrogen evolution reaction (HER). We have investigated strategies like phase-engineering or coupling with other active HER materials. Theoretical investigations have been carried out to improve our understanding of the catalysts. **Chapter 1** gives a general overview of photochemical hydrogen evolution including challenges and strategies. Further criteria to select a suitable catalyst with an emphasis on transition metal dichalcogenides (TMDs) as HER catalyst were discussed. **Chapter 2** explores group 6 TMDs for photochemical HER. HER properties of the 2H-form of TMDs as well as the phase engineered 1T-form have been studied. We observe selenides are better than sulfides and the 1T-form to be highly superior to the 2H-form as a catalyst. In **Chapter 3,** we covalently link MoS_2 with 2D materials and study their HER properties. For example, covalent assemblies of MoS_2 with RGO and C_3N_4 were synthesized and

characterized. These heterostructures involve covalently linked layered assemblies. These assemblies have superior HER activity as compared to the individual layers. The enhanced HER activity can be attributed to the enhanced surface area as well as charge transfer across the network through covalent bonds.

Chapter 4 describes the role of substitution of selenium in tungsten sulfide in HER. Sulfoselenides of tungsten were synthesized, characterized and their HER properties studied. We observe that sulfoselenides exhibit better catalytic activity than the sulfide or the selenide of tungsten. The superior catalytic activity is due to the distorted structure of the ternary compounds which activates inactive basal planes for HER. In **Chapter 5** we have explored a group-4 TMD (TiS_2) and a group-5 TMD (TaS_2) for photochemical HER. We have synthesized nanocomposites of TiS_2 and TaS_2 with CdS and explored their HER properties. We observe that nanocomposites of TaS_2 exhibit superior HER activity compared to those of TiS_2. The superior activity of TaS_2 is due to the metallic nature of TaS_2. Guided by theoretical investigations, we have explored the HER properties of gallium chalcogenides in **Chapter 6**. GaTe exhibits superior HER activity relative to other gallium chalcogenides.

In **Part 2** we explore topologically non-trivial materials like Weyl semimetals and topological insulators for photochemical HER. The superior catalytic is activity observed with the non-trivial type II Weyl semimetal. 1T'-$MoTe_2$, compared to the semiconducting 2H-form or trivially metallic 1T-TaS_2. This observation suggests that intrinsic metallicity by itself does not assure

catalytic activity. Further, we have explored transition metal pnictides (NbP, NbAs, TaP and TaAs), which are type I Weyl semimetals. The phosphides exhibited superior activity than arsenides. The robust surface states which protect electron scattering along with large room temperature mobility, both originate from the Dirac bands of the Weyl semimetals is responsible for the high HER activity. We further explored the activity of another class of topologically non-trivial material, topological insulators like Bi_2Te_3 and Bi_2Se_3. The activity in the topological insulators comes from both surface and the bulk, moreover, the surface states prolonged the lifetime of the electron on the surface which increases the probability of the HER. Though, topological insulators do not exhibit robust catalytic activity over an extended period.

Part 3 consists of studies of electrochemical hydrogen evolution reaction (HER), an alternative to photochemical means. The fullerene structure of MoS_2 has an advantage over the few-layer forms due to exposed MoS_2 edges due to its morphology. We have used doped fullerene of MoS_2, both n-type (Re-atom) and p-type (Nb-atom) and study HER overall pH ranges. We find that n-type MoS_2 fullerene is better at low pH, while the p-type fullerene is better at higher pH. Fullerenes of MoS_2 exhibit good HER activity in sea-water.

In **part 4,** we discuss the role of another hydrogen carrier, hydrazine. Hydrazine is a liquid at under normal conditions, and possesses high hydrogen content compared to water. Unlike water, decomposition of hydrazine is a downhill reaction. Thermocatalytic decomposition of hydrazine although achievable at room temperature, do not give control over the

reaction. We have studied the photocatalytic decomposition of hydrazine using CdS as catalyst. The rate of hydrazine decomposition can be controlled by changing reaction conditions like the concentration of hydrazine or pH. The hydrazine concentration as low as 0.2 % v/v can be effectively decomposed on the catalyst surface. The photocatalytic decomposition of hydrazine thus gives control over decomposition reaction unlike in thermochemical reaction.

Part 5 focuses on water oxidation, especially the role of the e_g^1 electronic configuration of transition metals in oxides. We have studied Co^{3+} $(t_{2g}^5 e_g^1)$ and Mn^{3+} $(t_{2g}^3 e_g^1)$ based lanthanum oxides and to establish role of the e_g^1 configuration of the transition metal in water oxidation. Both, perovskites cobaltites and Co^{3+} containing cubic rare-earth sesquioxides exhibit good catalytic activity. In rare-earth manganites, only the orthorhombic structure with octahedral Mn^{3+} ions exhibit good activity while the hexagonal manganites exhibited poor activity. We have used Pt nanoparticles as co-catalysts and find that they have a synergistic role in water oxidation.